Idaho National Engineering and Environmental Laboratory

INEEL/EXT-02-00589
Volume 5
Revision 2.2
October 2003

SCDAP/RELAP5-3D© CODE MANUAL

VOLUME 5: ASSESSMENT OF MODELING OF REACTOR CORE BEHAVIOR DURING SEVERE ACCIDENTS

SCDAP/RELAP5-3D© Code Development Team

BECHTEL BWXT IDAHO, LLC

INEEL/EXT-02-00589
Volume 5
Revision 2.2

SCDAP/RELAP5-3D© CODE MANUAL VOLUME 5: ASSESSMENT OF MODELING OF REACTOR CORE BEHAVIOR DURING SEVERE ACCIDENTS

SCDAP/RELAP5-3D© Code Development Team

October 2003

Idaho National Engineering and Environmental Laboratory
BECHTEL BWXT IDAHO, LLC
Idaho Falls, Idaho 83415

Prepared Under DOE Contract No. DE-AC07-99ID13737

ABSTRACT

The SCDAP/RELAP5-3D© code has been developed for best-estimate transient simulation of light water reactor coolant systems during a severe accident. The code models the coupled behavior of the reactor coolant system and reactor core during severe accidents as well as large and small break loss-of-coolant accidents, operational transients such as anticipated transient without SCRAM, loss of offsite power, loss of feedwater, and loss of flow. The coolant system behavior is calculated using a two-phase model allowing for unequal temperatures and velocities of the two phases of the fluid, and the flow of fluid through porous debris and around blockages caused by reactor core damage. The reactor core behavior is calculated using models for the ballooning and oxidation of fuel rods, the meltdown of fuel rods and control rods, fission product release, and debris formation. The code also calculates the heatup and structural damage of the lower head of the reactor vessel resulting from the slumping of reactor core material. A generic modeling approach is used that permits as much of a particular system to be modeled as necessary. Control system and secondary system components are included to permit modeling of plant controls, turbines, condensers, and secondary feedwater conditioning systems.

This report describes the most recently performed developmental assessment of the MOD3.3-specific refinements included in SCDAP/RELAP5-3D©. The assessment shows that the code's calculated behavior of fuel assemblies under severe accident conditions agree with available measurements. A wide range of fuel damage experiments and the TMI-2 accident were used to assess the following models: (1) integral diffusion model for oxidation of fuel rod cladding, (2) stress-based model for failure of oxide layer containing melted metallic cladding, (3) model for re-slumping of previously slumped and frozen cladding, (4) model for cracking of cladding oxide layer during reflood conditions and affect of cracking on oxygen transport, (5) models for flow losses and heat transfer in porous debris, (6) model for heat transfer in molten pool that has stratified into oxidic and metallic parts, and (7) model for break-up of jets of molten material slumping into a pool of water. The assessment results show improved predictions of the axial distribution in oxidation and meltdown of fuel assemblies and the behavior of fuel assemblies under reflood conditions. The assessment also demonstrates that the single set of models in the SCDAP/RELAP5-3D© allow users to accurately simulate fuel assembly damage phenomena in severe fuel damage experiments and nuclear power plants. The additional capabilities embodied in SCDAP/RELAP5-3D© models are not expected to affect results from this assessment.

CONTENTS

ABSTRACT iii

EXECUTIVE SUMMARY xi

1. INTRODUCTION 1-1
   - 1.1 References 1-1
2. Newer Models and Test Matrix for Assessment 2-1
   - 2.1 Reference 2-6
3. Assessment Using Results of Severe Fuel Damage Tests 3-1
   - 3.1 Models for Temperature Behavior of Fuel Assemblies 3-1
     - 3.1.1 Temperature Behavior of PWR Fuel Assemblies with Gradual Uncovery 3-2
     - 3.1.2 Temperature Behavior of PWR Fuel Assemblies with Complete Uncovery 3-2
     - 3.1.3 Temperature Behavior of BWR Fuel Assemblies with Complete Uncovery 3-8
     - 3.1.4 Temperature Behavior of Fuel Assemblies During Reflood 3-8
   - 3.2 Calculation of Hydrogen Production 3-9
   - 3.3 Model for Ballooning of Fuel Rod Cladding 3-11
   - 3.4 Models for Oxidation and Meltdown Using PIE Results 3-12
   - 3.5 Conclusions 3-14
4. Assessment of Late-Phase Models 4-1
   - 4.1 Models for Flow Loss and Heat transfer in Porous Debris 4-1
   - 4.2 Model for Heat Transfer In Stratified Molten Pool 4-4
   - 4.3 Model for Flow of Liquefied Material Through Porous Debris 4-7
   - 4.4 Model for Molten Fuel-Coolant Interaction 4-9
   - 4.5 TMI-2 Accident 4-12
   - 4.6 Conclusions 4-20
   - 4.7 References 4-21

FIGURES

3-1. Comparison of calculated and measured temperature at 2.37 m elevation for FLHT-5. 3-2
3-2. Comparison of calculated and measured temperatures at 0.7 m elevation for PBF SFD ST test. 3-3
3-3. Comparison of calculated and measured temperature at elevation of 0.7 m for PBF SFD 1-1 test. 3-4
3-4. Comparison of calculated and measured temperatures at 0.74 m and 0.54 m elevation for PBF SFD 1-4 test. 3-4
3-5. Comparison of calculated and measured temperature at 0.75 m for CORA-5 test. 3-5
3-6. Comparison of calculated and measured temperature at 0.75 m for CORA-7 test. 3-5
3-7. Comparison of calculated and measured temperatures of unheated fuel rod at elevation of 0.75 m for CORA-13 test. 3-6
3-8. Comparison of calculated and measured fuel temperatures at 0.7 m elevation for PHEBUS B9+ test. 3-7
3-9. Comparison of calculated and measured cladding temperatures at 0.7 m elevation for PHEBUS FPT0. 3-7
3-10. Comparison of calculated and measured temperatures of unheated rod at elevation 0.75 m for CORA-17 test. 3-8
3-11. Comparison of calculated and measured temperatures of fuel rod at elevation of 0.254 m for DF-4 test. 3-9
3-12. Comparison of calculated and measured temperatures at 0.5 m elevation for PBF SFD ST test. 3-10
3-13. Comparison of calculated and measured temperatures of unheated fuel rod at elevation of 0.55 m for CORA-13 test. 3-10
4-1. Schematic of debris bed analyzed for assessment of flow loss calculations. 4-2
4-2. Schematic of BNL quenching experiment. 4-3
4-3. Comparison of calculated and measured transient temperature distribution in debris bed. 4-4
4-4. Molten pool system analyzed for assessment of MOD3.3 models for heat transfer in stratified molten pool. 4-5
4-5. Temperature histories of oxidic and metallic parts of molten pool before and after stratification. 4-7
4-6. Ratio of heat flux to critical heat flux on external surface of lower head before and after stratification of molten pool. 4-8
4-7. Schematic of system analyzed and nodalization of system for calculation of melted material flowing through porous debris. 4-9
4-8. Distribution of debris bed saturation and temperature after melting of 30% of core plate (time of 1500 s). 4-10
4-9. Ratio of heat flux to CHF on external surface at bottom center of lower head. 4-10
4-10. Schematic of FARO Test Arrangement. 4-11
4-11. Comparison of calculated and measured pressure histories for FARO Test L-08. 4-12
4-12. History of calculated maximum temperature in reactor core. 4-15
4-13. History of calculated effective radius of molten pool. 4-16
4-14. Calculated hydrogen production during TMI-2 accident. 4-17

4-15. MOD3.3 calculated temperature histories of fuel rods in upper part of outer most fuel assemblies in reactor core. 4-18
4-16. MOD 3.3 calculated temperature history of location with porous debris (2.7 m elevation of fourth ring of fuel assemblies). 4-19

TABLES

2-1. Models tested in SCDAP/RELAP5/MOD3.3 2-2
2-2. Test matrix for developmental assessment of SCDAP/RELAP5/MOD3.3 2-4
2-3. Definition of test problems listed in Table 2-3. 2-4
3-1. Comparison of calculated and measured hydrogen production. 3-11
3-2. Comparison of calculated and measured ballooning behavior of fuel rods. 3-12
3-3. Comparison of calculated and measured axial distribution in fuel rod oxidation 3-13
4-1. Comparison of SCDAP/RELAP5 calculated flow losses for porous debris with those calculated by other benchmarked models 4-2
4-2. Comparison of SCDAP/RELAP5/MOD3.3 and benchmarked model calculations for heat transfer behavior of stratified molten pool with deep metallic layer. 4-5
4-3. Comparison of SCDAP/RELAP5/MOD3.3 and benchmarked model calculations for heat transfer behavior for case of shallow metallic pool 4-6
4-4. Calculated timing and sequence of core damage progression. 4-13

EXECUTIVE SUMMARY

The specific features of SCDAP/RELAP5-3D© are described in this five volume set of manuals covering the theory, use, and assessment of the code for severe accident applications.

The SCDAP/RELAP5-3D© computer code is designed to calculate for severe accident situations the overall reactor coolant system (RCS) thermal-hydraulic response, core damage progression, and reactor vessel heatup and damage. The SCDAP/RELAP5-3D© code evolved from the RELAP5 and SCDAP/RELAP5 codes developed at the Idaho National Engineering & Environmental Laboratory (INEEL) under sponsorship by the U.S. Nuclear Regulatory Commission (US NRC). Development of the RELAP5 code series began at the INEEL in 1975, while SCDAP development was initiated in the early 1970's with an active linkage to RELAP5 in 1979. The SCDAP/RELAP5-3D© code maintained all of the capabilities and validation history of the predecessor codes, plus the added capabilities sponsored by the DOE.

The RELAP5 code is based on a two-fluid model allowing for unequal temperatures and velocities of the fluids and the flow of fluid through porous debris and around blockages caused by reactor core damage. The models in SCDAP calculate the progression of damage to the reactor core. These models calculate the heatup, oxidation and meltdown of fuel rods and control rods, the ballooning and rupture of fuel rod cladding, the release of fission products from fuel rods, and the disintegration of fuel rods into porous debris and molten material. The SCDAP models also calculate the heatup and structural damage of the reactor vessel lower head resulting from the slumping to the lower head of reactor core material with internal heat generation. SCDAP/RELAP5-3D© can be used in analyses of fission product transport and deposition behavior and containment phenomena by linking it to the detailed fission product code, VICTORIA[1]or CONTAIN[2], respectively.

The SCDAP/RELAP5-3D© code includes many generic component models from which general systems can be simulated. The component models include fuel rods, control rods, pumps, valves, pipes, reactor vessel, electrical fuel rod simulators, jet pumps, turbines, separators, accumulators, and control system components. In addition, special process models are included for effects such as form loss, flow at an abrupt area change, branching, choked flow, boron tracking, and noncondensable gas transport. The code also includes a model for reactor kinetics.

This volume, Volume 5, contains detailed comparisons of measurements and calculations for a wide range of severe fuel damage experiments and for the TMI-2 accident. This report describes the most recently performed developmental assessment of the MOD3.3-specific refinements included in SCDAP/RELAP5-3D©. The assessment shows that the code's calculated behavior of fuel assemblies under severe accident conditions agree with available measurements. The assessment also demonstrates that the single set of models in the SCDAP/RELAP5-3D© allow users to accurately simulate fuel assembly damage phenomena in severe fuel damage experiments and nuclear power plants. The additional capabilities embodied in SCDAP/RELAP5-3D© models are not expected to affect results from this assessment.

---

1. N. E. Bixler, "VICTORIA2.0: A Mechanistic model for Radionuclide Behavior in a Nuclear Reactor Coolant System Under Severe Accident Conditions," NUREG/CR-6131, SAND93-2301, December 1998.
2. K. D. Bergeron et al., *User's Manual for CONTAIN 1.0, A Computer Code for Severe Nuclear Reactor Accident Containment Analysis*, NUREG/CR-4085, SAND84-1204, May 1985

1. INTRODUCTION

This report describes the most recently performed developmental assessment of models in the SCDAP/RELAP5-3D© code. Developmental assessments achieve four objectives: First, they apply the code to a broad range of problems in order to reveal and resolve errors not uncovered in previous applications. Second, they verify that the code is capable of modeling the most important phenomena that occur during severe accidents. Third, they verify that the new models implemented into the code performs correctly in the context of severe accidents in Light Water Reactors (LWRs). Fourth, they evaluate the capability of the most recent version of the code relative to previous versions.

The assessments described in this volume were performed for MOD3.3-specific refinements[1-1] included in SCDAP/RELAP5-3D©. The developmental assessment of MOD3.2 of the SCDAP/RELAP5 code is described in Reference 1-2. It is not anticipated that new models implemented into the SCDAP/RELAP5-3D© code will impact the assessments documented in this volume. However, additional assessments will be included prior to the next revision of this report.

This report has three additional sections that correspond with the three major elements in the developmental assessment effort. Section 2 summarizes the models that were not in the MOD3.2 version of the code and includes the test matrix devised to assess these new models. Section 3 summarizes the assessment of the code using the results of a broad range of severe fuel damage experiments. Section 4 summarizes the assessment of the models implemented into MOD 3.3 for late-phase damage progression. This section also evaluates the capability to calculate accident sequences such as the TMI-2 accident, TMLB’ accident sequences in a PWR, and a severe accident sequence in a BWR. The detailed results of each developmental assessment test problem are presented in Appendix A.

1.1 References

1-1. L. J. Siefken, E. W. Coryell, E. A. Harvego and J. K. Hohorst, *SCDAP/RELAP5/MOD3.3 Code Manuals, Volumes 1 though 5,* NUREG/CR-6150, Revision 2, INEL-96/0422, January 2001.

1-2. The SCDAP/RELAP5 Development Team, *SCDAP/RELAP5/MOD3.2 Code Manual, Volume V: Developmental Assessment,* NUREG/CR-6150 Rev. 1, INEL-96/0422, July 1998.

2. Newer Models and Test Matrix for Assessment

Several new models were implemented into more recent versions of SCDAP/RELAP5-3D©. The new models and the capabilities added to MOD3.3 of the code are summarized in Table 2-1. The new models include; (1) an integral diffusion method for calculating oxidation and hydrogen uptake in fuel rod cladding, (2) a model for the configuration of melted metallic cladding retained by an oxide layer and accounting for size of fuel-cladding gap, (3) a stress-based model for calculating failure of cladding oxide retaining melted metallic cladding, (4) heat transfer correlations specific to porous debris, (5) a model for calculating flow losses in porous debris that is based on Darcy's Law and relative permeabilities and passabilities (6) a core plate model for calculating heatup of the core plate and its interaction with material that slumps from the core region, (7) a model for calculating heat transfer for the case of a molten pool in the lower head stratified into oxidic and metallic pools, (8) a model for calculating the movement of melted core plate material through porous debris in the lower head and (9) a model for calculating the behavior of jets of core material slumping into a pool of water in the lower head of the reactor vessel.

Several models in previous versions of the code were also improved. The calculations of the oxidation of in situ and slumped cladding were extended to account for the effective surface areas for oxygen uptake. Corrections were made to the models for calculating the internal gas pressure in fuel rods and the conductance of the fuel-cladding gap.

MOD3.3 of the code also had changes made to improve its maintenance and use. Several features of Fortran 90 programming were implemented into the code so as to reduce the size of files used for restart and plotting. The Fortran 90 features also improve the efficiency of code maintenance operations. The output of the code was extended to include tables summarizing the timing and spatial distribution of various damage progression events.

A broad assessment was required of MOD3.3 due to the broad scope of the new models added to the code and other changes made to the code. The calculations of almost every aspect of reactor core behavior during the early-phase of a severe accident (phase before beginning of slumping of material to lower head) have been impacted by the new models and other changes. The results of severe fuel damage tests provide data for assessing the models calculating reactor core behavior during the early-phase of a severe accident. Some new models have also been added for calculating late-phase behavior, such as lower head heat transfer and the behavior of slumping core material. Although only a limited number of experiments have been performed for investigation of the late-phase of a severe accident, data exist for assessing some of these models, including the model for the behavior of jets slumping into a pool of water and the model for heat transfer in a stratified molten pool. Other new late-phase models, such as the model for the movement of melted core plate material through porous debris, can be assessed only by evaluating for internal consistency.

A test matrix for MOD3.3 with twenty two test problems was compiled to achieve the objective of a broad assessment. The test matrix is shown in Table 2-2. The test matrix includes problems ranging from the analyses of several severe fuel damage experiments to the analysis of the behavior of nuclear power plants during a severe accident. Each row in Table 2-2 corresponds with a model or code update unique to

MOD3.3. Each column in Table 2-2 corresponds with a test problem for which a solution by MOD3.3 provides information for assessing one or more models in MOD3.3. A short description of each test problem is given in Table 2-3 and a more detailed description of most of the test problems is given in Appendix A. For each column, an "X" is placed in the rows corresponding with models or code updates that can be assessed with that test problem. The problems are listed from left to right in the order of ascending fuel assembly damage. This order of solution is based on the logic that the calculation of late-phase damage is dependent on the calculation of the early-phase damage progression, which in turn is dependent upon the calculation of the rate of boiloff and convective cooling in fuel assemblies with deficient cooling. So the assessment began with the bundle boiloff test problem, then advanced to test problems solving experiments involving early-phase fuel damage progression and for which a significant amount of measurements are available, and then advanced to test problems calculating late-phase damage progression in LWRs. The broad range of the test problems resulted in an assessment of code updates such as the conversion of the code from Fortran 77 to Fortran 90, and improvements in code architecture, which involved changes in models whose mathematical basis was not changed but whose Fortran programming was changed.

Table 2-1. Models tested in SCDAP/RELAP5/MOD3.3.

Name	Extensions in capability provided by model
Integral diffusion[2-1]	(1) Thinning of oxide layer at steam-starved locations, which was not calculated by the previous parabolic kinetics model, (2) applicability to rapidly changing temperature and fluid conditions, which was not the case for the previous parabolic kinetics model, (3) representation of acceleration in oxygen uptake caused by cracks occurring in the oxide layer during reflood, which was represented in a more simplified fashion by the previous parabolic kinetics model, and (4) calculation of hydrogen uptake and associated heatup and embrittlement, which was not calculated by the previous parabolic kinetics model
Circumferential relocation[2-2]	(1) Melted metallic cladding retained by oxide layer configured as segment of annulus, which is consistent with PIE results of severe fuel damage tests, instead of as axisymmetric cylinder.

Table 2-1. Models tested in SCDAP/RELAP5/MOD3.3. (Continued)

Name	Extensions in capability provided by model
Oxide layer failure[2-2]	(1) Timing of failure of oxide layer retaining melted metallic cladding based on stress in oxide layer instead of on empirical model based on cladding temperature and fraction of oxidation. As a result, differences between timing of oxide failure in LWR and in severe fuel damage tests are consistent with differences in the basic mechanism causing failure of the oxide layer. This basic mechanism is the stress induced in the oxide layer by the temperature gradient in it, which is much larger for severe fuel damage tests than for fuel bundles in a LWR, because in severe fuel damage tests the nuclear heat generation rate is atypically large to compensate for heat loss from the relatively small test bundles (2) timing of failure of oxide layer based on whether it retains melting metallic cladding with no space for expansion during phase change from solid to liquid, as is the case for cladding oxidized on both outer and inner surfaces. In the case of double-sided oxidation, expansion of the metallic portion during the phase change causes stresses that fail the oxide layer.
Heat transfer in porous debris[2-3]	(1) Convective heat transfer at locations with porous debris calculated by correlations specific to debris, and which calculate heat transfer as function of debris characteristics, debris temperature, and local coolant conditions.
Flow loss in porous debris[2-3]	(1) Flow losses at locations with porous debris calculated by correlations specific to debris, and which calculate flow losses for liquid and vapor phases as function of debris characteristics and local volume fractions of liquid and vapor phases.
Core plate[2-5]	(1) Calculation of heatup of core plate and extent of its interaction with core material that slumps below bottom elevation of core.
Heat transfer in stratified pool[2-4]	(1) Heat transfer in molten pool in lower head calculated based on whether constituents of pool are well-mixed or stratified into oxidic and metallic pools.
Material movement in porous debris[2-6]	(1) Calculation of movement of melted core plate through porous debris in lower head, and affect of this movement on heatup of lower head.
Fuel-Coolant Interaction (FCI)[2-7]	(1) Calculation of behavior of jets of material slumping into pool of water in lower head. Aspects of behavior calculated include; (1) fraction of jet that breaks up into drops and fraction that slumps to bottom of lower head without break up, (2) convective and radiative heat transfer from drops resulting from break up, and (3) increase in system pressure caused by vapor generation, which in turn is caused by heat transfer from drops, and (4) motion and settling to bottom of lower head of drops resulting from break up of jets.

Table 2-2. Test matrix for developmental assessment of SCDAP/RELAP5/MOD3.3.

Model or code update	**Test problem**									
	boff	**pbfst** **flht5**	**pbf11** **pbf14** **fpt0** **df4**	**cora5** **cora7** **cora13** **cora17**	**b9+**	**pdrop1** **pdrop2** **pdrop3** **debqn**	**qstrat**	**mltdb**	**fci**	**sur** **tmi** **bf**
Integral diffusion		X	X	X	X					X
Circumferential relocation			X	X	X					X
Oxide layer failure		X	X	X	X					X
Heat transfer in porous debris						X				X
Flow loss in porous debris						X				X
Core plate								X		
Heat transfer in stratified pool							X			X
Material movement in porous debris								X		
FCI									X	
Fortran 90	X	X	X	X	X	X	X	X	X	X
Other code improvements		X	X	X	X					

Table 2-3. Definition of test problems listed in Table 2-3.

Abbreviation of test problem	**Description of test problem**
boff	Boiloff of water in bundle of fuel rods with deficient cooling. Boiloff and heatup of fuel rods as calculated with fuel rods represented by SCDAP heat structures compared with that calculated with fuel rods represented by RELAP5 heat structures.

Table 2-3. Definition of test problems listed in Table 2-3. (Continued)

Abbreviation of test problem	Description of test problem
pbfst	PBF SFD ST test; nuclear heatup of PWR fuel assembly. Top of fuel assembly uncovered due to coolant boiloff. Measurements of rate of boiloff, temperature and damage of fuel rods, and H_2 production.
flht5	FLHT-5 test; nuclear heatup of full-length PWR fuel assembly. Gradual boiloff of coolant. Measurements of rate of boiloff, temperature and damage of fuel rods, and H_2 production.
pbf11	PBF SFD 1-1 test; nuclear heatup of PWR fuel assembly. Steam flow through assembly. Measurements of temperature and damage of fuel rods, and H_2 production.
pbf14	PBF SFD 1-4 test; nuclear heatup of PWR fuel assembly. Flow of steam and Ar through assembly. Measurements of temperature and damage of fuel rods, and H_2 production.
fpt0	PHEBUS FPT0 test; nuclear heatup of PWR fuel assembly. Flow of steam through assembly. Measurements of temperature and damage of fuel rods, and H_2 production.
df4	ACRR DF-4 test; nuclear heatup of BWR fuel assembly. Flow of steam through assembly.
cora5	FzK CORA-5 test; PWR fuel assembly with electrical heater rods.
cora7	FzK CORA-7 test; PWR fuel assembly with electrical heater rods. Flow of steam and Ar through assembly. Measurements of temperature and damage of fuel rods, and H_2 production.
cora13	FzK CORA-13 test; PWR fuel assembly with electrical heater rods. Flow of steam and Ar through assembly, followed by rapid reflood of hot assembly. Measurements of temperature and damage of fuel rods, and H_2 production.
cora17	FzK CORA-17 test; BWR fuel assembly with electrical heater rods. Flow of steam and Ar through assembly, followed by rapid reflood of hot assembly. Measurements of temperature and damage of fuel rods, and H_2 production.
b9+	PHEBUS B9+ test; nuclear heating of PWR fuel assembly. Flow of steam through assembly until assembly hot, then flow of He through assembly so as to represent situation of extreme steam starvation. Measurements of temperature and damage of fuel rods, and H_2 production.
pdrop1	Steam flow through porous debris bed. SCDAP/RELAP5 calculations compared with pressure drop in steam obtained from benchmarked model described in literature.
pdrop2	Flow of liquid water through porous debris bed. SCDAP/RELAP5 calculations compared with pressure drop in water obtained from benchmarked model described in literature.

Table 2-3. Definition of test problems listed in Table 2-3. (Continued)

Abbreviation of test problem	Description of test problem
pdrop3	Flow of two-phase water though porous debris bed with internal heat generation. SCDAP/RELAP5 calculations compared with pressure drop in two-phase water obtained from benchmarked model described in literature.
debqn	BNL debris quenching experiment. Quenching from bottom of porous debris at initial temperature of 775 K. Measurements of transient temperature of several locations in debris bed.
qstrat	Molten pool stratified into oxidic and metallic parts, and contained in hemispherical lower head; SCDAP/RELAP5 calculations compared with solution obtained from literature of temperature of oxidic and metallic parts, and heat flux at boundaries of molten pool
mltdb	Theoretical situation of core plate melting on top of ceramic porous debris bed in lower head of reactor vessel. Solution of the posed problem presents results that can be evaluated for reasonableness and consistency.
fci	ISPRA FARO-8 test. Slumping of mixture of molten UO_2 and ZrO_2 into pool of water in a vessel. Measurement of transient pressure response in vessel, temperature of plate supporting the settled slumped material, fraction of breakup of the slumped material, and particle size distribution of the slumped material.
sur	Theoretical situation of TMLB’ accident in PWR. Solution of the posed problem can be compared with solution of MOD3.2, and evaluated for reasonableness and consistency.
tmi	TMI-2 accident. Measurements of transient system pressure, heatup of parts of reactor system piping, and final state of reactor core. Indirect measurement of H_2 production.
bf	Unmitigated large break Loss of Coolant Accident in Browns Ferry BWR

2.1 Reference

2-1. L. J. Siefken, “Calculation of Hydrogen and Oxygen Uptake in Fuel Rod Cladding During Severe Accidents Using the Integral Diffusion Method,” INEEL/EXT-99-00571, May 1999.

2-2. L. J. Siefken, “Models for the Configuration and Integrity of Partially Oxidized Fuel Rod Cladding at High Temperatures,” INEEL/EXT-98-0066 Rev. 1, January 1999.

2-3. L. J. Siefken, E. W. Coryell, S. Paik, and H. Kuo, “SCDAP/RELAP5 Modeling of Heat Transfer and Flow Losses in Lower Head Porous Debris,” INEL/EXT-98-00820, Rev. 2, July 1999.

2-4. L. J. Siefken and M. S. Sohal, “A Heat Transfer Model for a Stratified Corium-Metal Pool in the Lower Plenum of a Nuclear Reactor,” INEL/EXT-99-00763, Rev. 1, January 2000.

2-5. E. W. Coryell and F. P. Griffin, “SCDAP/RELAP5 Lower Core Plate Model,” INEEL/EXT-99-01029, September 1999.

2-6. L. J. Siefken, “SCDAP/RELAP5 Modeling of Movement of Melted Material Through Porous Debris in Lower Head,” INEEL/EXT-98-01178 Rev. 2, October 1999.

2-7. M. S. Sohal and L. J. Siefken, “Design Report on Model Development for Molten Fuel Coolant Interaction During Melt Slumping,” INEL/EXT-97-00084, Rev. 1, March 1998.

3. Assessment Using Results of Severe Fuel Damage Tests

This section summarizes the assessment of SCDAP/RELAP5/MOD3.3 using the results of the ten severe fuel damage experiments identified in Section 2. The experiment results provided information over a broad range of conditions for assessing the MOD3.3 calculations of the following important early-phase damage progression events; (1) heatup due to uncovery and oxidation of fuel assembly, (2) oxidation of fuel assembly during uncovery and during fuel assembly reflood, (3) fuel rod ballooning and rupture, and (4) fuel assembly meltdown. The assessment was performed by comparing measured results of the experiments with the corresponding calculated results of MOD3.3 and MOD3.2. Appendices A1 through A7 describe in detail each of these ten experiments and the MOD3.3 and MOD3.2 calculations for these experiments.

The comparison of both MOD3.3 and MOD3.2 calculations with the measured results provided information for assessing the affects of the modeling improvements in MOD3.3. The modeling improvements to be assessed included; (1) integral diffusion method for calculating the oxidation of fuel rod cladding, (2) model for configuration of melted metallic cladding retained by oxide layer and accounting for size of fuel-cladding gap, (3) stress-based model for calculating the time at which failure occurs to a fuel rod oxide layer retaining melted metallic cladding, and (4) model for re-slumping of previously frozen slumped cladding. These new modeling improvements impact the MOD3.3 calculations of the heatup, oxidation, and meltdown of fuel assemblies. Experiment results applicable to the assessment these modeling improvements included transient measurements of test fuel assembly temperatures and test fuel assembly hydrogen production and Post-Irradiation Evaluations (PIE) of the axial distribution in oxidation of the test fuel assembly and the location of blockages due to meltdown in the test fuel assembly.

3.1 Models for Temperature Behavior of Fuel Assemblies

The assessment of the MOD3.3 model for fuel rod heatup showed that the calculated rates of heatup were in good agreement with the measured rates of heatup for most of the severe fuel damage tests. The comparisons of calculated and measured rates of heatup were divided into four categories of test fuel assemblies; (1) heatup of PWR fuel assembly with gradual uncovery of fuel assembly, (2) heatup of PWR fuel assembly with complete uncovery of fuel assembly throughout the heatup period of the test, (3) temperature behavior following reflood of hot PWR fuel assembly, and (4) heatup of BWR fuel assembly with complete uncovery of fuel assembly throughout the heatup period of the test. The experiments in the first category were; (1) FLHT-5, (2) PBF SFD ST, and (3) PBF SFD 1-1. The experiments in the second category were; (1) PBF SFD 1-4, (2) CORA-5, (3) CORA-7, (4) CORA-13, (5) PHEBUS B9+, and (6) PHEBUS FPT0. The experiments in the third category were; (1) PBF SFD ST test, and (2) PBF CORA-13 test. The experiments in the fourth category were; (1) DF-4, and (2) CORA-17. For each of these tests, the calculated and measured rates of heatup were compared at the location 3/4 of the fuel pellet stack height above the bottom of the fuel pellet stack. This location was generally near the first location in the test fuel assembly to undergo rapid oxidation and a temperature measurement was generally available. Also, the temperature at this location was usually not influenced by blockages caused by fuel rod meltdown or influenced by cold structures above the test fuel assembly.

3.1.1 Temperature Behavior of PWR Fuel Assemblies with Gradual Uncovery

The MOD3.3 calculated rate of heatup of PWR fuel assemblies with a gradual boiloff of coolant was in general agreement with the measured rate of heatup. The comparisons of calculated and measured temperature are shown in Figure 3-1, Figure 3-2, and Figure 3-3 for the FLHT-5, PBF SFD ST, and PBF SFD 1-1 tests, respectively. The MOD3.2 calculations are also shown in these figures. In general, the temperature measurements fail before the fuel rod temperature exceeds 2000 K and before melting of the fuel rod cladding has occurred. For the PBF SFD ST test and the PBF SFD 1-1 test, the calculated and measured rate of heatup are in good agreement. For the FLHT-5 test, the calculated rate of heatup is somewhat less than the measured rate of heatup. The reason for this underprediction of the rate of heatup was not identified. As shown in Figure 3-1, Figure 3-2, and Figure 3-3, MOD3.2 calculated a temperature behavior similar to MOD3.3. Since the measurements did not fail until after rapid oxidation of the fuel rod cladding had begun, the generally good agreement in temperatures of the MOD3.3 calculations and the measurements indicates that the integral diffusion model for oxidation is performing correctly.

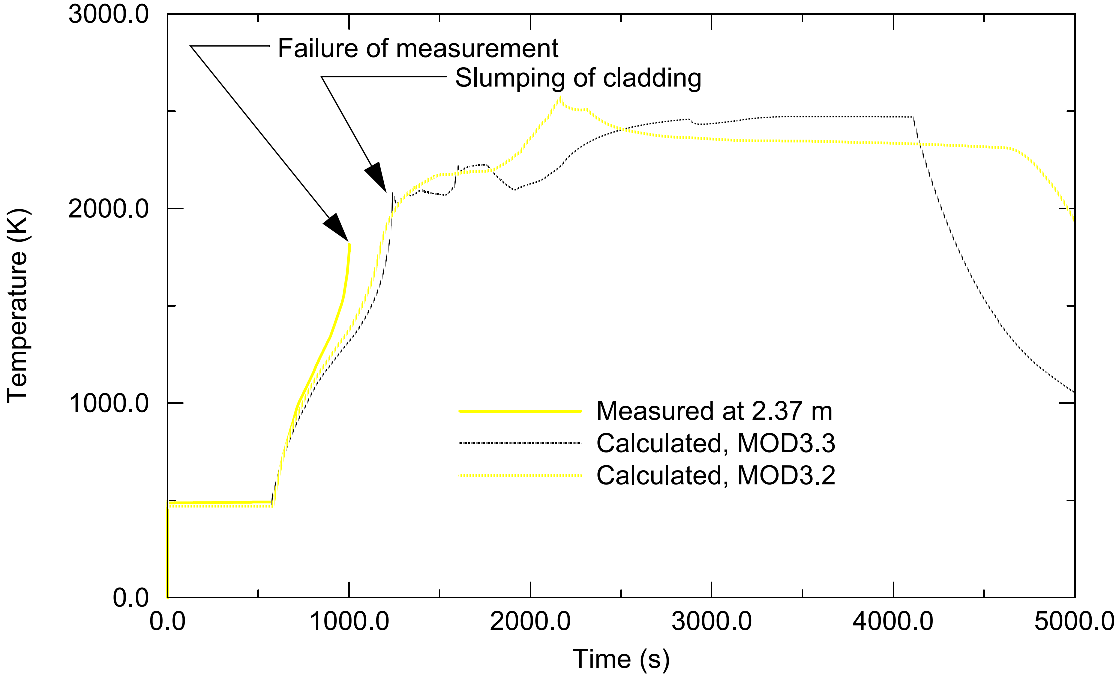

Figure 3-1. Comparison of calculated and measured temperature at 2.37 m elevation for FLHT-5.

3.1.2 Temperature Behavior of PWR Fuel Assemblies with Complete Uncovery

The MOD3.3 calculated rates of heatup of PWR fuel assemblies with a constant and complete uncovery were found to be in good agreement with the measured rates of heatup. The calculated and measured rates of heatup are compared in Figure 3-4, Figure 3-5, Figure 3-6, Figure 3-7, Figure 3-8, and Figure 3-9 for the PBF SFD 1-4, CORA-5, CORA-7, CORA-13, PHEBUS B9+, and PHEBUS FPT0 tests, respectively. The MOD3.2 calculations are also shown in these figures. The agreement between calculated and measured rates of heatup ranged from very close agreement for the CORA-7, CORA-13 and PHEBUS B9+ tests to a significant overprediction of the rate of heatup for the PHEBUS FPT0 test. For the PBF SFD

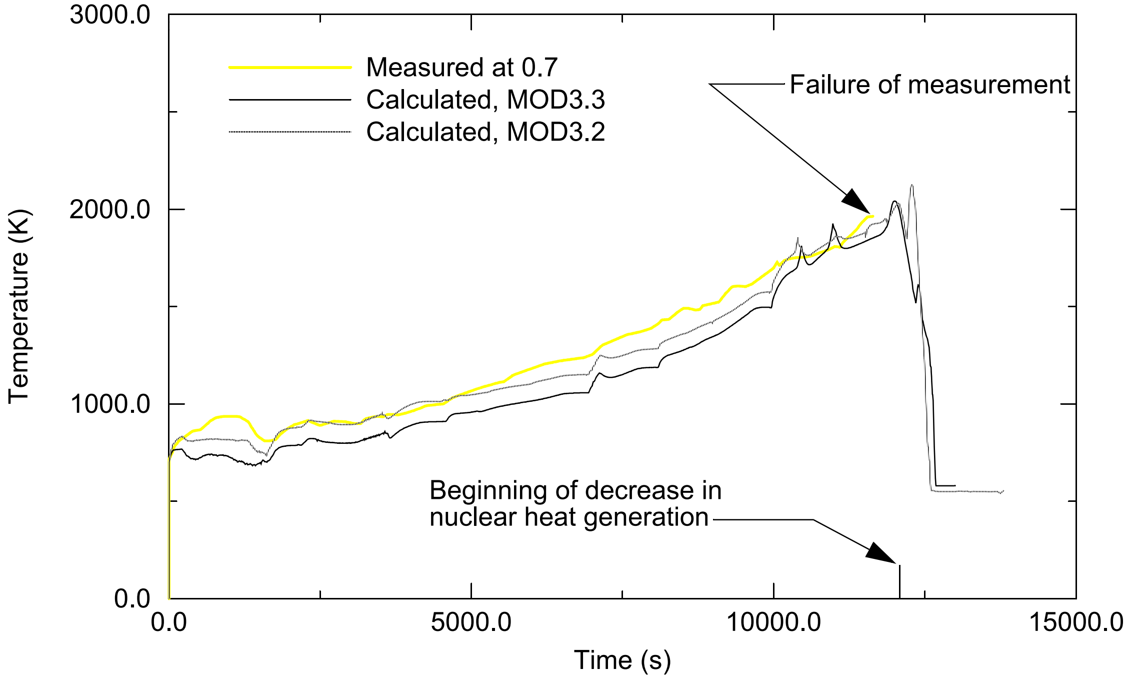

Figure 3-2. Comparison of calculated and measured temperatures at 0.7 m elevation for PBF SFD ST test.

1-4 test, MOD3.3 calculated a relatively slow rate of heatup at the 0.74 m elevation in the period of 1800 s to 1900 s due to steam starvation, while the measurement indicated a rapid increase in temperature at this elevation during this period. At the 0.54 m elevation and where steam starvation was calculated to not occur, the MOD3.3 calculated temperature and the measured temperature were in close agreement. Since for these six tests the measurements of the temperatures did not fail until after rapid oxidation of the fuel rod cladding had begun, the generally good agreement of the MOD3.3 calculations and the measurements indicates that the integral diffusion model for oxidation is performing correctly.

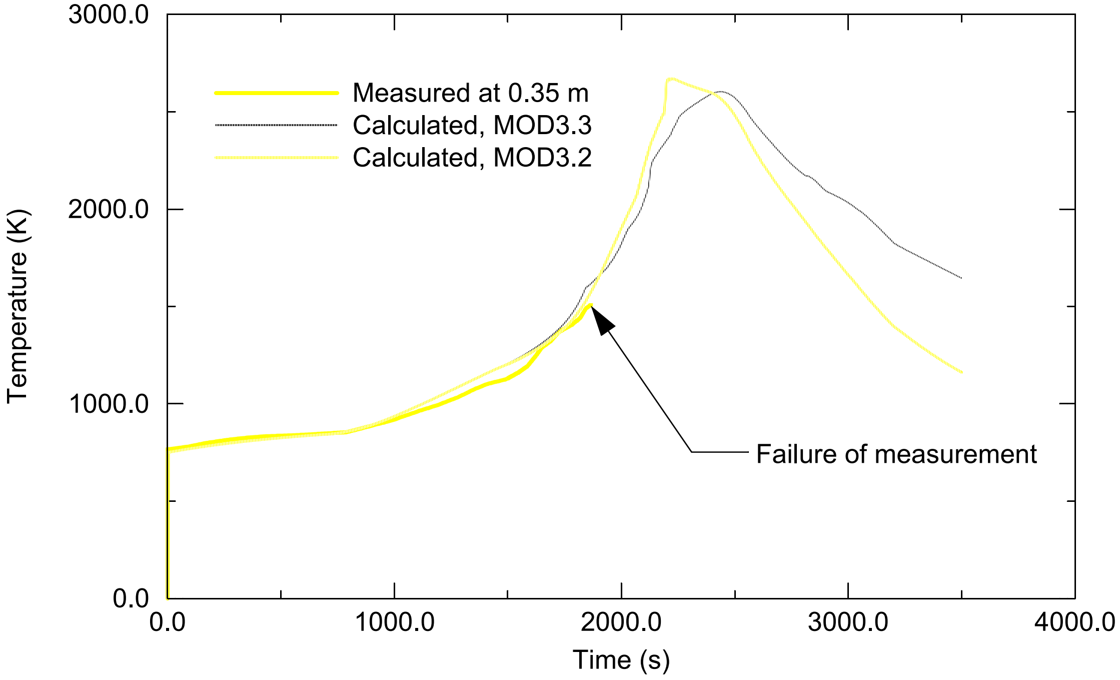

Figure 3-3. Comparison of calculated and measured temperature at elevation of 0.7 m for PBF SFD 1-1 test.

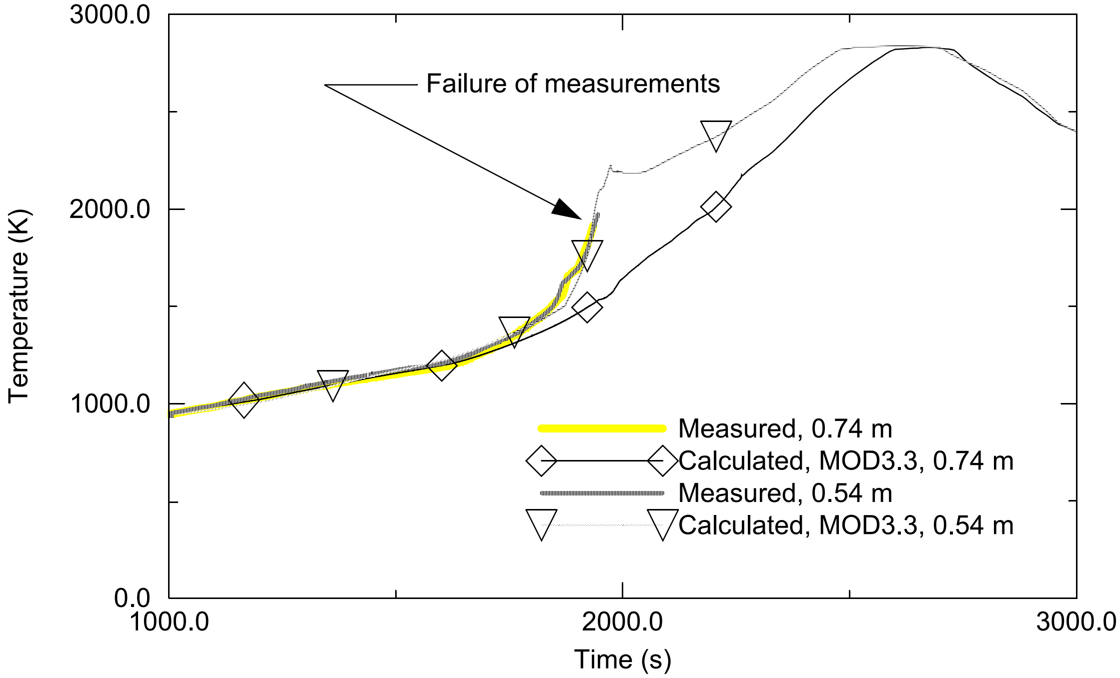

Figure 3-4. Comparison of calculated and measured temperatures at 0.74 m and 0.54 m elevation for PBF SFD 1-4 test.

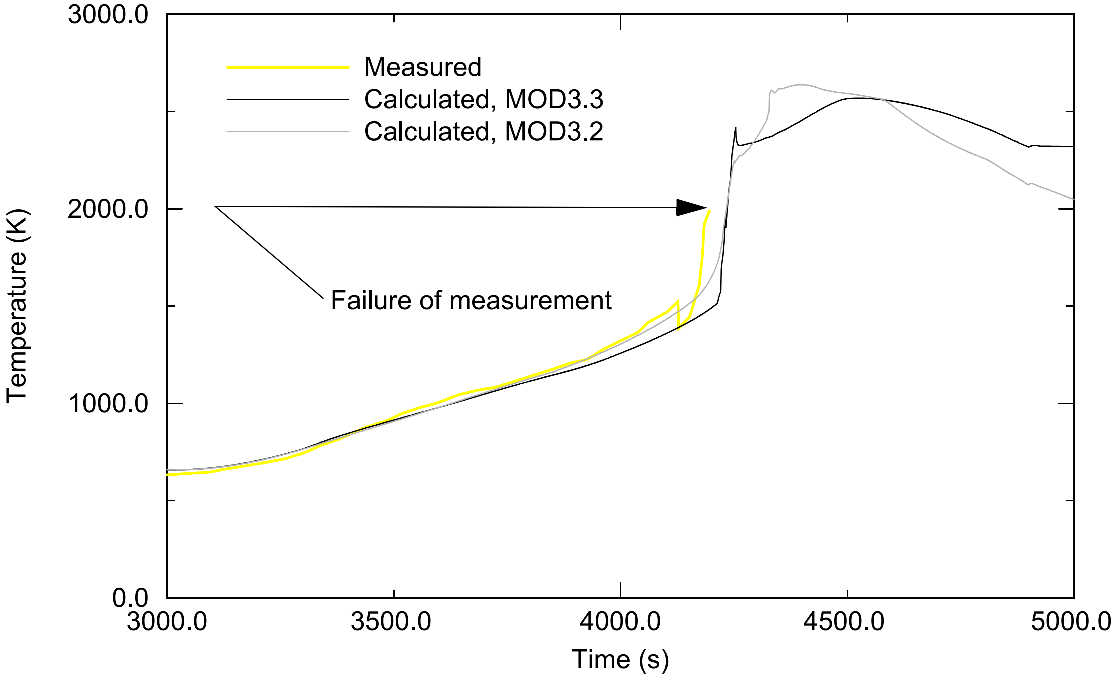

Figure 3-5. Comparison of calculated and measured temperature at 0.75 m for CORA-5 test.

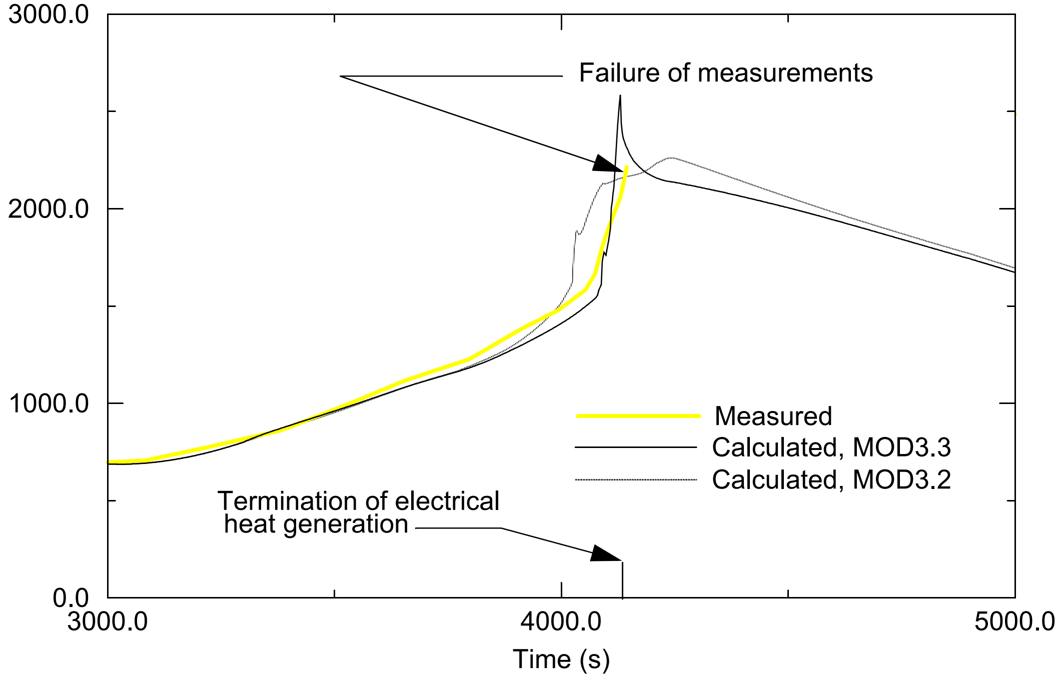

Figure 3-6. Comparison of calculated and measured temperature at 0.75 m for CORA-7 test.

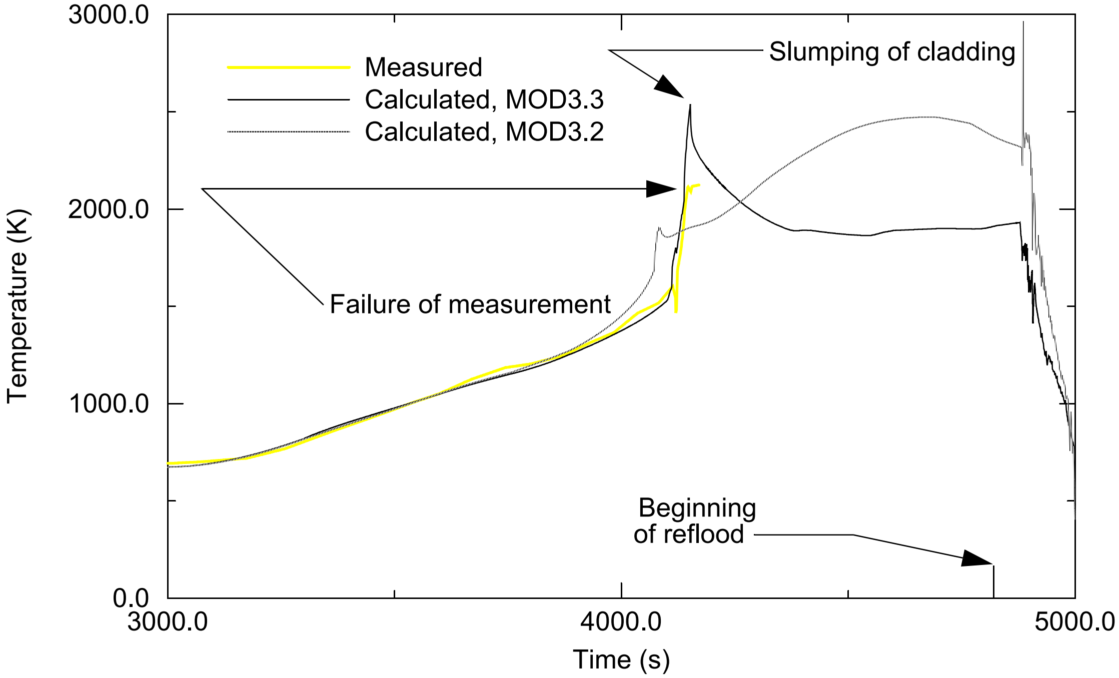

Figure 3-7. Comparison of calculated and measured temperatures of unheated fuel rod at elevation of 0.75 m for CORA-13 test.

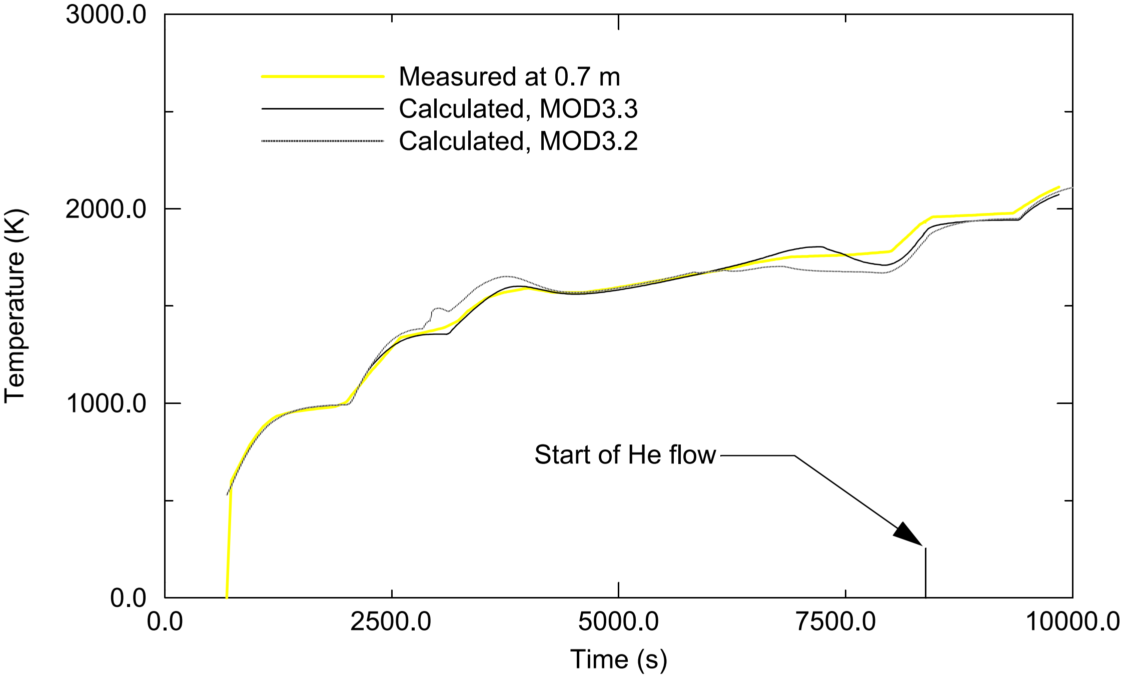

Figure 3-8. Comparison of calculated and measured fuel temperatures at 0.7 m elevation for PHEBUS B9+ test.

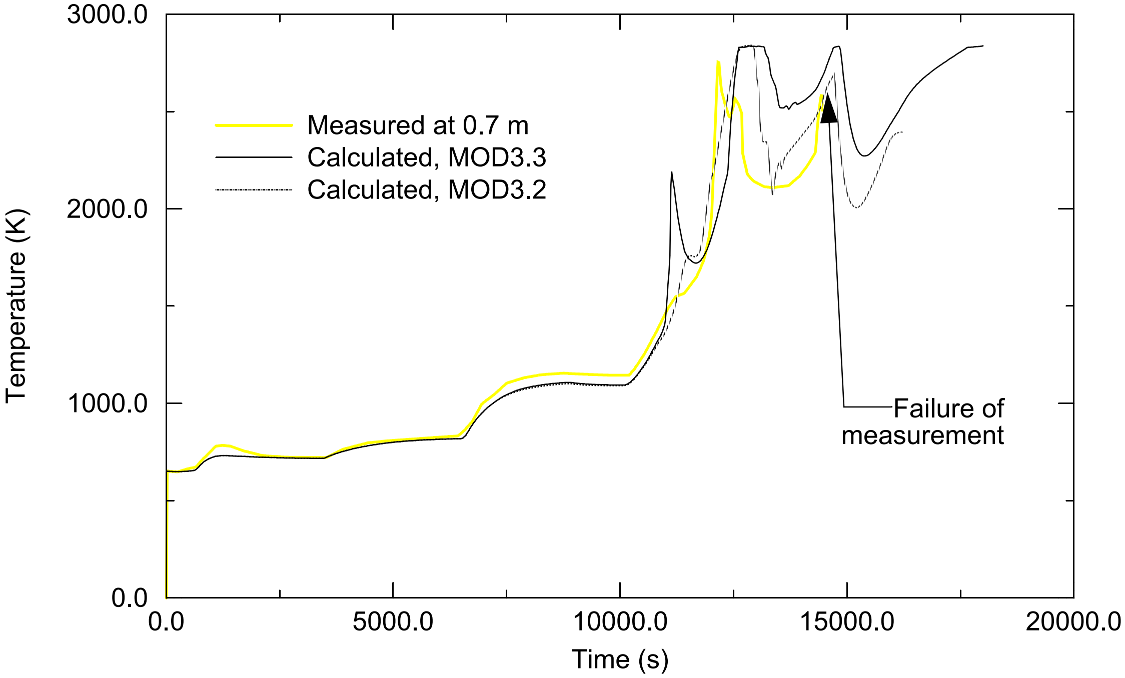

Figure 3-9. Comparison of calculated and measured cladding temperatures at 0.7 m elevation for PHEBUS FPT0.

3.1.3 Temperature Behavior of BWR Fuel Assemblies with Complete Uncovery

The MOD3.3 calculated rate of heatup of BWR fuel assemblies with a constant and complete uncovery were found to be in generally good agreement with the measured rate of heatup. The calculated and measured rates of heatup are compared in Figure 3-10 and Figure 3-11 for the CORA-17 and ACCR DF-4 tests, respectively.

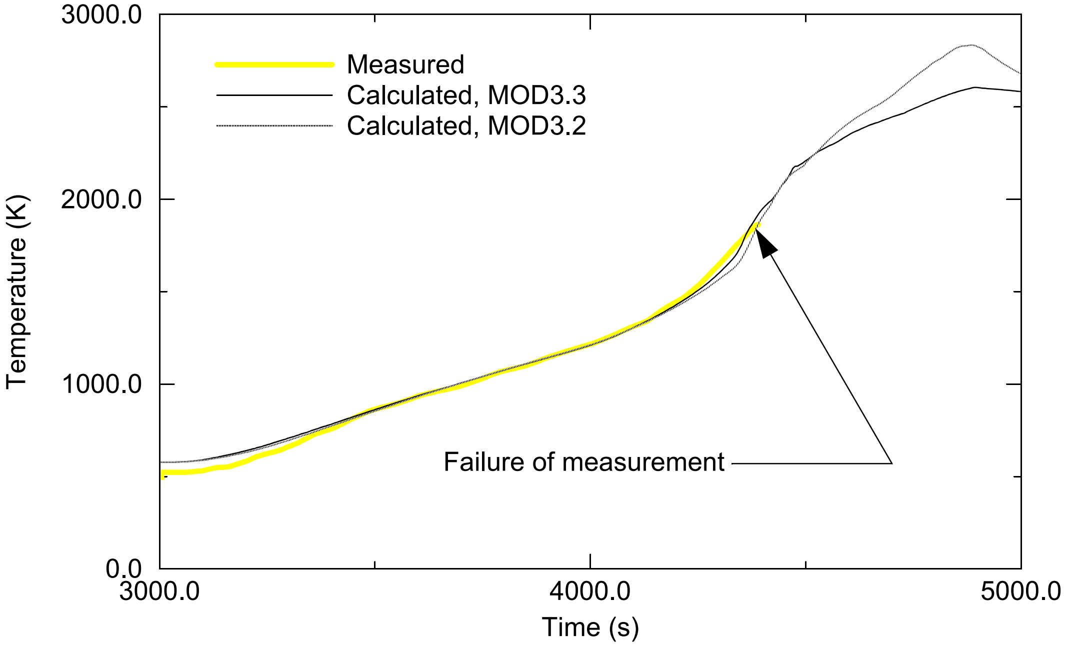

Figure 3-10. Comparison of calculated and measured temperatures of unheated rod at elevation 0.75 m for CORA-17 test.

3.1.4 Temperature Behavior of Fuel Assemblies During Reflood

An acceleration in heatup after the start of reflood was calculated by MOD3.3 to occur at locations that were hot and partially oxidized at the start of reflood. The PBF SFD ST test and the CORA-13 test were the only tests in the set of assessment problems that involved the reflood of a hot fuel assembly. For both of these tests, the location 1/2 of the fuel pellet stack height above the bottom of the fuel pellet stack was hot and partially oxidized at the beginning of reflood. Locations higher in the test fuel assembly generally did not undergo an acceleration in heatup during reflood due to the cladding at those locations either being completely oxidized or the metallic part of the cladding having slumped before reflood. The calculated heatup at the location 1/2 of the fuel pellet stack height above the bottom of the fuel pellet stack for the PBF SFD ST test and the CORA-13 test are shown in Figure 3-12 and Figure 3-13, respectively. For the PBF SFD ST test, the temperature was calculated to decrease to 1500 K in response to the decrease in nuclear heat generation and the corresponding increase in water level, and then increase to 1800 K in response to the increase in oxidation caused by cracking of the oxide layer on the fuel rod cladding. For the CORA-13 test, the temperature was calculated to decrease to 1750 K due to the increased steam flow

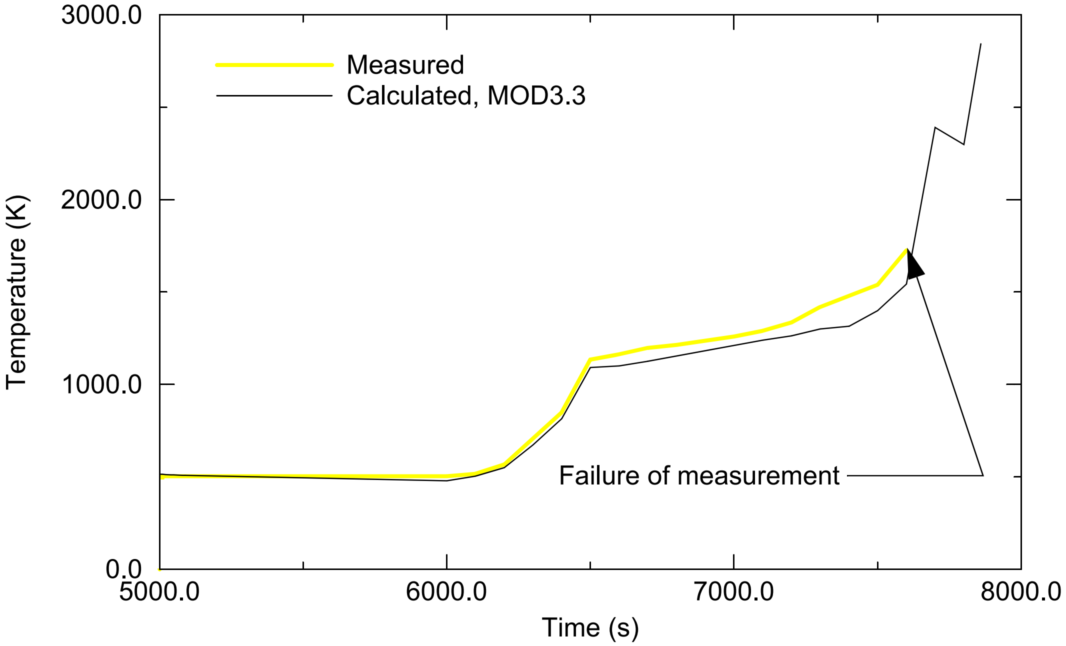

Figure 3-11. Comparison of calculated and measured temperatures of fuel rod at elevation of 0.254 m for DF-4 test.

caused by reflood and then increase to 2300 K due to the acceleration in oxidation resulting from cracking of the cladding oxide layer. For both of these tests, the temperature measurements in the test fuel assembly failed before the beginning of reflood and thus comparisons of calculated versus measured temperature during the reflood period could not be made. Nevertheless, measurements of the rate of hydrogen production indicated that an acceleration in oxidation occurred during the reflood period of these tests, and thus the calculated increase in the rate of heatup was consistent with experiment results.

3.2 Calculation of Hydrogen Production

The MOD3.3 calculation of hydrogen production was generally in good agreement with the measured hydrogen production. Comparisons of calculated and measured hydrogen production are shown in Table 3-1 for the nine experiments for which hydrogen production was measured. MOD3.2 calculations are also shown in order to evaluate the affect of the improvements implemented into MOD3.3. The MOD3.3 calculated hydrogen production was less than the measured hydrogen production for four of the tests, greater than the measured hydrogen production for two of the tests, and within the measured uncertainty in hydrogen production for the other tests. The deviations in calculated hydrogen production ranged from being 50% too large for the PBF SFD 1-1 test to 15% too small for the PHEBUS FPT0 test.

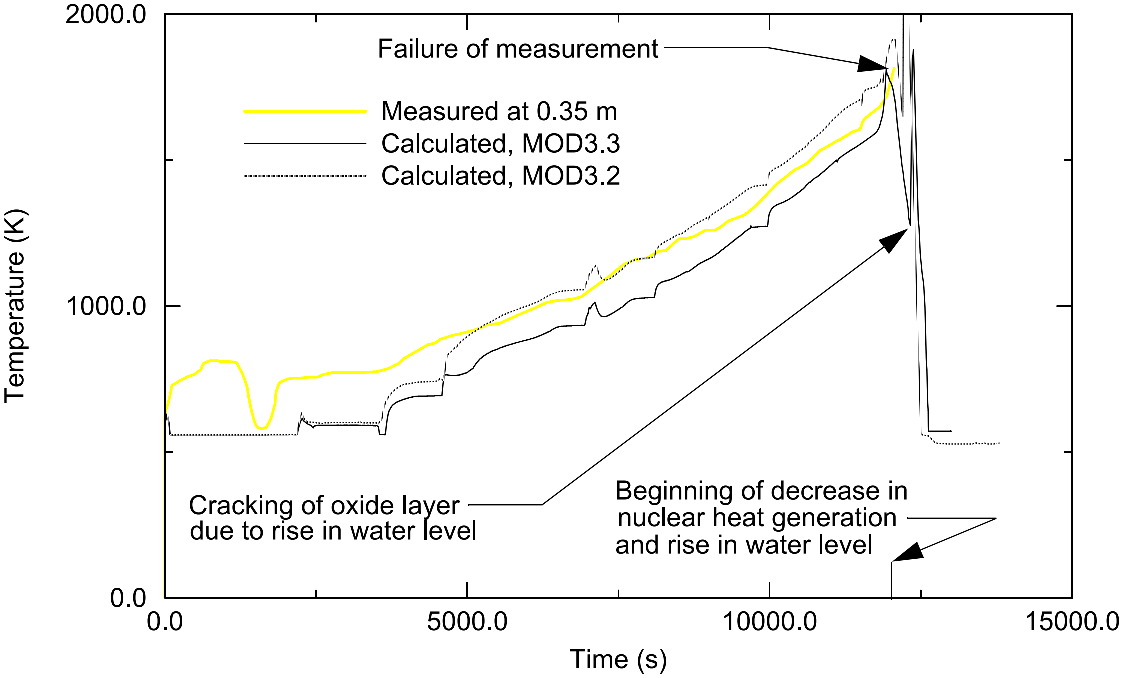

Figure 3-12. Comparison of calculated and measured temperatures at 0.5 m elevation for PBF SFD ST test.

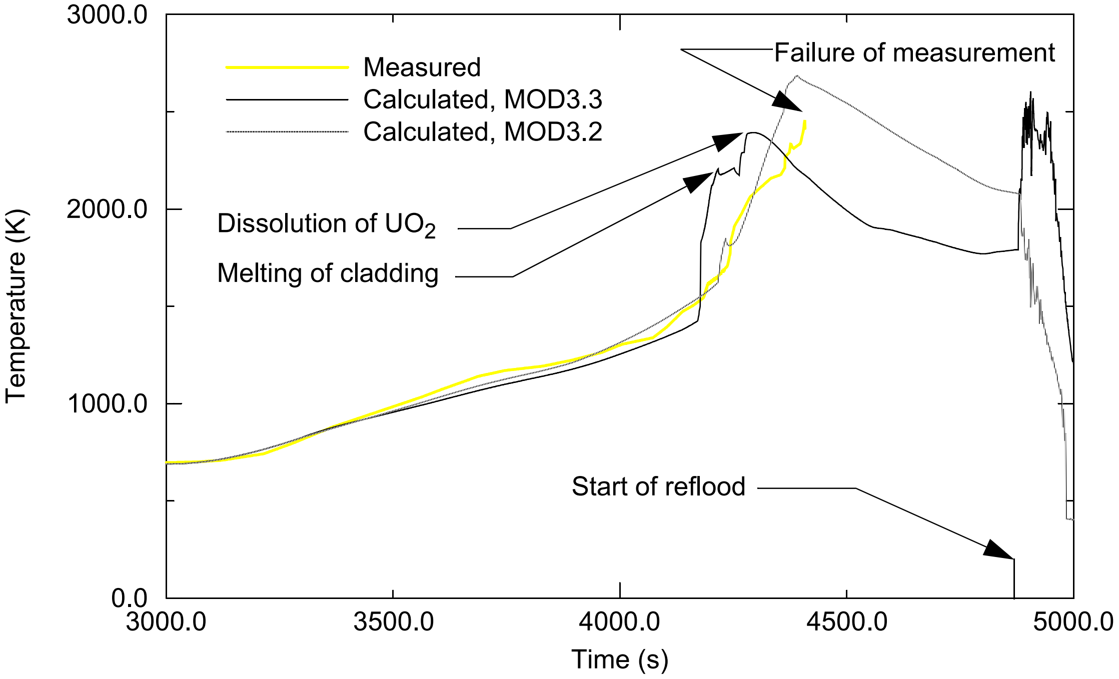

Figure 3-13. Comparison of calculated and measured temperatures of unheated fuel rod at elevation of 0.55 m for CORA-13 test.

Table 3-1. Comparison of calculated and measured hydrogen production.

Experiment	Hydrogen production (g)					
	Measured		MOD3.3		MOD3.2	
	Pre-reflood	Total	Pre-reflood	Total	Pre-reflood	Total
FLHT-5	-	300 ± 30	-	231	-	265
PBF SFD ST	-	150 ± 35	98	125	121	121
PBF SFD 1-1	-	64 ± 7	-	105	-	94
PBF SFD 1-4	-	86 ± 12	-	82	-	94
CORA-7	-	114	-	91	-	79
CORA-13[a]	97	161	78	158	145	175
PHEBUS B9+	-	39	-	46	-	49
PHEBUS FPT0	-	90	-	77	-	63
ACRR DF-4		40	-	29	-	-

a. Estimated hydrogen production from oxidation of structures above the test fuel rods was subtracted from the measured hydrogen production to obtain estimate of measured hydrogen production from oxidation only of structures within the heated elevation interval of the test.

3.3 Model for Ballooning of Fuel Rod Cladding

The assessment of the MOD3.3 model for the ballooning and rupture of fuel rod cladding showed a possibility for improvement of this model. The results of the assessment of this event in severe accident early-phase damage progression are summarized in Table 3-2. Only a few of the experiments provided information on the timing of cladding rupture. For the FLHT-5, PBF SFD ST and PHEBUS FPT0 tests, the calculated and measured times of cladding rupture and temperature at rupture were in fairly good agreement. For the PBF SFD 1-1 test, the calculated time of cladding rupture was significantly later than the measured time of cladding rupture. For the PBF SFD 1-4 test, the calculated time of cladding rupture was significantly earlier than the measured time of cladding rupture.

Table 3-2. Comparison of calculated and measured ballooning behavior of fuel rods.

Test	Rupture temperature		Time of cladding rupture	
	Measured	MOD3.3	Measured	MOD3.3
	(K)	(K)	(s)	(s)
FLHT5	1950[a]	1900	1010	1230
PBF SFD ST	1150 - 1200	1050	5850 - 6260	6015 - 6385
PBF SFD 1-1	1538 - 1632	1785 - 1798	1150 - 1280	1785 - 1795
PBF SFD 1-4	1720 - 1900	1360 - 1530	1300 - 1600	1100 - 1150
FPT0	973	1060 - 1070	--	7350 - 7410

[a] Since the coolant pressure was greater than the internal gas pressure, the cladding failed by compression instead of by ballooning.

3.4 Models for Oxidation and Meltdown Using PIE Results

The integral diffusion model for oxidation and the stress-based model for breach of the cladding oxide layer in MOD3.3 contributed to a significant improvement in the calculated oxidation and meltdown of fuel rod cladding. The comparison of calculated and measured axial distribution in oxidation of fuel rod cladding provided a basis for assessing these models. The timing of cladding slumping is as important of a factor in determining the total extent of oxidation of the cladding as the rate of oxidation. The calculated and measured axial distribution cladding oxidation are compared in Table 3-3 for the six severe fuel damage tests for which this information was available. The calculations of both MOD3.3 and MOD3.2 are shown in the table. In this table, elevation is expressed as fractional height, wherein a fractional height of 0.85 indicates the elevation of the point located the distance of 85% of the height of the fuel pellet stack above the bottom of the fuel pellet stack. As shown in Table 3-3, the almost complete oxidation of the upper half of the cladding of the test fuel rods occurred for the three tests involving a slow boiloff of coolant or a slow heatup in steam flow, namely FLHT-5, PBF SFD ST, and PHEBUS B9+. For these tests, the calculated and measured fraction of oxidation are in good agreement. Only a small amount of slumping of the metallic part of the cladding was measured to occur for these tests, and only a small amount of slumping of the metallic part of the cladding was calculated to occur. For the PBF SFD 1-1 test, PBF SFD 1-4 test, and CORA-13 test, the extent of oxidation of the cladding in the upper half of the test fuel rods was limited by meltdown of the cladding and the extent of oxidation of the lower part of the test fuel assembly was accelerated by the meltdown of the cladding. MOD3.2 tended to overpredict the extent of oxidation in the upper half of the test fuel rods and underpredict the extent of oxidation of the fuel rod cladding in the lower half of the test fuel rods. While the MOD3.3 calculations of the axial distribution in oxidation for these three tests was not in close agreement with the measured results, nevertheless the MOD3.3 calculations were an improvement over the MOD3.2 calculations. For example, at the fractional elevation of 0.85 for the PBF SFD 1-4 test, the measured, MOD3.3 calculated, and MOD3.2 calculated values of fraction of cladding oxidation were 0.22, 0.24, and 0.86, respectively. For a second example, at the fractional elevation of 0.45 for the CORA-13 test, the measured, MOD3.3 calculated, and MOD3.2 calculated values of fraction of cladding oxidation were 1.0, 1.0, and 0.10, respectively. For a third example, at the fractional elevation of 0.25 for the PBF SFD 1-4 test, the measured, MOD3.3 calculated, and MOD3.2 calculated values of fraction of cladding oxidation were 1.0, 0.63, and 0.11, respectively. The better agreement of calculations with measurements was achieved primarily due to implementation of the following models into MOD3.3; (1) integral diffusion model for oxidation, (2) stress-based model for breach of the cladding oxide layer, and (3) model for re-slumping of previously frozen slumped material.

Table 3-3. Comparison of calculated and measured axial distribution in fuel rod oxidation

Elevation		**Fraction of cladding oxidized**					
(Fractional height)		**FLHT-5**	**PBF SFD ST**	**PBF SFD 1-1**	**PBF SFD 1-4**	**CORA-13**	**PHEBUS B9+**
0.85	Measured	1.0	1.0	0.20[a]	0.22[a]	-<1.0	-
	MOD3.3	1.0	1.0	0.16[a]	0.24[a]	0.30[a]	-
	MOD3.2	-	-	0.34	0.86	0.43[a]	-
0.75	Meas.	1.0	1.0	0.11[a]	0.37[a]	1.00	0.75
	MOD3.3	1.0	1.0	0.18[a]	0.22[a]	0.30[a]	0.90
	MOD3.2	-	-	0.46	0.26[a]	0.20[a]	0.52
0.65	Meas.	1.0	1.0	0.45	-	1.00	1.00
	MOD3.3	0.43[a]	1.0	0.25[a]	0.33	1.00	0.99
	MOD3.2	-	-	0.38	-	0.36[a]	1.00
0.55	Meas.	1.0	1.0	-	<0.30[a]	1.00	0.70
	MOD3.3	1.0	1.0	0.36[a]	0.67	1.00	1.00
	MOD3.2	-	-	-	0.37	0.16[a]	1.00
0.45	Meas.	1.0	1.0	0.65	-	1.00	0.40
	MOD3.3	1.0	1.0	0.38[a]	0.68	0.69	0.70
	MOD3.2	-	-	0.36	-	0.10[a]	0.86
0.35	Meas.	1.0	1.0	0.25	0.50[a]	0.60	0.25
	MOD3.3	0.97	1.0	0.78	0.67	1.00	0.49
	MOD3.2	-	-	0.16	0.52	0.70	0.71

Table 3-3. Comparison of calculated and measured axial distribution in fuel rod oxidation

Elevation		Fraction of cladding oxidized					
(Fractional height)		FLHT-5	PBF SFD ST	PBF SFD 1-1	PBF SFD 1-4	CORA-13	PHEBUS B9+
0.25	Meas.	0.0	1.0	1.00	1.00	0.07	0.10
	MOD3.3	0.04	0.03	0.80	0.61	1.00	0.30
	MOD3.2	-		0.51	0.11	0.43	0.21
0.15	Meas.	0.0	0.03	1.00	1.00	0.0	0.03
	MOD3.3	0.0	0.0	0.01	0.03	1.00	0.07
	MOD3.2	-	-	0.0	0.02	0.17	0.06
0.05	Meas.	0.0	0.0	0.60	0.10	0.0	0.0
	MOD3.3	0.0	0.0	0.01	0.0	0.03	0.02
	MOD3.2	-	-	0.0	0.0	0.21	0.02

a. Metallic part of cladding slumped.

3.5 Conclusions

The assessment of MOD3.3 showed that its calculations of fuel rod behavior during severe accident conditions were in general agreement with measured behavior. The assessment was performed using various results from a wide range of severe fuel damage tests. The MOD3.3 calculations of fuel rod meltdown and the axial distribution in fuel rod oxidation were significantly improved over MOD3.2 calculations. MOD3.2 tended to overpredict the extent of oxidation of fuel rod cladding in the upper part of a fuel assembly due to the lack of a model for the dissolution of the oxide layer in a steam-starved region. MOD3.2 also tended to underpredict the extent of oxidation of fuel rod cladding in the bottom part of a fuel assembly due to the lack of a model to calculate the re-slumping of previously slumped cladding and a tendency to underpredict the rate of oxidation in a steam-rich region. The MOD3.3 calculations of the behavior of fuel assemblies under reflood conditions was also improved over the MOD3.2 calculations. The improvements in the calculation of fuel assembly meltdown, axial distribution in oxidation, and reflood behavior were the result of implementing the following models into MOD3.3; (1) integral diffusion model for oxidation and dissolution, (2) model for calculating the timing of failure of an oxide layer that is based on stress and accounts for the affect of oxide dissolution on stress, (3) model for re-slumping of previously slumped cladding, and (4) models for cracking of oxide layer during reflood conditions and affect of cracking on oxygen transport.

4. Assessment of Late-Phase Models

This section summarizes the assessment of models implemented into MOD3.3 for improving the code's calculation of the behavior of a reactor core during the late-phase of a severe accident. Five models were implemented into MOD3.3 for this purpose; (1) model for flow losses in porous debris, (2) model for heat transfer in porous debris, (3) model for heat transfer from molten pool that has stratified into oxidic and metallic parts, (4) model for flow of liquefied core plate material through porous debris in the lower head of the reactor vessel, and (5) model for break-up of jets of molten core material penetrating into a pool of water in the lower head. These five models were assessed using experimental results and numerical solutions available from the literature. Appendices A8 through A11 describe in detail the assessment of these five models. These models along with the early-phase models were also assessed by calculating the TMI-2 accident, which is presented in Appendix A12. Models in MOD3.3 for heat transfer from a homogeneous molten pool and for structural failure of the crust supporting a molten pool are the same as in MOD3.2, so these models were not assessed for MOD3.3. The assessments of these models are described in the developmental assessment report for MOD3.2.[4-1]

A summary of the assessment of the five late-phase models implemented into MOD3.3 and the TMI-2 calculation are summarized in the following sections of the report. The assessment of the models for flow loss and heat transfer in porous debris is described in Section 4.1. The assessment of the model for heat transfer from a stratified molten pool is described in Section 4.2. The assessment of the model for flow of liquefied material through porous debris is described in Section 4.3. The assessment of the model for break-up of jets of slumping molten material is described in Section 4.4. The assessment of the code using benchmarking data obtained during and after the TMI-2 accident is described in Section 4.5. Conclusions are presented in Section 4.6 and the references are presented in Section 4.7.

4.1 Models for Flow Loss and Heat transfer in Porous Debris

The models for flow loss and heat transfer in porous debris were assessed by comparisons of SCDAP/RELAP5/MOD3.3 calculated thermal hydraulic behavior of debris with measurements and the calculations of benchmarked models presented in the literature. The details of the assessment are described in Appendix A8.

The assessment of the flow loss models showed that MOD3.3 is calculating in an acceptable manner the flow losses in porous debris. The MOD3.3 flow loss models were assessed by comparing MOD3.3 calculated flow losses with the calculated flow losses of other benchmarked models. A schematic of a system analyzed for the assessment is shown in Figure 4-1. The system consisted of a 1-m deep bed of porous debris with a porosity of 0.4 and particles with a diameter of 3 mm. The assessment was performed for coolant conditions ranging from subcooled liquid to superheated steam. The assessment included coolant conditions involving an axial distribution in two-phase coolant conditions typical of a covered debris bed resulting from a severe accident in a LWR.[4-2] A summary of the assessment of the flow loss models is shown in Table 4-1. For all the cases analyzed, the coolant pressure was 6.9 MPa. The MOD3.3 calculated flow losses are in approximate agreement with the values calculated by benchmarked models.

Table 4-1. Comparison of SCDAP/RELAP5 calculated flow losses for porous debris with those calculated by other benchmarked models

Coolant conditions	**Superficial velocity at bottom of bed**	**Pressure drop due to flow losses (Pa)**	
	(m/s)	**MOD3.3**	**Benchmarked model** [4.2, 4.3]
superheated steam	0.132	1.03×10^3	1.14×10^3
subcooled liquid	1.39×10^{-2}	1.00×10^3	1.28×10^3
two-phase water in debris bed with internal heat generation	1.47×10^{-2}	10.6×10^3	12.6×10^3

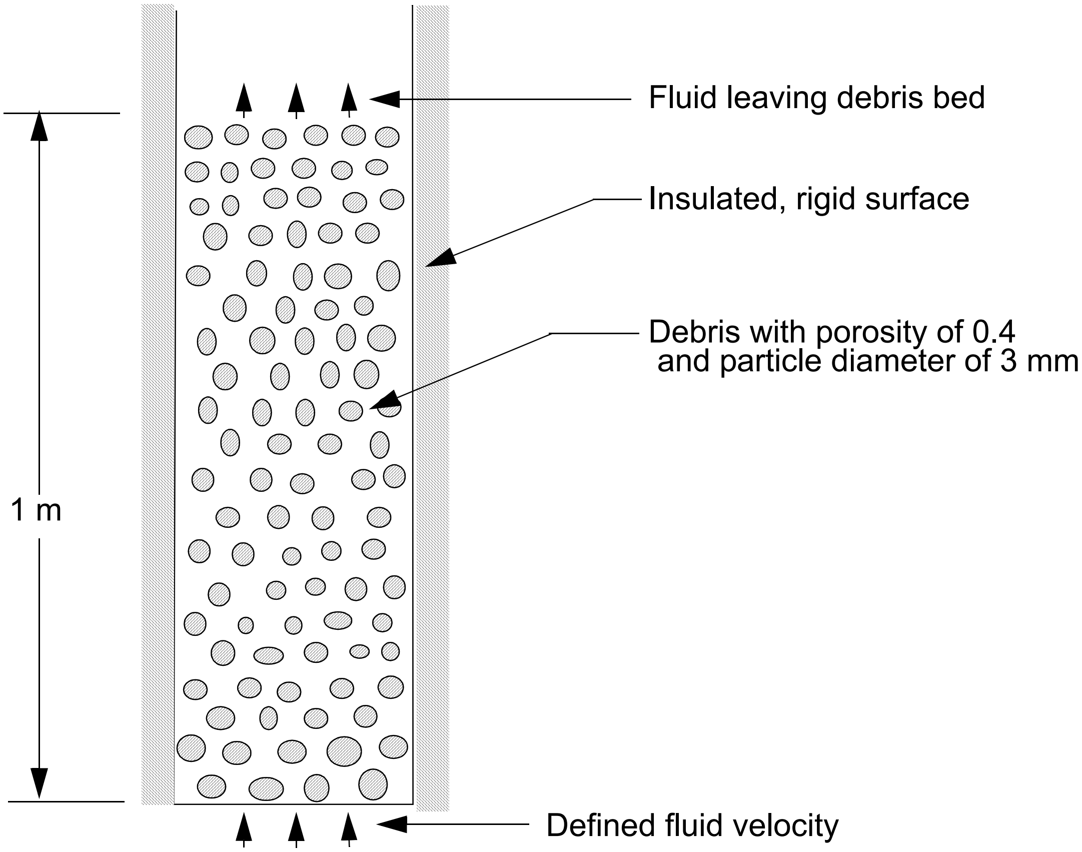
Fluid leaving debris bed
Insulated, rigid surface
Debris with porosity of 0.4 and particle diameter of 3 mm
1 m
Defined fluid velocity

Figure 4-1. Schematic of debris bed analyzed for assessment of flow loss calculations.

The MOD3.3 modeling of heat transfer in porous debris was assessed using the results of a BNL debris experiment involving the quenching from the bottom of a hot and porous debris bed.[4-4] During this experiment, measurements were obtained of the transient temperature at various locations within the debris bed. Since the transient temperatures were a function of flow losses, this experiment in an indirect manner also provided an assessment of flow loss models. A schematic of the experiment is shown in Figure 4-2.

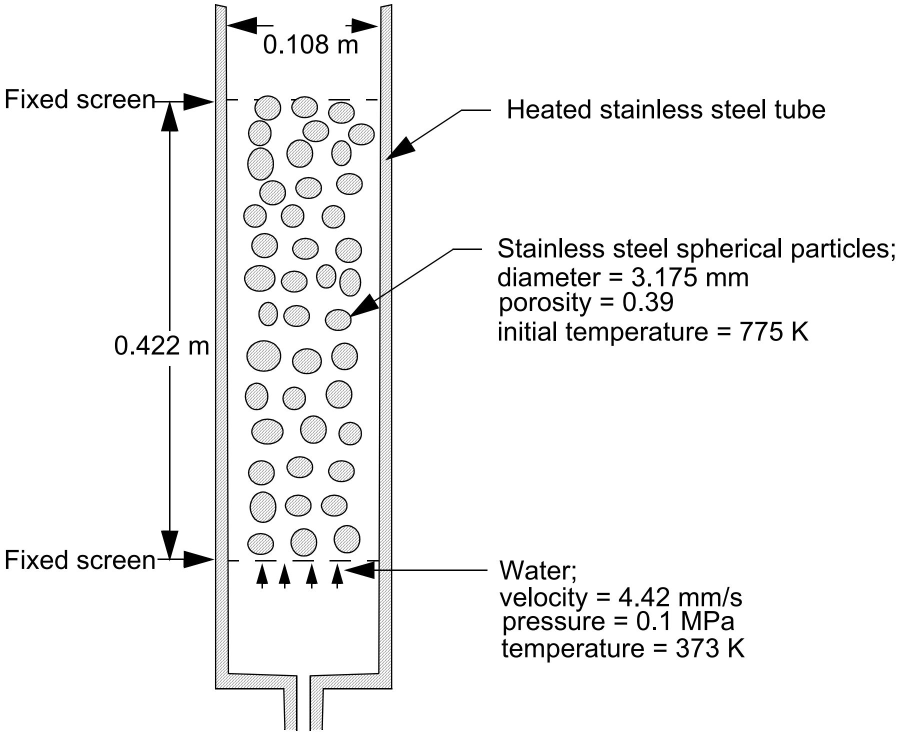
0.108 m
Fixed screen
Heated stainless steel tube
Stainless steel spherical particles;
diameter = 3.175 mm
porosity = 0.39
initial temperature = 775 K
0.422 m
Fixed screen
Water;
velocity = 4.42 mm/s
pressure = 0.1 MPa
temperature = 373 K

Figure 4-2. Schematic of BNL quenching experiment.

The calculated transient temperatures in the debris bed were in general agreement with the measured transient temperatures. The calculated and measured transient temperatures at the elevations of 0.025 m and 0.24 m are compared in Figure 4-3. The elevation of 0.025 m is near the bottom of the debris bed, where reflood began, and the elevation of 0.24 m is slightly above the midplane of the debris bed. The overprediction of the temperature at the 0.24 m elevation in the period of 40 s to 50 s is considered to be due to two-dimensional hydrodynamic behavior, wherein the liquid phase moved up along the wall, formed a pool at the top, and then some of the water flowed down the center region of the debris bed. Since such behavior is not expected in a debris bed resulting from a severe accident in a LWR due to the much larger size of such a debris bed and due to such a debris bed not having cold walls, the calculated and measured temperature comparisons indicate that MOD3.3 is calculating in an acceptable manner the heat transfer in porous debris.

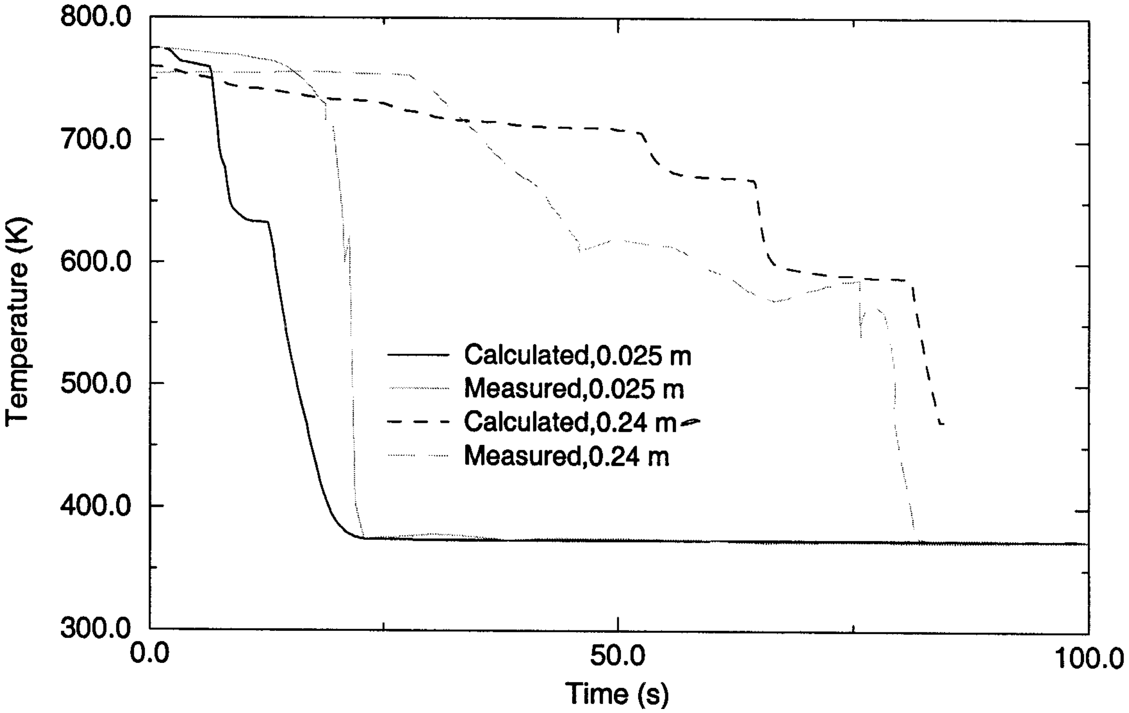

Figure 4-3. Comparison of calculated and measured transient temperature distribution in debris bed

4.2 Model for Heat Transfer In Stratified Molten Pool

The model for heat transfer in a stratified molten pool was assessed by comparing its steady state calculations with those of a model[4-5] benchmarked using the results of experiments with simulant materials. The model was also assessed for internal consistency by examining its calculations of the transient analysis of a stratified molten pool. The lack of experimental data for LWR materials and geometry excluded the assessment of the model by direct comparison with experimental results. A detailed description of the assessment is described in Appendix A9.

A schematic of the system analyzed for assessment purposes is shown in Figure 4-4. The system consisted of a lower head of a reactor vessel containing a pool of molten reactor core material. The lower head was submerged in a pool of water. The lower oxidic part of the molten pool was composed of a mixture of UO_2 and ZrO_2 with a liquidus temperature of 3000 K. The upper metallic part of the molten pool was composed of stainless steel with a liquidus temperature of 1630 K. The oxidic part of the molten pool had a volumetric heat generation rate of 1.4 MW/m^3 and the metallic part did not have any internal heat generation. No heat transfer was assumed to occur from the top surface of the metallic pool. The boundary conditions and the liquidus temperatures were fixed to these values in order to be consistent with the calculations of the benchmarked model with which the MOD3.3 model was being compared.

The MOD3.3 calculated steady state heat transfer behavior was similar to that calculated by the benchmarked model. The MOD3.3 and the benchmarked model calculations for the heat transfer from the stratified molten pool are compared in Table 4-2. The elevation on the external surface of the lower head

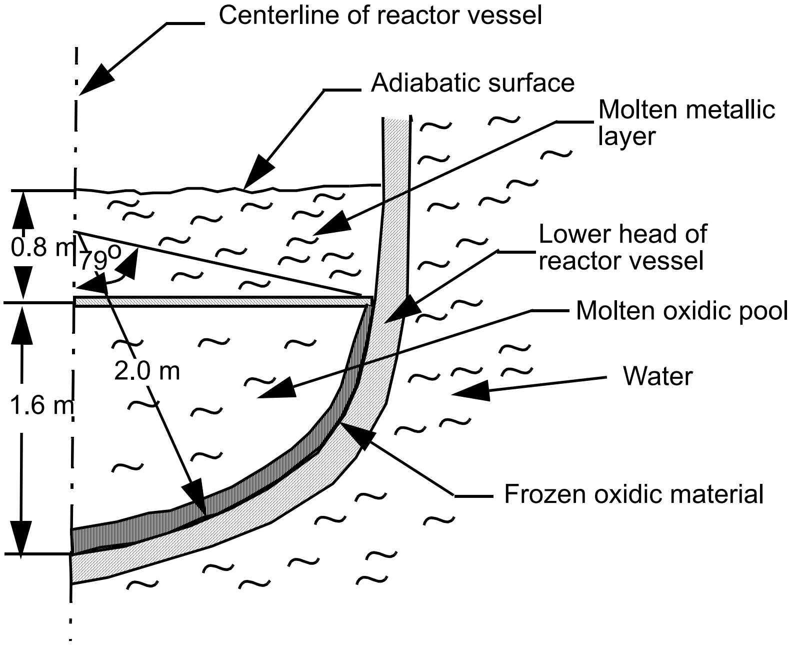

Figure 4-4. Molten pool system analyzed for assessment of MOD3.3 models for heat transfer in stratified molten pool.

with the minimum margin to CHF may be the location with the maximum heat flux from the molten pool to the lower head. For stratified molten pools, the maximum heat flux into the lower head generally occurs near the interface of the metallic pool with the lower head; so the most important result in the calculations is the sideward heat flux into the lower head at this elevation. The MOD3.3 and the benchmarked model calculations for the sideward heat flux at this interface were 0.66 MW/m^2 and 0.55 MW/m^2, respectively. Several other aspects of heat transfer behavior are also compared in Table 4-2. The MOD3.3 and benchmarked model calculations of the heat flux into the lower head at the elevation of the interface of the oxidic and metallic molten pools were 0.83 MW/m^2 and 0.77 MW/m^2, respectively. Both models calculated that this elevation was the elevation of the maximum heat flux into the lower head from the molten pool. The MOD3.3 and the benchmarked values of the bulk temperature of the oxidic part of the molten pool were 3102 K and 3110 K, respectively. The MOD3.3 and benchmarked model calculations for the thickness of the crust on top of the molten pool were 3.7 mm and 5.5 mm, respectively.

Table 4-2. Comparison of SCDAP/RELAP5/MOD3.3 and benchmarked model calculations for heat transfer behavior of stratified molten pool with deep metallic layer.

Aspect of heat transfer	MOD3.3	Benchmarked model
Sideward heat flux of metallic pool (MW/m^2)	0.66	0.55
Sideward heat flux at elevation of interface of oxidic and metallic pools (MW/m^2)	0.83	0.77
Downward heat flux at bottom center of oxidic pool (MW/m^2)	0.06	0.13

Table 4-2. Comparison of SCDAP/RELAP5/MOD3.3 and benchmarked model calculations for heat transfer behavior of stratified molten pool with deep metallic layer.

Aspect of heat transfer	MOD3.3	Benchmarked model
Bulk temperature of oxidic pool (K)	3102	3110
Bulk temperature of metallic pool (K)	1691	1680
Thickness of crust on top of metallic pool (mm)	3.7	5.5

MOD3.3 and the benchmarked model also calculated similar heat transfer for a molten pool with a shallow metallic layer. For the case of a shallow metallic pool, the depth of the metallic pool was 0.22 m instead of 0.80 m and the depth of the oxidic pool was 1.18 m instead of 1.60 m. The other parameters were the same as for the deep metallic pool case. The MOD3.3 and benchmark model calculations for this case are compared in Table 4-3. Both models calculated a significantly greater heat flux into the lower head from the metallic pool for this case than for the case of a deep metallic pool. The MOD3.3 and benchmarked model calculations for this heat flux were 1.91 MW/m^2 and 1.22 MW/m^2, respectively.

Table 4-3. Comparison of SCDAP/RELAP5/MOD3.3 and benchmarked model calculations for heat transfer behavior for case of shallow metallic pool

Aspect of heat transfer	MOD3.3	Benchmarked model
Sideward heat flux of metallic pool (MW/m^2)	1.91	1.22
Sideward heat flux at elevation of interface of oxidic and metallic pools (MW/m^2)	0.55	0.50
Downward heat flux at bottom center of oxidic pool (MW/m^2)	0.04	0.14
Bulk temperature of oxidic pool (K)	3080	3086
Bulk temperature of metallic pool (K)	1799	1736
Thickness of crust on top of metallic pool (mm)	4.6	6.2

A temporary decrease in the margin to CHF may occur during the transition of a molten pool from the condition of being well-mixed to being stratified. The MOD3.3 transient analysis of a well-mixed molten pool that switches to a stratified molten pool was performed for the case of a molten pool with a deep metallic pool after stratification. Except for being initially well-mixed, the molten pool parameters were the same as for the case presented in Table 4-2. The molten pool was assumed to be well-mixed for the first 2000 s of the analysis. At 2000 s, the metallic part of the molten pool was assumed to segregate from the oxidic part and form a metallic pool on top of the oxidic pool. The MOD3.3 calculated transient temperatures of the oxidic and metallic parts of the molten pool are shown in Figure 4-5. After segregation, the metallic pool was calculated by MOD3.3 to cool from 2970 K to 1690 K in about 500 s. The margin to

CHF on the external surface at the elevation of the metallic pool was calculated to be a minimum at the time about midway through the cool down period of the metallic pool. Figure 4-6 is a plot as a function of time of the MOD3.3 calculated ratio of heat flux to critical heat flux for the external surface of the lower head at the elevation of the interface of the oxidic and metallic parts of the molten pool. As shown in the figure, at the instant of stratification, the heat flux ratio was calculated to be 0.26. After stratification, the heat flux ratio was calculated to increase to 0.33 in 320 s, and then gradually decrease to a steady state value of 0.26. MOD3.3 applied the Cheung model[4.6] for the critical heat flux model for the external surface of the lower head.

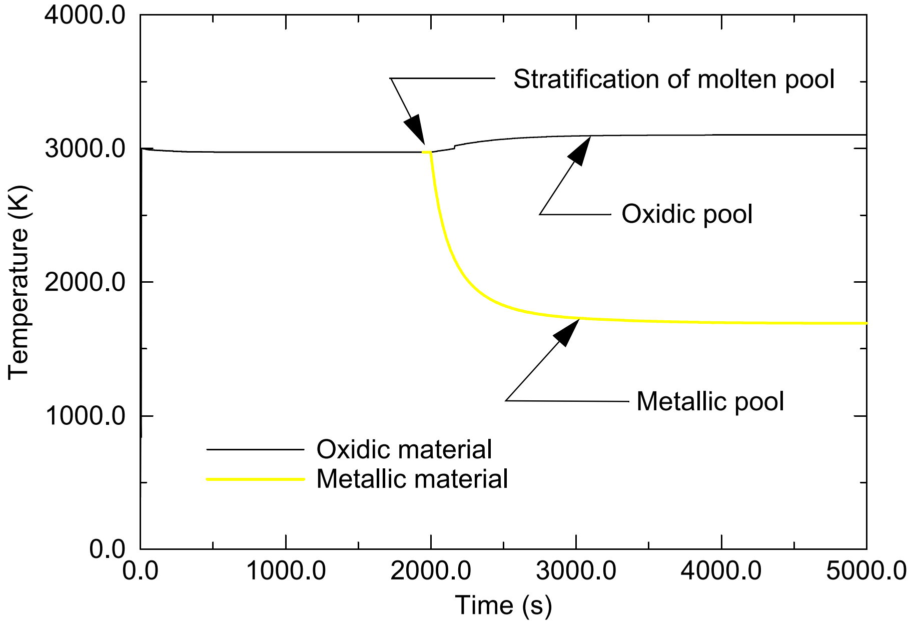

Figure 4-5. Temperature histories of oxidic and metallic parts of molten pool before and after stratification.

4.3 Model for Flow of Liquefied Material Through Porous Debris

The assessment of the model for flow of liquefied core plate material through porous debris indicated that this model was functioning in MOD3.3 in an acceptable manner. No experimental results or calculations of a benchmarked model were available for assessment. So the assessment was limited to a test of the operation of the model and to an evaluation of the internal consistency of the model and the reasonableness of its calculations. A detailed description of the assessment is presented in Appendix A10.

The assessment was performed by analysis of a system composed of porous debris with liquefied core plate material permeating through the porous debris. The porous debris was supported by the lower head of a reactor vessel. A schematic of the system analyzed is shown in Figure 4-7. The porous debris bed had a porosity of 0.4 and was composed of UO_2 particles with a diameter of 3 mm. The debris bed had a volumetric heat generation rate of 1 MW/m^3. The depth of the debris bed along the center line of the

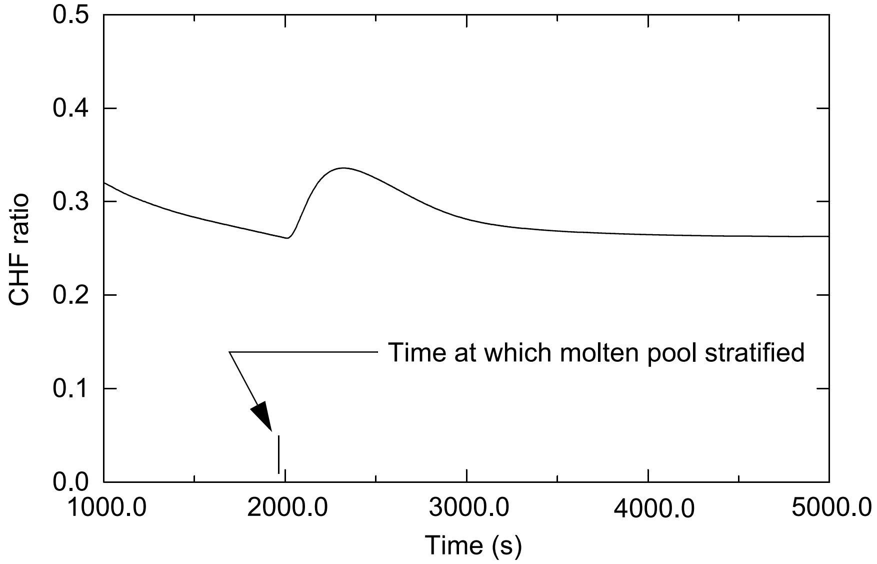

Figure 4-6. Ratio of heat flux to critical heat flux on external surface of lower head before and after stratification of molten pool.

reactor vessel was 0.9 m and its initial temperature was 1727 K. The core plate above the debris bed was melting due to heat transfer by radiation from the top surface of the debris bed. The core plate was composed of stainless steel and had a mass of 25,000 kg. The outer surface of the lower head supporting the debris bed was in contact with a pool of water. The dashed lines in Figure 4-7 represent the finite elements and control volumes used in the numerical solution to represent the debris, lower head, and the core plate material permeating through the debris.

The melted core plate material was calculated to permeate to within 0.05 m of the bottom surface of the lower head and then freeze. The distribution of core plate material within the debris bed along its center line at the time of 1500 s, when 30% of the core plate had melted, is shown in Figure 4-8. The temperature distribution in the debris bed is also shown in Figure 4-8. The debris near the inner surface of the lower head was calculated to be significantly cooler than the debris located several cm above the inner surface. The permeating core plate material was calculated to be blocked by a frozen crust of previously frozen core plate material. The crust caused a region saturated with core plate material to accrete near the inner surface of the lower head.

The permeating core plate material was calculated to not significantly decrease the margin to CHF at the external surface of the lower head. The MOD3.3 calculated ratio of heat flux to critical heat flux for the external surface of the lower head at its bottom center is shown in Figure 4-9. The critical heat flux was calculated using the Cheung model.[4-6] The figure also shows the heat flux ratio for the case of no core plate material permeating through the debris bed. At 2500 s, the heat flux ratios for the case of permeating core plate material and no permeating material were 0.18 and 0.16, respectively. If the core plate material had permeated to the inner surface of the lower head, the heat flux ratio may have increased significantly

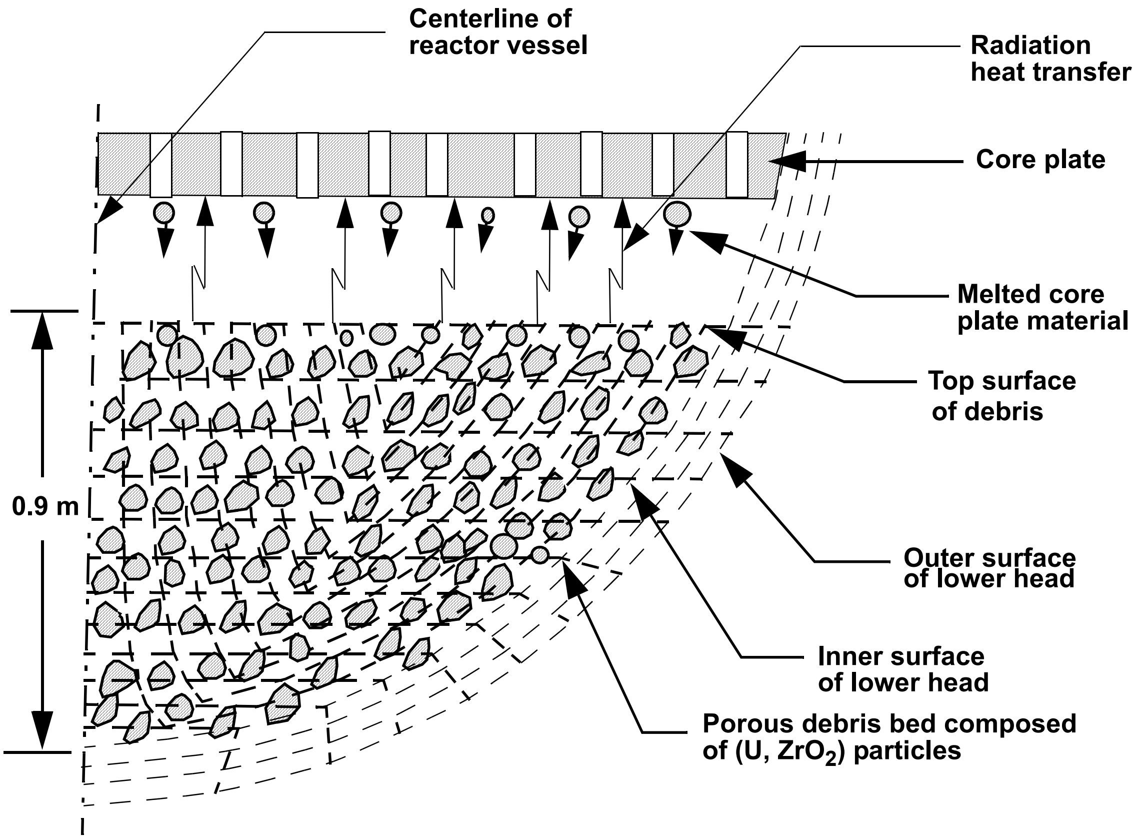
Centerline of reactor vessel
Radiation heat transfer
Core plate
Melted core plate material
Top surface of debris
0.9 m
Outer surface of lower head
Inner surface of lower head
Porous debris bed composed of (U, ZrO2) particles

Figure 4-7 Schematic of system analyzed and nodalization of system for calculation of melted material flowing through porous debris.

due to filling in of voids at the interface of the debris and lower head. The effective thermal conductivity of the region saturated with core plate material was a factor of four greater than that for a region with no core plate material. This increase in effective thermal conductivity was the main contributor to the increase in heat flux ratio.

4.4 Model for Molten Fuel-Coolant Interaction

The assessment of the Fuel-Coolant Interaction (FCI) model in MOD3.3 indicated that this model was representing the basic features of FCI and possibly needs improvements for representation of some of the finer features of FCI. The model was assessed using the results of two FCI experiments and by testing the operation of the model in the context of severe accident analysis. A detailed description of the assessment is presented in Appendix A11. The model has application to the calculation of the extent of break-up of jets of molten material slumping from the core region into a pool of water in the lower head of the reactor vessel.

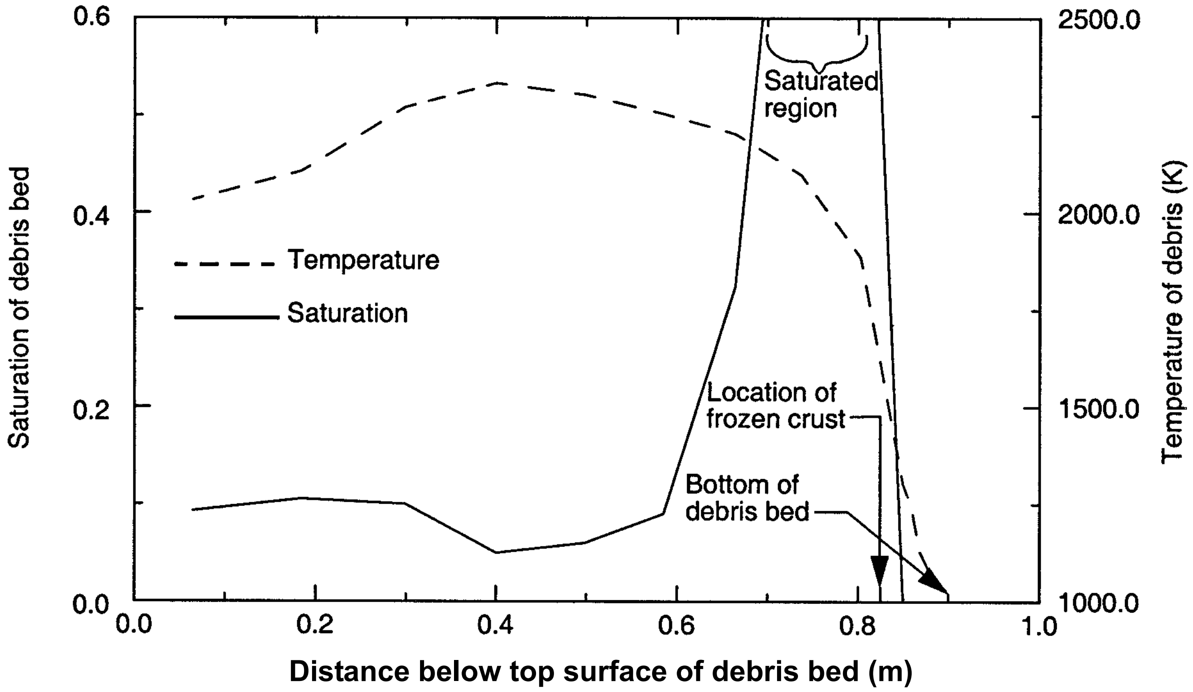

Figure 4-8. Distribution of debris bed saturation and temperature after melting of 30% of core plate (time of 1500 s).

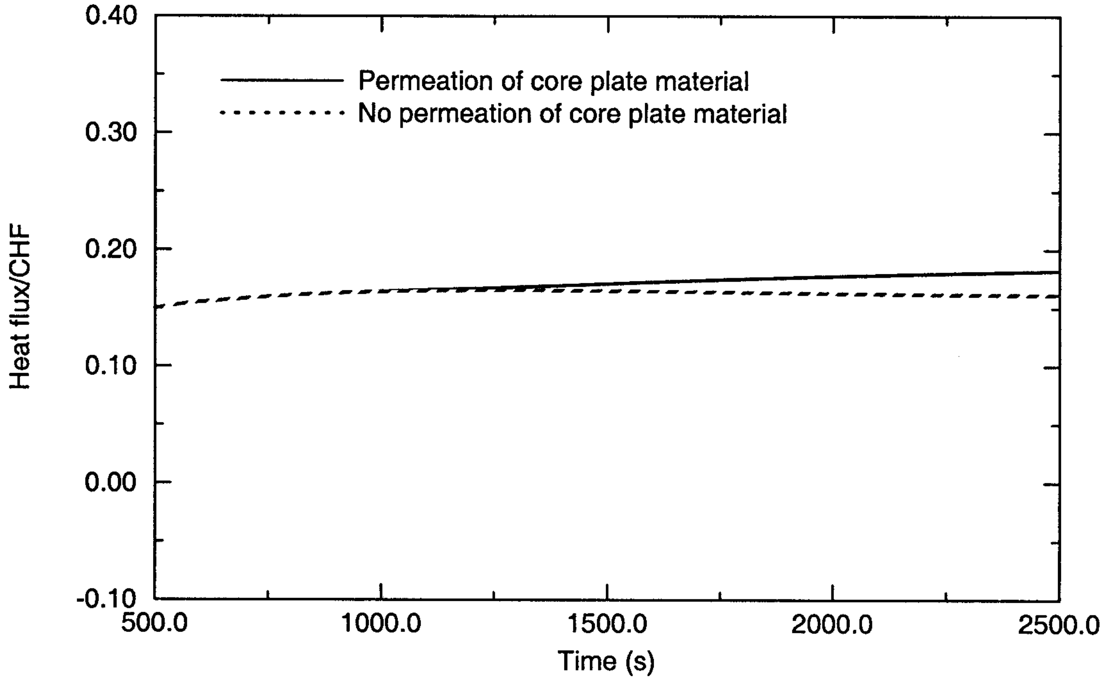

Figure 4-9 Ratio of heat flux to CHF on external surface at bottom center of lower head.

The extent of break-up has a significant influence on the rate of heat transfer from the slumped material to the fluid in contact with it. The extent of break-up also has an influence on the rate of heat transfer from the slumped material to the lower head supporting the slumped material.

The MOD3.3 calculated transient pressure in a vessel with FCI was in general agreement with the measured transient pressure. The FARO L-08 experiment[4-7]obtained a measurement of the transient pressure in a vessel in which FCI occurred. This experiment was used to assess the FCI model in MOD 3.3. A schematic of this experiment is shown in Figure 4-10. In this experiment, a molten mixture of 80 wt% UO_2 and 20 wt% ZrO_2 was injected into a 1.0 m deep pool of water at an initial temperature of 536 K and a subcooling of 10 K. The initial pressure in the test vessel was 5.8 MPa. The MOD3.3 calculated and measured pressure history in the reactor vessel are compared in Figure 4-11. The calculated and measured pressure histories in the test vessel are similar in shape but the calculated rate of increase of pressure is about 50% greater than the measured rate of increase in pressure. The maximum calculated increase in vessel pressure was about 12% greater than the measured maximum increase in pressure. The MOD 3.3 calculated and measured extents of break-up of the jet of slumping material were 70% and 68%, respectively. The MOD3.3 calculated and measured maximum increases in temperature of the bottom plate of the test vessel on which the slumped material settled were 275 K and 352 K, respectively.

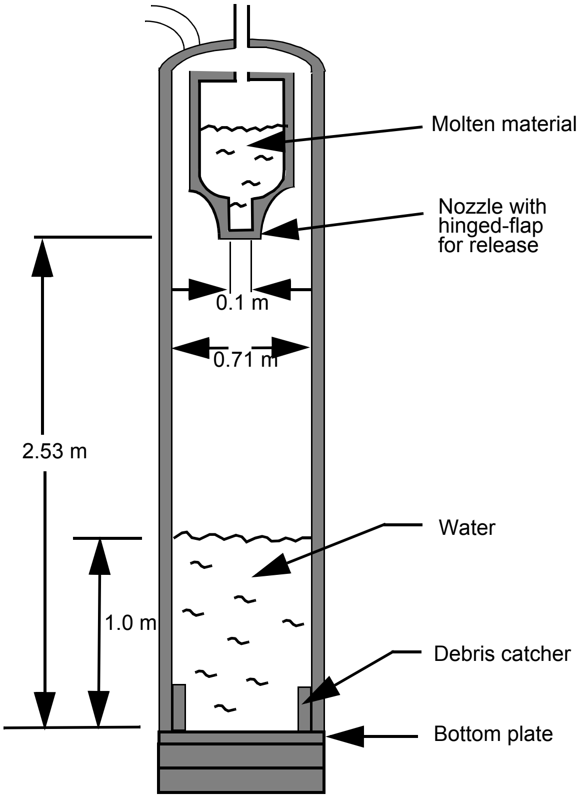

Figure 4-10. Schematic of FARO Test Arrangement.

A significant discrepancy in the MOD3.3 calculation was the calculated size of the particles resulting from FCI; the MOD3.3 and measured calculated sizes of particles were 0.56 mm and 3.8 mm, respectively. One reason for this discrepancy may be the use of an incorrect value for the interfacial tension of a mixture of UO_2 and ZrO_2 in contact with water and steam. The particle size is calculated to be proportional to this

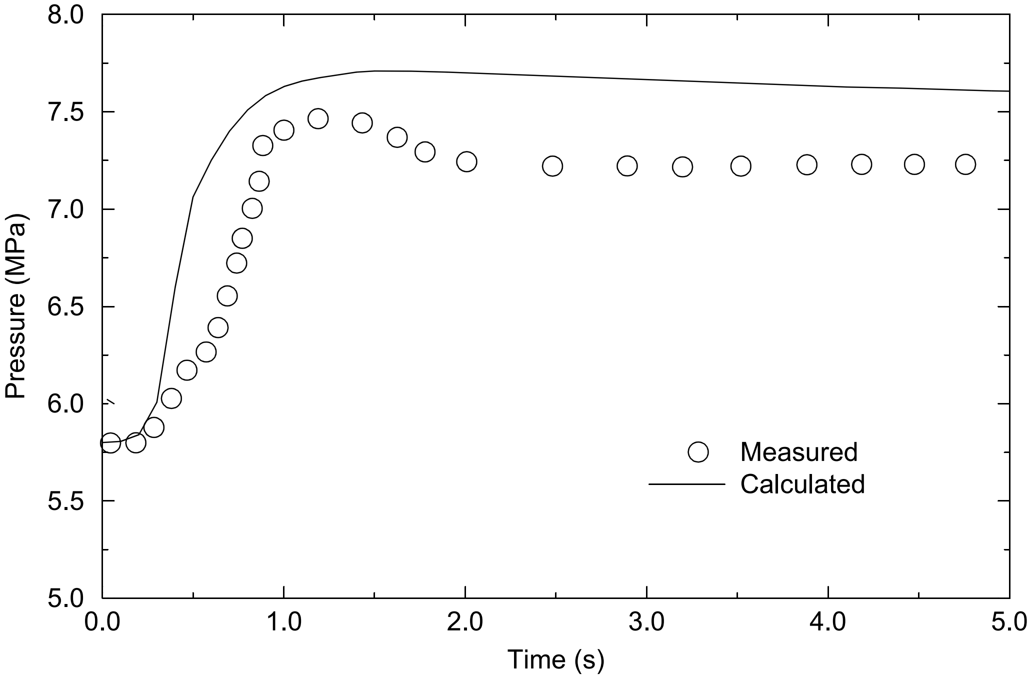

Figure 4-11. Comparison of calculated and measured pressure histories for FARO Test L-08.

material property for which there is large amount of uncertainty in value.

4.5 TMI-2 Accident

The TMI-2 accident involved a wide range of damage progression and thus is useful for assessing severe accident computer codes. The damage progression included; (1) ballooning of fuel rods, (2) intense oxidation and rapid heatup to temperatures that melted a part of the reactor core, (3) reflood of a hot, partially oxidized core, (4) formation of a molten region across the entire diameter of the reactor core, and (5) slumping of a significant amount of molten material to the lower head.[4-8] During and following the TMI-2 accident, measurements and analyses based on measurements have provided a basis for a quantitative assessment of some of the most important variables calculated by a severe accident computer code. These variables include the increase in primary coolant system pressure following reflood of a hot core, cumulative hydrogen production before and after reflood of a hot and partially oxidized core, maximum mass of molten material and its location within the reactor core, and timing of slumping of molten material from the core region to the lower head. Since most of the processes causing damage progression are interdependent, these limited number of measurements and values inferred from measurements provide a basis for assessing most of the damage progression models in the SCDAP/RELAP5/MOD3.3 code. The detailed description of the assessment of MOD3.3 using data from the TMI-2 accident is presented in Appendix A12.

The MOD3.3 calculation of the progression of damage in the TMI-2 reactor during its severe accident was in general agreement with the measurements of damage progression and the post-accident observation of the state of the reactor core. Table 4-4 summarizes the comparison of calculated and measured damage progression. The MOD3.2 calculations of the TMI-2 accident are also included in this table. After core uncovery was calculated to occur at 6270 s, core damage was calculated to occur quite rapidly. Cladding failure due to ballooning was calculated by MOD3.3 to begin at 8445 s. MOD3.2 calculated cladding failure to be due to chemical attack by the Inconel spacer grids and to not occur until 9418 s. After cladding failure, double-sided oxidation of the cladding was calculated by MOD3.3 to occur in the vicinity of the cladding failure. The melting of fuel and the formation of a molten pool were calculated by MOD3.3 to begin at 9530 s. MOD3.2 calculated molten pool formation to begin at 10,330 s. The start-up of the 2B-pump at 10,446 s was calculated by both MOD3.3 and MOD3.2 to cause a rapid increase in the pressure of the primary coolant system and to accelerate the rate of hydrogen production. These calculations are in agreement with the measurements. MOD3.3 calculated 15,000 kg of molten material in the core region at the start of the 2-B pump and 27,600 kg of molten material in the core just before the slumping of core material to the lower head at 12,890 s. MOD3.2 calculated 1734 kg of molten material in the core region at the start-up of the 2B-pump and 37,400 kg of molten material in the core just before the slumping of core material to the lower head at 13,379 s. The post-accident examination of the TMI-2 reactor indicated that 40,800 kg of the reactor core was molten at some time. Inferences from the measured system pressure and other measurements indicated that 15,800 kg of molten material slumped to the lower head at 13,500 s. Both the MOD3.3 and MOD3.2 calculated masses of molten material and the time of slumping are in general agreement with the measured values.

The MOD3.3 calculated location of molten core material was in good agreement with the post-accident observation of the TMI-2 reactor. The elevations of the bottom surface of the in-core molten pool at the center line of the core were calculated and observed to be 1.10 m and 0.71 m, respectively. The highest location in the core to become molten was calculated to be 2.9 m and to be located along the center line of the core. The molten pool was calculated to extend in the radial direction from the center line of the reactor vessel to the periphery of the reactor core. The bottom surface of the molten pool at the periphery of the core was calculated by MOD3.3 to be at the elevation of 2.2 m. These calculated results were in agreement with the post-accident observation of the TMI-2 core.

Table 4-4. Calculated timing and sequence of core damage progression.

Damage progression parameter	Measured or inferred	MOD3.2	MOD3.3
Beginning of long term core uncovery (s).	-	6,390	6,270
Beginning of cladding failure due to ballooning (s).	-	9,417	8,445
Beginning of spacer grid slumping (s).	-	9,418	9,112
Beginning of molten pool (s).	-	10,330	9,530
Cumulative hydrogen production at start-up of 2B-pump at 10,446 s (kg).	300	275	365

Table 4-4. Calculated timing and sequence of core damage progression. (Continued)

Damage progression parameter	Measured or inferred	MOD3.2	MOD3.3
Primary coolant system pressure at start-up of 2B-pump (MPa).	8.20	5.03	6.96
Mass of molten material at start-up of 2B-pump (kg).	-	1734	15,000
Increase in primary coolant system pressure after start-up of 2B-pump (MPa).	6.30	5.21	7.00
Final cumulative hydrogen production (kg).	460	453	417
Mass of core material that was molten during some period of accident (kg).	40,800	37,400	27,600
Elevation of bottom of molten region relative to bottom of core (m).	0.71	1.46	1.10
Smallest distance from side of molten pool to periphery of core (m).	0.0	0.0	0.0
Time at which bulk of material in molten material slumped to lower head (s).	13,500	13,379	12,890
Mass of molten material that slumped to lower head (kg).	15,800	37,400	27,600
Percent of molten material that slumped to lower head (%).	39	100	100

MOD3.3 calculated severe core damage to begin about 800 s earlier than MOD3.2. The onset of melting of the reactor fuel and the beginning of molten pool formation is a mark of the beginning of severe core damage. The timing of damage progression is indicated by plots of the history of the maximum temperature in the reactor core and of the effective radius of the molten pool, as shown in Figures 4-12 and 4-13, respectively. The effective radius is the radius of a hemisphere with a volume equal to the calculated volume of molten material. The MOD3.3 and MOD3.2 calculated timings for the beginning of fuel melting were 9530 s and 10,330 s, respectively. MOD3.3 calculated a significantly more rapid heatup of the reactor core after the beginning of oxidation than did MOD3.2. In the temperature range of 1800 K to 2200 K, when rapid oxidation occurs, MOD3.3 calculated a heatup rate of nearly 50 K/s. The MOD3.2 calculated rate of heatup in this range of temperature was significantly less than that calculated by MOD3.3. Both

MOD3.3 and MOD3.2 calculated that activation of the 2B-pump at 10,446 s did not result in any reduction in the maximum core temperature. A reduction in temperature was calculated to not occur because a significant part of the core was in the form of a large molten pool and because of an increase in oxidation of fuel rod cladding due to cracking of oxide layers and more flow of steam. The activation of HPIS at 12,012 s was calculated to not cause any cooling of the molten part of the reactor core. MOD3.3 calculated no further melting of fuel after 10,480 s (34 s after activation of 2B-pump), while MOD3.2 calculated fuel melting to occur until 13,000 s. MOD3.3 calculated the maximum effective radius of the molten pool to be 1.2 m. This value is in general agreement with the corresponding measured value of 1.4 m. When using a special model for failure of an oxide layer retaining melted metallic cladding, MOD3.2 also calculated the amount of molten core material to be similar to the measured value. But when using the same oxide failure model as used for the analyses of severe accident experiments, MOD3.2 underpredicted the amount of molten material by a factor of two.

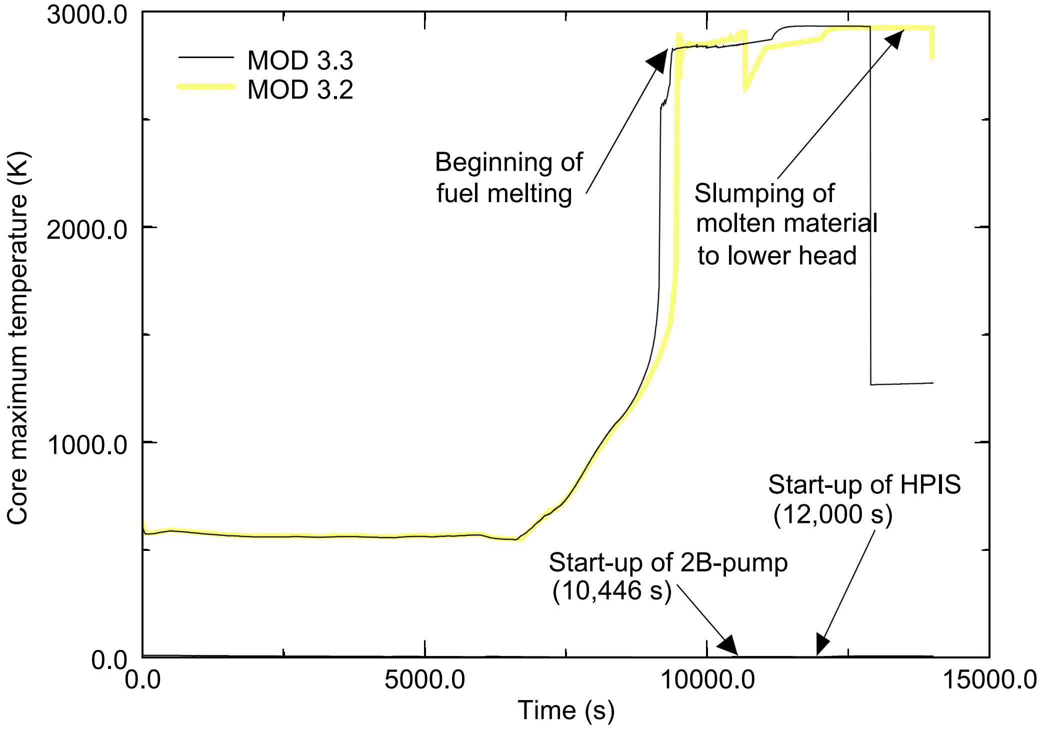

Figure 4-12. History of calculated maximum temperature in reactor core.

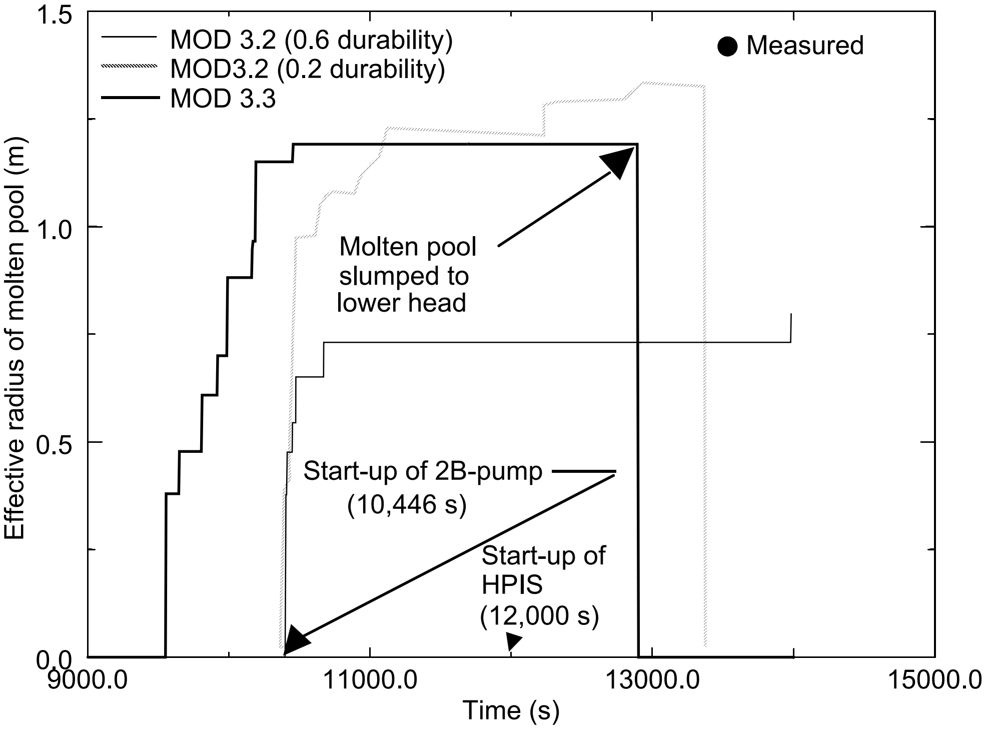

Figure 4-13. History of calculated effective radius of molten pool.

The calculated hydrogen production was in general agreement with the hydrogen production estimated from post-accident observations and inferences. The MOD3.3 calculated cumulative hydrogen production is compared with the measured hydrogen production in Figure 4-14. The MOD3.2 calculated hydrogen production is also shown in the figure. MOD3.3 calculated the rapid production of hydrogen to begin sooner than MOD3.2. Nevertheless, both the MOD3.3 and MOD3.2 calculations of hydrogen production are in approximate agreement with the measured hydrogen production. At the start-up of the 2B-pump, the MOD3.2 and MOD3.3 calculations of cumulative hydrogen production were 275 kg and 365 kg, respectively. The measured hydrogen production at the start-up of the 2B-pump was 300 kg. The MOD3.3 calculated and measured total hydrogen productions were 417 kg and 460 kg, respectively. The MOD3.2 total hydrogen production was 453 kg. Both MOD3.3 or MOD3.2 calculated that no significant amount of hydrogen production occurred 50 s after the start-up of the 2B-pump (10,500 s). Hydrogen production was calculated to not occur after 10,500 s because the portions of the core with intact fuel rods and some metallic cladding were too cool to rapidly oxidize. This behavior is shown in Figure 4-15, where the MOD3.3 calculated temperature histories are shown for the fuel rods in the outer most fuel assemblies of the reactor core at the elevations of 3.11 m and 3.47 m, respectively. As shown in this figure, hydrogen production at the 3.11 m elevation and at the 3.47 m elevation was calculated to stop due to the cooling caused by the start-up of the 2B-pump. The oxide layer at these locations was calculated to be too thin to crack during the reflood caused by start-up of the 2B-pump.

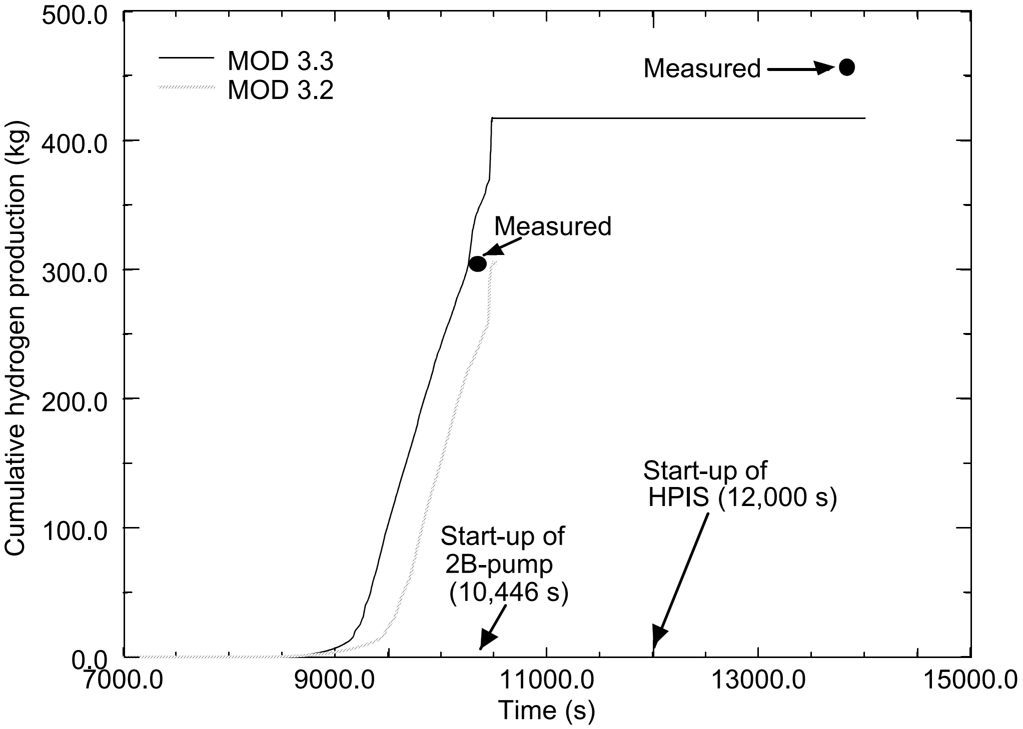

Figure 4-14. Calculated hydrogen production during TMI-2 accident.

The MOD3.3 calculation of the disintegration of fuel rods into porous debris was in agreement with the post-accident observation of the locations in the reactor core with porous debris. Porous debris regions were calculated to form in the outer most fuel assemblies in the elevation interval of 0.5 m to 1.2 m and across the entire diameter of the reactor core in the elevation interval of 2.6 m to 3.6 m. The calculation of porous debris in the elevation interval of 2.6 m to 3.6 m was consistent with the post-accident observation of the state of the reactor core.

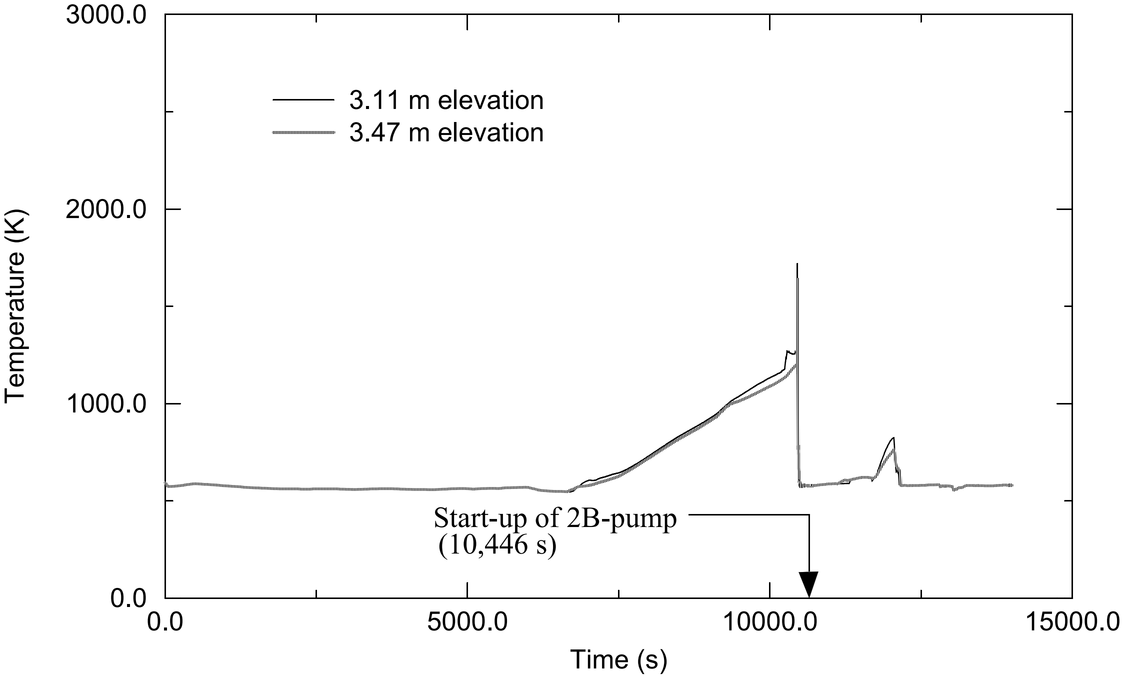

Figure 4-15. MOD3.3 calculated temperature histories of fuel rods in upper part of outer most fuel assemblies in reactor core.

The porous debris thermal hydraulic models in MOD3.3 performed properly after activation of the HPIS, which resulted in two-phase coolant conditions in porous debris in the upper part of the reactor core. The calculated temperature history at a location with porous debris is shown in Figure 4-16. The plot applies for the location 2.7 m in elevation and in the fourth ring of fuel assemblies. This location disintegrated from intact fuel rods to porous debris soon after start-up of the 2B-pump, and thus was porous debris at the time of start-up of HPIS. As a result, the flow losses and heat transfer at this location during the reflood period beginning with the start-up of HPIS were calculated with the porous debris thermal hydraulic models implemented into MOD3.3. The debris had a porosity of 0.46 and a particle diameter of 3.5 mm. Since the molten pool was located below this location and blocked the upward flow of water from the HPIS, the debris was flooded from the top down. The calculated temperature history of this location following reflood of the reactor core beginning at 12,012 s was consistent with that seen in experiments on the quenching of porous debris, as described in Appendix 8.

The implementation into MOD3.3 of the integral diffusion model for fuel rod oxidation caused it to calculate a more rapid progression of damage to the reactor core than calculated by MOD3.2. The onset of severe damage was calculated to begin at 9530 s by MOD3.3 and at 10,330 s by MOD3.2. This difference is due to the integral diffusion model for oxidation in MOD3.3 calculating a more rapid heatup due to oxidation at locations with a rich supply of steam than that calculated by the parabolic kinetics model for oxidation in MOD3.2. These differences in calculated behavior also occurred in the analyses of severe fuel damage experiments described in Appendices A2 through A4.

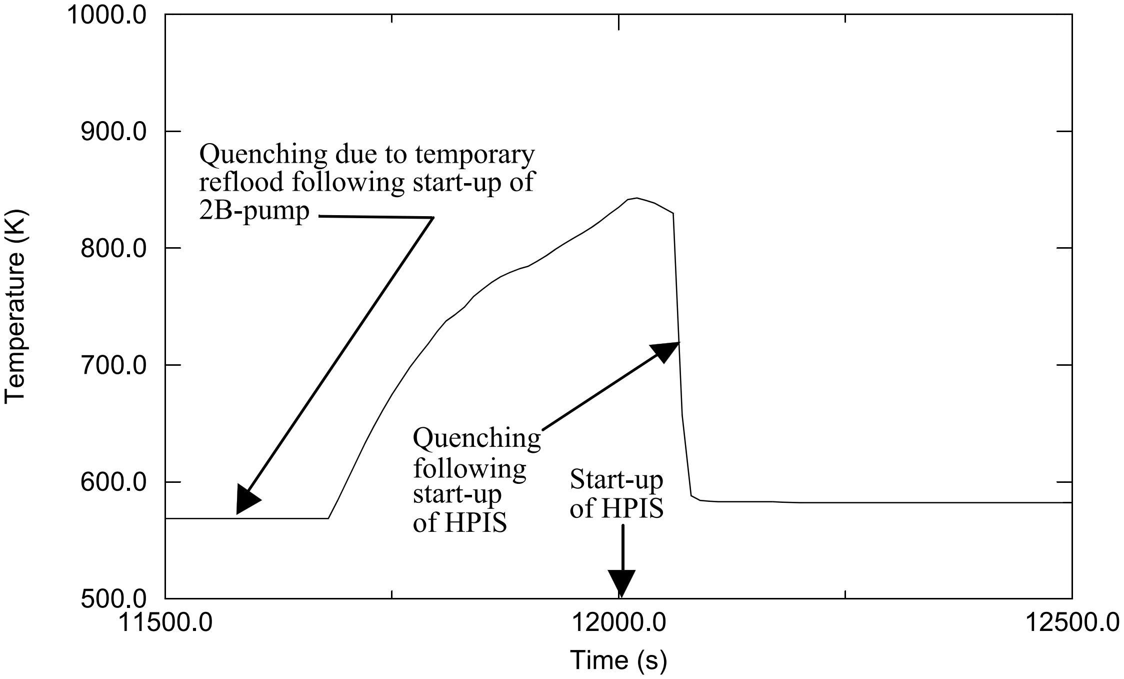

Figure 4-16. MOD 3.3 calculated temperature history of location with porous debris (2.7 m elevation of fourth ring of fuel assemblies).

The MOD3.3 calculation of the TMI-2 accident was improved by the implementation into MOD3.3 of the stress-based model for calculating the time of failure of an oxide layer retaining the melted metallic part of the fuel rod cladding. While MOD3.2 applied one model for failure of the oxide layer for analysis of severe fuel damage experiments and another model for the analysis of the TMI-2 accident, MOD3.3 applied the same oxide failure model for analysis of severe fuel damage experiments and the TMI-2 accident. The calculations of the oxide failure model have a strong influence on the calculations of hydrogen production and the extent of melting of fuel assemblies. With the stress-based model for calculating oxide failure, MOD3.3 calculated hydrogen production and extent of melting in general agreement with measurements for both severe fuel damage experiments and the TMI-2 accident. On the other hand, when using the same oxide failure model for the TMI-2 analysis as used for analysis of severe fuel damage experiments, MOD3.2 underpredicted by a factor of two the extent of melting of the reactor core, and did not predict any slumping of molten core material to the lower head.

Another difference in calculated reactor core behavior between MOD3.3. and MOD3.2 was in the calculated ballooning and rupture of fuel rods; MOD3.3 calculated ballooning and rupture of fuel rod cladding to occur significantly earlier than MOD3.2. This difference in calculated behavior is due to corrections made in MOD3.3 to the model for ballooning of the fuel rod cladding.

4.6 Conclusions

The assessment of MOD3.3 showed that the five new models implemented into the code for calculating the behavior of LWRs during the late-phase of a severe accident are fully operational and extend the range of applicability of the code. The first two new models, namely the models for flow loss and heat transfer in a porous debris, furnish MOD3.3 with the capability to correctly calculate the blockage to flow caused by the formation of porous debris and to calculate the temperature behavior of porous debris for a wide range of coolant conditions. The third new model, namely the model for heat transfer from a stratified molten pool, furnishes MOD3.3 with the capability to calculate the heat transfer from molten pools that stratify into oxidic and metallic parts. This model calculated that stratification of a molten pool decreases the margin to CHF on the external surface of a flooded lower head. The fourth new model, namely the model for the flow of melted core plate material through porous debris in the lower head, extends the range of application of the code to the situation in which the core plate is melting above a porous debris bed. This model calculated that melted core plate material does not significantly decrease the margin to CHF for a flooded lower head. The fifth new model, namely the model for the interaction of jets of molten fuel with a pool of water in the lower head, calculated a transient pressure increase due to fuel-coolant interaction in general agreement with the measured pressure increase.

The MOD3.3 calculation of the TMI-2 accident showed that its new models result in calculated behavior of the reactor core and primary coolant system in general agreement with measurements and post-accident observations. The new models that were an integral part of the MOD3.3 calculation of the TMI-2 accident included; (1) integral diffusion model for oxidation of fuel rod cladding, (2) stress-based model for failure of oxide layer containing melted metallic cladding, (3) cracking model for cladding oxide layer during reflood conditions, and (4) porous debris thermal hydraulic models. The calculated and measured behavior of the TMI-2 reactor during its accident are summarized as follows. The calculated and measured hydrogen productions were 417 kg and 460 kg, respectively. The calculated and measured masses of molten material in the core region were 27,600 kg and 40,800 kg, respectively. The calculation of the locations of porous debris regions in reactor core was for the most part in agreement with the observed locations of porous debris. The calculated temperature behavior of the porous debris was consistent with temperature behavior expected during debris quenching. The calculated and measured rapid increase in primary coolant system pressure following the start-up of the 2B-pump were in general agreement. The calculated location of molten material in the core region and the timing of the slumping of this molten material to the lower head were in general agreement with inferences from measurements and the post-accident observation of the reactor core.

While MOD3.3 and MOD3.2 calculated similar final damage states for the TMI-2 reactor, nevertheless the two versions of the code calculated transient aspects of behavior to be significantly different. MOD3.3 calculated damage progression in the reactor core to occur significantly more rapid than MOD3.2. This difference is due to oxidation of fuel rod cladding in MOD3.3 being calculated by the integral diffusion model instead of by the parabolic kinetics model in MOD3.2. MOD3.3 calculated the ballooning and rupture of fuel rod cladding to occur significantly earlier than MOD3.2. This difference is due to corrections to the ballooning model implemented into MOD3.3. The stress-based model in MOD3.3 for the failure of an oxide layer retaining melted cladding resulted in good agreement of calculations with measurements for both the analysis of the TMI-2 accident and the analyses of severe fuel damage experiments. On the other hand, MOD3.2 underpredicted the extent of core melting by a factor of two when using for the TMI-2 analysis the same oxide failure model as used for the analyses of severe fuel damage experiments. In the modeling of phenomena causing damage to fuel assemblies during severe accident conditions, MOD3.3 does not require a distinguishing of models for the analyses of severe fuel damage experiments from the models for the analyses of nuclear power plants; one set of models applies for both types of analyses, and all of the models used for nuclear power plant analyses have been assessed using severe fuel damage experiments.

4.7 References

4-1. The SCDAP/RELAP5 Development Team, "SCDAP/RELAP5/MOD3.2 Code Manual, Developmental Assessment," NUREG/CR-6150, Vol. 5, Rev. 1, INEL-96/0422, July 1998

4-2. V. X. Tung, V. K. Dhir, and D. Squarer, "Forced Flow Cooling Studies of Volumetrically Heated Porous Layers," Second International Topical Meeting on Nuclear Reactor Thermal-Hydraulics, Santa Barbara, California, USA, January 11-14, 1983.

4-3. S. Ergun, "Fluid Flow Through Packed Columns," Chem. Eng. Prog. 48 (1952) pp. 89-94.

4-4. N. K. Tutu et al, "Debris Bed Quenching Under Bottom Flood Conditions (In-Vessel Degraded Core Cooling Phenomenology)", NUREG/CR-3850, 1984.

4-5. T. G. Theofanous, C. Liu, S. Additon, S. Angelini, O. Kymalainen, and T. Salmassi, "In-Vessel Coolability and Retention of Core Melt," Report DOE/ID-10640, Vol. 1, July 1995.

4-6. F. B. Cheung, K. H. Haddad, and Y. C. Liu, "A Scaling Law for the Local CHF on the External Bottom Side of a Fully Submerged Reactor Vessel," NUREG/CR-0157, Vol. 2, February 1997, pp. 253-277.

4-7. D. Magallon and H. Hohmann, "Experimental Investigations of 150-kg Scale Corium Melt Jet Quenching in Water," Proceedings of the 7-th International Meeting on Nuclear Reactor Thermal Hydraulics (NURETH-7), Saratoga Springs, NY, September 1995, NUREG/CP-0412, pp 1688-1711.

4-8. J. M. Broughton, P. Kuan, D. A. Petti, and E. L. Tolman, "A Scenario of the Three Mile Island Unit 2 Accident," Nuclear Technology, 87, August 1989, pp. 34-53.

APPENDIX A - SCDAP/RELAP5-3D© ASSESSMENT

CONTENTS

A1. BOILOFF IN BUNDLE A1-1
  A1.1 References A1-5

A2. FLHT-5 TEST A2-1
  A2.1 Nodalization A2-1
  A2.2 Boundary Conditions A2-2
  A2.3 Comparison of Calculations and Measurements A2-3
  A2.4 References A2-7

A3. PBF SFD SERIES OF EXPERIMENTS A3-1
  A3.1 Assessment Using PBF SFD-ST Test A3-2
    A3.1.1 Nodalization A3-2
    A3.1.2 Boundary Conditions A3-2
    A3.1.3 Results A3-5
  A3.2 Assessment Using the PBF SFD 1-1 Test A3-10
    A3.2.1 Nodalization and Boundary Conditions A3-11
    A3.2.2 Comparison of Calculations and Measurements A3-11
  A3.3 Assessment Using the PBF SFD 1-4 Test A3-17
    A3.3.1 Nodalization A3-18
    A3.3.2 Initial Conditions A3-19
    A3.3.3 Boundary Conditions A3-19
    A3.3.4 Comparison of Calculations and Measurements A3-20
    A3.3.5 References A3-26

A4. CORA TESTS A4-1
  A4.1 General Description of the CORA Test Facility A4-1
  A4.2 Nodalization of the CORA Test Facility A4-2
  A4.3 Test Conditions for the CORA Tests A4-3
  A4.4 Assessment Using CORA-5 TEST A4-4
    A4.4.1 Description of the Experimental Bundle A4-4
    A4.4.2 Comparison of Calculations and Measurements A4-4
  A4.5 Assessment Using the CORA-7 Test A4-8
    A4.5.1 Description of the CORA-7 Experimental Bundle and Test A4-8
    A4.5.2 Assessment Results A4-9
  A4.6 Assessment Using the CORA-13 Test A4-13
    A4.6.1 References A4-17

A4.7 Assessment Using the CORA-17 Test....A4-18
  A4.7.1 Nodalization....A4-18
  A4.7.2 Boundary Conditions....A4-19
  A4.7.3 Comparison of Calculations and Measurements....A4-19
A5. PHEBUS B9+ TEST....A5-1
A5.1 Bundle Nodalization....A5-2
A5.2 Boundary and Initial Conditions....A5-2
A5.3 Comparison of Calculations and Measurements....A5-2
A5.4 Reference....A5-9
A6. PHEBUS FPT0 TEST....A6-1
A6.1 Introduction....A6-1
A6.2 Test Description....A6-1
A6.3 Nodalization of Test Fuel Assembly....A6-2
A6.4 Comparison of Calculations and Measurements....A6-3
A6.5 References....A6-8
A7. ACRR DF-4 TEST....A7-1
A7.1 Nodalization of Test Fuel Assembly and Boundary Conditions....A7-2
A7.2 Comparison of Calculations and Measurements....A7-4
A7.3 References....A7-5
A8. FLOW LOSS AND HEAT TRANSFER IN POROUS DEBRIS....A8-1
A.8.1 Flow Loss....A8-1
A8.3 Heat Transfer....A8-2
A8.3 Thermal Hydraulic Behavior in Lower Head....A8-5
A8.4 Conclusions....A8-6
A8.5 References....A8-9
A9. HEAT TRANSFER IN STRATIFIED MOLTEN POOL....A9-1
A9.1 Comparison of Calculations With Benchmarks....A9-1
A9.2 Conclusions....A9-6
A9.3 References....A9-7
A10. FLOW OF MELTED MATERIAL THROUGH POROUS DEBRIS....A10-1
A10.1 Testing By Application To PWR Severe Accident Situation....A10-1
A10.2 Testing By Evaluation of Internal Consistency and Reasonability....A10-5
A10.3 References....A10-7

A11. MOLTEN FUEL-COOLANT INTERACTION A11-1
A11.1 Assessment with a MAGICO-2000 experiment A11-1
A11.2 Assessment with a FARO Experiment A11-4
A11.3 Application of FCI Model to Severe Accident Analysis A11-7
A11.4 Summary of Assessment Results A11-12
A11.5 References A11-14
A12. TMI-2 ACCIDENT A12-1
A12.1 Introduction A12-1
A12.2 Description of TMI-2 Accident Problem A12-1
A0.2.1 Boundary Conditions A12-10
A12.3 Assessing Using TMI-2 Accident A12-12
A12.4 Conclusions A12-21
A12.5 References A12-22
A13. BROWNS FERRY BWR LOCA SEVERE ACCIDENT A13-1
A13.1 Nodalization A13-1
A13.2 Description of the Modeled BWR Severe Accident A13-5
A13.3 Results A13-5
A14. SURRY PWR SEVERE ACCIDENT A14-1
A14.1 Introduction A14-1
A14.2 Model Description and Nodalization A14-1
A14.3 Boundary Conditions for TMLB' Severe Accident A14-7
A14.4 References A14-9

FIGURES

A1-1. Schematic of test problem and nodalization of fuel bundle. A1-2
A1-2. History of flow rate at inlet of bundle. A1-3
A1-3. Comparison of SCDAP and RELAP5 calculated cladding surface temperatures at elevations of 0.40 m and 0.86 m. A1-5
A1-4. Bundle uncovery histories as calculated by SCDAP and RELAP5 heat structures at elevations of 0.40 and 0.86 m. A1-6
A1-5. Heat transfer rate to coolant at axial node 5. ....A1-6
A2-1. RELAP5 nodalization and bundle configuration for FLHT-5. ....A2-2
A2-2. Calculated and measured temperature at 2.37 m elevation for FLHT-5. ....A2-3
A2-3. Calculated and measured temperature at 1.64 m elevation for FLHT-5. ....A2-4
A2-4. Comparison of calculated and measured temperature at 1.22 m elevation for FLHT-5. ....A2-5
A2-5. Comparison of calculated and measured cumulative hydrogen production for FLHT-5 test. A2-6
A2-6. Comparison of calculated and measured hydrogen production rate. A2-7
A3-1. RELAP5 nodalization of the test train for the SFD-ST experiment. A3-3
A3-2. SCDAP core representation of the SFD-ST experimental bundle. A3-3
A3-3. Total bundle power for the SFD-ST experiment. A3-4
A3-4. Comparison of calculated and measured cladding temperatures at the 0.7 m elevation for PBF SFD ST test. A3-6
A3-5. Calculated and measured temperatures at 0.5 m elevation for PBF SFD ST test. A3-7
A3-6. Calculated and measured temperatures at 0.35 m elevation for PBF SFD ST test. ...A3-7
A3-7. Calculated cumulative hydrogen production for PBF SFD ST test. A3-9
A3-8. Comparison of calculated and measured collapsed liquid level in test fuel assembly for PBF SFD ST test. A3-10
A3-9. RELAP5 nodalization of the test train for the SFD1-1 experiment. A3-12
A3-10. SCDAP nodalization of the PBF SFD1-1 experimental bundle. A3-13
A3-11. Calculated and measured temperatures at 0.35 m elevation for PBF SFD 1-1 test. A3-14
A3-12. Calculated and measured temperature at elevation of 0.5 m for PBF SFD 1-1 test. A3-14
A3-13. Calculated and measured temperature at elevation of 0.7 m for PBF SFD 1-1 test. A3-15
A3-14. Calculated and measured rate of hydrogen production for PBF SFD 1-1 test. A3-17
A3-15. SCDAP nodalization of the PBF SFD 1-4 test bundle. A3-18
A3-16. RELAP5 nodalization of the PBF SFD 1-4 test bundle. A3-19
A3-17. Calculated and measured temperatures at 0.4 m elevation for PBF SFD 1-4 test. A3-20
A3-18. Calculated and measured temperatures at 0.54 m elevation for PBF SFD 1-4 test. A3-21
A3-19. Calculated and measured temperatures at 0.74 m elevation for PBF SFD 1-4 test. A3-22
A3-20. Calculated and measured temperatures at shroud mid-wall at 0.91 m for PBF SFD 1-4 test. A3-22

A3-21. Comparison of calculated and measured rates of hydrogen production for PBF SFD 1-4. ....A3-24
A3-22. Calculated cumulative hydrogen production for PBF SFD 1-4 test. A3-25
A4-1. General CORA RELAP5 nodalization used for all PWR tests. A4-2
A4-2. CORA-13 bundle cross-section basic design used for all PWR tests. A4-3
A4-3. Calculated and measured temperatures of unheated fuel rod at 0.35 m elevation for CORA-5 test. A4-5
A4-4. Calculated and measured temperatures of unheated fuel rod at 0.55 m elevation for CORA-5 test. A4-5
A4-5. Calculated and measured temperatures of unheated fuel at 0.75 m elevation for CORA-5 test. A4-6
A4-6. Calculated and measured temperature of unheated fuel rod at 0.85 m elevation for CORA-5 test. A4-6
A4-7. Calculated and measured temperature of unheated fuel rod at 0.95 m elevation for CORA-5 test. A4-7
A4-8. Calculated and measured temperature of control rod at 0.55 m elevation for CORA-5 test. A4-8
A4-9. CORA-7 large bundle cross-section. A4-9
A4-10. Calculated and measured temperature at the 0.35 m elevation for CORA-7 test. A4-10
A4-11. Calculated and measured temperature at 0.55 m elevation for CORA-7 test. A4-10
A4-12. Calculated and measured temperature at 0.75 m elevation for CORA-7 test. A4-11
A4-13. Calculated and measured temperature at 0.95 m elevation for CORA-7 test. A4-11
A4-14. Calculated cumulative hydrogen production for CORA-7 test. A4-12
A4-15. Calculated and measured temperatures of unheated fuel rod at elevation of 0.35 m for CORA-13 test. A4-14
A4-16. Calculated and measured temperatures of unheated fuel rod at elevation of 0.55 m for CORA-13 test. A4-14
A4-17. Calculated and measured temperatures of unheated fuel rods at elevation of 0.75 m for CORA-13 test. A4-15
A4-18. Calculated and cumulative hydrogen production for CORA-13 tests. A4-17
A4-19. RELAP5 nodalization of the CORA-17 experiment. A4-18
A4-20. CORA-17 bundle cross-section. A4-19
A4-21. Calculated and measured temperatures of channel box at 0.55 m for CORA-17 test. A4-20
A4-22. Calculated and measured temperatures of control blade at 0.55 m for CORA-17 test. A4-21
A4-23. Calculated and measured temperatures of unheated fuel rod at elevation of 0.55 m for CORA-17 test. A4-21
A4-24. Calculated and measured temperatures of unheated rod at elevation of 0.75 m for CORA-17 test. A4-22
A5-1. RELAP5 nodalization used for the PHEBUS B9+ experiment. A5-3
A5-2. SCDAP representation of the fuel bundle. A5-4
A5-3. Calculated and measured cladding temperatures at 0.2 m elevation for PHEBUS B9+ test. A5-5
A5-4. Calculated fuel temperatures at 0.4 m elevation for PHEBUS B9+ test. A5-5

A5-5. Calculated and measured fuel temperatures at 0.6 m elevation for PHEBUS B9+ test. A5-6

A5-6. Calculated and measured cladding temperatures at 0.7 m elevation for PHEBUS B9+ test. A5-6

A5-7. MOD3.3 calculated nuclear and oxidation heat generation histories in test fuel assembly for PHEBUS B9+ test. A5-7

A5-8. Calculated cumulative hydrogen production for PHEBUS B9+ test. A5-8

A6-1. Cross-section of bundle of test rods for PHEBUS FPT0 experiment. A6-1

A6-2. Inlet flow rate history of test bundle. A6-2

A6-3. Power history of test bundle. A6-3

A6-4. Schematic of nodalization of test rods, insulated shroud, and flow channels. A6-4

A6-5. Calculated and measured cladding temperatures at 0.7 m elevation for PHEBUS FPT0. A6-5

A6-6. Calculated and measured cladding temperatures at 0.4 m elevation for PHEBUS FPT0 test. A6-6

A6-7. Calculated and measured cladding temperatures at 0.3 m elevation for PHEBUS FPT0 test. A6-6

A6-8. Calculated cumulative hydrogen production for PHEBUS FPT0 test. A6-8

A7-1. Cross section of the DF-4 experiment bundle. A7-1

A7-2. SCDAP/RELAP5 nodalization for the DF-4 experiment analysis. A7-3

A7-3. Calculated and measured temperatures of fuel rod at elevation of 0.254 m for DF-4 test. A7-4

A7-4. Calculated and measured temperatures of fuel rod at elevation of 0.096 m for DF-4 test. A7-5

A8-1. Schematic of debris bed analyzed for assessment of flow loss calculations. A8-1

A8-2. Nodalization of debris bed analyzed for assessment of flow loss calculations. A8-3

A8-3. Schematic of BNL quenching experiment. A8-4

A8-4. Comparison of calculated and measured transient temperature distribution in debris bed A8-5

A8-5. Nodalization of debris bed in lower head of reactor vessel. A8-6

A8-6. RELAP5 nodalization for analysis of porous debris in lower head A8-7

A8-7. Volume fraction of liquid in RELAP5 control volume containing the flooded debris bed. A8-7

A8-8. Transient temperature at center of debris bed. A8-8

A8-9. Comparison of debris bed power and heat transfer to coolant A8-8

A9-1. Molten pool system analyzed in literature and by SCDAP/RELAP5. A9-1

A9-2. Temperature histories of oxidic and metallic parts of molten pool before and after stratification. A9-5

A9-3. Ratio of heat flux to critical heat flux on external surface of lower head before and after stratification of molten pool. A9-6

A10-1. Schematic of system analyzed and nodalization of system. A10-1

A10-2. Distribution of debris bed saturation and temperature after melting of 30% of core plate (time of 1500 s). A10-3

A10-3. Temperature history of debris bed along its centerline. A10-4

A10-4. Ratio of heat flux to CHF on external surface at bottom center of lower head. A10-4

A10-5. Axial distribution in velocity of melted material at 1500 s as calculated by melt movement model. A10-6
A11-1. Schematic of MAGICO - 2000 Test Arrangement. A11-1
A11-2. Comparison of calculated and measured advancement of the front of cloud of particles for MAGICO-2000 experiment. A11-3
A11-3. Calculated and measured volume fraction of liquid at elevation of 0.65 m for MAGICO-2000 experiment........A11-3
A11-4. Calculated and measured water level swell for MAGICO-2000 experiment........A11-4
A11-5. Schematic of FARO Test Arrangement. A11-5
A11-6. Calculated and measured pressure histories for FARO Test L-08........A11-6
A11-7. Schematic of application of FCI model to severe accident analysis. A11-7
A11-8. Calculated transients pressures in vessel for Case 1 (1 large jet) and Case 2 (25 small jets). A11-10
A11-9. Calculated transient pressure in vessel for Case 3 (1 small jet), Case 4 (2 small jets) and Case 5 (4 small jets). A11-10
A11-10. Transient volume fractions of liquid water at various elevations for Case 1 (single large jet). A11-11
A11-11. Transient volume fractions of liquid at various elevations for Case 2 (25 small jets). A11-11
A12-1. RELAP5 nodalization of the reactor vessel and core. A12-2
A12-2. RELAP5 nodalization of primary coolant loop A. A12-3
A12-3. RELAP5 nodalization of steam generator A. A12-4
A12-4. RELAP5 nodalization of the pressurizer. A12-5
A12-5. Cross-sections of core showing fuel assembly grouping and radial peaking factors. A12-7
A12-6. Makeup flow history for TMI-2 calculation........A12-11
A12-7. Reactor power versus time curve used for TMI-2 calculation. A12-11
A12-8. Timing of closure of PORV block valve and history of calculated rate of flow through PORV valve........A12-12
A12-9. History of calculated collapsed liquid level in reactor vessel. A12-15
A12-10. Comparison of calculated and measured liquid level in pressurizer. A12-15
A12-11. History of calculated maximum temperature in reactor core. A12-16
A12-12. History of calculated effective radius of molten pool. A12-17
A12-13. Calculated and measured pressures of primary coolant system. A12-17
A12-14. Comparison of calculated and measured pressure histories of primary coolant system for case of boundary conditions from Annunziato. A12-18
A12-15. Calculated hydrogen production during TMI-2 accident. A12-19
A12-16. MOD3.3 calculated temperature histories of fuel rods in upper part of outer most fuel assemblies in reactor core........A12-20
A12-17. MOD 3.3 calculated temperature history of location with porous debris (2.7 m elevation of fourth ring of fuel assemblies)........A12-21
A13-1. Nodalization diagram of Browns Ferry. A13-1
A13-1. Nodalization diagram of lower reactor vessel. A13-2
A13-1. Component guide for detailed Browns Ferry SCDAP model. A13-3
A13-1. Browns Ferry radial power profile for 4 radial rings. A13-4
A13-1. Browns Ferry power profiles for 13 axial nodes. A13-4

A13-1. Predicted radial temperature distribution across reactor core of control blades. A13-6
A13-1. Predicted radial temperature distribution across reactor core of channel boxes. A13-7
A13-1. Predicted radial temperature distribution across reactor core of fuel rods at the 0.5334 m elevation. A13-8
A13-1. Predicted radial temperature distribution across reactor core of fuel rods at the 0.9906 m elevation. A13-8
A13-1. Predicted radial temperature distribution across reactor core of fuel rods at the 2.2210 m elevation. A13-9
A13-1. Predicted Browns Ferry system pressure. A13-9
A13-1. Predicted integral hydrogen production. A13-10
A14-1. RELAP5 nodalization of the Surry reactor core and vessel for 5 x 10 cases. A14-2
A14-2. RELAP5 nodalization of the Surry primary system loop.......................................A14-3
A14-3. Radial cross-section of Surry reactor vessel showing nodalization of the core. A14-4
A14-4. Nodalization for modeling natural circulation in hot leg and steam generator. A14-5
A14-5. Arrangement of junction and valves for modeling natural circulation....................A14-6
A14-6. MOD3.3 calculation of pressurizer steam dome pressure for the Surry TMLB’ with failed SG ADV and intentional depressurization. A14-8
A14-7. MOD3.3 calculation of reactor vessel collapsed liquid level for the Surry TMLB’ with failed SG ADV and intentional depressurization. A14-8
A14-8. MOD3.3 calculation of pressurizer loop accumulator liquid inventory for the Surry TMLB’ with failed SG ADV and intentional depressurization.....................A14-9
A14-9. MOD3.3 calculation of core maximum peak cladding temperature for the Surry TMLB’ with failed SG ADV and intentional depressurization...................A14-10
A14-10. MOD3.3 calculation of total hydrogen production for the Surry TMLB’ with failed SG ADV and intentional depressurization. A14-10
A14-11. MOD3.3 calculation of surge line nozzle volume average temperature for the Surry TMLB’ with failed SG ADV and intentional depressurization...................A14-11

TABLES

A1-1. Axial power profile in fuel bundle. A1-3
A2-1. Calculated and measured axial distributions in oxidation and meltdown for FLHT-5 test. A2-5
A3-1. History of inlet flow rate to the test fuel assembly for PBF SFD ST Test A3-4
A3-2. Calculated and measured axial distributions in oxidation and meltdown for PBF SFD ST Test. A3-8
A3-3. Calculated and measured axial distributions in oxidation and meltdown for PBF SFD 1-1 test. A3-15
A3-4. Calculated and measured axial distributions in oxidation and meltdown for PBF SFD 1-4 test. A3-23
A4-1. Calculated and measured axial distributions in oxidation and meltdown for CORA-13 test. A4-16
A5-1. Comparison of calculated and measured axial distributions in oxidation and meltdown for PHEBUS B9+ test. A5-7
A6-1. MOD3.3 calculated axial distribution in oxidation and meltdown for PHEBUS FPT0 test. A6-7
A8-1. . Characteristics of debris bed and coolant conditions for pressure drop calculations. A8-2
A8-2. Comparisons of SCDAP/RELAP5 calculated flow losses with those presented in literature for corresponding cases. A8-3
A8-3. Summary description of BNL quenching experiment. A8-4
A9-1. Characteristics of system analyzed that were same for each test problem. A9-2
A9-2. Characteristics of molten pool that varied with test problems. A9-2
A9-3. SCDAP/RELAP5 and Reference A9-1 solutions for Test Problem 1 (deep metallic pool). A9-4
A9-4. SCDAP/RELAP5 and Reference A9-2 solutions for Test Problem 2 (shallow metallic pool). A9-4
A9-5. Sensitivity of calculated molten pool behavior to correlations for flux shape and sideward heat transfer in metallic pool A9-6
A10-1. Initial conditions and boundary conditions. A10-2
A10-2. Effect of level of debris saturation on thermal conductivity of debris. A10-5
A11-1. Characteristics of Run Z1500/0.2 of MAGICO-2000 Experiment. A11-2
A11-2. Characteristics of Test L-08 of FARO Experiments A11-4
A11-3. Summary of comparison of measured and calculated values for Test L-08 of FARO. A11-6
A11-4. Characteristics of typical severe accident conditions with possibility for FCI. A11-8
A11-5. Summary of results for FCI under conditions typical for severe accident in PWR. A11-9
A11-6. Experiment parameters for FARO series of experiments A11-13
A11-7. Summary of FARO experimental results. A11-13
A11-8. Summary of CCM-5 and CCM-6 experimental parameters A11-14
A12-1. TMI-2 axial power peaking factors. A12-6
A12-2. Total fuel assemblies, fuel rods, and control rods in each core region. A12-7
A12-3. SCDAP input parameters. A12-8

A12-4. TMI-2 initial conditions at turbine trip. A12-9
A12-5. Steam generator initial conditions. A12-10
A12-6. Calculated timing and sequence of core damage progression. A12-13
A14-1. Comparison of SCDAP/RELAP5/MOD3.3 and SCDAP/RELAP5/MOD3.2 calculations of timing of events in primary coolant system and in damage progression for Surry TMLB’ with failed SG ADV and intentional RCS depressurization. A14-7

A1. BOILOFF IN BUNDLE

The Boiloff in Bundle test problem is used to assess the models for convective heat transfer and coolant boil off. The assessment was performed by comparing the calculations of the temperature behavior of a fuel assembly during coolant boiloff using the SCDAP fuel rod model with that calculated using a previously benchmarked model.

The Boiloff in Bundle Test Problem requires for solution the steady-state heat transfer in a bundle of fuel rods and then the transient uncovery of the bundle and transient heat up of the bundle in response to a reduced rate of flow through the bundle. A schematic and the nodalization of the test bundle are shown in Figure A1-1. The bundle consists of 32 identical fuel rods. The bundle is 0.9144 m in height. The fuel rods in the bundle have an outer diameter of 9.63 mm and a pitch of 12.80 mm. Except for height, the design of the fuel rods is typical of PWR fuel rods. The flow area of the bundle of fuel rods is equal to 3.685×10^{-3} m^2. The bundle of fuel rods is surrounded by an adiabatic boundary through which no flow of heat occurs. The SCDAP/RELAP5 code represented the fuel bundle as eight equally sized axial nodes and eight equally sized hydrodynamic control volumes.

The bundle power was constant with time and equal to 58.5 KW. The bundle has a cosine shaped axial power distribution. The peak power in the bundle was 1.33 times the axially averaged power and occurs at an elevation of 0.46 m above the bottom of the fuel stack. The axial power profile of the fuel rod bundle is shown in Table A1-1.

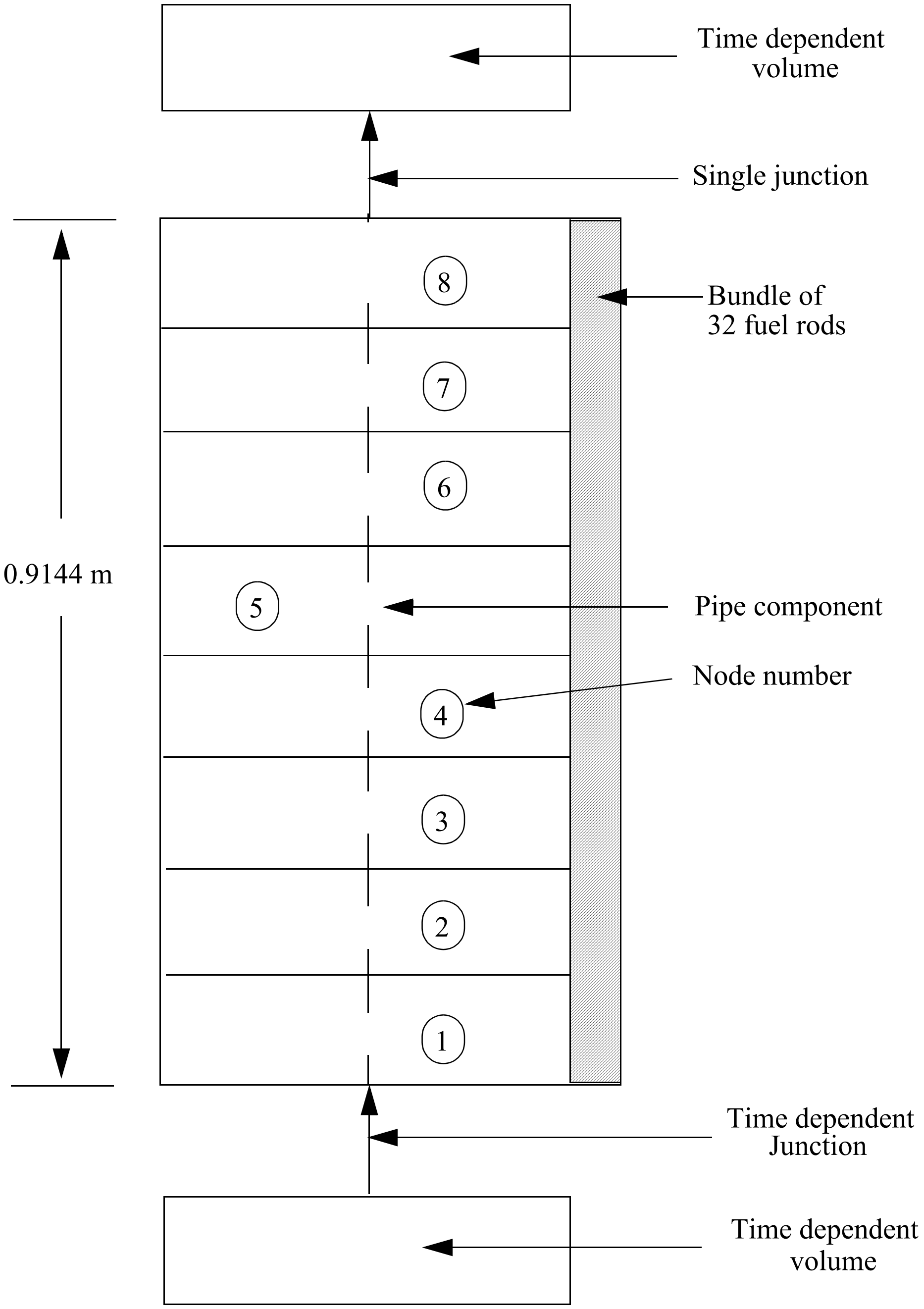
Time dependent volume
Single junction
8
Bundle of 32 fuel rods
7
6
0.9144 m
5
Pipe component
Node number
4
3
2
1
Time dependent Junction
Time dependent volume

Figure A1-1. Schematic of test problem and nodalization of fuel bundle.

Table A1-1. Axial power profile in fuel bundle.

Elevation above bottom of fuel stack (m)	Axial power factor
0.0571	0.5941
0.1714	0.9406
0.2858	1.1881
0.4000	1.3267
0.5143	1.3267
0.6287	1.1881
0.7430	0.9109
0.8573	0.5248

The coolant condition history in the fuel bundle was designed to show calculated convective heat transfer under steady-state pre-CHF conditions and then show transient convective heat transfer under the conditions of a boil off of the coolant. The pressure in the bundle was constant and equal to 6.89 MPa. The flow rate history at the inlet of the bundle is shown in Figure A1-2. The inlet flow rate was 1 kg/s in the period of 0.0 s to 50 s, 0.1 kg/s in the period of 50 to 100 s, and zero from 100 s through the end of the problem. The inlet temperature of the water was 558 K, which was equal to the saturation temperature at the bundle pressure of 6.89 MPa.

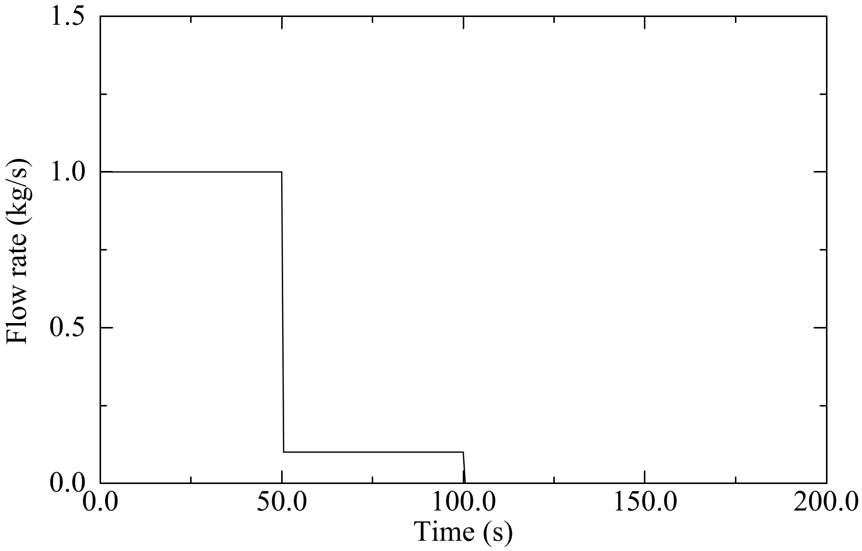

Figure A1-2. History of flow rate at inlet of bundle.

The SCDAP modeling for convective heat transfer was assessed by using as a benchmark the solution for the test problem obtained by representing the fuel bundle by RELAP5 heat structures.[A1-1] The test problem was solved with the fuel bundle represented by RELAP5 heat structures and twice with the fuel bundle represented as SCDAP heat structures, once using the explicit calculation of coolant conditions (Table 4 variable nhysol equal to 3) and once using the implicit calculation of coolant conditions (Table 4 variable equal to 7). The SCDAP calculation of convective heat transfer coefficients was assessed by comparing the SCDAP calculated cladding surface temperature histories with those calculated using RELAP5 heat structures. The SCDAP calculation of the rate of coolant boil off was assessed by comparing the SCDAP calculated histories of the liquid void fraction of the coolant in the bundle with those obtained using RELAP5 heat structures. The SCDAP convective heat transfer modeling was also checked using an energy balance.

The calculated convective heat transfer coefficients through a range of two-phase coolant conditions corresponding with coolant boil off were virtually identical for the two SCDAP models and the RELAP5 heat structure model. This evaluation is based on comparisons of the cladding surface temperature histories as calculated by SCDAP and the RELAP5 heat structure models. Figure A1-3 is a plot of the calculated surface temperatures at the elevations of 0.40 m and 0.86 m above the bottom of the fuel stack. For the 0.86 m elevation, the explicit and implicit SCDAP models and the RELAP5 heat structure model calculate that film boiling begins at 107 s, which is 7 s after the time at which the fuel bundle inlet flow rate drops to zero. After initiation of film boiling, all three models calculate an almost identical rate of heat up of the cladding surface. This similarity in rate of heatup indicates that all three models are calculating almost identical convective heat transfer. Similar results were obtained for the 0.4 m elevation. For this elevation, all three models calculate that film boiling begins at 135 s. After film boiling occurs, all three models calculate an almost identical rate of heat up. At 180 s, the calculated rate of heat up is 8.4 K/s.

The SCDAP explicit and implicit convective heat transfer models and the RELAP5 heat structure model calculate identical void fraction histories for the fuel bundle. Figure A1-4 shows plots of the histories of the volume fraction of liquid at the elevations of 0.86 m and 0.40 m. In the period of 60 s to 100 s, the three models calculate a liquid volume fraction of 0.6 at the 0.86 m elevation and a liquid volume fraction of 0.72 at the 0.40 m elevation. For the 0.86 m elevation, bundle uncovery is calculated to begin at 101 s and is completed by 107 s. For the 0.40 m elevation, bundle uncovery is calculated to begin at 124 s and is completed by 136 s.

The SCDAP convective heat transfer modeling results in an energy balance between fuel rod power and heat transferred to the coolant. This energy balance was checked by comparing fuel rod power with the calculated rate of heat transfer to the coolant. The nuclear heat generation rate at axial node 5 is 9,730 W. The elevation span of this node is from 0.457 m to 0.572 m above the bottom of the fuel bundle. The heat transfer rate to the coolant at this axial node is plotted in Figure A1-5. The heat transfer rate to the coolant is also equal to 9,730 W until bundle uncovery occurs at 113 s. The two SCDAP convective heat transfer models and the RELAP5 heat structure model calculate similar histories for the heat transfer rate to the coolant.

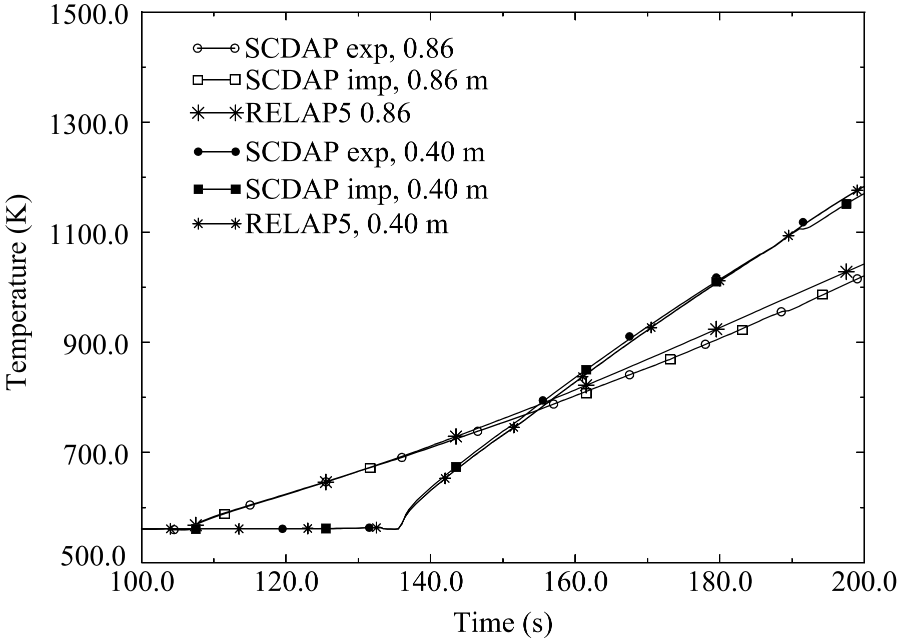

Figure A1-3. Comparison of SCDAP and RELAP5 calculated cladding surface temperatures at elevations of 0.40 m and 0.86 m.

The CPU time required for solution of the test problem was almost identical for the implicit and explicit convective heat transfer models in SCDAP. The CPU time for the solution of the test problem was 50 s on a DEC 3000 work station. The CPU time was evenly distributed through the time span of the test problem.

In summary, this test problem has produced two results. First, it has shown that SCDAP heat structures accurately calculate the boil off and heatup that occurs in a bundle of fuel rods subjected to a deficiency in coolant flow. Second, the implicit convective heat transfer model does not result in any increase in computational efficiency or accuracy relative to the explicit convective heat transfer model. Since the explicit model has been applied and assessed much more than the implicit model and is as efficient and accurate as the implicit model, this result is a basis for recommending the explicit convective heat transfer model as the default model for convective heat transfer in SCDAP/RELAP5/MOD3.3.

A1.1 References

A1-1. The RELAP5 Development Team, *RELAP5/MOD3 Code Manual, Volume IV,* NUREG/CR-5535, INEL-95/0174, August 1995.

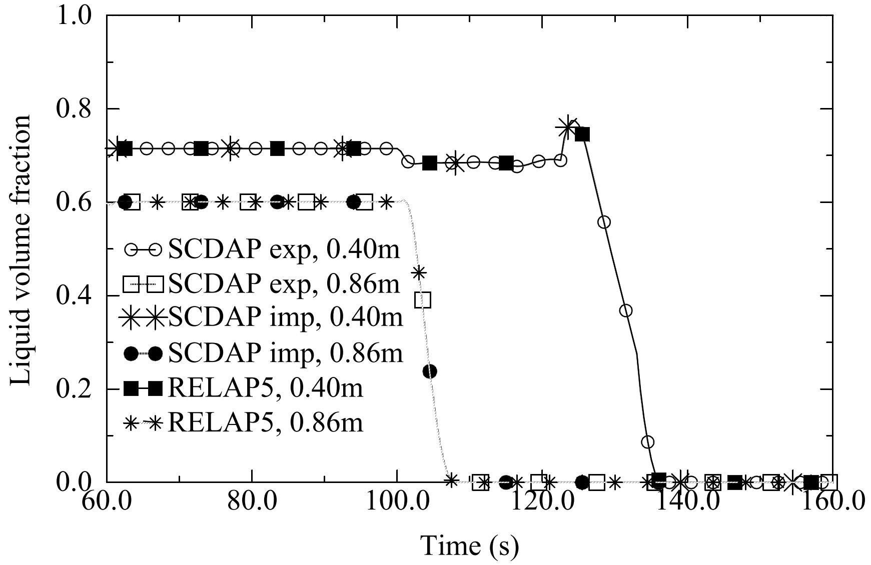

Figure A1-4. Bundle uncovery histories as calculated by SCDAP and RELAP5 heat structures at elevations of 0.40 and 0.86 m.

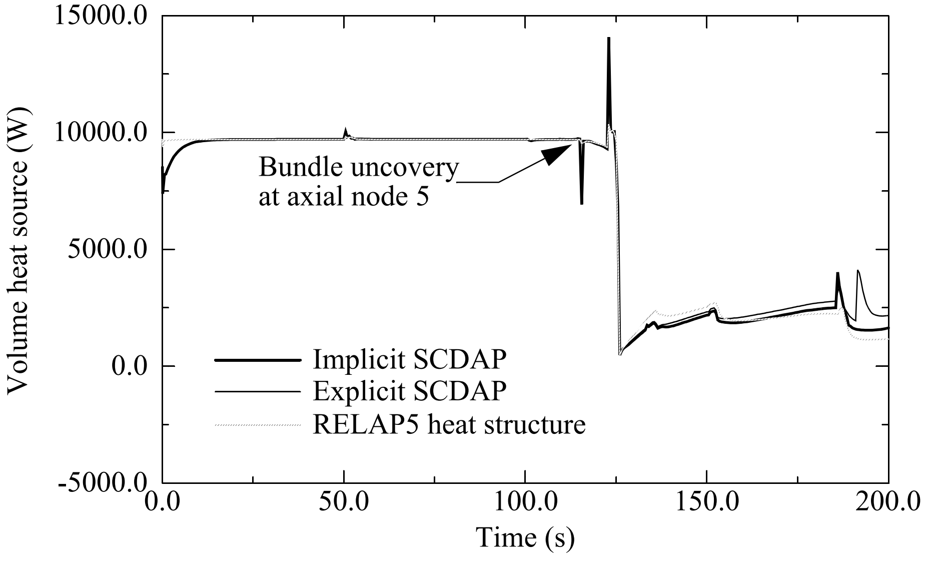

Figure A1-5. Heat transfer rate to coolant at axial node 5.

A2. FLHT-5 TEST

FLHT-5, the fourth in a series of full length, high temperature severe core damage tests, was conducted by Pacific Northwest National Laboratory (PNNL) in the National Research Universal (NRU) reactor at Chalk River Nuclear Laboratory (CRNL), Ontario, Canada.[A2-1] The objectives of this test, which simulated conditions in a light water reactor (LWR) core during a loss-of-coolant accident, were; (1) to heat up fuel rods to the point of severe fuel damage at 30 kW nuclear power during a boildown and the subsequent heatup, (2) to determine the time at which oxidation and hydrogen production ceased within the test assembly and characterize the cause of the cessation of oxidation, and (3) to characterize the release, transport, and deposition of gaseous and volatile fission products. To accomplish the goals of the test, the bundle was held at a maximum temperature of 2,500 K for 60 minutes, instrumented with numerous thermocouples, flow meters and pressure transducers, and examined visually after completion of the test.

The FLHT-5 test assembly consisted of 12 fuel rods surrounded by a multilayer low density zirconia shroud, with a zircaloy liner. The fuel bundle, a modified 4 x 4 array, is shown in Figure A2-1. The corner rod positions in the array were replaced with angled zircaloy carrier pieces that routed and protected instrument wires in the test bundle. Ten of the remaining 12 positions in the fuel bundle were fresh fuel rods, fabricated at PNNL. Eight of the nonirradiated rods were instrumented. One of the remaining positions in the array contained a three-cycle irradiated PWR fuel rod from the H. B. Robinson reactor, the other a stainless steel rod centered in a zircaloy guide tube. The irradiated rod had an initial UO_2 pellet enrichment of 2.55%, a nominal rod-average burnup of 28 MWd/kgU, and a cooling time of 13 years. The 3.6 m in height fuel rods in the test bundle were held in place by 8 instrumented grid spacers, four composed of inconel and four zircaloy (the bottom three and top grid spacers were inconel, the other four were zircaloy).

The test was conducted in five phases; (1) equipment installation and checkout, (2) commissioning, which included the injection of metered hydrogen and nitrogen gas flows into the effluent piping to check the response and calibration of the various hydrogen sampling and analysis systems and to perform leak checks on the system, (3) preconditioning of the assembly to ensure adequate fuel pellet cracking of the fresh rods, (4) the boilaway transient, where 30-kW of nuclear power and a coolant makeup flow of 1.26 g/s were maintained for 60 minutes beyond the first cladding temperature escalation to 2,500 K, and (5) post-test activities, which included deposition rod removal and gamma scanning, visual inspection of the damaged test assembly, sectioning of the test assembly, stack release analyses, and flux wire gamma scanning.

A2.1 Nodalization

As shown in Figure A2-1, the nodalization of the FLHT-5 test assembly was represented by SCDAP/RELAP5/MOD3.3 using ten, 0.3648 m in height, RELAP5 hydrodynamic volumes in the test bundle region and a single RELAP5 volume to represent the bypass. Five SCDAP components were used to represent rods and structures in the core region. Component 1 represented the unirradiated fuel rods,

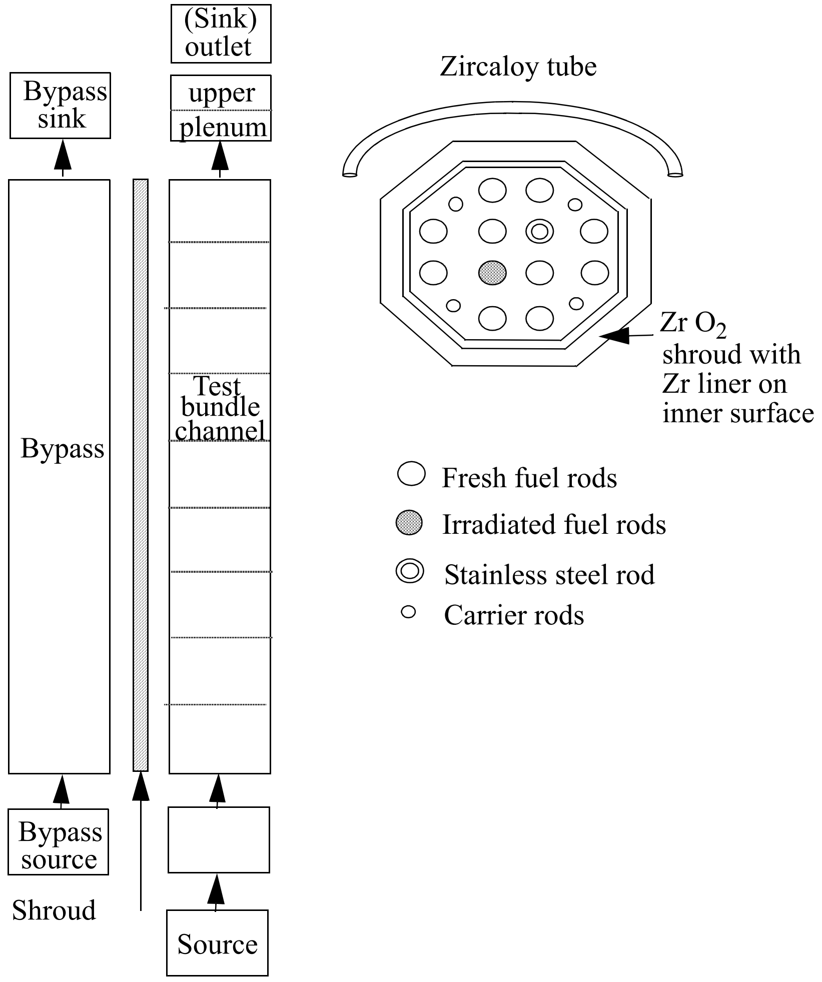
(Sink) outlet
Bypass sink
upper plenum
Zircaloy tube
Bypass
Test bundle channel
Zr O_2 shroud with Zr liner on inner surface
Fresh fuel rods
Irradiated fuel rods
Stainless steel rod
Carrier rods
Bypass source
Shroud
Source

Figure A2-1. RELAP5 nodalization and bundle configuration for FLHT-5.

Component 2 represented the single irradiated H. B. Robinson fuel rod, Component 3 represented the zircaloy guide tube containing a centered stainless steel rod; input in the assessment deck as a control rod with an extremely small quantity of control material. Component 4 represented the corner carrier tubes. Component 5 represented the insulating shroud.

A2.2 Boundary Conditions

Prior to initiating the test, steady-state conditions were established at a system pressure of 1.38 MPa with a coolant flow rate of 11.3 g/s and an initial liquid level at the elevation of 2.9 m above the bottom of the test bundle. After the establishment of steady-state conditions in the test bundle, the test was initiated by decreasing the inlet flow of the coolant to 1.26 g/s and applying 30 kW nuclear power to the test assembly. The initiation of power started the boilaway phase of the experiment.

A2.3 Comparison of Calculations and Measurements

Results for the FLHT-5 experiment provide benchmarks for early-phase damage progression models in a severe accident analysis computer code. The experiment subjected the test fuel rods to conditions that caused rapid oxidation and some meltdown of the cladding of the test fuel rods. The temperature history of the test fuel assembly at three different elevations was obtained during the period in which oxidation was causing a rapid heatup of the test fuel assembly. A measurement was obtained of the amount of hydrogen produced by oxidation of the cladding of the test fuel rods and other structures. The hydrogen production rate was also measured. A limited post-irradiation examination (PIE) obtained some information on the extent of oxidation of the test fuel assembly and the location of slumped fuel rod material.

The MOD3.3 calculated temperature behavior of the test fuel assembly was generally in good agreement with its measured temperature behavior. The MOD3.3 calculated and measured temperature history of a test fuel rod at the 2.37 m elevation (referenced from bottom of fuel rod) are shown in Figure A2-2. The 2.37 m elevation is the highest elevation at which a temperature measurement was obtained for the test fuel rods. A temperature increase due to uncovery of the test bundle occurred first at this location. The calculated rate of temperature increase for a temperature greater than 1500 K was about 16 K/s. The calculated rate of temperature increase is slightly slower than the measured rate of temperature increase. The temperature measurement failed after the temperature exceeded 1600 K. The temperature history calculated by MOD3.2 at this elevation is also shown in Figure A2-2. The temperature histories calculated by MOD3.2 and MOD3.3 are similar. The calculated and measured temperature histories of the test fuel rods at the 1.64 m and 1.22 m elevations are compared in Figure A2-3 and Figure A2-4, respectively. The

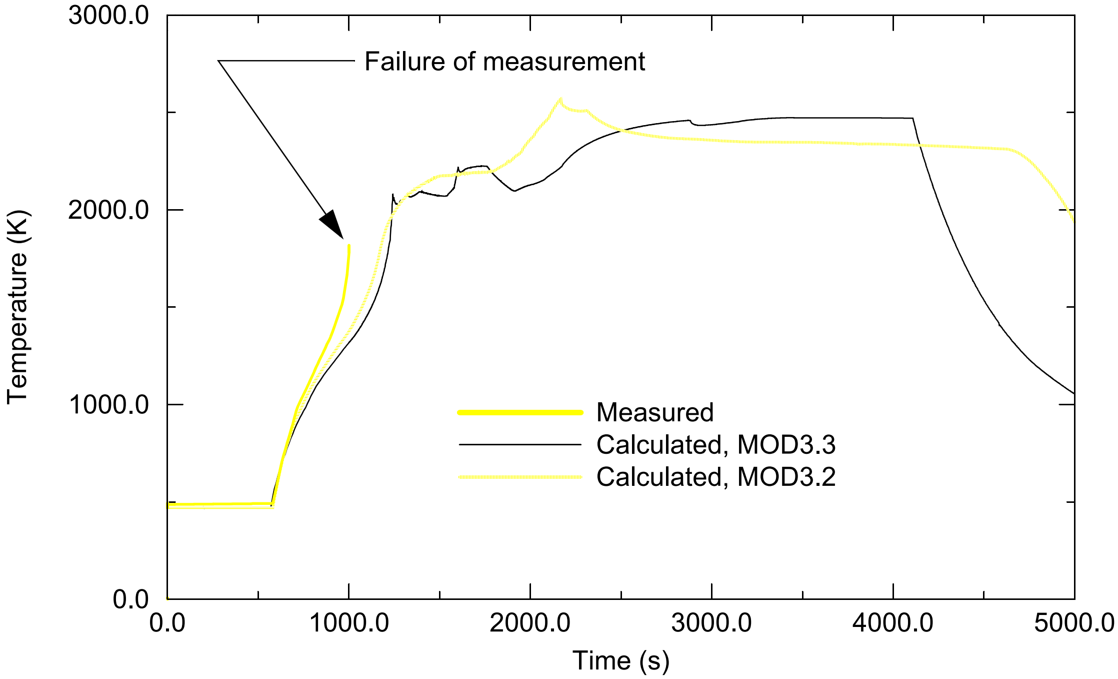

Figure A2-2. Calculated and measured temperature at 2.37 m elevation for FLHT-5.

calculated rate of temperature increase was slightly less than the measured rate of increase. A maximum temperature of 2670 K was calculated at the elevations of 1.22 m and 1.64 m. Based on measurements of the temperature of the outside of the insulated flow shroud surrounding the test fuel assembly, the maximum fuel assembly temperature was estimated to exceed 2600 K.[A2-1] The temperature histories calculated by MOD3.2 are also shown in Figures A2-2 through A2-4. The MOD3.3 and MOD3.2 calculations are similar for the 1.64 m elevation, but at the 1.22 m elevation the MOD3.3 calculations are in better agreement with the measured temperature history than the MOD3.2 calculations.

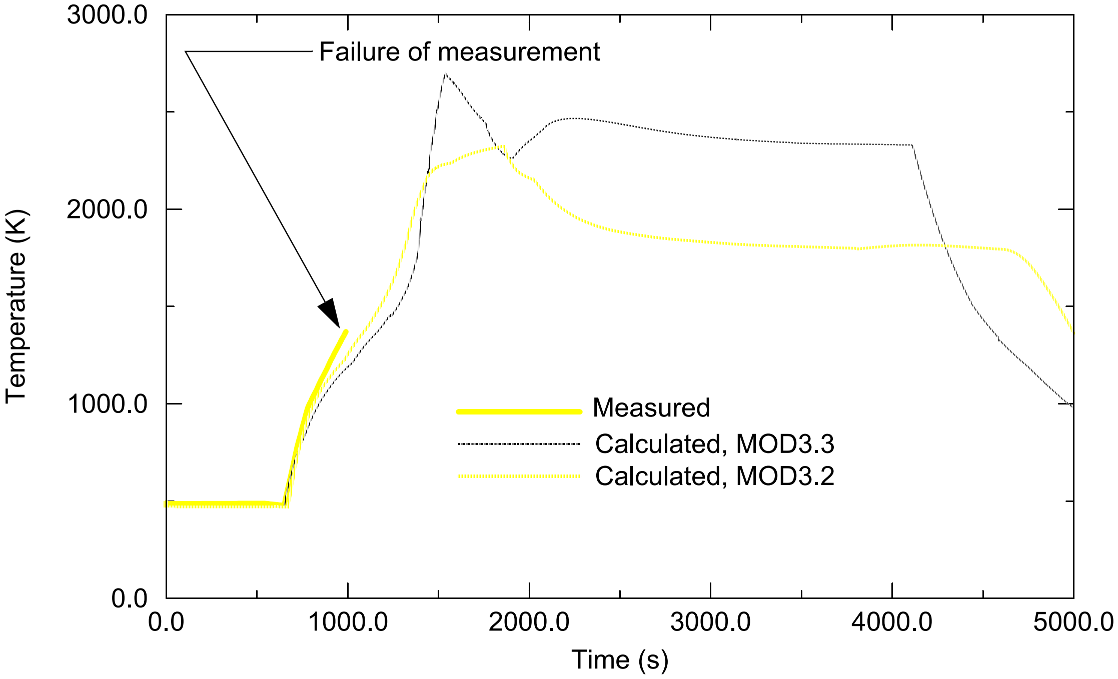

Figure A2-3. Calculated and measured temperature at 1.64 m elevation for FLHT-5.

The calculated axial distribution in oxidation of test fuel rod cladding was in general agreement with the axial distribution obtained from the PIE performed on the test fuel assembly. Although the PIE was limited in scope, information was obtained indicating almost 100% oxidation of the cladding of the test rods above an elevation of 1.3 m. The measured and the MOD3.3 and MOD3.2 calculated axial distributions in the fraction of the fuel rod cladding oxidized are tabulated in Table A2-1. As shown in this table, MOD3.3 calculated almost 100% oxidation of the cladding above the 1.3 m elevation. The only exception was at the 2.37 m elevation, where cladding oxidation was limited to 43% due to slumping of the melted metallic cladding at that location. Double-sided oxidation was calculated to not occur at any location in the test fuel assembly. Since meltdown has an influence on the axial distribution in oxidation, the calculated locations of cladding slumping and blockages are also shown in Table A2-1. The blockage is defined to be the fraction of coolant space filled with slumped material. The PIE indicated that some slumping of melted cladding occurred but that the slumping was limited and did not cause any extensive blockage. The limited scope of the PIE precluded a quantitative measurement of fuel rod meltdown. MOD3.3 also calculated only a small amount of cladding slumping, and thus the calculated amount of fuel rod meltdown was consistent with the measured amount.

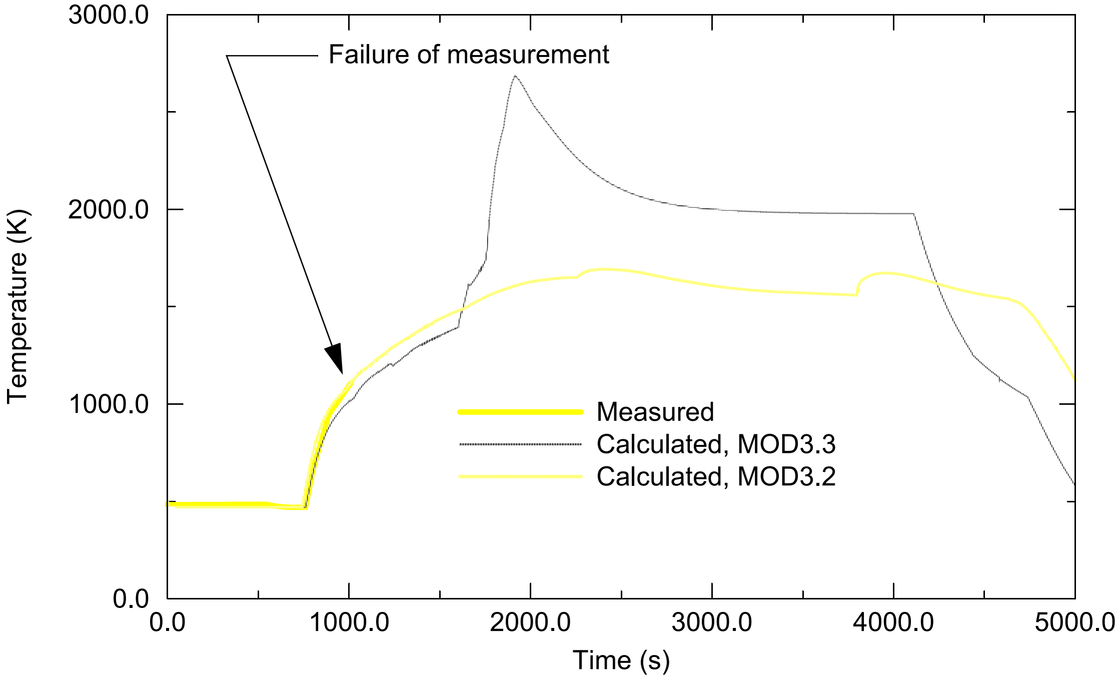

Figure A2-4. Comparison of calculated and measured temperature at 1.22 m elevation for FLHT-5.

Table A2-1. Calculated and measured axial distributions in oxidation and meltdown for FLHT-5 test.

Elevation	**Fraction cladding oxidized**		**Fraction blockage due to meltdown/ slumping from location (yes or no)**
(m)	**MOD3.3**	**Measured**	**MOD3.3**
0.18	0.0	~0.0	0.0/no
0.55	0.0	~0.0	0.0/no
0.91	0.04	~0.0	0.15/no
1.28	0.97	~1.0	0.0/no
1.64	1.00	~1.0	0.0/n0
2.00	1.00	~1.0	0.0/no
2.37	0.43	~1.0	0.0/yes
2.75	1.00	~1.0	0.0/no
3.10	1.00	~1.0	0.0/no
3.47	1.00	~1.0	0.0/no

The calculated hydrogen production was somewhat less than the measured hydrogen production. The calculated and measured hydrogen production are compared in Figure A2-5. The MOD3.3 calculated andmeasured hydrogen productions were 231 g and 300 g + or - 30 g. The hydrogen production calculated by MOD3.2 was 249 g. The general agreement of calculated and measured axial distribution in oxidation indicates that the underprediction in hydrogen production may be due to an underprediction of the oxidation of other components in the test train for the test fuel assembly, such as the shroud with a Zr inner liner and Zircaloy carriers for instrument wires. The calculated and measured rate of hydrogen production are compared in Figure A2-6. The measured rate was obtained from the Noncondensable Turbine Flowmeter. The measured rate of hydrogen production lags the calculated rate of hydrogen production because the measurement was performed a considerable distance downstream of the test fuel assembly. Both the calculations and the measurements showed that most of the hydrogen production occurred in the period of 1000s to 3000 s. During this period, most of the uncovered portions of the test fuel rods were at a temperature greater than the melting temperature of the metallic part of the fuel rod cladding, as shown in Figure A2-2 through Figure A2-4. The calculated and measured maximum rates of hydrogen production were about 1.3x10^{-4} kg/s. This rate of hydrogen production corresponds with oxidation in the test assembly consuming 100% of the makeup coolant flowing into the test bundle.

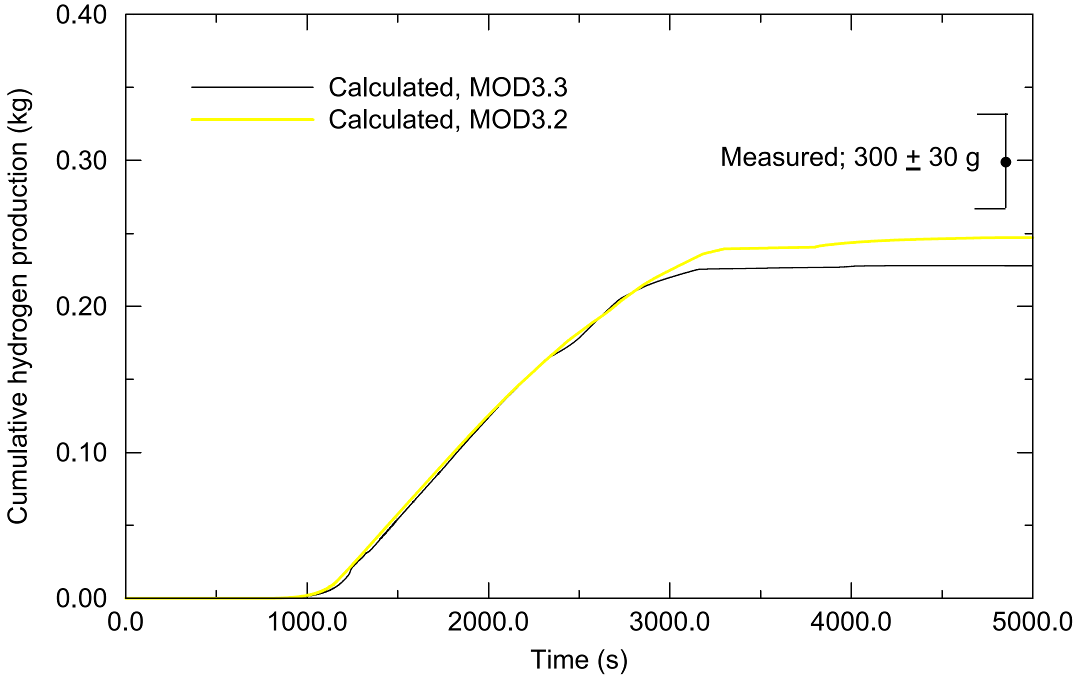

Figure A2-5. Comparison of calculated and measured cumulative hydrogen production for FLHT-5 test.

In summary, the calculated and measured behavior of the test fuel assembly for the FLHT-5 test are in good agreeement. Both the calculations and the measurements showed an oxidation driven heatup rate in excess of 15 K/s in the portion of the test assembly uncovered by the boiloff of water. The calculations and measurements indicated that cladding melting did not reduce the the rate of oxidation. The calculations and measurements indicated 100% consumption of the makeup coolant flow during the high temperature

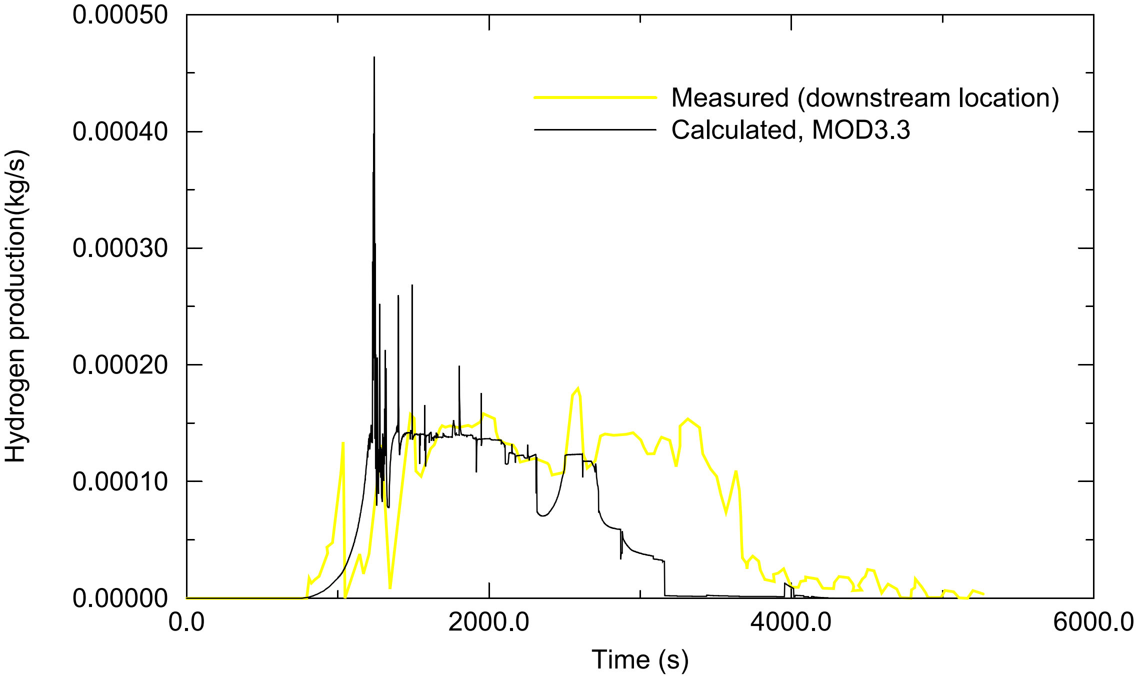

Figure A2-6. Comparison of calculated and measured hydrogen production rate.

period of the test and almost 100% oxidation of the cladding of the fuel rods uncovered by coolant boiloff. Both the calculations and measurements indicated that the meltdown of the test fuel assembly was limited even though the maximum temperature in the test fuel assembly exceeded 2600 K, and that no significant flow blockage occurred.

A2.4 References

A2-1. D. D. Lanning et al., “Data Report: Full-Length High Temperature Experiment 5,” PNL6540, April 1988

A3. PBF SFD SERIES OF EXPERIMENTS

A severe fuel damage (SFD) research program was initiated by the U.S. Nuclear Regulatory Commission (NRC) to develop a data base and models to predict (a) the overall response of a reactor core and associated structures, (b) the rate of release of fission products; their chemical forms, and characteristics of their transport and deposition in the primary system, (c) the rate of hydrogen generation from the interaction of coolant with the fuel, cladding, and reactor structure, and (d) the coolability of the damaged fuel following reflood.

Several severe fuel damage experiments were performed at the PBF test reactor at the INEEL. This test reactor had a uranium dioxide driver core and a central flux trap contained in an open tank reactor vessel. An independent, pressurized water coolant loop gave the capability to provide a wide range of thermal hydraulic conditions within the reactor core. A complete description of the Power Burst Facility can be found in the test results reports for each of the individual experiments.[A3-1, A3-3]The PBF core was a right-circular annulus, 1.3 m in diameter and 0.91 m in height, enclosing a vertical flux trap, 0.21 m in diameter. The reactor core was designed for both steady-state and power burst operation and contained eight control rods for reactivity control during steady-state operation and four transient rods for dynamic control during rapid reactivity transients. Each control and transient rod consisted of a stainless-steel canister which contained a cylindrical annulus of boron carbide. The control and transient rods were operated in an air-filled shroud.

An in-pile tube, placed in the central flux trap region, contained the test assembly. The in-pile tube used for the PBF reactor was a thick walled, Inconel, high strength pressure tube designed to contain the steady-state operating pressure and subsequent pressure surges resulting from the failure of any test fuel rod. Therefore, any conceivable failure of the test fuel during the experiment such as clad failure, gross fuel melting, fuel-coolant interactions, fuel failure propagation, fission product release or metal-water interactions, would be contained by the in-pile tube without damage to the driver core.

A flow tube was positioned in the in-pile tube. This tube directed coolant flow during the experiment. The coolant entered the top of the in-pile tube above the reactor core and flowed down the annulus between the in-pile tube wall and the flow tube. The flow through the reactor reversed at the bottom, flowed upward around the outside wall of the test train assembly maintaining the appropriate heat transfer and keeping the shroud properly cooled during an experiment.

The objectives of the PBF SFD test series were to obtain data to better understand fuel behavior, fission product release, deposition and transport, and hydrogen generation during severe fuel damage accidents. The data from each of these well controlled and instrumented tests was verified and qualified by an independent data review committee. Two additional purposes of these tests were to reconstruct the TMI-2 accident scenario and to investigate other risk-dominant accident scenarios that could lead to severe core damage during an incident in a nuclear power plant.

Three PBF SFD tests were used to assess SCDAP/RELAP5/MOD3.3. These tests were; (1) PBF SFD-ST test, which involved a gradual boiuloff of coolant, (2) PBF SFD 1-1 test, which involved heatup in a steam environment, and (3) PBF SFD 1-4 test, which involved heatup of a bundle of fuel rods with burnup and with a control rod. The assessment results obtained for each of these three experiments follows.

A3.1 Assessment Using PBF SFD-ST Test

The PBF SFD Scoping Test[A3-1] was used to assess code calculated reflood behavior and evaluate the models for cladding meltdown and oxidation.

The SFD-ST test train incorporated a fuel bundle containing 32, 0.92 m in length pressurized, trace irradiated fuel rods with an average burnup of 91 MWd/MtU in a 6 x 6 array with the corners removed. The spacing between the fuel rods in the test bundle was maintained by three inconel spacer grids, 40 mm in height, located at the 0.05, 0.45 and 0.86 m elevations. The fuel bundle was surrounded by an insulating shroud to minimize heat losses during the test. The shroud consisted of an inner zircaloy liner, a layer of porous zirconia, and an outer wall constructed of zircaloy. The fuel rods and shroud were instrumented with numerous thermocouples and pressure sensors. All test data was verified or categorized by a data integrity review committee.

A3.1.1 Nodalization

The entire test assembly for Scoping Test was modeled with SCDAP/RELAP5. Ten (10) 0.1 m in length RELAP5 hydrodynamic volumes were used to represent the core region, a single RELAP5 volume to represent the bypass region, and time dependent volumes to represent a sink and source for the test bundle flow channel and core bypass. The RELAP5 nodalization scheme used for the analysis is shown in Figure A3-1. The bundle components, fuel rods and insulating shroud are represented by four SCDAP components as shown in Figure A3-2. The fuel rods in the 36 rod test bundle were represented by three SCDAP components as follows: (1) component 1, the four fuel rods of the inner ring, (2) component 2, the twelve fuel rods of the middle ring, and (3) component 3, the sixteen fuel rods of the outer ring. A fourth SCDAP component was used to represent the flow shroud. The SCDAP components were modeled with ten axial nodes 0.1 m in height which interfaced with the 10 corresponding RELAP5 hydrodynamic control volumes. The external surface of the bundle shroud was connected to the single RELAP5 hydrodynamic control volume that was used to represent the bypass. The fuel rods for this test were modeled using 4 radial nodes and the insulating shroud modeled using 19 radial nodes.

A3.1.2 Boundary Conditions

The nuclear power used for the SFD-ST assessment calculations was obtained from reactor power measurements and reactor physics calculations. The total bundle power is shown in Figure A3-3. At 11960 s, the bundle power was ramped down attaining a value of zero at 12520 s. The uncertainty envelope for the total measured power was $\pm$ 15%. During the test the axial power profile varied in response to changes in the water level in the reactor core, therefore three discrete power profiles were used, one profile represented the partially water filled bundle, a second a 10% water filled bundle, and the third a steam

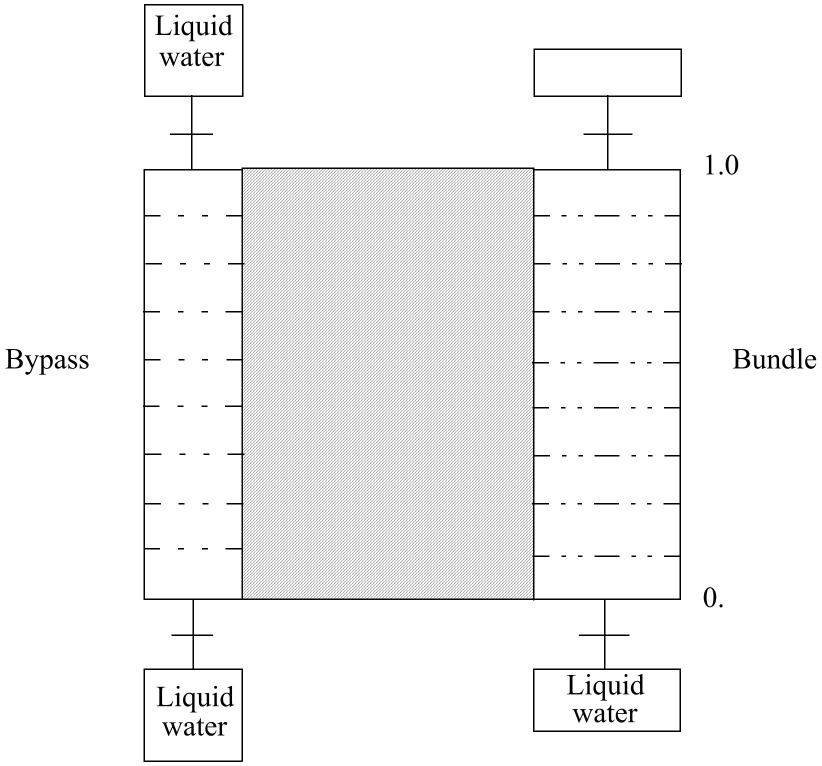
Liquid water
1.0
Bypass
Bundle
0.
Liquid water
Liquid water

Figure A3-1. RELAP5 nodalization of the test train for the SFD-ST experiment.

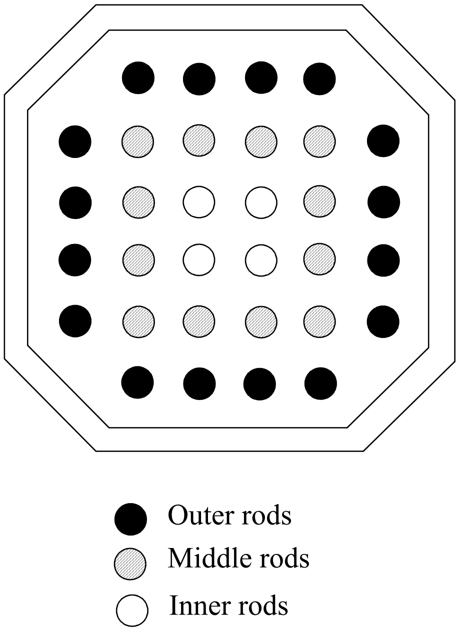
Outer rods
Middle rods
Inner rods

Figure A3-2. SCDAP core representation of the SFD-ST experimental bundle.

filled bundle. The measured initial conditions for the water inlet flow rate, 16 g/s at 525 K, and a system pressure of 6.65 MPa were used for the calculation. The pre-test measured thermal conductivity for the shroud material was used for the analysis even though there was evidence that variations in the shroud thermal conductivity occurred during the test.

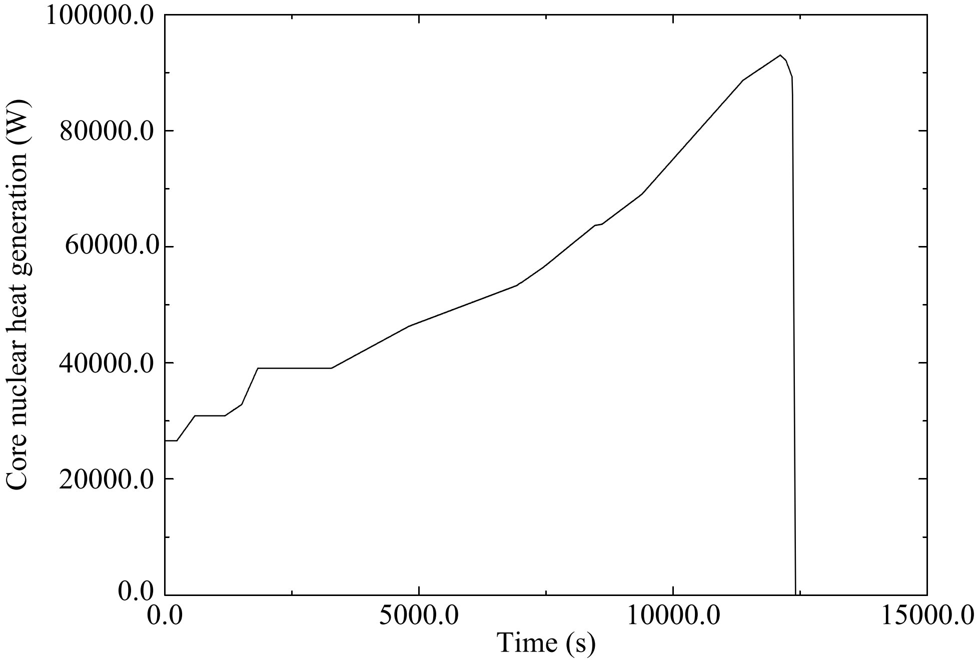

Figure A3-3. Total bundle power for the SFD-ST experiment.

The flow rate of coolant at the inlet of the test fuel assembly varied with time. From 1889 s to 11760 s, the inlet flow rate was 16 g/s. At 11913 s, the inlet flow was reduced to 15 g/s. At 12230 s, the inlet flow was reduced to 12 g/s. At 12739 s, the inlet flow rate was increased to 30 g/s to reflood the hot test fuel assembly. The history of the inlet flow rate to the test fuel assembly is tabulated in Table A3-1.

Table A3-1. History of inlet flow rate to the test fuel assembly for PBF SFD ST Test

Time	Inlet flow rate
(s)	(g/s)
0.0	12.75
1889.	16.20
2752.	16.92
4517.	16.74
5000.	16.79
6892.	16.60

Table A3-1. History of inlet flow rate to the test fuel assembly for PBF SFD ST Test (Continued)

Time	Inlet flow rate
(s)	(g/s)
7870.	16.57
9000.	16.52
10000.	16.20
11739.	16.20
11913.	15.02
12091.	15.02
12230.	12.24
12326.	12.51
12400.	15.05
12509.	16.20
12557.	15.18
12617.	15.32
12739.	29.51
15000.	30.00
5000.	16.79

A3.1.3 Results

The results for the PBF SFD Scoping Test provide benchmarks for the modeling of early-phase damage progression in fuel assemblies and for the modeling of the affect of reflood on the behavior of hot partially oxidized fuel assemblies. The experiment also involved heat transfer and flow losses in porous debris. The experiment subjected the fuel rods with only a trace amount of burnup to conditions that caused oxidation of the cladding of the test fuel rods. The boiloff of coolant in the test fuel assembly occurred over an extended period of time. After a significant oxidation and heatup of the upper part of the test fuel assembly, the test fuel assembly was reflooded. The temperature history of the test fuel assembly at three different elevations was obtained during the period in which oxidation was causing a heatup of the test fuel rods. A measurement was obtained of the amount of hydrogen produced by oxidation of the cladding of the test fuel rods and other structures. An instrument obtained the time of rupture of the fuel rod cladding due to excessive stress and ballooning. A post-irradiation examination (PIE) obtained information on the extent of oxidation of the test fuel assembly and the location of slumped fuel rod material.

The MOD3.3 calculated temperature behavior of the test fuel assembly was in good agreement with its measured temperature behavior. The MOD3.3 calculated and measured temperature histories of a test fuel rod in the center of the test fuel assembly at the 0.7 m elevation (referenced from bottom of fuel rod) are shown in Figure A3-4. The MOD3.2 calculated temperature history is also shown. The temperature measurement failed after the temperature exceeded 2000 K. The MOD3.3 calculated temperature history and the measured temperature history are in good agreement. The temperature was calculated to begin to decrease beginning at 11960 s due to the rapid decrease in the nuclear heat generation in the test fuel assembly. The calculated and measured temperature histories of the test fuel rods at the 0.5 m and 0.35 m elevations are compared in Figure A3-5 and Figure A3-6, respectively. The 0.5 m elevation is near the midplane of the test fuel rods. For both the 0.5 m and 0.35 m elevations, MOD3.3 calculated a significant increase in temperature to occur after the beginning of reflood. MOD3.2 did not calculate any increase in temperature after the beginning of reflood. The PIE results indicated that the maximum temperature in the test fuel assembly exceeded 2670 K. The maximum temperature of the test fuel rods was calculated by MOD3.3 to be 2585 K and to occur at 12375 s, which was during the beginning of the reflood period of the test.

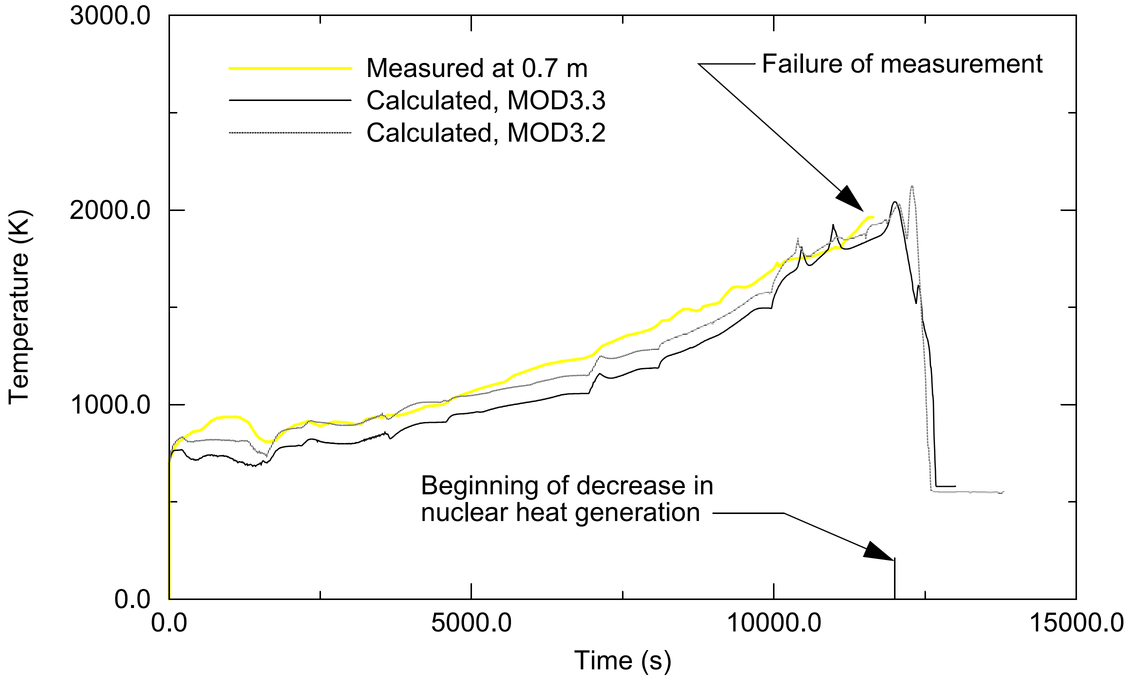

Figure A3-4. Comparison of calculated and measured cladding temperatures at the 0.7 m elevation for PBF SFD ST test.

The calculated axial distribution in oxidation of the cladding of the test fuel rods was in general agreement with the axial distribution obtained from the PIE performed on the test fuel assembly. The measured and the MOD3.3 and MOD3.2 calculated axial distributions in the fraction of the fuel rod cladding oxidized are tabulated in Table A3-2. Double-sided oxidation of the fuel rod cladding was calculated to occur in the elevation interval of 0.8 m to 0.9 m. The PIE results showed 100% oxidation of the cladding of the test rods in the elevation interval of 0.35 m to 0.95 m (top of fuel rods). MOD3.3

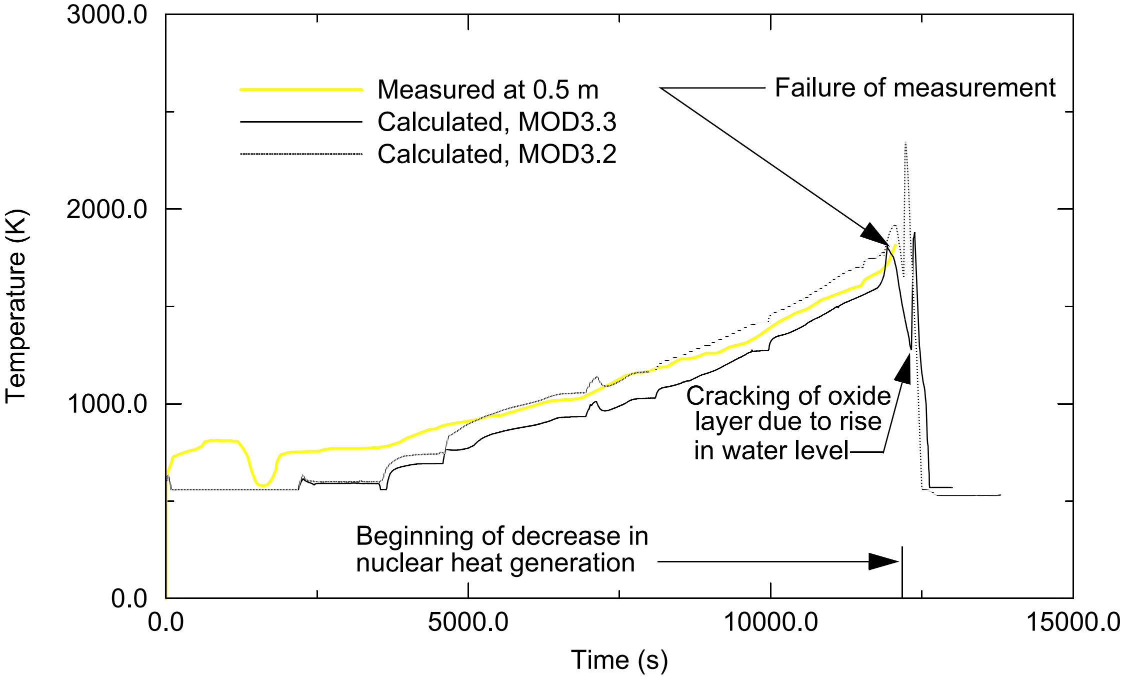

Figure A3-5. Calculated and measured temperatures at 0.5 m elevation for PBF SFD ST test.

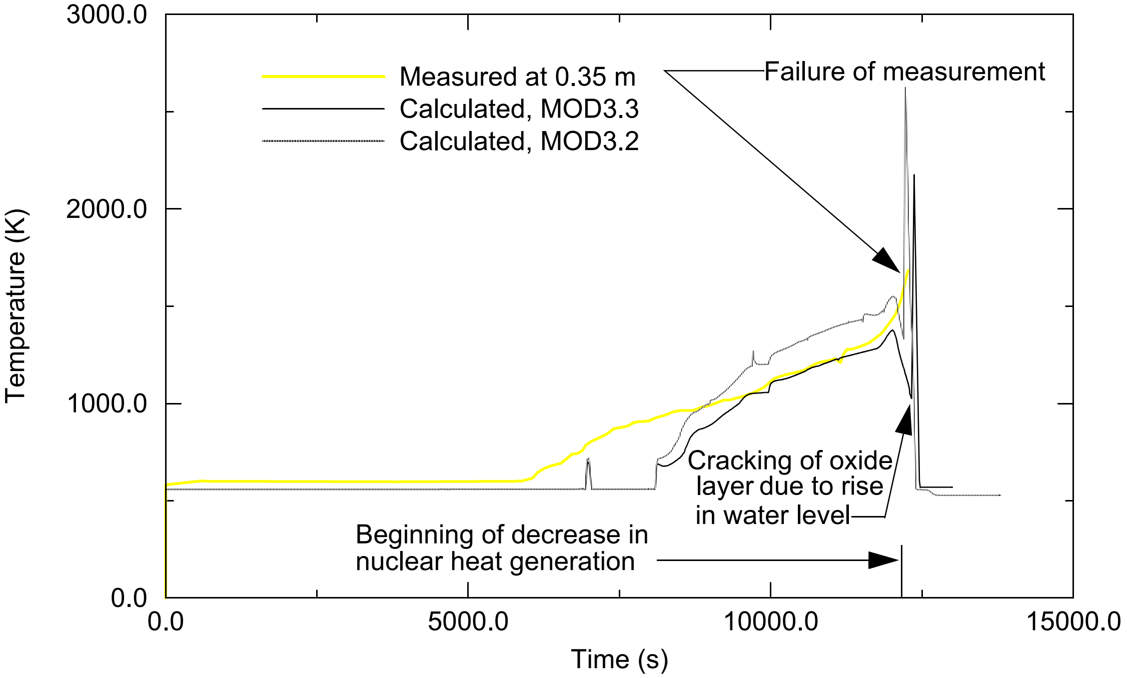

Figure A3-6. Calculated and measured temperatures at 0.35 m elevation for PBF SFD ST test.

calculated 100% oxidation of the cladding in the interval of 0.25 m to 0.95 m. Since cladding meltdown has an influence on the axial distribution in oxidation, the calculated locations of cladding slumping and blockages are also shown in Table A3-2. The blockage is defined to be the fraction of coolant space filled with slumped material. The PIE indicated some slumping of fuel and cladding in the elevation interval of 0.4 m to 0.6 m, and some slumped material at the elevation of 0.15 m. The PIE indicated that a large amount of material slumping did not occur. The slumping of cladding was calculated by MOD3.3 to not occur. The only material calculated by MOD3.3 to slump was the Inconel spacer grid material and the Zr cladding melted due to eutectec reaction with the spacer grids.

Table A3-2. Calculated and measured axial distributions in oxidation and meltdown for PBF SFD ST Test.

Elev.	Fraction cladding oxidized		Fraction blockage due to meltdown/ slumping from location (yes or no)	
(m)	MOD3.3	Measured	MOD3.3	Measured
0.05	0.0	0.0	0.0/no	0.0/no
0.15	0.0	0.03	0.0/no	>0.0/no
0.25	0.03	1.0	0.0/no	0.0/no
0.35	1.0	1.0	0.0/no	0.0/no
0.45	1.0	1.0	0.0/no	0.0/yes
0.55	1.0	1.0	0.0/no	0.0/yes
0.65	1.0	1.0	0.0/no	0.0/no
0.75	1.0	1.0	0.0/no	0.0/no
0.85	1.0	1.0	0.0/no	0.0/no
0.95	1.0	1.0	0.0/no	0.0/no

The MOD3.3 calculated hydrogen production was in good agreement with the measured hydrogen production. A hydrogen production of 150 g + or - 35 g was measured. MOD3.3 calculated a hydrogen production of 125 g. The hydrogen production calculated by MOD3.2 was 130 g. The MOD3.3 calculated cumulative hydrogen production is shown in Figure A3-7. The bulk of the hydrogen production was calculated to occur in the period of 8500 s to 12400 s. About 25% of the hydrogen production was calculated to occur after the beginning of reflooding of the test fuel assembly, when the nuclear heat generation rate in the test fuel assembly was decreasing rapidly and the flow of coolant into the test fuel assembly was increasing. These MOD3.3 results are consistent with the measured rate of hydrogen production, which had a large amount of uncertainty but nevertheless provided a measurement of the trend of the hydrogen production. The MOD3.2 calculated cumulative hydrogen production is also shown in Figure A3-7. MOD3.2 did not calculate any hydrogen production after the beginning of reflooding.

The ballooning and rupture of the fuel rod cladding affects the temperature history, oxidation and meltdown of the fuel rods. The fuel rod cladding was measured to rupture in the period of 5850 s to 6260 s.

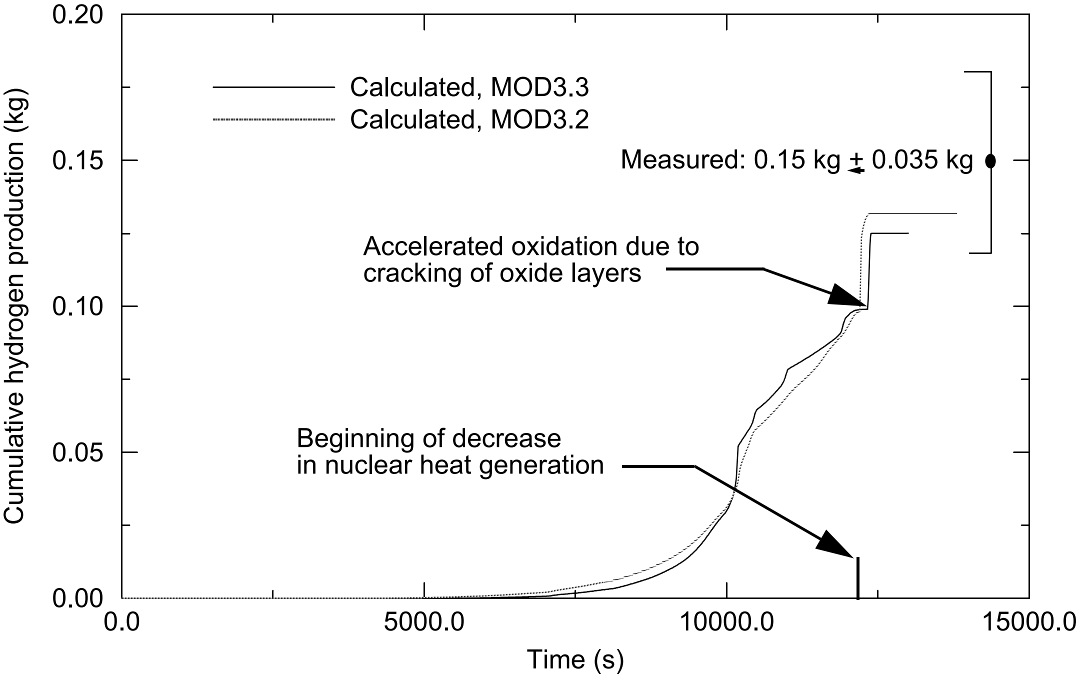

Figure A3-7. Calculated cumulative hydrogen production for PBF SFD ST test.

The fuel rod cladding was calculated by MOD3.3 to rupture in the period of 6015 s to 6325 s and at a cladding temperature of about 1050 K. The location of cladding rupture was calculated by MOD3.3 to be at the elevation of 0.85 m. The severely damaged post-test state of the test fuel rods precluded a measurement of the elevation interval of cladding ballooning.

The calculated boiloff of water in the test fuel assembly was generally in good agreement with the measured boiloff. The boiloff at water was mapped by the collapsed liquid level in the test fuel assembly. The MOD3.3 calculated and measured collapse liquid levels are compared in Figure A3-8.

The comparison of calculated and measured test fuel assembly pressure differentials indicates that the model in MOD3.3 for flow losses in porous debris is consistent with experimental results. The experimental results were useful only for identifying trends in the thermal hydraulic behavior of the test fuel assembly, in part due to an uncertainty in measured pressure caused by failure of the shroud. Both the measured pressure differential and the MOD3.3 calculations indicated a significant increase in flow losses after the test fuel assembly disintegrated into porous debris in the period of 12300 s to 12600 s. The MOD3.3 calculated and measured increases in test fuel assembly pressure differentials during the period of disintegration of the test fuel assembly were 6 kPa and 20 kPa, respectively.

In summary, this test problem showed that MOD3.3 calculates early-phase damage progression in agreement with experimental results. The MOD3.3 calculated time of rupture of the cladding of the test fuel rods was in good agreement with the measured time of cladding rupture. The calculated boiloff of coolant and oxidation of the test fuel assemly resulted in a calculated heatup of the test fuel assembly in good agreement with the measured heatup. The calculated and measured axial distribution in the fraction

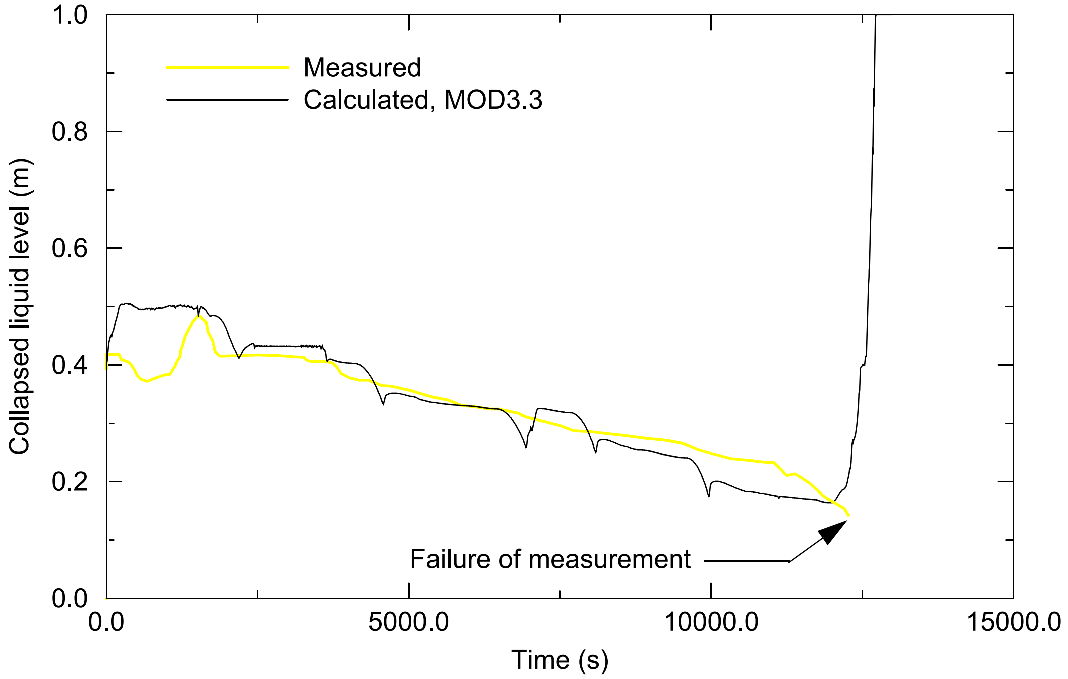

Figure A3-8. Comparison of calculated and measured collapsed liquid level in test fuel assembly for PBF SFD ST test.

of oxidation of the cladding of the test fuel assembly were in good agreement. MOD3.3 calculated that the meltdown of the test fuel assembly was limited to meltdown resulting from the eutectic reaction of Inconel spacer grids with Zircaloy cladding. The PIE indicated a limited amount of slumping of liquefied cladding with dissolved fuel. While the measured extent of meltdown was greater than the calculated extent of meltdown, nevertheless the differences in calculated and measured meltdown were not large. Both the MOD3.3 calculations and the measurements indicated a significant oxidation excursion and heatup after reflood of the test fuel assembly began and its nuclear heat generation rate was rapidly decreasing. The test problem also provided a limited test of the model in MOD3.3 for calculating the flow losses in porous debris. Both the MOD3.3 calculations and the measurements indicated a significant increase in flow losses after the beginning of reflood and the disintegration of part of the test fuel assembly into porous debris.

A3.2 Assessment Using the PBF SFD 1-1 Test

PBF SFD 1-1 Test[A3-2] was the second in the series of severe fuel damage experiments performed in the Power Burst Facility at the INEEL. The SFD 1-1 test train incorporated a fuel bundle containing 32, 1 m in length pressurized trace-irradiated fuel rods with an average burnup of 70 MWd/MtU surrounded by a multi-layer insulating shroud. The fuel rods in the test assembly were held in position by three 40 mm in height inconel spacer grids located at the 0.05, 0.45, and 0.86 m elevations above the bottom of the test bundle. The insulating shroud consisted of an inner zircaloy liner, a porous zirconia insulating layer, and a zircaloy wall. The experimental bundle was positioned in a zircaloy flow tube, which was inserted into the test facility in-pile-tube. The insulated region was pressured with argon and the gap between the inner and outer shroud walls was pressurized with helium. Numerous thermocouples recorded fuel rod and shroud temperatures during the test and pressure sensors recorded changes in system pressure. All test data was verified, validated and qualified by an independent data integrity review committee.

A3.2.1 Nodalization and Boundary Conditions

The entire test assembly for PBF SFD 1-1 was modeled with SCDAP/RELAP5. Ten (10) 0.1 m in length RELAP5 hydrodynamic volumes were used to represent the core region, a single RELAP5 volume to represent the bypass region, and time dependent volumes to represent a sink and source for the test bundle flow channel and core bypass. The test facility nodalization used RELAP5 hydrodynamic volumes and heat structures to represent the entire test facility including the deposition rod, steam line, condenser, and knockout drum. The RELAP5 nodalization scheme used for the analysis is shown in Figure A3-9. The bundle components, fuel rods and insulating shroud are represented by four SCDAP components as shown in Figure A3-10. The fuel rods in the 36 rod test bundle were represented by three SCDAP components as follows: (1) component 1 represented the four fuel rods of the inner ring, (2) component 2 represented the twelve fuel rods of the middle ring, and (3) component 3 represented the sixteen fuel rods of the outer ring. A fourth SCDAP component was used to represent the insulating shroud. Each SCDAP component was divided into ten axial nodes with each axial node 0.1 mm height. The axial nodes interfaced the 10 corresponding RELAP5 hydrodynamic control volumes. The external surface of the insulating shroud interfaced with the RELAP5 control volume that was used to represent the coolant in the bypass. The fuel rods for this test were modeled using 4 radial nodes and the insulating shroud was modeled using 19 radial nodes.

The bundle nuclear power generation and bundle coolant boundary conditions were defined according to experimental results. An estimation of nuclear power generated in the test bundle, as well as the uncertainty envelop of + 7% and -15%, was obtained from the measured reactor power and uncertainty calculations. This estimation was used for the power input for the assessment calculations. The single axial power profile used for the calculations was determined from measurements recorded from the fission chambers located on the outer wall of the shroud and reactor physics calculations. The measured water inlet flow rate of 0.64 g/s at 531 K with a measured system pressure of 6.8 MPa was defined in the input deck. Argon injected at a flow rate 1.3 g/s, beginning at 3,200 s and continuing to the end of the experiment, was also modeled.

A3.2.2 Comparison of Calculations and Measurements

The results for the PBF SFD 1-1 experiment provide benchmarks for the early-phase damage progression models in a severe accident analysis computer code.[A3-2] The experiment subjected the test fuel rods to conditions that caused rapid oxidation and meltdown of the cladding of the test fuel rods. The temperature history of the test fuel assembly at three different elevations was obtained during the period in which oxidation was causing a rapid heatup of the test fuel rods. A measurement was obtained of the amount of hydrogen produced by oxidation of the cladding of the test fuel rods and other structures. An instrument obtained the time of rupture of the fuel rod cladding due to excessive stress and ballooning. A post-irradiation examination (PIE) obtained information on the extent of oxidation of the test fuel assembly and the location of slumped fuel rod material.

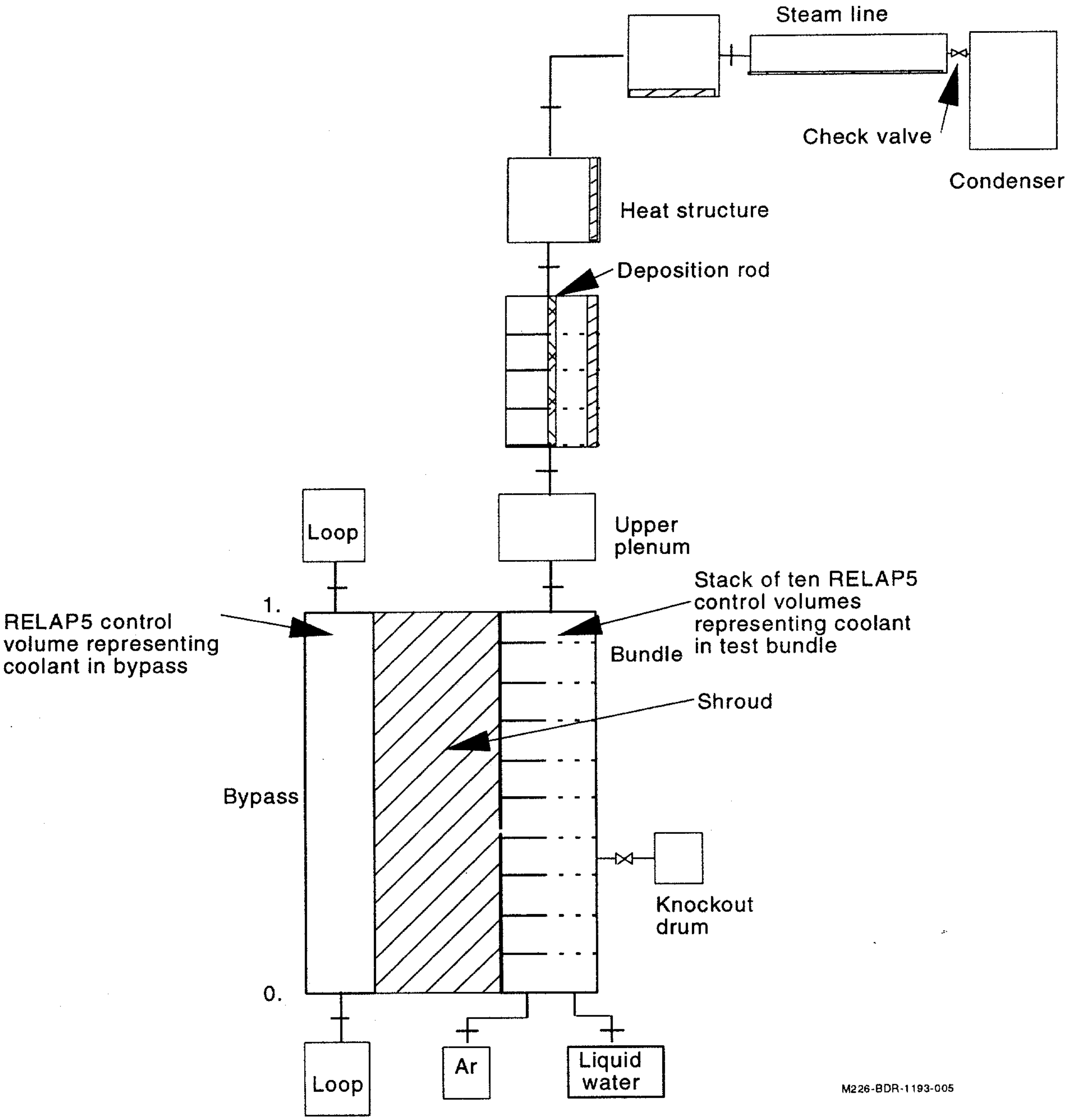
Steam line
Check valve
Condenser
Heat structure
Deposition rod
Loop
Upper plenum
Stack of ten RELAP5 control volumes representing coolant in test bundle
1.
RELAP5 control volume representing coolant in bypass
Bundle
Shroud
Bypass
Knockout drum
0.
Loop
Ar
Liquid water
M226-BDR-1193-005

Figure A3-9. RELAP5 nodalization of the test train for the SFD1-1 experiment.

The MOD3.3 calculated temperature behavior of the test fuel assembly was generally in good agreement with its measured temperature behavior. The MOD3.3 calculated and measured temperature history of the test fuel rods in the middle row of test fuel assembly at the 0.35 m elevation (referenced from bottom of fuel rod) are shown in Figure A3-11. The calculated rate of temperature increase at the temperature of 1700 K was about 13 K/s. The calculated rate of temperature increase was in agreement with the measured rate of temperature increase. The temperature measurement failed after the temperature exceeded 1700 K. The calculated temperature history has an inflection point at the time of 1976 s

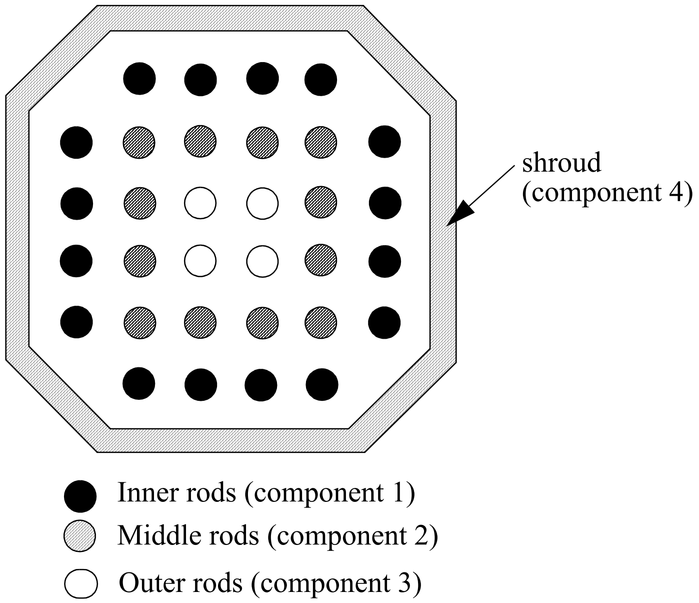

Figure A3-10. SCDAP nodalization of the PBF SFD1-1 experimental bundle.

(temperature of 2200 K) due to the relocation of the cladding in the circumferential direction, which in turn was due to melting of the cladding. The temperature history calculated by MOD3.2 at this elevation is also shown in Figure A3-11. The temperature histories calculated by MOD3.2 and MOD3.3 are similar. The calculated and measured temperature histories of the test fuel rods at the 0.5 m and 0.7 m elevations are compared in Figure A3-12 and Figure A3-13, respectively. The 0.5 m elevation is near the midplane of the test fuel rods. The calculated temperature history at the 0.5 m elevation has an inflection point at 1960 s due to the slumping of melted cladding. The calculated temperature history at the 0.7 m elevation has a similar inflection point due to the slumping of melted cladding. The maximum calculated temperature of the test fuel rods was 2818 K in the elevation interval of 0.3 m to 0.5 m. The maximum measured temperature of the test fuel rods, obtained from PIE results, was 2890 K at the elevation of 0.15 m.[A3-1] The temperature histories calculated by MOD3.2 are also shown in Figure A3-12 through Figure A3-13. The MOD3.3 and MOD3.2 calculations are similar.

The calculated axial distribution in oxidation of the cladding of the test fuel rods was in general agreement with the axial distribution obtained from the PIE performed on the test fuel assembly. The measured and the MOD3.3 and MOD3.2 calculated axial distributions in the fraction of the fuel rod cladding oxidized are tabulated in Table A3-3. The entries in the table without any data are due to measurements not being obtained at that elevation. Double-sided oxidation of the fuel rod cladding was calculated to occur in the elevation interval of 0.4 m to 0.6 m. The PIE results showed almost 100% oxidation of the cladding of the test rods in the elevation interval of 0.1 m to 0.3 m. MOD3.3 calculated about 80% oxidation of the cladding in the interval of 0.1 m to 0.4 m. MOD3.2 underpredicted significantly the extent of oxidation in the interval of 0.1 m to 0.4 m. Both MOD3.3 and MOD3.2 underpredicted somewhat the extent of oxidation in the elevation interval of 0.4 m to 0.7 m. In the 0.7 m to 0.9 m interval of elevation, the MOD3.3 calculations are in generally good agreement with the measured

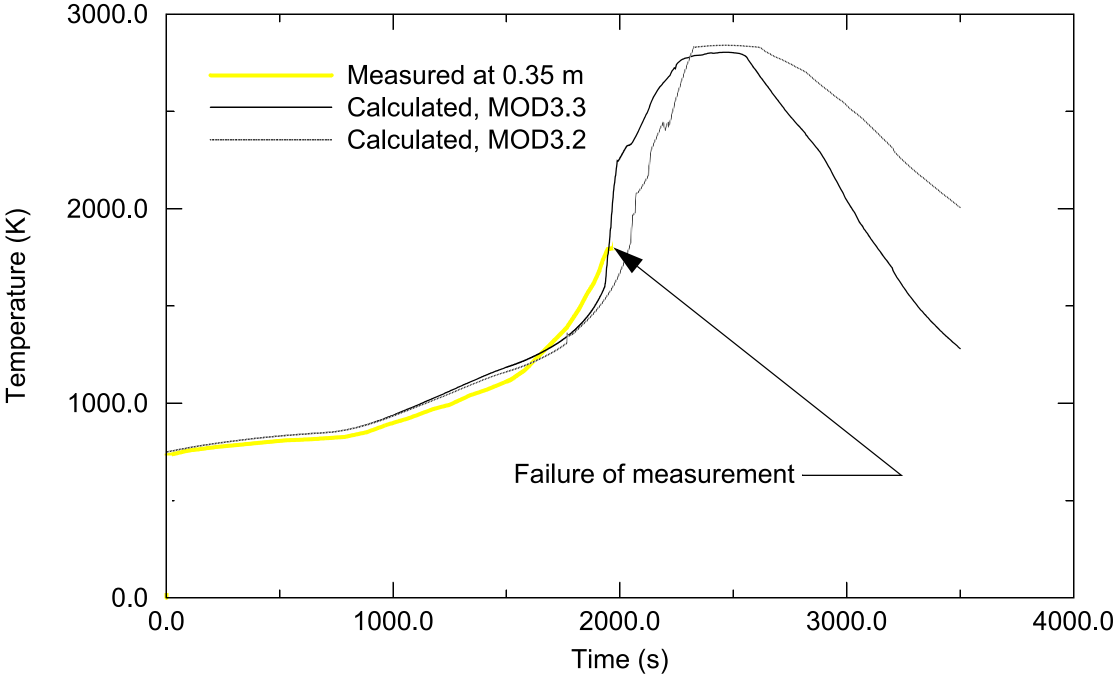

Figure A3-11. Calculated and measured temperatures at 0.35 m elevation for PBF SFD 1-1 test.

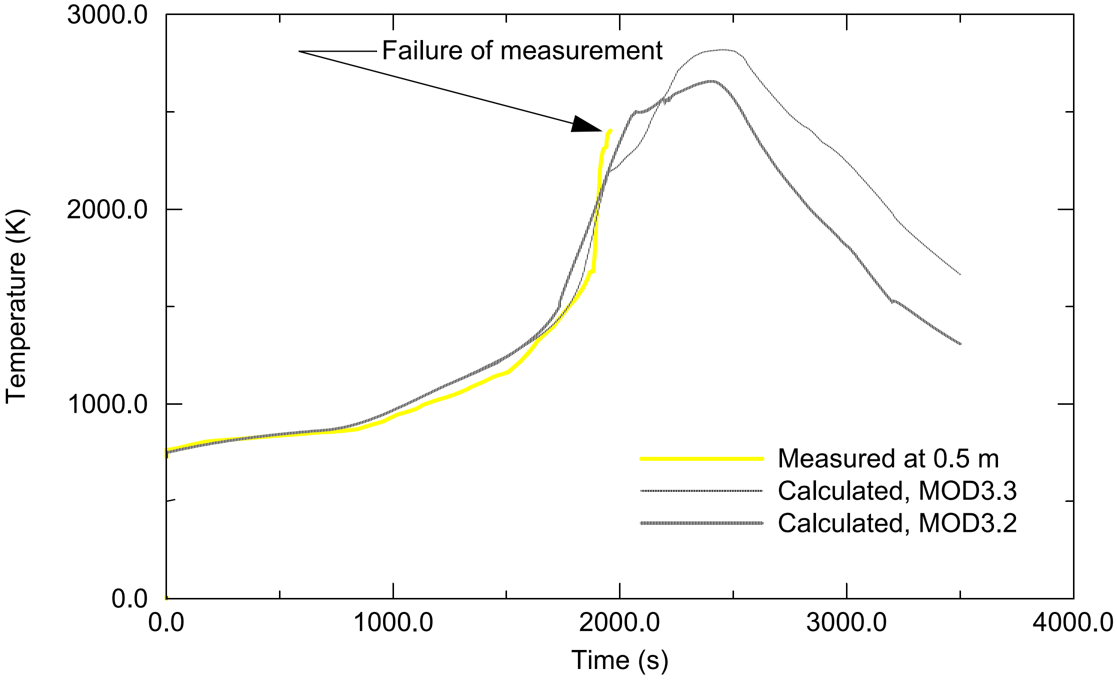

Figure A3-12. Calculated and measured temperature at elevation of 0.5 m for PBF SFD 1-1 test.

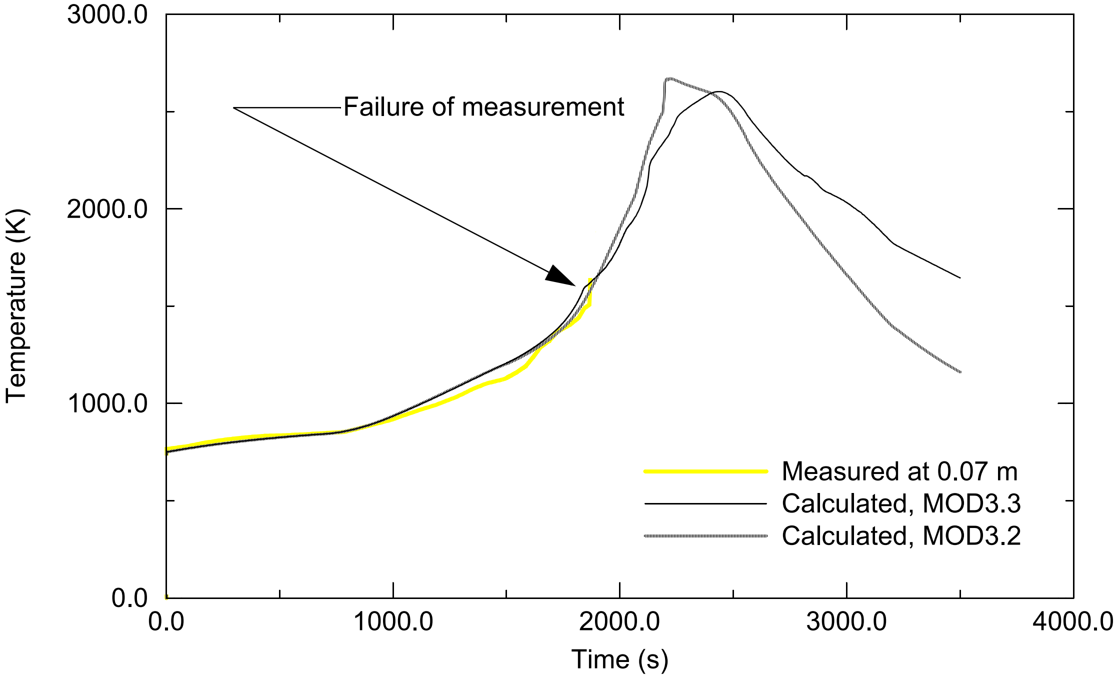

Figure A3-13. Calculated and measured temperature at elevation of 0.7 m for PBF SFD 1-1 test.

results, while the MOD3.2 calculations significantly overpredicted the extent of oxidation. Since meltdown has an influence on the axial distribution in oxidation, the calculated locations of cladding slumping and blockages are also shown in Table A3-3. The blockage is defined to be the fraction of coolant space filled with slumped material. The PIE indicated a significant blockage due to meltdown in the interval of elevation from 0.1 m to 0.2 m. Both MOD3.3 and MOD3.2 calculated a significant blockage in the same interval of elevation as indicated by the PIE results. The PIE results indicated the slumping of melted cladding in the elevation interval of 0.7 m to 0.9 m. MOD3.3 also calculated slumping in this interval of elevation but MOD3.2 did not. This improvement by MOD3.3 in modeling the slumping of cladding is the reason MOD3.3 did not overpredict the extent of oxidation of cladding in this interval of elevation, as did MOD3.2.

Table A3-3. Calculated and measured axial distributions in oxidation and meltdown for PBF SFD 1-1 test.

Elevation	Fraction cladding oxidized			Fraction blockage due to meltdown/ slumping from location (yes or no)		
(m)	MOD3.3	MOD3.2	Measured	MOD3.3	MOD3.2	Meaured
0.05	0.01	0.0	0.60	0.28/no	0.0/no	0.0/no
0.15	0.80	0.51	1.00	0.61/no	1.0/no	~0.5/no
0.25	0.78	0.13	1.00	0.0/no	-/-	0.0/no
0.35	0.78	0.16	0.25	0.0/no	-/-	0.0/yes

Table A3-3. Calculated and measured axial distributions in oxidation and meltdown for PBF SFD 1-1 test.

0.45	0.38	0.36	0.65	0.06/yes	-/-	0.0/no
0.55	0.36	-	-	0.0/yes	-/-	-
0.65	0.25	0.38	0.45	0.0/yes	-/-	0.0/no
0.75	0.18	0.46	0.11	0.0/yes	0.0/no	0.0/yes
0.85	0.16	0.34	0.20	0.0/yes	0.0/no	0.0/yes
0.95	0.63	-	-	0.0/no	0.0/no	-

The MOD3.3 calculated hydrogen production was greater than the measured hydrogen production. A hydrogen production of 64 + or - 7 g was measured by analysis of the contents of the collection tank. A hydrogen production of 99 g was measured from PIE results. MOD3.3 calculated a hydrogen production of 105 g. The hydrogen production calculated by MOD3.2 was 94 g. The calculated and measured rate of hydrogen production are compared in Figure A3-14. The bulk of the hydrogen production was calculated to occur in the period of 1800 s to 2300 s. The bulk of the hydrogen production was measured to occur in the period of 2100 s to 2600 s. The calculated rate of hydrogen production was somewhat greater than the measured rate of hydrogen production. Since the rate of hydrogen production was measured down stream of the test fuel assembly, the measured rate of hydrogen production lagged the rate of hydrogen production in the test fuel assembly and the peak measured rate of hydrogen production was a round off of the peak rate of hydrogen production in the test fuel assembly. The lag time is estimated to be 300 s.[A3-1] Taking into account this lag in the measured rate and round off of the measured rate, the calculated and measured rates are in fair agreement. Both the calculations and measurements show most of the hydrogen production occuring within a 500 s period. Both the calculations and the measurements show a sharp decrease in hydrogen production occurring almost right after the maximum rate of production. According to the calculations, this sharp decrease in the rate of hydrogen production was due to slumping of melted cladding.

The ballooning and rupture of the fuel rod cladding affects the temperature history, oxidation and meltdown of the fuel rods. The fuel rod cladding was measured to rupture in the period of 1538 s to 1632 s. The fuel rod cladding was calculated to rupture in the period of 1785 s to 1798 s. Although the severely damaged post-test state of the test fuel rods precluded an accurate measurement of the elevation interval of cladding ballooning, nevertheless sufficient evidence was present to estimate the elevation interval of cladding ballooning to be from 0.3 m to 0.7 m above the bottom of the fuel rods. The calculated elevation interval of cladding ballooning was from 0.4 m to 0.6 m above the bottom of the fuel rods. In reference to the elevation interval of cladding ballooning, ballooning is defined to have occurred where the cladding hoop strain exceeded 0.12. In the calculations, double-sided oxidation occurred where the cladding hoop strain exceeded 0.12 and the cladding had ruptured.

In summary, this test problem showed that MOD3.3 calculates early-phase damage progression in agreement with experiment results. The calculated oxidation driven heatup of the test fuel assembly was in

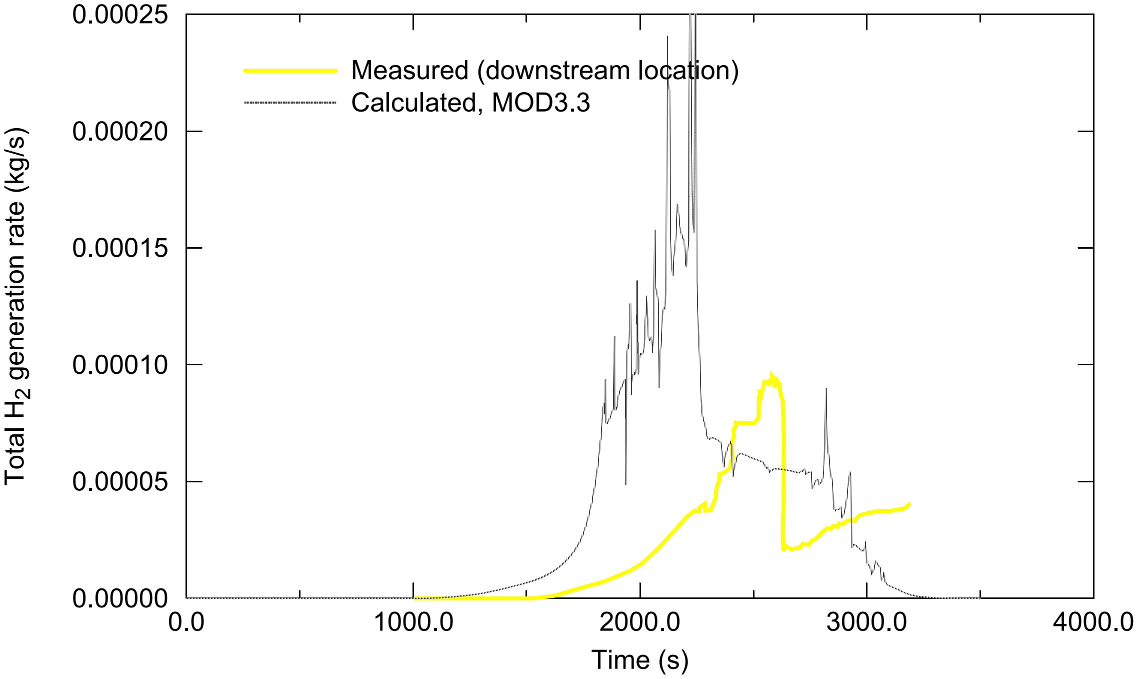

Figure A3-14. Calculated and measured rate of hydrogen production for PBF SFD 1-1 test.

good agreement with the measured oxidation driven heatup of the test fuel assembly. The calculated meltdown of the test fuel assembly was in good agreement with the measured meltdown of the test fuel assembly. The rapid production of hydrogen was both calculated and measured to occur within a 500 s period. The rate of production of hydrogen was calculated to decrease rapidly after the time of the peak rate of hydrogen production. This characteristic of hydrogen production was also in the measured rate of hydrogen production. The MOD3.3 calculations of the axial distribution in oxidation of the test fuel assembly was an improvement over the MOD3.2 calculations of axial distribution in oxidation. MOD3.3 correctly calculated a significant oxidation of the lower part of the test fuel assembly and a meltdown of the upper part of the test fuel assembly. Both MOD3.2 and MOD3.3 underpredicted somewhat the extent of oxidation of the slumped cladding in the blockage area near the bottom of the test fuel assembly. The MOD3.3 calculated time of rupture of the cladding of the test fuel rods was later than the measured time of cladding rupture. Nevertheless, the overall calculation of early-phase damage progression was in good agreement with the measurements of early-phase damage progression.

A3.3 Assessment Using the PBF SFD 1-4 Test

The SFD 1-4 test [A3-3] was the fourth in a series of severe core damage experiments performed in the Power Burst Facility at the Idaho National Engineering and Environmental Laboratory (INEEL). The SFD 1-4 test train incorporated a fuel bundle containing 26 pre-irradiated fuel rods with an average burnup of 36 GWd/MtU, two fresh, instrumented fuel rods and four silver-indium-cadmium control rods in a 6 x 6 array with the corner removed. All of the fuel rods were pressurized. One of the four control rods was instrumented. The absorber material in the control rods was an alloy consisting of 80% Ag, 15% In, and 5% Cd by weight. The spacing between fuel rods and control rod tubes in the test assembly was maintained by three inconel spacer grids ~40 mm in height located at the 0.09, 0.49, and 0.94 m elevations above the bottom of the test bundle. The active length of the fresh and irradiated fuel rods was 1 m.

The fuel bundle was housed in an insulated shroud to minimize radial heat losses. The layered shroud was composed of a zircaloy liner, insulating material (porous zirconia), a zircaloy wall region surrounding the shroud. The shrouded test bundle was inserted in a zircaloy flow tube, which in turn was centered in the in-pile tube. The insulated region was pressurized with argon, and the gap between the inner and other shroud walls was pressurized with helium.

A3.3.1 Nodalization

As shown in Figure A3-15, the test bundle was represented by seven SCDAP components; (1) component 1 represented the three irradiated fuel rods in the inner ring of bundle fuel rods, (2) component 2 represented the fresh fuel rod in the inner ring, (3) component 3 represented the fresh fuel rods in the middle ring, (4) component 4 represented the seven irradiated fuel rods in the middle ring, (5) component 5 represented the four control rods in the middle ring, (6) component 6 represented the 16 irradiated fuel rods in the outer ring, and (7) component 7 represented the insulating shroud. The rods fuel components for this experiment were modeled radially with four radial nodes, the control rods were modeled using five radial nodes, and the shroud was modeled using 19 radial nodes.

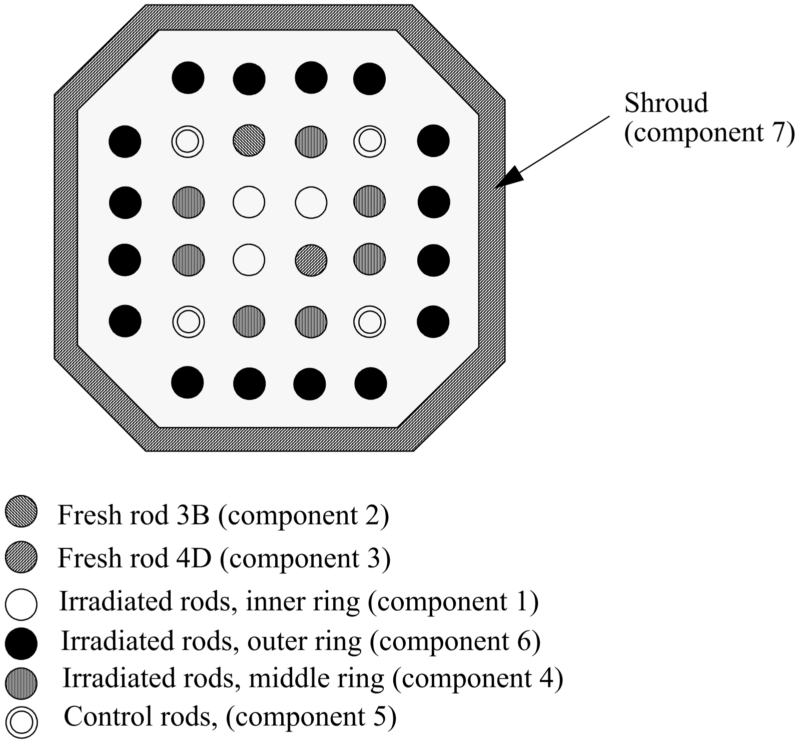
Shroud
(component 7)
Fresh rod 3B (component 2)
Fresh rod 4D (component 3)
Irradiated rods, inner ring (component 1)
Irradiated rods, outer ring (component 6)
Irradiated rods, middle ring (component 4)
Control rods, (component 5)

Figure A3-15. SCDAP nodalization of the PBF SFD 1-4 test bundle.

As shown in Figure A3-16, all components were modeled using 10 axial nodes, each node being 0.1 m in height and interfacing with one of the ten corresponding RELAP5 hydrodynamic control volumes. The external surface of the shroud was connected to a single RELAP5 hydrodynamic volume representing the bypass.

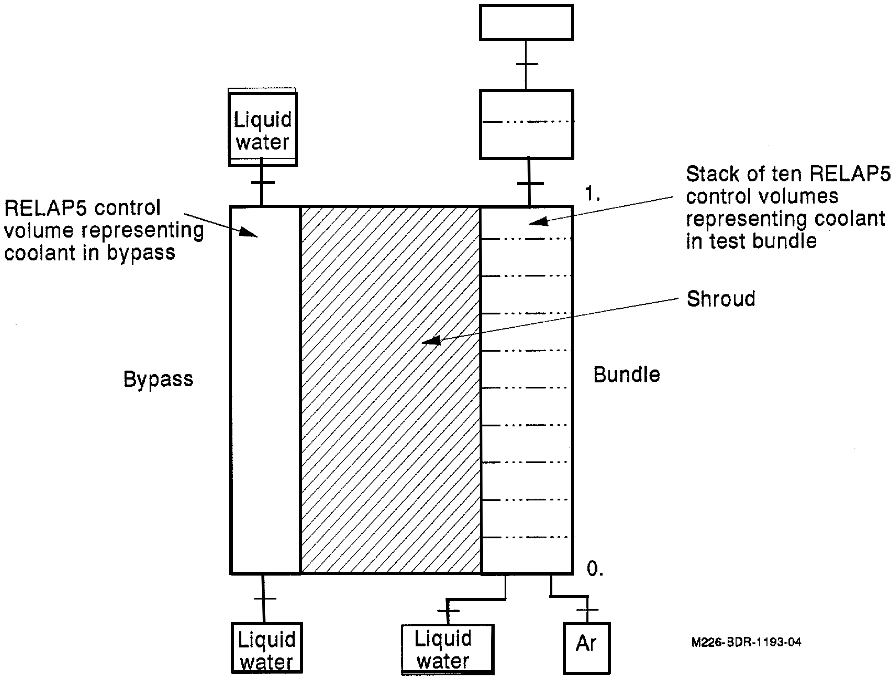
Liquid water
RELAP5 control volume representing coolant in bypass
Stack of ten RELAP5 control volumes representing coolant in test bundle
1.
Shroud
Bypass
Bundle
0.
Liquid water
Liquid water
Ar
M226-BDR-1193-04

Figure A3-16. RELAP5 nodalization of the PBF SFD 1-4 test bundle.

A3.3.2 Initial Conditions

All fuel rods were pressurized with helium to 2 MPa at room temperature, with the exception of fresh fuel rod (4D), which was pressurized to 3.8 MPa. The calculations started at the experiment time of 1,000 s, at which was the time for completion of the boildown phase and when the two-phase level in the bundle was ~0.20 m. At this time, the mean temperature of the bundle fuel rods was 810 K.

A3.3.3 Boundary Conditions

The best-estimate fuel rod power history was used in the calculations. The transient axial power profiles were represented in the calculations using three discrete curves. The calculations were started using a profile corresponding to an intact bundle partially filled with water, then shifted to a profile representing an intact bundle filled with steam (1,020 seconds) and finally to a profile representing a damaged bundle with relocated control rod materials and filled with steam (2,050 seconds).

A constant water inlet flow rate of 0.6 g/s with a temperature of 532 K and a pressure of 6.95 MPa was used over the experimental transient. Throughout the experiment, argon injected from the bottom flowed through the test bundle. For the first 1965 seconds of the experiment argon flow was maintained at a rate of 0.26 g/s; from 1,965 to 3,280 seconds the argon flow rate was maintained at 0.58 g/s; from 3,280 seconds to the termination of the experiment the argon flow rate was maintained at 1.88 g/s.

A3.3.4 Comparison of Calculations and Measurements

The results for the PBF SFD 1-4 experiment provide benchmarks for the modeling of early-phase damage progression in fuel assemblies with a significant amount of burnup.[A3-3] The experiment subjected the test fuel rods with a burnup of 36 MWd/kgU to conditions that caused rapid oxidation and meltdown of the cladding of the test fuel rods. The temperature history of the test fuel assembly at three different elevations was obtained during the period in which oxidation was causing a rapid heatup of the test fuel rods. A measurement was obtained of the amount of hydrogen produced by oxidation of the cladding of the test fuel rods and other structures. An instrument obtained the time of rupture of the fuel rod cladding due to excessive stress and ballooning. A post-irradiation examination (PIE) obtained information on the extent of oxidation of the test fuel assembly and the location of slumped fuel rod material.

The MOD3.3 calculated temperature behavior of the test fuel assembly was in good agreement with its measured temperature behavior. The MOD3.3 calculated and measured temperature histories of the fresh test fuel rod in the center of the test fuel assembly at the 0.4 m elevation (referenced from bottom of fuel rod) are shown in Figure A3-17. The MOD3.2 calculated temperature history is also shown. The temperature measurement failed after the temperature exceeded 2000 K. The MOD3.3 calculated temperature history and the measured temperature history are in good agreement. The rate of heatup calculated by MOD3.3 is slightly faster than that calculated by MOD3.2. The MOD3.3 calculated

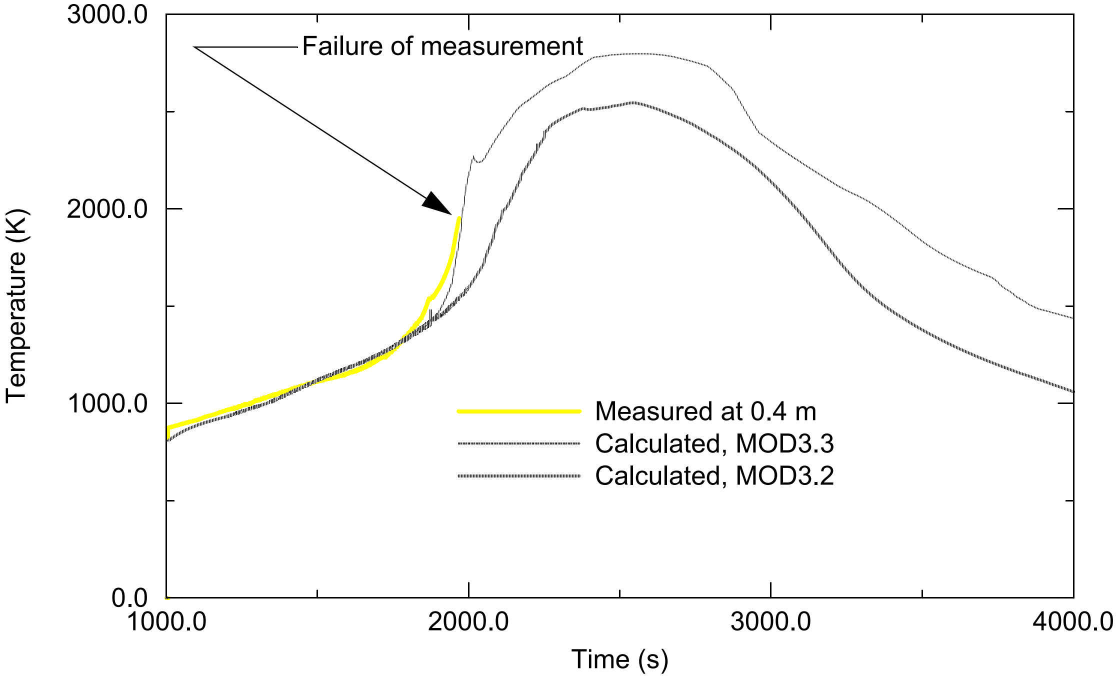

Figure A3-17. Calculated and measured temperatures at 0.4 m elevation for PBF SFD 1-4 test.

temperature history at the time of 2040 s (temperature of 2350 K) has an inflection point due to a reduction in the rate of oxidation caused by the presence of dissolved fuel in the metallic part of the cladding. The rate of heatup was calculated by MOD3.3 to begin to decrease at 2350 s due to complete oxidation of the cladding and melting of the fuel. The calculated and measured temperature histories of the test fuel rods at the 0.54 m and 0.74 m elevations are compared in Figure A3-18 and Figure A3-19, respectively. The 0.54 m elevation is near the midplane of the test fuel rods. The calculated rate of heatup at the 0.74 m elevation was limited due to steam starvation. The rate of heatup at the this elevation was calculated to be significantly less than that at the 0.4 m elevation due to steam starvation. The rate of heatup at 0.74 m elevation began to decrease at 2600 s due to the decrease at this time in the nuclear heat generation rate in the test fuel bundle. The maximum temperature of the test fuel rods was calculated by MOD3.3 to be 2870 K and to occur in the outer row of fuel rods in the elevation interval of 0.4 m to 0.6. The PIE results indicated the maximum temperature of the test fuel assembly to be greater than 2800 K and to occur in the elevation interval of 0.5 m to 0.6 m.[A3-3] A measurement was obtained of the temperature of the shroud mid-wall through out the high temperature period of the experiment. The MOD3.3 calculated and measured temperature of the shroud mid-wall at 0.91 m are compared in Figure A3-20. The good agreement of the calculated and measured temperatures indicates that MOD3.3 correctly calculated the temperature behavior of the test fuel assembly during the high temperature period of the test.

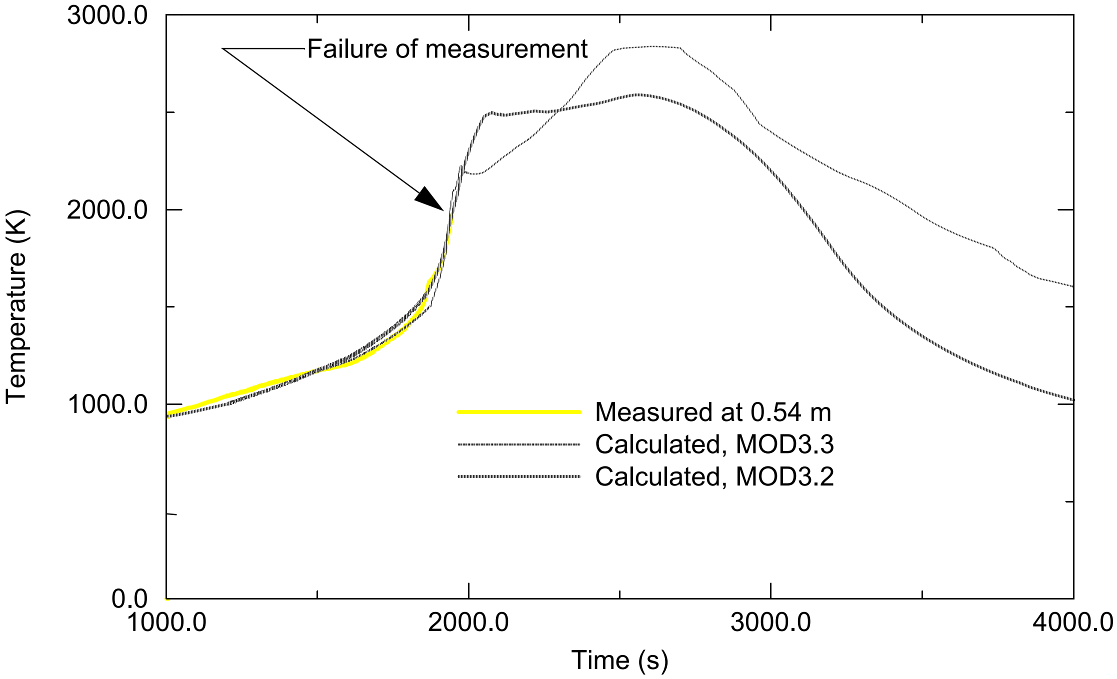

Figure A3-18. Calculated and measured temperatures at 0.54 m elevation for PBF SFD 1-4 test.

The calculated axial distribution in oxidation of the cladding of the test fuel rods was in general agreement with the axial distribution obtained from the PIE performed on the test fuel assembly. The measured and the MOD3.3 and MOD3.2 calculated axial distributions in the fraction of the fuel rod cladding oxidized are tabulated in Table A3-4. The entries in the table without any data are due to

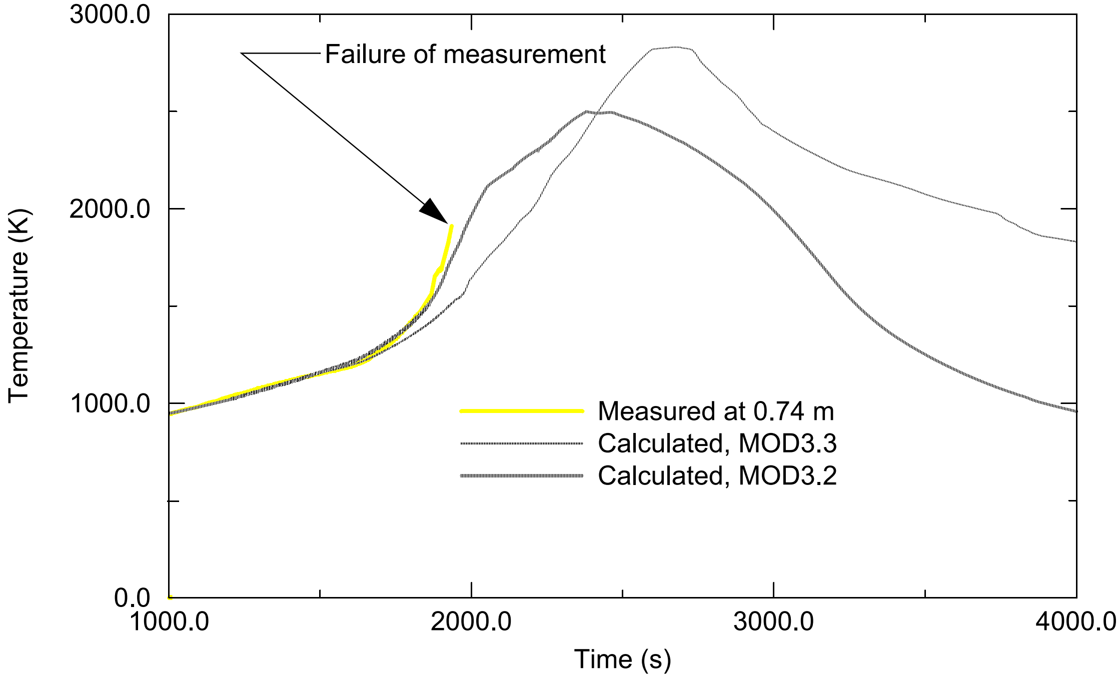

Figure A3-19. Calculated and measured temperatures at 0.74 m elevation for PBF SFD 1-4 test.

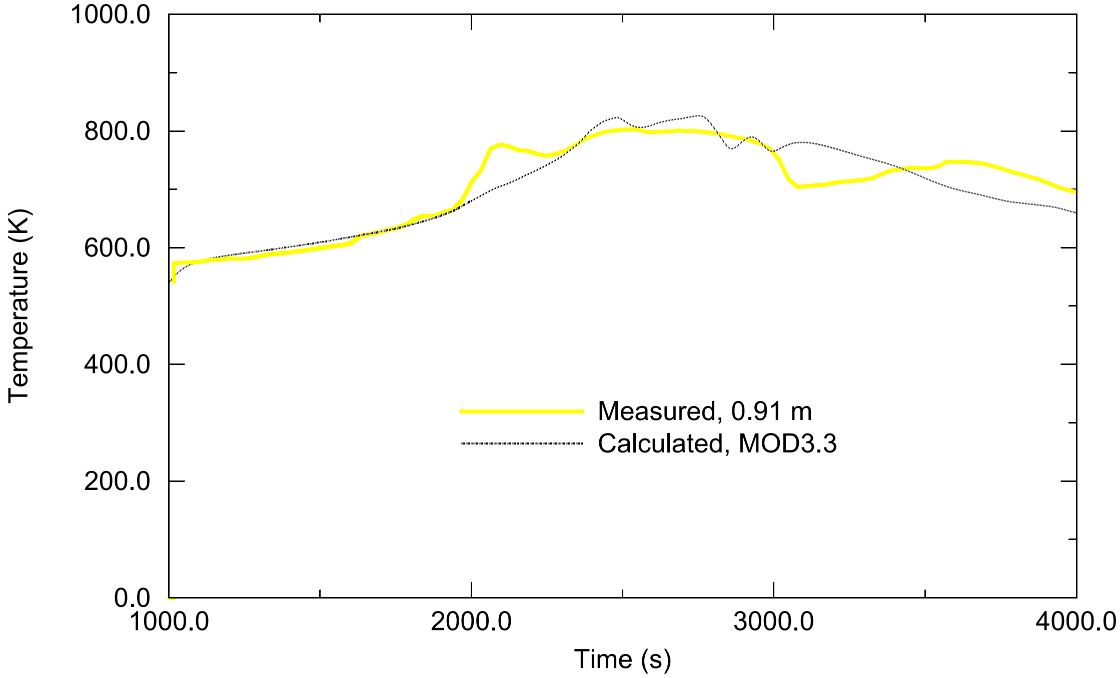

Figure A3-20. Calculated and measured temperatures at shroud mid-wall at 0.91 m for PBF SFD 1-4 test.

measurements not being obtained at that elevation. Double-sided oxidation of the fuel rod cladding was calculated to occur in the elevation interval of 0.6 m to 0.8 m. The PIE results showed almost 100% oxidation of the cladding of the test rods in the elevation interval of 0.1 m to 0.3 m. MOD3.3 calculated about 70% oxidation of the cladding in the interval of 0.2 m to 0.6 m. MOD3.2 underpredicted significantly the extent of oxidation in the interval of 0.2 m to 0.3 m. MOD3.3 overpredicted by about a factor of two the extent of oxidation in the elevation interval of 0.5 m to 0.6 m. The overprediction of the extent of oxidation in this interval of elevation may be due to the code not calculating the slumping of cladding in this interval of elevation. The PIE results indicate that cladding in this interval of elevation slumped. In the 0.7 m to 0.9 m interval of elevation, the MOD3.3 calculations of the fraction of cladding oxidation are in generally good agreement with the measured results. Both the calculations and the measurents indicate that the extent of oxidation of the cladding in this interval of elevation was limited by slumping of cladding. MOD3.2 did not predict the slumping of cladding in the elevation interval of 0.8 m to 0.9 m, and as a result the extent of oxidation of the cladding in this interval of elevation was overpredicted. Since cladding meltdown has an influence on the axial distribution in oxidation, the calculated locations of cladding slumping and blockages are also shown in Table A3-4. The blockage is defined to be the fraction of coolant space filled with slumped material. The PIE indicated a significant blockage due to meltdown in the interval of elevation from 0.1 m to 0.2 m. Both MOD3.3 and MOD3.2 calculated a significant blockage in the same interval of elevation as indicated by the PIE results. The PIE results indicated the slumping of melted cladding in the elevation interval of 0.3 m to 0.9 m. MOD3.3 calculated slumping of the cladding in the interval of elevation from 0.6 m to 0.9 m. MOD3.2 did not predict slumping of the cladding in the elevation interval of 0.8 m to 0.9 m.

Table A3-4. Calculated and measured axial distributions in oxidation and meltdown for PBF SFD 1-4 test.

Elev.	Fraction cladding oxidized			Fraction blockage due to meltdown/ slumping from location (yes or no)		
(m)	MOD3.3	MOD3.2	Measured	MOD3.3	MOD3.2	Measured
0.05	0.0	0.0	0.10	0.0/no	0.0/no	0.0/no
0.15	0.03	0.02	1.00	0.5/no	0.5/no	~0.5/no
0.25	0.61	0.11	1.00	0.0/no	0.0/-	~0.1/no
0.35	0.67	0.52	0.50	0.0/no	0.0/-	0.0/yes
0.45	0.68	-	-	0.0/no	0.0/-	0.0/yes
0.55	0.67	0.37	<0.30	0.0/no	0.0/-	0.0/yes
0.65	0.33	-	-	0.0/yes	0.0/-	0.0/yes
0.75	0.22	0.26	0.37	0.0/yes	0.0/-	0.0/yes
0.85	0.24	0.86	0.22	0.0/yes	0.0/no	0.0/yes
0.95	0.90	-	-	0.0/no	0.0/no	-/-

The MOD3.3 calculated hydrogen production was in good agreement with the measured hydrogen production. A hydrogen production of 86 + or - 12 g was measured by analysis of the contents of the collection tank. MOD3.3 calculated a hydrogen production of 81 g. The hydrogen production calculated by MOD3.2 was 94 g. The PIE results did not provide a quantitative measurement of the extent of oxidation of the slumped material in the large blockage region in the elevation interval of 0.1 m to 0.2 m, but did indicate that a significant fraction of the slumped material in this region was oxidized. MOD3.3 calculated that 30% of the slumped cladding in the blockage region was oxidized. The MOD3.3 calculated and measured rates of hydrogen production and cumulative hydrogen production are compared in Figure A3-21 and Figure A3-22. The bulk of the hydrogen production was calculated to occur in the period of 1900 s to 3000 s. The bulk of the hydrogen production was measured to occur in the period of 2100 s to 3300 s. The calculated rate of hydrogen production during the first 120 s of intensive oxidation was greater than the measured rate of hydrogen production by about a factor of two. Since the rate of hydrogen production was measured down stream of the test fuel assembly, the measured rate of hydrogen production lagged the rate of hydrogen production in the test fuel assembly and the peak measured rate of hydrogen production was a round off of the peak rate of hydrogen production in the test fuel assembly. The lag time is estimated to be about 300 s.[A3-3]Taking into account this lag in the measured rate and round off of the measured rate, the calculated and measured rates are in fair agreement. Both the calculations and measurements showed that most of the hydrogen production occurred within a 1000 s period. The measured rate of hydrogen production showed a leveling off at 2100 s, when intensive oxidation was just beginning and which may have been due to slumping of cladding at the onset of intensive oxidation. The rate of hydrogen production was calculated to decrease due to the slumping of cladding after about 120 s of intensive oxidation.

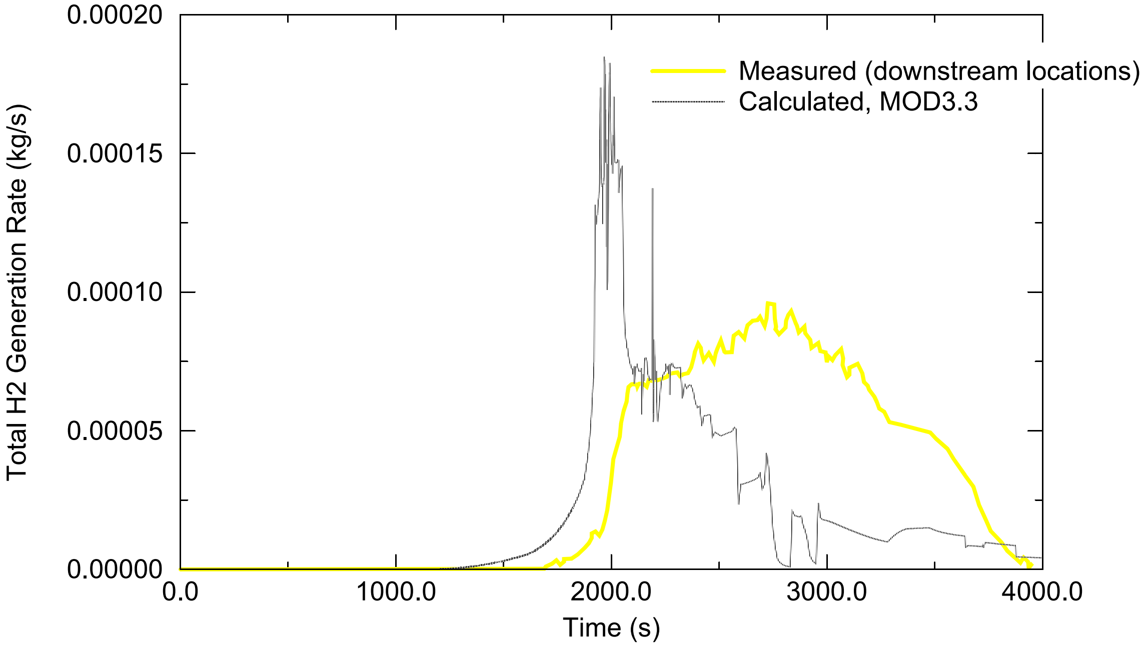

Figure A3-21. Comparison of calculated and measured rates of hydrogen production for PBF SFD 1-4.

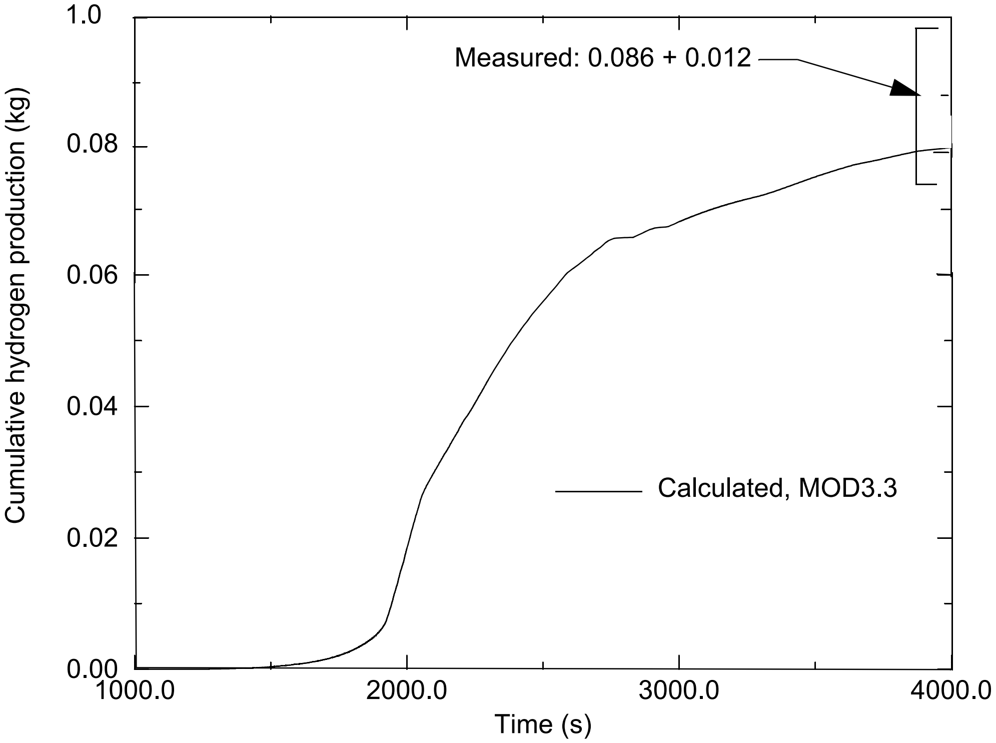

Figure A3-22. Calculated cumulative hydrogen production for PBF SFD 1-4 test.

The ballooning and rupture of the fuel rod cladding affects the temperature history, oxidation and meltdown of the fuel rods. The fuel rod cladding was measured to rupture in the period of 1720 s to 1900 s. The fuel rod cladding was calculated to rupture in the period of 1360 s to 1530 s and at cladding temperatures in the range of 1100 K to 1150 K. The severely damaged post-test state of the test fuel rods precluded a measurement of the elevation interval of cladding ballooning. The calculated elevation interval of cladding ballooning for the fuel rods with burnup was from 0.5 m to 0.8 m above the bottom of the fuel rods. In reference to the elevation interval of cladding ballooning, ballooning is defined to have occurred where the cladding hoop strain exceeded 0.12. In the calculations, double-sided oxidation occurred where the cladding hoop strain exceeded 0.12 and the cladding had ruptured.

In summary, this test problem showed that MOD3.3 calculates early-phase damage progression in agreement with experiment results. The calculated oxidation driven heatup of the test fuel assembly was in good agreement with the measured oxidation driven heatup of the test fuel assembly. The calculated meltdown of the test fuel assembly was in fair agreement with the measured meltdown of the test fuel assembly. The calculated and measured cladding meltdown were in good agreement in the lower and upper parts of the test fuel assembly. The cladding meltdown at the midplane of the test fuel assembly was underpredicted. The rapid production of hydrogen was both calculated and measured to occur within about a 1000 s period. The maximum calculated rate of hydrogen production was somewhat greater than themaximum measured rate of hydrogen production. This discrepancy may be due to an underprediction of the measured maximum rate of hydrogen proiduction caused by the downstream position of the measuring devises. The MOD3.3 calculations of the axial distribution in oxidation of the test fuel assembly was an improvement over the MOD3.2 calculations of axial distribution in oxidation. MOD3.3 correctly calculated a significant oxidation of the lower opart of the test fuel assembly and a meltdown of the upper part of the test fuel assembly. The MOD3.3 calculated time of rupture of the cladding of the test fuel rods was sooner than the measured time of cladding rupture. Nevertheless, the overall calculation of earlyphase damage progression was is good agreement with the measurements of early-phase damage progression.

A3.3.5 References

A3-1. A. D. Knipe, S. A. Ploger, and D. J. Osetek, "PBF Severe Fuel Damage Scoping Test - Test Results Report," NUREG/CR-4683, EGG-2413. August 1986.

A3-2. Z. R. Martinson, D. A. Petti, and B. A. Cook, "Volume 1: "PBF Severe Fuel Damage Test 1-1 Test Results Report," NUREG/CR-4684, EGG-2463, October 1986.

A3-3. D. A. Petti, Z. R. Martinson, R. R. Hobins, C. M. Allison et al., "Power Burst Facility (PBF) Severe Fuel Damage Test 1-4 Test Results Report," NUREG/CR-5163, EGG-2542, April 1989.

A4. CORA TESTS

A series of bundle heating and melting experiments were conducted in the CORA test facility at Forschungszentrum, Karlsruhe, (FzK) to examine core damage progression under severe accident conditions. These steam-fed out-of-pile tests used a combination of electrically heated and unheated bundle fuel rods to simulate decay heating in a reactor core. Due to the ease in configuring the test bundle and the ability to systematically control test conditions, key severe accident phenomena, such as fuel rod ballooning, bundle meltdown, and quench-induced fragmentation for both PWR and BWR-configured bundles were studied. The results of these experiments are useful for assessing models in severe accident computer codes. A general description of the test facility, a description of the experiments used to assess SCDAP/RELAP5/MOD3.3, and assessment results are presented in the following sections.

A4.1 General Description of the CORA Test Facility

The CORA test facility consisted of an experimental fuel bundle (25 or 56 rods, heated, unheated, and optional control rods for the PWR tests, and 16 or 48 unheated and heated fuel rods with a centered stainless steel clad boron carbide control blade for the BWR tests), an insulating zirconia shroud, a quench tank, and a high temperature shield. The experimental bundle consisted of a representative 2-m high fuel rod bundle with a 1-m electrically heated region to simulate decay heat. The inlet for superheated steam and argon was on a side near the bottom of the heated section of the experimental bundle, and the hot gases flowed through the experimental bundle and then into a condenser. The non-condensable gases, hydrogen formed during zircaloy oxidation and the argon cover gas, are expanded to atmospheric pressure in a mixing chamber. For safety reasons the hydrogen fraction was diluted by adding compressed air. After dilution, the composition of the released gas and the mass of hydrogen produced during the experiment was determined. The fuel rod bundle was surrounded by a porous zirconia insulating shroud. The insulated test bundle was surrounded by a ceramic high temperature radiation shield.

A steam generator positioned within the containment provided the steam supply to the bundle. A superheater was used to heat the steam and argon cover gas to temperatures in excess of 800^{o}C. The maximum allowed pressure in the facility was 10 bars, though all experiments used for the MOD3.2 assessment were performed at 2 bar (1 bar overpressure). The temperature of the gases leaving the superheater dropped about 200^{o}C as it flowed through the pipe connecting the superheater to the test bundle.

The experimental test apparatus had viewing ports through which the melt progression in the test bundle could be continuously observed. Video recording and high-resolution still photography were used to provide a permanent visual record of the melt progression and core damage events occurring in the test bundle during the experiment. Thermocouples mounted on the zircaloy cladding of the heated and unheated fuel rods, at the fuel centerline of some unheated fuel rods, on the control rod or blade, and at various locations in the insulating shroud and high temperature shield recorded each component’s temperature change during the test. Mass flow rates of gases, system pressure, and power were continuously monitored and recorded during the test.

A4.2 Nodalization of the CORA Test Facility

The RELAP5 nodalization diagram of the CORA test facility used to model the CORA PWR experiments for the assessment is shown in Figure A4-1. The bundle nodalization used for calculations employed a second shroud component to model the high temperature shield. The two SCDAP shrouds calculated the radiation heat transfer between the insulating flow shroud and the high temperature shield. A cross-section of a typical small bundle, CORA-13, is shown in Figure A4-2. The ceramic high temperature shield was represented by a second SCDAP shroud component surrounding the test bundle. The rod configuration of each small bundle PWR test is similar to that used for the CORA-13 test with minor modifications such as the presence or absence of control rods in the test bundle. The initial conditions used in all assessment input decks were obtained from test data supplied to the INEEL by FzK.

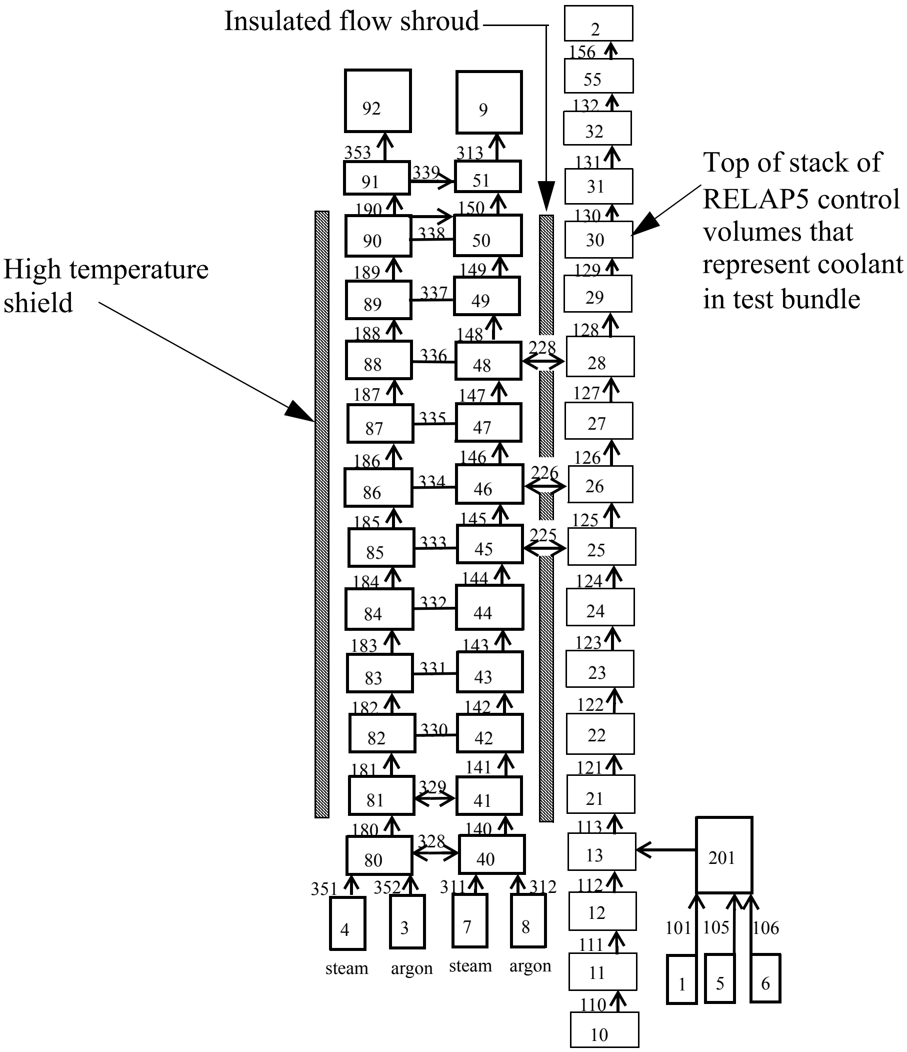
Insulated flow shroud
Top of stack of RELAP5 control volumes that represent coolant in test bundle
High temperature shield
92
9
2
156
55
132
32
131
31
130
30
129
29
128
28
127
27
126
26
125
25
124
24
123
23
122
22
121
21
113
13
112
12
111
11
110
10
201
101
105
106
1
5
6
353
313
91
339
51
190
150
90
338
50
189
149
89
337
49
188
148
88
336
48
228
187
147
87
335
47
186
146
86
334
46
226
185
145
85
333
45
225
184
144
84
332
44
183
143
83
331
43
182
142
82
330
42
181
141
81
329
41
180
140
80
328
40
351
352
311
312
4
3
7
8
steam
argon
steam
argon

Figure A4-1. General CORA RELAP5 nodalization used for all PWR tests.

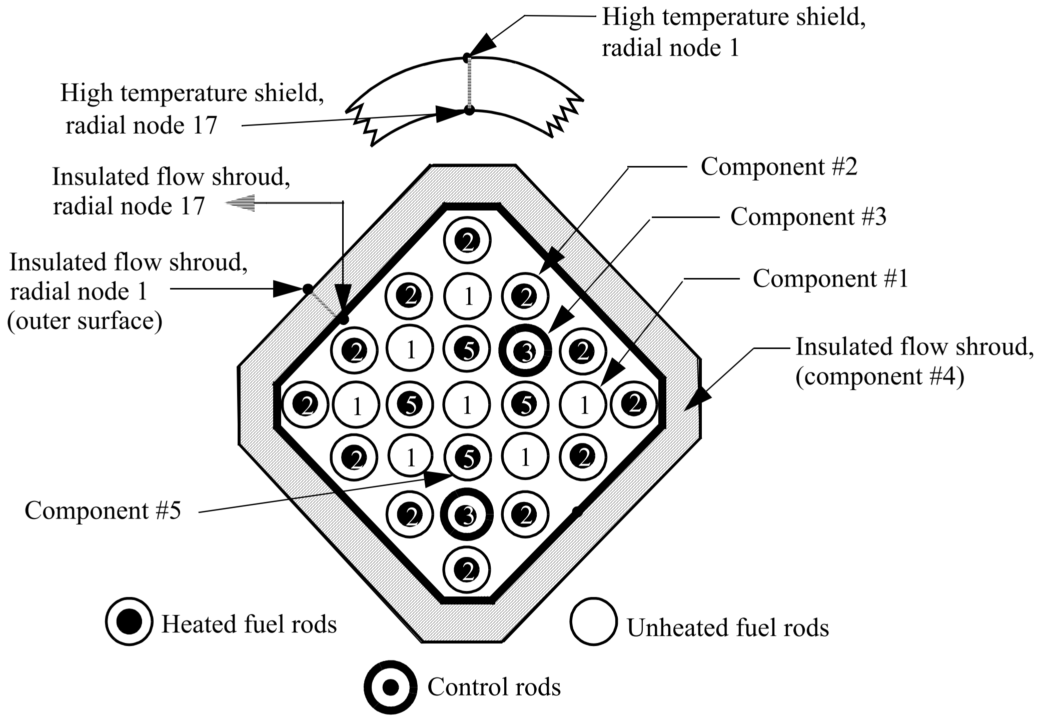
High temperature shield, radial node 1
High temperature shield, radial node 17
Insulated flow shroud, radial node 17
Insulated flow shroud, radial node 1 (outer surface)
Component #2
Component #3
Component #1
Insulated flow shroud, (component #4)
Component #5
1
2
3
5
Heated fuel rods
Unheated fuel rods
Control rods

Figure A4-2. CORA-13 bundle cross-section basic design used for all PWR tests.

A4.3 Test Conditions for the CORA Tests

Each CORA tests was divided into three distinct phases. The test phases were (a) the gas preheat phase, (b) the transient phase, and (c) the cooling phase. During the gas preheat phase a low constant power of 0.65 KW was input to the heater rods while preheated argon flowed through the bundle. During this phase, the bundle insulation was equilibrated at temperatures sufficiently high to prevent steam condensation during the test. System pressure during this phase was maintained at the desired test pressure of 0.22 MPa. During the transient phase, power to the heater rods was increased linearly with time to develop in the bundle a heatup rate equal to 1 K/s up to the onset of oxidation. Power to the heater rods for most tests was maintained at the maximum value for several hundred seconds. Throughout each test, argon flow through the bundle was maintained at a constant flow rate. Steam for most of the tests was introduced into the bundle 300 seconds after the initiation of power to the heater rods. The superheated steam flowed through the bundle for a predetermined period of time, usually until termination of power to the heater rods. The argon or argon/steam mixture, heated to ~ 1,000 K in a superheater, cooled as it flowed through the 40 foot connecting pipe to the bundle inlet. The bundle inlet temperature remained near 800 K during the early phase of the simulated accident, increasing by approximately 200 K 500 seconds after the initiation of power to the heater rods. In quench tests, such as CORA-13, where the addition of cooling water was used to quickly cool the test bundle, the cooling phase was initiated by the raising of a water filled cylinder at a rate of 1 cm/s to quench the bundle. In non-quench tests the test bundles were allowed to cool slowly in flowing argon after termination of power to the heater rods.

A4.4 Assessment Using CORA-5 TEST

A4.4.1 Description of the Experimental Bundle

The CORA-5 experiment was a small bundle PWR test containing a single control rod centered in the bundle. The CORA-5 bundle consisted of twenty five (25) rods in a 7 x 7 array with the corners removed. The bundle, similar to the one shown in Figure A4-2, contained 8 unheated fuel rods, 16 heated rods and a single stainless steel clad silver-indium-cadmium control rod centered in the bundle. The unheated fuel rods used in this CORA experiment were prototypical KWU fuel rods. The argon flow rate through the test bundle for this experiment was maintained 8.2 g/s. Steam flowed through the bundle at a rate of 6.8 g/s starting 300 s after the initiation of power to the heater rods and continued until the end of the experiment. While most CORA experiments had open viewing windows cut into the insulating shroud, the viewing windows for the CORA-5 experiment were made of quartz, therefore eliminating the possibility of gas or heat leakage through the bundle windows.

A4.4.2 Comparison of Calculations and Measurements

The results of the CORA-5 test were applied to the assessment of MOD3.3 by comparing calculated temperature histories for several different elevations in the test fuel assembly with the measured temperature histories at those elevations.

The MOD3.3 calculated temperature behavior of the test fuel assembly was in generally good agreement with the measured temperature behavior. The MOD3.3 calculated and measured temperature histories are shown in Figures A4-4 through A4-8 for the elevations of 0.35 m, 0.55 m, 0.75 m, 0.85 m, and 0.95 m, respectively. The elevations are referenced with respect to the bottom of the fuel rods. The MOD3.2 calculated temperature histories are also shown. At the 0.35 m elevation, the MOD3.3 calculated heatup of an unheated rod was more rapid than the measured heatup. The heatup was calculated to be accelerated by the slumping of hot material from above to a location just above the 0.35 m elevation and then the conduction of heat in the axial direction to the location of the 0.35 m elevation. At the 0.55 m elevation, the MOD3.3 calculated heatup was slightly faster the measured heatup. At the 0.75 m and 0.85 m elevations, the MOD3.3 calculated heatup was slightly slower than the measured heatup. At the 0.95 m elevation, the measured temperature decreased due to contact with water from the condensation of steam in the upper part of the test fuel assembly. The calculation did not represent the upper part of the test fuel assembly and the condensation of steam, and as a result the calculated rate of heatup was more rapid than the measured rate of heatup. The MOD3.3 calculated and measured temperature histories of a control rod at the elevation of 0.55 m are compared in Figure A4-9. The calculated and measured temperature histories are in good agreement.

The MOD3.3 calculated hydrogen production was 25% greater than that calculated by MOD3.2. The MOD3.3 and MOD3.2 calculations of hydrogen production were 125 g and 100 g, respectively. A measurement of hydrogen production was not obtained.

The elevation of the primary blockage caused by fuel rod meltdown was calculated to be lower than the measured elevation. The calculated and measured elevations of primary blockage were 0.05 m and

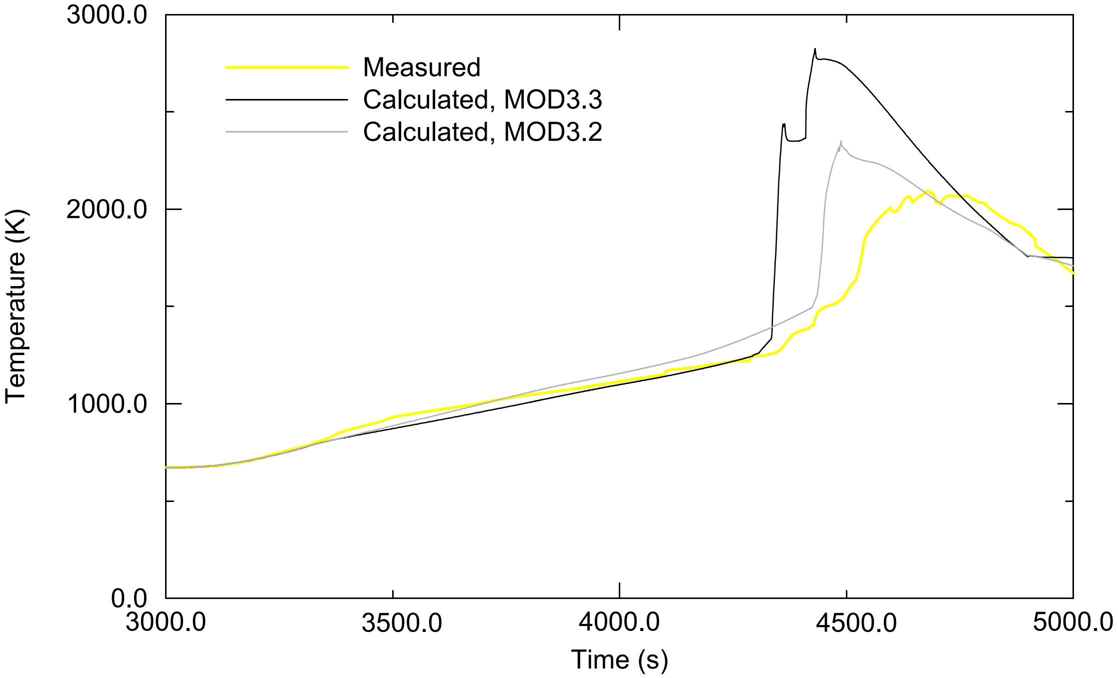

Figure A4-3. Calculated and measured temperatures of unheated fuel rod at 0.35 m elevation for CORA-5 test.

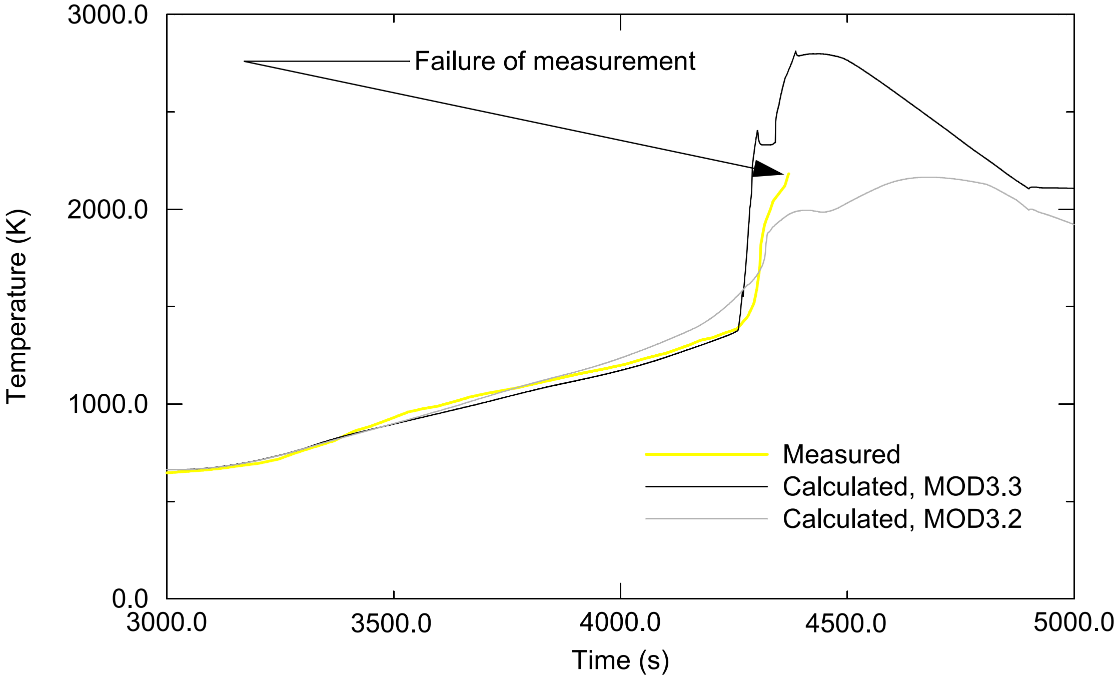

Figure A4-4. Calculated and measured temperatures of unheated fuel rod at 0.55 m elevation for CORA-5 test.

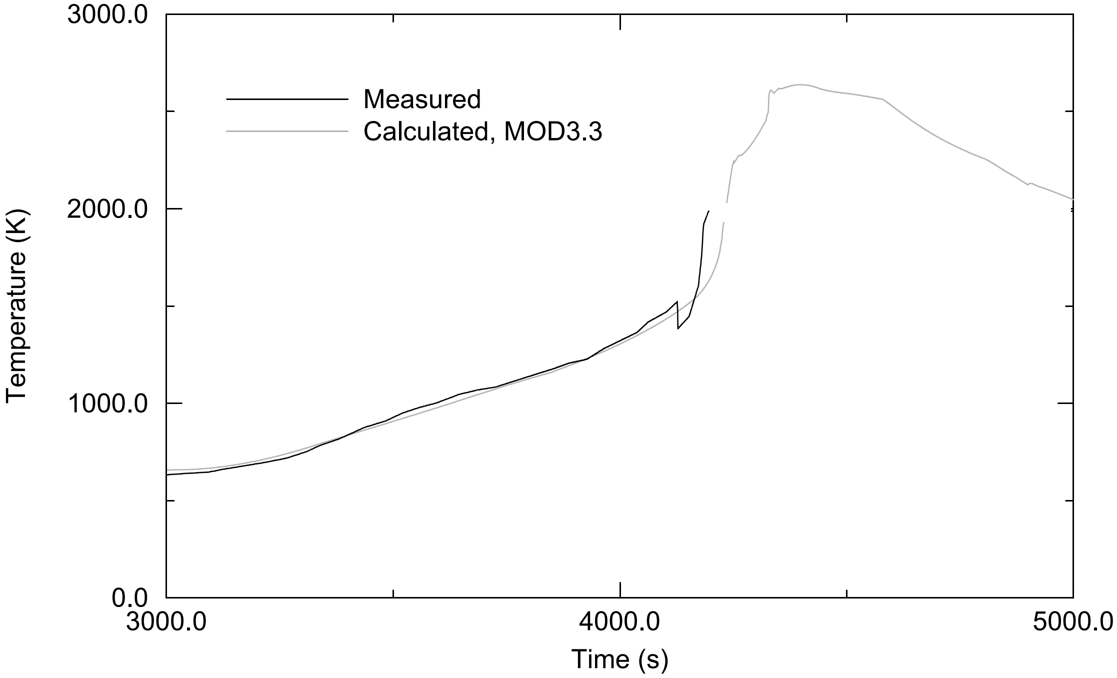

Figure A4-5. Calculated and measured temperatures of unheated fuel at 0.75 m elevation for CORA-5 test.

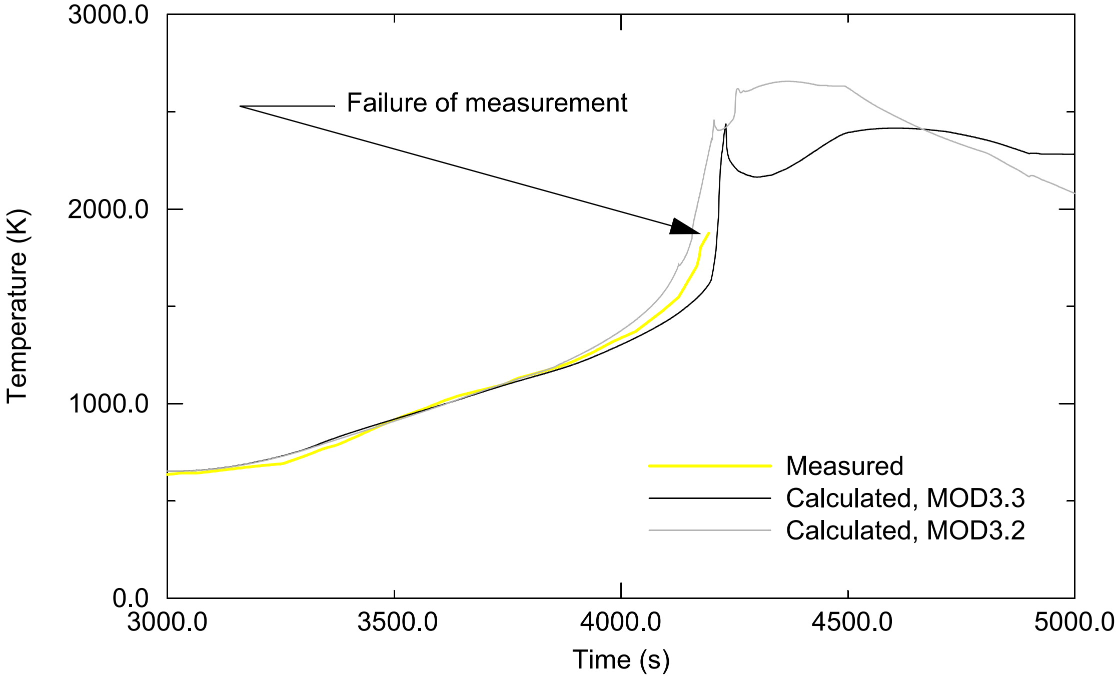

Figure A4-6. Calculated and measured temperature of unheated fuel rod at 0.85 m elevation for CORA-5 test.

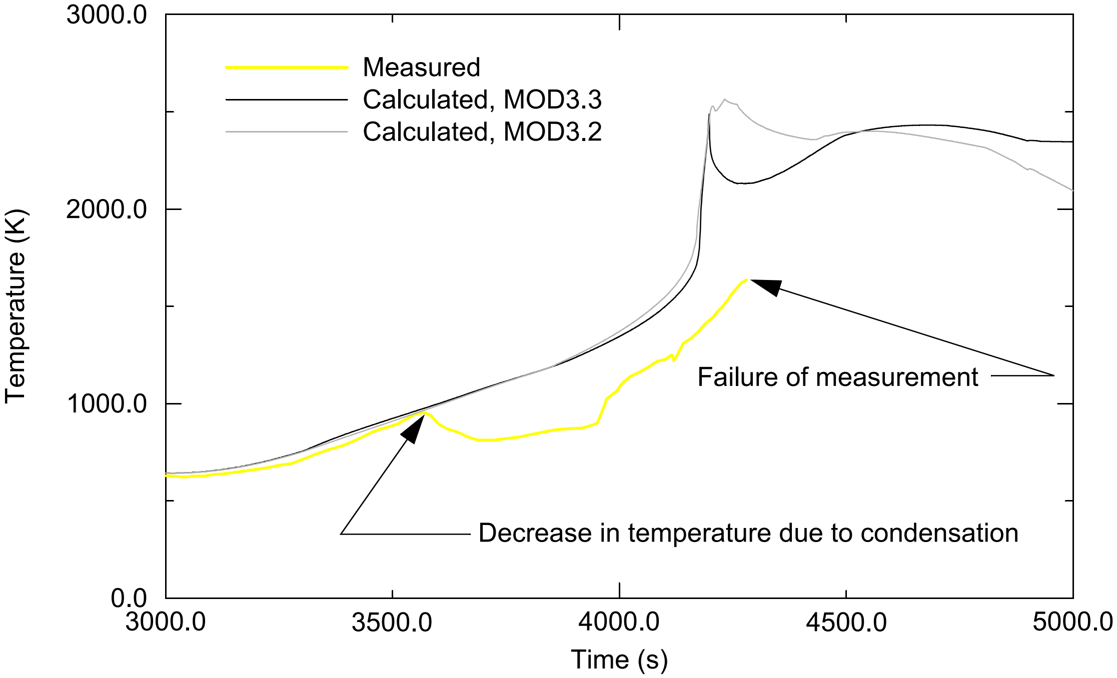

Figure A4-7. Calculated and measured temperature of unheated fuel rod at 0.95 m elevation for CORA-5 test.

0.45 m, respectively. MOD3.2 calculated the primary blockage to be located at the elevation of 0.20 m. The discrepancy between calculated and measured elevations of blockage may be due to the calculated behavior of the test fuel assembly not accounting for condensation occurring above the test fuel assembly and the reflux caused by the condensation. MOD3.2 calculated a higher location of blockage than MOD3.3 because it does not have a model for calculating the re-slumping of cladding that has slumped and frozen.

In summary, this problem showed that the integral diffusion model in MOD3.3 correctly calculates the heatup of fuel rods due to oxidation. The MOD3.3 calculated rate of fuel rod heatup were generally in good agreement with the measured rate of heatup. MOD3.3 calculated about 25% more hydrogen production than MOD3.2. MOD3.3 may overpredict the distance of slumping of melted fuel rod cladding.

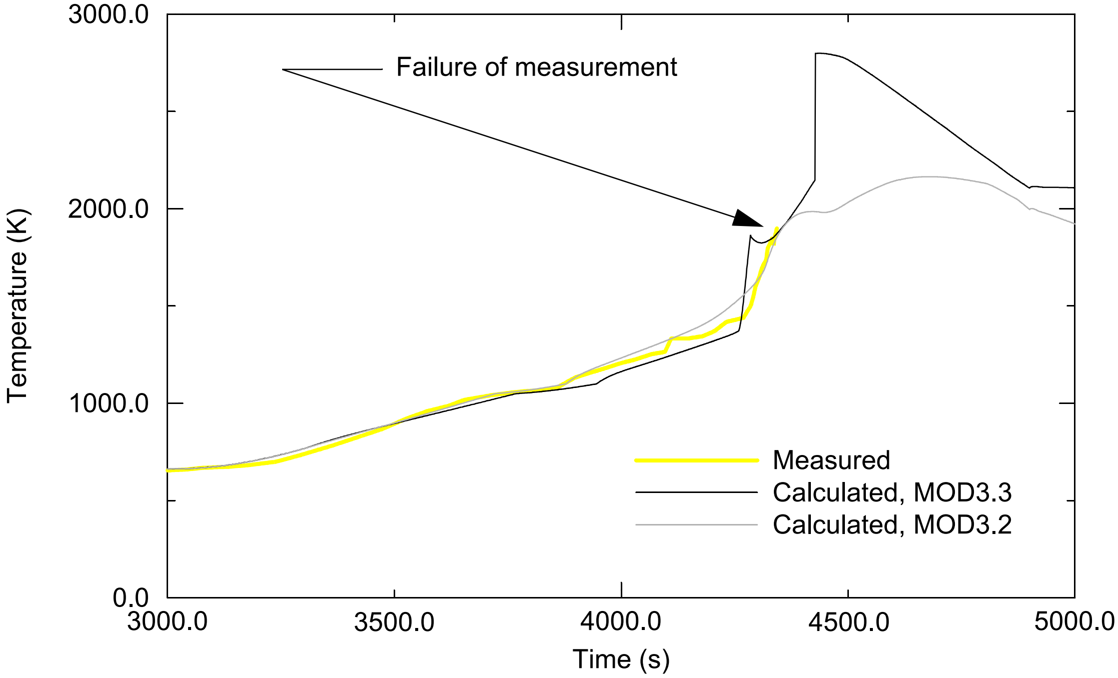

Figure A4-8. Calculated and measured temperature of control rod at 0.55 m elevation for CORA-5 test.

A4.5 Assessment Using the CORA-7 Test

A4.5.1 Description of the CORA-7 Experimental Bundle and Test

CORA-7 was the first of two large bundle experiments performed in the CORA test facility. The utilization of the larger bundle resulted in smaller radial heat losses. The 56 rod CORA-7 bundle, Figure A4-9, contained 32 electrically heated simulator rods, 19 fresh PWR-type fuel rods, and 5 typical PWR silver-indium-cadmium control rods. The test was conducted in three stages. During the pre-conditioning phase, the hot argon gas flowed through the bundle for 12 hours prior to establishing a thermal equilibrium in the test assembly. The transient phase of the experiment was initiated by applying power to the heater rods while the argon gas flow continued. Five minutes (300 s) after the initiation of power, superheated steam was mixed with the flowing argon and power was linearly increased. Steam flow was terminated at 4,180 s. Power was applied to the bundle until the desired maximum temperature of 2,100 K was attained. At 4195 s, power to the heater rods was then terminated and the bundle cooled gradually. Due to smaller radial heat losses, the time needed to reach the maximum desired temperature was considerably less than for the small bundle tests. Bundle temperatures were monitored and recorded by numerous thermocouples attached to components in the test bundle, heated and unheated fuel rods, control rods, the insulating shroud, and the high temperature shield. The damage progression in the bundle during the test was viewed on video displays. Steam and argon mass flow rates, system pressure, fuel rod pressure and hydrogen production were also measured during the test.

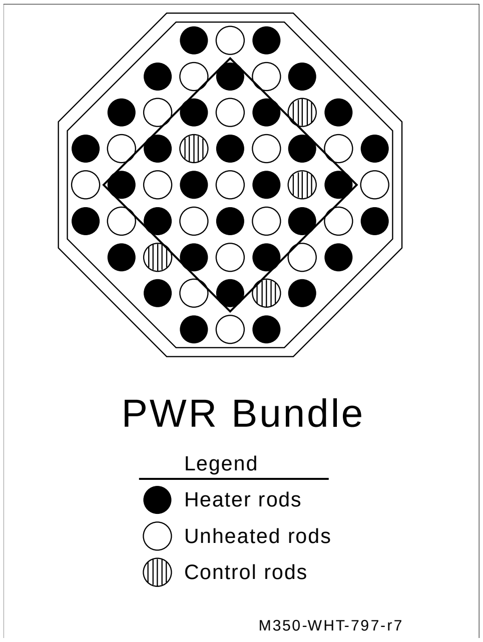

Figure A4-9. CORA-7 large bundle cross-section.

A4.5.2 Assessment Results

The MOD3.3 calculated temperature behavior of the test fuel assembly was in good agreement with its measured temperature behavior. The MOD3.3 calculated and measured temperature histories of an unheated fuel rod near the center of the test fuel assembly at several different elevations are shown in Figure A4-10 through Figure A4-13. The elevations are referenced with respect to the bottom of the fuel rods. The MOD3.2 calculated temperature histories are also shown. In general, the temperature measurements failed after the temperature exceeded about 2000 K. Double-sided oxidation was calculated by MOD3.3 to occur in the elevation interval of 0.7 m to 1.0 m. The rate of heatup calculated by MOD3.3 at the 0.95 m elevation was somewhat more rapid than the measured temperature. This difference may be due the calculations not accounting for cooling affects at the top of the test fuel assembly. At the 0.75 m elevation, the MOD3.3 calculated rate of heatup is slightly slower than the measured rate of heatup. The rapid increase in temperature at the 0.55 m elevation in the period of 4220 s to 4230 s was calculated by MOD3.3 to be partly due to hot material from above slumping into that location and partly due to oxidation. During this 10 s period, the cladding at this location was calculated to increase in temperature from 1520 K to 1970 K. The maximum temperature of the test assembly was calculated to be 2650 K. Overall, the calculated and measured rates of heatup of the test fuel assembly were in general agreement

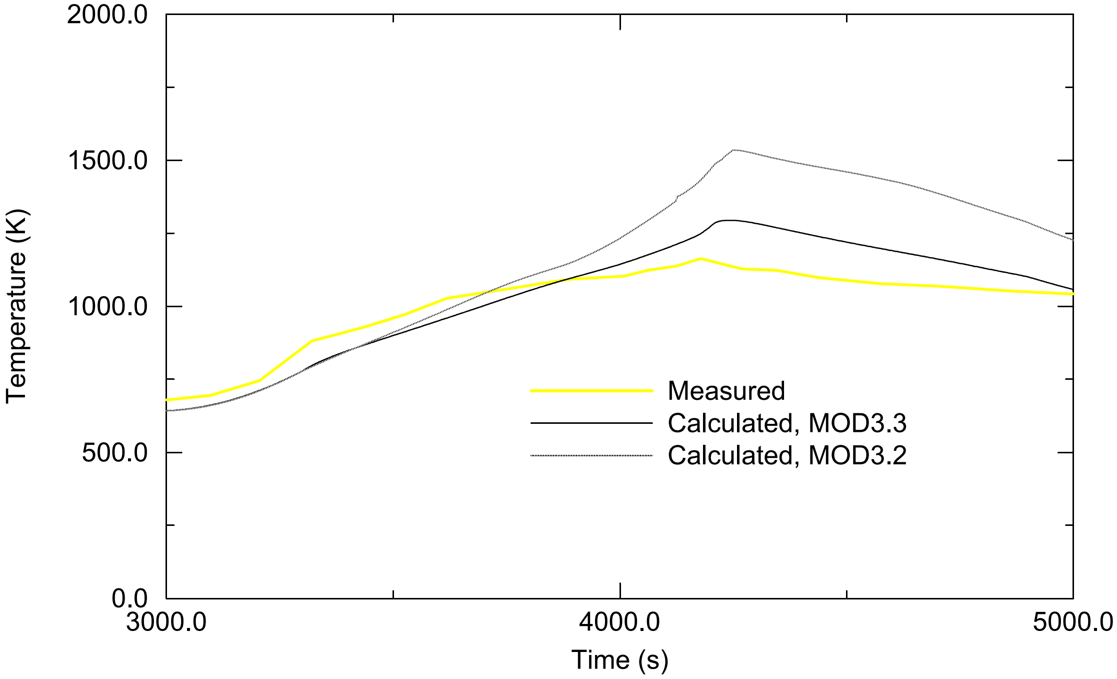

Figure A4-10. Calculated and measured temperature at the 0.35 m elevation for CORA-7 test.

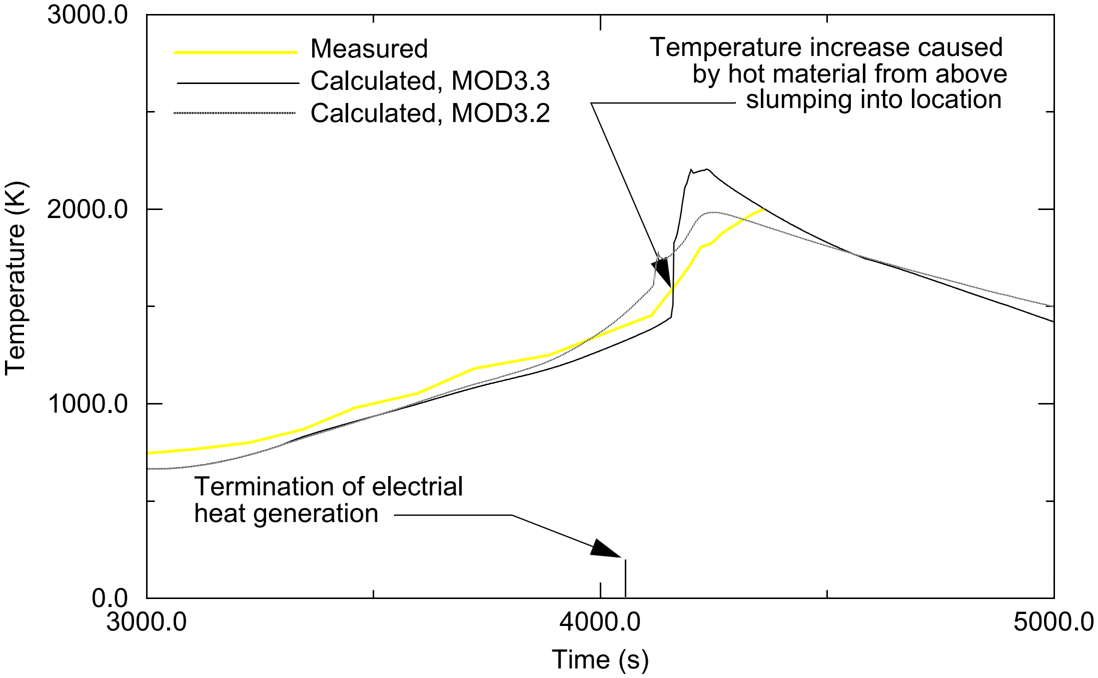

Figure A4-11. Calculated and measured temperature at 0.55 m elevation for CORA-7 test.

The MOD3.3 calculated location of the blockage caused by meltdown of the fuel rods was in fairly good agreement with the measured location of blockage. Both the PIE and the calculations indicated that

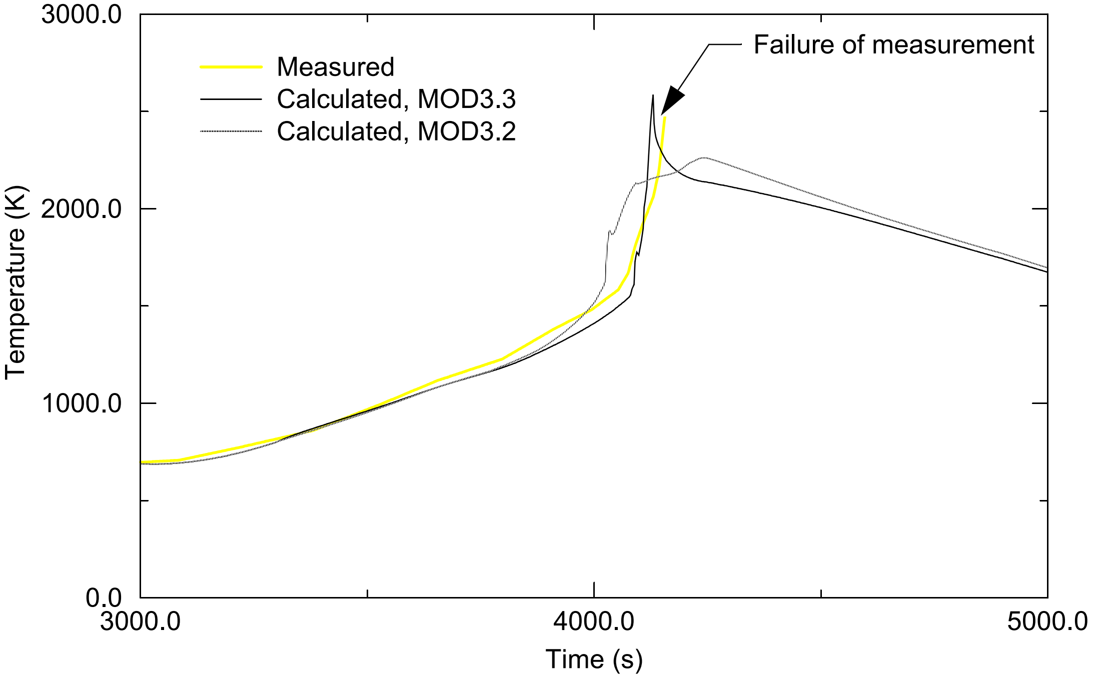

Figure A4-12. Calculated and measured temperature at 0.75 m elevation for CORA-7 test.

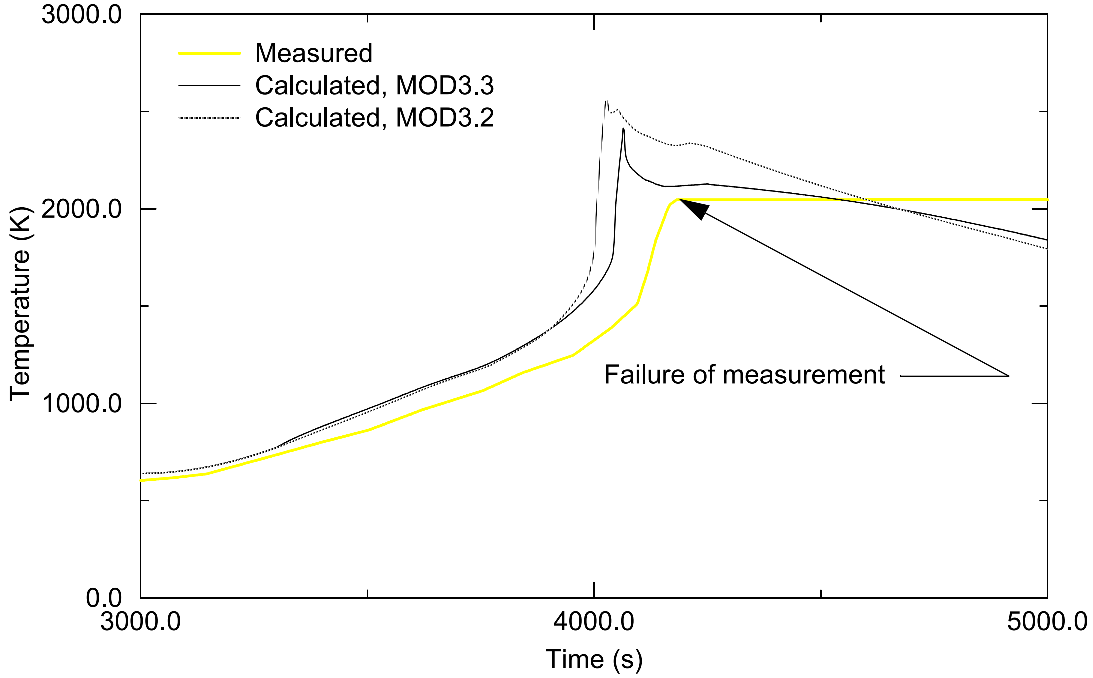

Figure A4-13. Calculated and measured temperature at 0.95 m elevation for CORA-7 test.

the meltdown and the blockage resulting from meltdown were limited in extent. The location of blockage was determined from the PIE to be in the elevation interval of 0.35 m to 0.50 m. MOD3.3 calculated the blockage to be in the elevation interval of 0.50 m to 0.60 m. In the elevation interval of 0.5 m to 0.6 m, MOD3.3 calculated that 49% of the pre-blockage coolant space was filled with slumped material. MOD3.2 calculated the blockage to be in the elevation interval of 0.70 m to 0.91 m, which was significantly higher than the PIE indicated location of blockage. The improvement in the MOD3.3 calculation with respect to the MOD3.2 calculation is due to MOD3.3 having a model for the re-slumping of slumped fuel rod material that froze and then re-melted, while MOD3.2 does not have such a model.

The hydrogen production calculated by MOD3.3 was in fairly good agreement with the measured hydrogen production. The calculated cumulative production in hydrogen is shown in Figure A4-14. Most of the hydrogen was calculated to be produced in the period of 3800 s to 4250 s. Intense oxidation was calculated to occur for about 50 s after the termination of electrical heat generation in the test fuel assembly. The total hydrogen production was calculated by MOD3.3 to be 80 g. MOD3.2 calculated a total hydrogen production of 79 g. The total hydrogen production was measured to be 114 g. The measured hydrogen production includes hydrogen produced by oxidation of the 0.4 m long extension of fuel rod and simulator Zircaloy cladding above the heated length of the test fuel assembly. Thus, the hydrogen produced in the heated portion of the test fuel assembly was somewhat less than 114 g. Since the calculations represented only the heated portion of the test fuel assembly, the MOD3.3 and measured hydrogen production are in fairly good agreement.

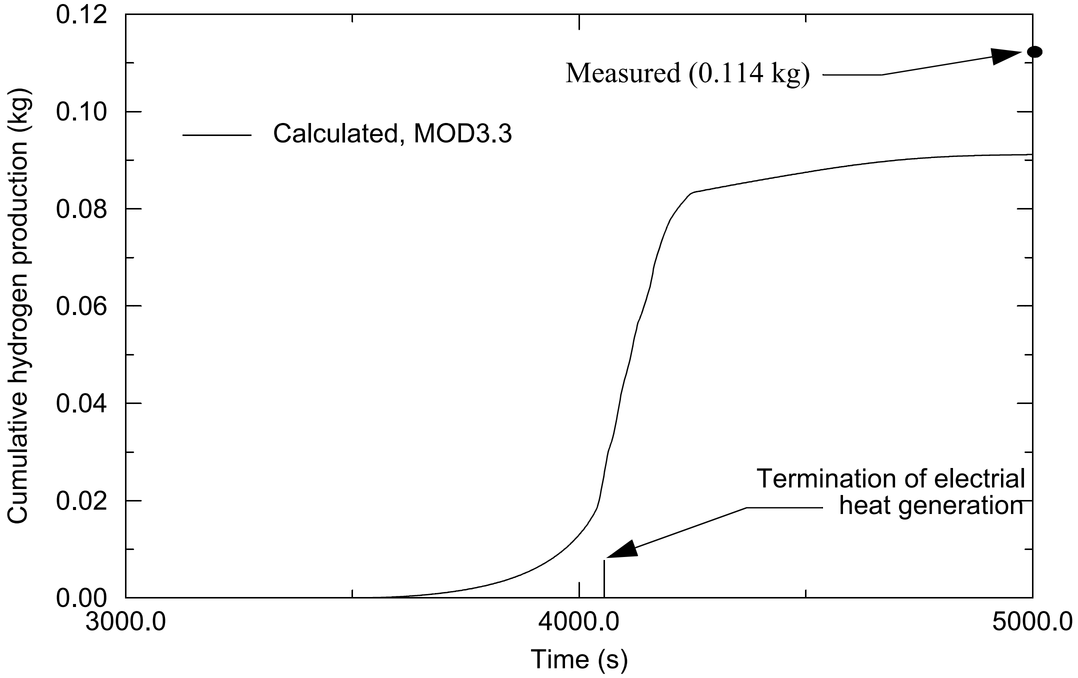

Figure A4-14. Calculated cumulative hydrogen production for CORA-7 test.

In summary, the MOD3.3 calculated behavior of the test fuel assembly is in good agreement with the measured behavior. The calculated heatup and meltdown of the test fuel assembly are in general agreement with the measurements of these aspects of the behavior of the test fuel assembly. The calculation of meltdown of the fuel assembly was improved by the addition to SCDP/RELAP5 of a model to calculate the re-slumping of slumped fuel rod material that froze and then re-melted. The heatup of the lower part of a fuel assembly was calculated to be accelerated by the slumping of hot material from above. After accounting for hydrogen production from oxidation of the parts of the test fuel assembly above its heated portion, the calculated and measured hydrogen production are estimated to be in fairly good agreement.

A4.6 Assessment Using the CORA-13 Test

In the CORA-13 experiment, a PWR fuel bundle was heated to the point of severe damage and then was quenched. The experiment was used to define International Standard Problem 31. The configuration of the CORA-13 bundle is shown in Figure A4-2. Viewing windows were cut in the insulating shroud at three elevations, 390, 590, and 790 mm. The dimensions of these windows were 30 x 40 mm. The high temperature shield was represented by a second SCDAP shroud component. The use of a second shroud to represent the high temperature shield results in the calculation of radiation heat transfer from the outer surface of the flow shroud to the inner surface of the high temperature shield. Beginning at 4,869 s, the test bundle was reflooded by raising the quench tank at a rate of 0.01 m/s.

The MOD3.3 calculated temperature behavior of the test fuel assembly was in good agreement with its measured temperature behavior. The MOD3.3 calculated and measured temperature histories of an unheated fuel rod near the center of the test fuel assembly are shown in Figures A4-15 through A4-17 for the elevations of 0.35 m. 0.55 m, and 0.75 m, respectively. The elevations are referenced with respect to the bottom of the fuel rods. The MOD3.2 calculated temperature histories are also shown. In general, the temperature measurements failed after the temperature exceeded about 2000 K. At the 0.35 m elevation, MOD3.3 calculated a small increase in temperature at the beginning of reflood. At the 0.55 m elevation, the MOD3.3 calculated temperature in the period of from 4100 s to 4300 s, when the temperature increased from 1250 K to 2400 K, was influenced by contact with hot slumped material. The unevenness in the measured curve during this period may also be due to the affect of slumping material. At this elevation, MOD3.3 calculated the temperature to increase from 1750 K to 2500 K during the reflood period. At the 0.75 m elevation, the MOD3.3 calculated temperature and the measured temperature are in excellent agreement. Double-sided oxidation was calculated by MOD3.3 to occur at this location and at all locations in the elevation interval of 0.7 m to 1.0 m. The maximum temperature of the test assembly was calculated to be 2650 K. Overall, the calculated and measured rates of heatup of the test fuel assembly are in general agreement.

The calculated axial distribution in oxidation of the cladding of the test fuel rods was in general agreement with the axial distribution obtained from the PIE performed on the test fuel assembly. The measured and the MOD3.3 and MOD3.2 calculated axial distributions in the fraction of the fuel rod cladding oxidized are tabulated in Table A4-1. The elevations in the table without any data are due to measurements not being obtained at that elevation. Double-sided oxidation of the fuel rod cladding was calculated to occur in the elevation interval of 0.7 m to 1.0 m. The PIE results showed almost 100% oxidation of the cladding of the test rods in the elevation interval of 0.4 m to 0.8 m. MOD3.3 calculated almost 100% oxidation of the cladding in the interval of 0.1 m to 0.7 m. MOD3.2 underpredicted significantly the extent of oxidation in the interval of 0.4 m to 0.8 m, while MOD3.3 overpredicted the

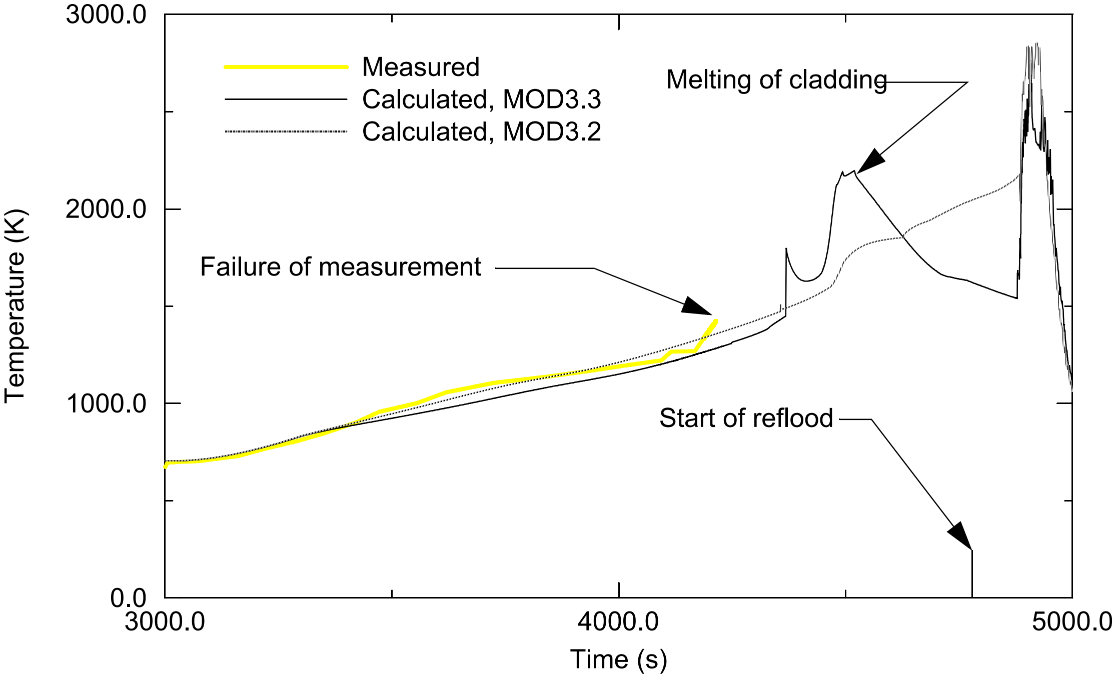

Figure A4-15. Calculated and measured temperatures of unheated fuel rod at elevation of 0.35 m for CORA-13 test.

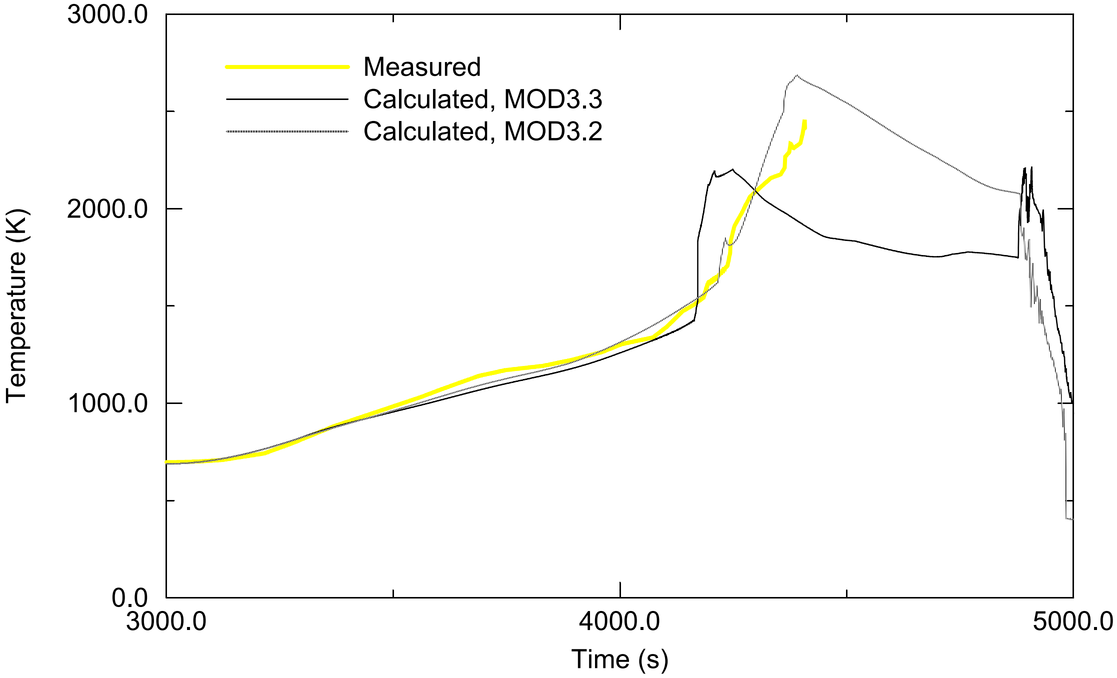

Figure A4-16. Calculated and measured temperatures of unheated fuel rod at elevation of 0.55 m for CORA-13 test.

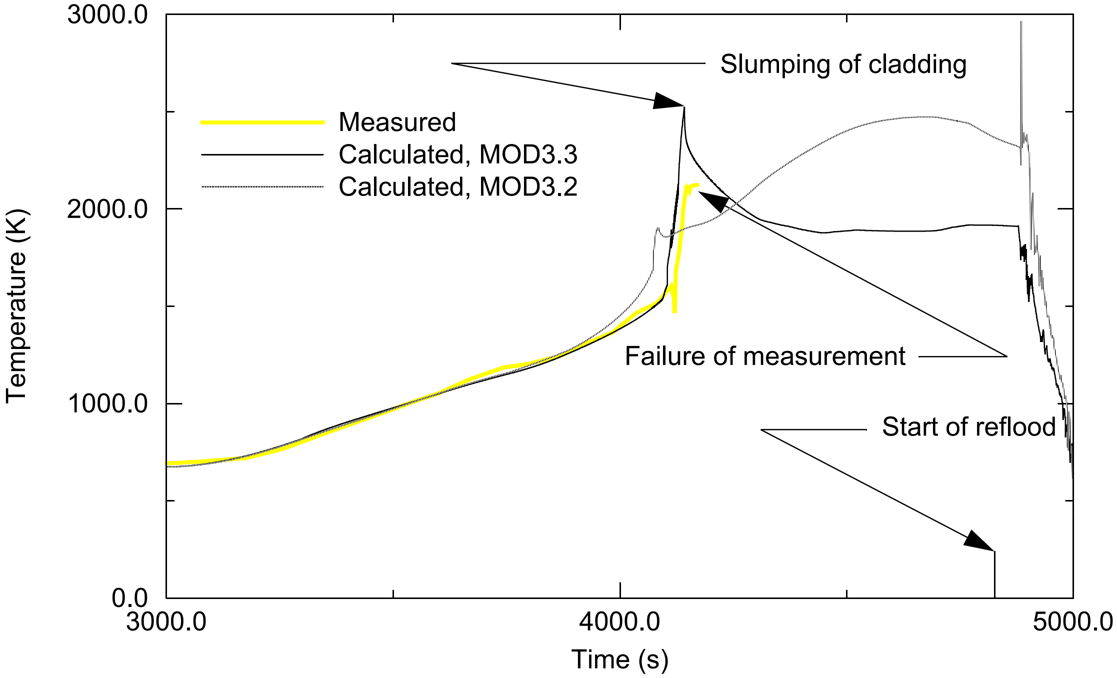

Figure A4-17. Calculated and measured temperatures of unheated fuel rods at elevation of 0.75 m for CORA-13 test.

extent of oxidation in the elevation interval of 0.1 m to 0.4 m. The overprediction of the extent of oxidation in this interval of elevation may be due to an incomplete modeling of the boundary conditions at the bottom of the test fuel bundle and the cooling affect of these boundary conditions. Since cladding meltdown has an influence on the axial distribution in oxidation, the calculated locations of cladding slumping and blockages are also shown in Table A4-1. The blockage is defined to be the fraction of pre-blockage coolant space filled with slumped material. The PIE indicated a significant blockage due to meltdown in the interval of elevation from 0.4 m to 0.5 m and minor blockages in the elevation interval of 0.1 m to 0.3 m. The location and extent of blockage calculated by MOD3.3 is in good agreement with the test results. The location of blockage calculated by MOD3.2 is significantly higher than the measured location of blockage. The improvement by MOD3.3 in the calculation of the location of blockage is due to the model added to MOD3.3 to calculate re-slumping of previously frozen slumped material.

Table A4-1. Calculated and measured axial distributions in oxidation and meltdown for CORA-13 test.

Elevation	**Fraction cladding oxidized**			**Fraction blockage due to meltdown/ slumping from location (yes or no)**		
(m)	**MOD3.3**	**MOD3.2**	**Measured**	**MOD3.3**	**MOD3.2**	**Measured**
0.05	0.03	0.21	0.0	0.02/no	0.0/no	0.0/no
0.15	1.00	0.17	0.0	0.0/no	0.0/no	0.15/no
0.25	1.00	0.43	0.07	0.02/no	0.0/no	0.15/no
0.35	1.00	0.70	0.60	0.0/no	0.0/no	0.0/no
0.45	0.64	0.10	1.00	0.40/no	0.0/no	0.43/no
0.55	1.00	0.16	1.00	0.0/yes	0.0/no	0.0/yes
0.65	1.00	0.36	1.00	0.0/no	0.0/no	0.0/yes
0.75	0.30	0.20	1.00	0.0/yes	0.5/no	0.0/yes
0.85	0.30	0.43	< 1.0	0.0/yes	0.0/yes	0.0/yes
0.95	0.34	0.40	-	0.0/yes	0.0/yes	0.0/yes

The MOD3.3 calculated hydrogen production was in good agreement with the measured hydrogen production. The measured cumulative hydrogen production from the start of the experiment to the start of reflood was 126 g. The measured hydrogen production during the reflood period of the experiment was 84 g, with the total cumulative hydrogen production of 210 g. Some of the produced hydrogen came from the oxidation of the cladding of the test rods that extended above the heated elevation interval of the experiment. The PIE analysis showed no metallic material left in the first 0.3 m of the test fuel rod cladding extending above heated elevation interval of the test fuel assembly.[A.4-1] If the cladding in this 0.3 m elevation did not slump away, then oxidation of this portion of the test fuel assembly produced 49 g of hydrogen and the oxidation of the heated portion of the test fuel assembly produced 161 g. Assuming the hydrogen production above the heated portion was of the test fuel assembly was divided between pre-reflood and reflood like the overall hydrogen production, then the amount of hydrogen production before reflood in the heated portion of the test fuel assembly is estimated to be 97 g. MOD3.3 and MOD3.2 calculated the hydrogen production only in the heated portion of the test fuel assembly; the test rod cladding above the heated elevation interval was not modeled. MOD3.3 calculated a hydrogen production of 78 g for the pre-reflood period of the experiment and a total hydrogen production of 158 g.

The cumulative hydrogen production calculated by MOD3.3 is shown in Figure A4-18. The MOD3.2 hydrogen production is also shown in this figure. The MOD3.3 calculation of hydrogen production is in good agreement with the test results, while the MOD3.2 calculation overpredicted somewhat the hydrogen production in the pre-reflood period and underpredicted the hydrogen production during the reflood period.

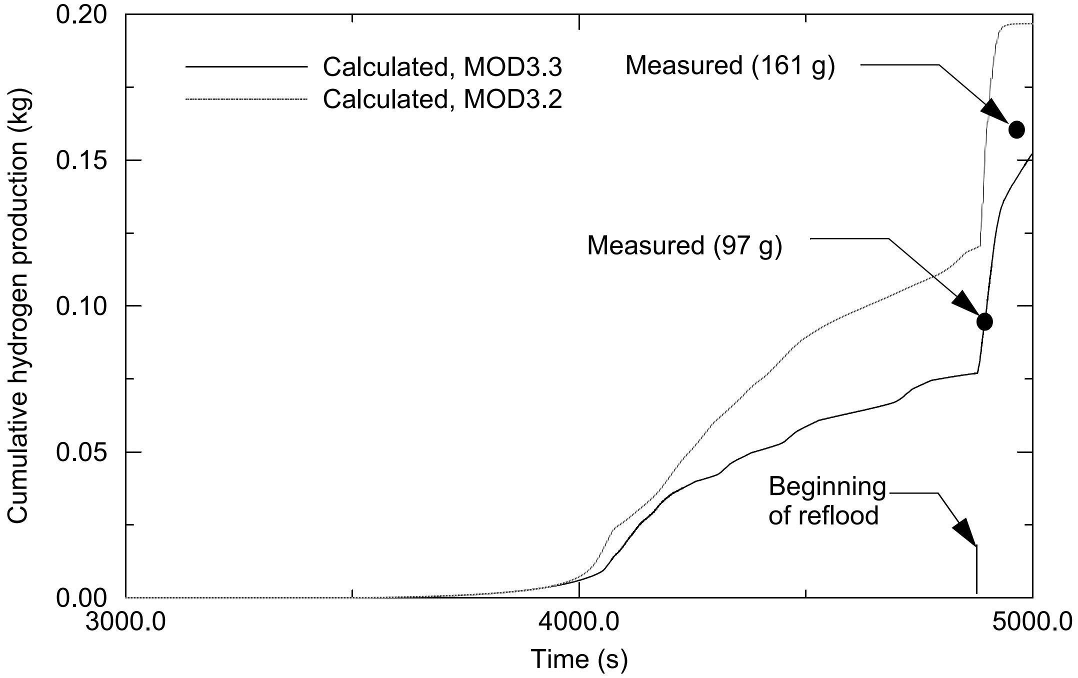

Figure A4-18. Calculated and cumulative hydrogen production for CORA-13 tests.

In summary, the MOD3.3 calculated behavior of the test fuel assembly was in good agreement with the measured behavior. The calculated transient temperature distribution in the test fuel assembly was in good agreement with the measured transient temperature distribution. The calculated meltdown of the test fuel assembly was in good agreement with the measured meltdown. Except for an overprediction of the extent of oxidation of the cladding in the bottom portion of the test fuel assembly, the calculated extent of oxidation was in good agreement with the measured extent of oxidation. The discrepancy in extent of oxidation for the bottom portion of the test fuel assembly may have been due to an incomplete modeling of the boundary conditions at the bottom of the test fuel assembly. The MOD3.3 calculated hydrogen production before reflood and during reflood were in good agreement with the measured hydrogen production. The MOD3.3 calculation of the behavior of the test fuel assembly was improved over the MOD3.2 calculation in four areas; (1) location of blockages from meltdown of the test fuel assembly, (2) axial distribution in the oxidation of the test fuel assembly, (3) hydrogen production during the reflood period of the experiment and (4) temperature history in upper part of test fuel assembly where heatup may be limited by steam strarvation. These improvements are due to the implementation into MOD3.3 of the following models; (1) model for re-slumping of previously frozen slumped cladding, (2) model for cracking of cladding during reflood, and (3) integral diffusion model for oxidation of cladding.

A4.6.1 References

A4-1. S. Hagen et al., “Results of SFD Experiment CORA-13 (OECD International Standard Problem 31),” KfK 5054, February 1993.

A4.7 Assessment Using the CORA-17 Test

CORA-17 was one of five BWR configured heating and melting tests performed in the CORA test facility at FzK and the only BWR configuration test bundle cooled by quenching the hot degraded test bundle after termination of power to the heater rods. The test procedure for the BWR configured tests was similar to that used for the PWR tests with the following exceptions. The rate of steam and argon flow through the bundle during the test was considerably less than those for the PWR tests. Steam flow was maintained at a rate of approximately 2.5 g/s and the argon flow was 8 g/s.

A4.7.1 Nodalization

The input model for the CORA-17 test used two SCDAP shroud components to model the test train, one shroud component modeled the insulated flow shroud surrounding the test bundle, the other shroud component modeled the high temperature shield. The RELAP5 nodalization of the BWR bundle, as shown in Figure A4-19, used three RELAP5 flow channels. One flow channel contained the fuel rods, heated and

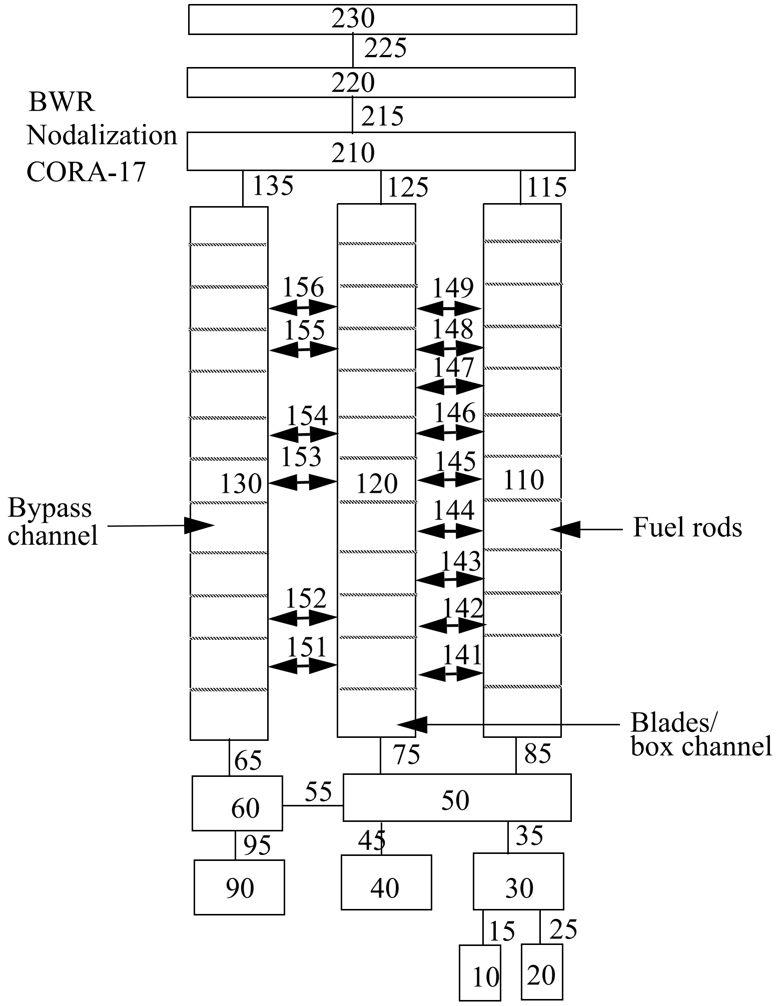
230
225
220
215
210
BWR
Nodalization
CORA-17
135
125
115
156
155
154
153
152
151
149
148
147
146
145
144
143
142
141
130
120
110
Bypass
channel
Fuel rods
Blades/
box channel
65
75
85
60
55
50
95
45
35
90
40
30
15
25
10
20

Figure A4-19. RELAP5 nodalization of the CORA-17 experiment.

unheated, a second flow channel contained the BWR control blade and channel box, and the third flow channel represented the bypass. Each flow channel was modeled using a single RELAP5 pipe component divided into 12 equal volumes. The lower ten volumes were connected with the heated zone of the test bundle, the upper two volumes were connected with the volumes immediately above the top of the heated simulator rods that contained molybdenum and copper electrodes. The CORA-17 BWR bundle was modeled using five SCDAP components. Figure A4-20 shows a cross-section of the CORA-17 test bundle. The bundle components were; Component 1 to represent the unheated fuel rods, Component 2 to represent the simulator rods, Component 3 to represent the control blade and channel box, Component 4 to represent the insulating shroud, and Component 5 to represent the high temperature shield.

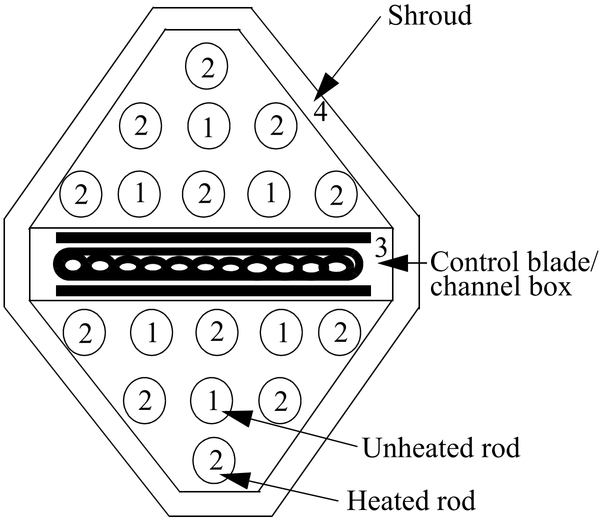

Figure A4-20. CORA-17 bundle cross-section.

A4.7.2 Boundary Conditions

The test was performed using a system pressure of 2.2 MPa (1.2 Bar overpressure). Argon flow was maintained at 8 g/s, until reflood. As the quench tank moved upward in the bundle, argon flow was terminated. Once the quench tank surrounded the test bundle, argon flow at a rate 8 g/s was resumed. Steam at a rate of 2 g/s was mixed with the argon gas beginning at 100 s after the test. One hundred seconds after the termination of electrical power to the heater rods, at 4,800 s, steam flow was stopped. Power to the heater rods was ramped up over a period of 1,500 s to 22 KW and held at 22 KW for 300 s. The maximum power was somewhat less than the 27 KW power needed in CORA-13 test to reach maximum desired temperature. At 5,080 s, reflood of the test bundle began by raising the quench tank at a rate of 0.01 m/s.

A4.7.3 Comparison of Calculations and Measurements

The results of the CORA-17 test were applied to the assessment of MOD3.3 by comparing calculated temperature histories for several different elevations in the test fuel assembly with the measured temperature histories at those elevations. The calculated and measured hydrogen production were also compared.The results of the CORA-17 test were applied to the assessment of MOD3.3 by comparing calculated temperature histories for several different elevations in the test fuel assembly with the measured temperature histories at those elevations. The calculated and measured hydrogen production were also compared.

The MOD3.3 calculated temperature behavior of the test fuel assembly was in good agreement with the measured temperature behavior. The MOD3.3 calculated and measured temperature histories of an unheated fuel rod are shown in Figures A4-21 and A4-22 for the elevations of 0.55 m and 0.75 m, respectively. The elevations are referenced with respect to the bottom of the fuel rods. The MOD3.2 calculated temperature histories are also shown. The temperature measurement for the 0.55 m elevation beyond the time of 4500 s has a high degree of uncertainty. The MOD3.3 calculated and measured temperatures are in good agreement. The comparison of calculated and measured temperatures indicates that MOD3.3 calculates more accurately than MOD3.2 the reduction in rate of heatup caused by cladding melting and steam starvation of oxidation. The calculated and measured temperatures of the channel box for the elevation of 0.55 m are compared in Figure A4-23. The calculated and measured temperatures of the control blade for the elevation of 0.55 m are compared in Figure A4-24. The calculated and measured temperatures of these components of the test fuel assembly are also in good agreement.

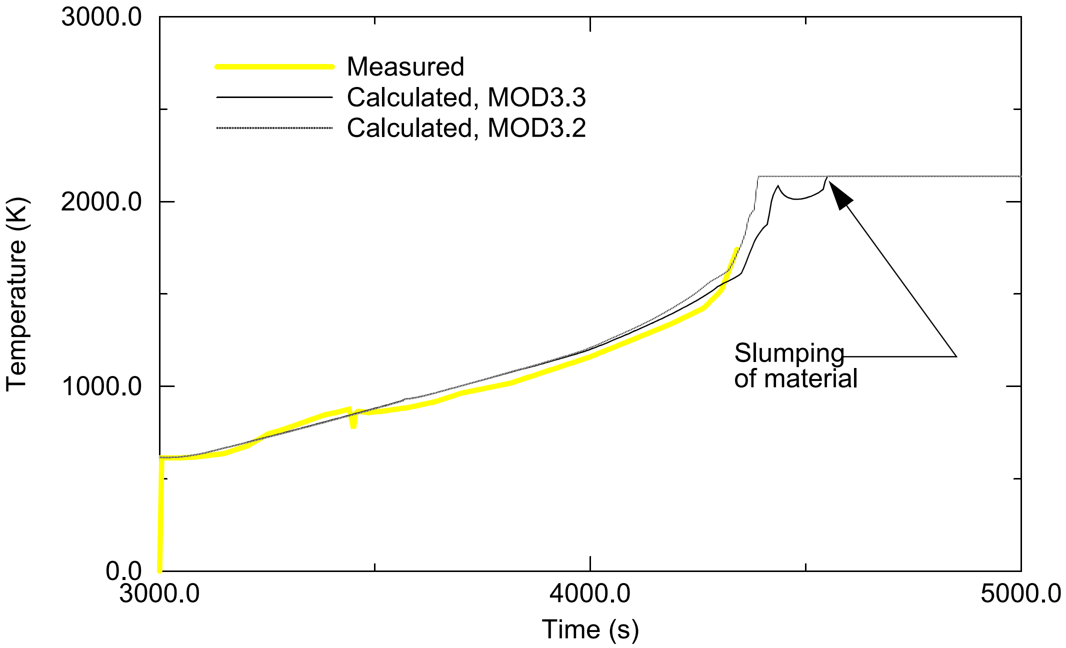

Figure A4-21. Calculated and measured temperatures of channel box at 0.55 m for CORA-17 test.

The calculated hydrogen production was about 9% less than the measured hydrogen production. The calculated and measured hydrogen production were 132 g and 150 g, respectively.

In summary, this test problem confirms that the integral diffusion model in MOD3.3 correctly calculates the heatup of fuel rods due to oxidation. The MOD3.3 calculated rates of heatup of the fuel rods in the test fuel assembly were in good agreement with the measured rates of heatup. The calculated heatup of the channel box and control blade were also in good agreement with the measured heatup. The calculated hydrogen production was 9% less than the measured hydrogen production.

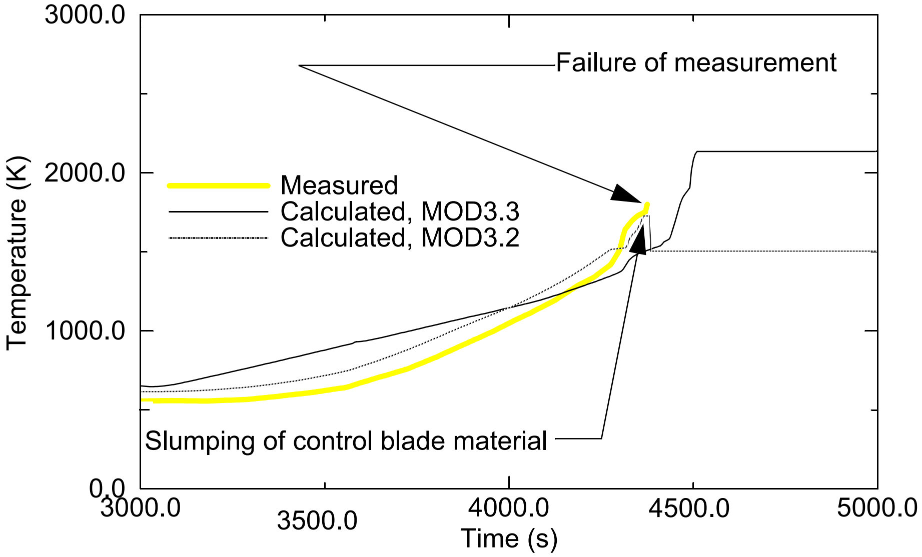

Figure A4-22. Calculated and measured temperatures of control blade at 0.55 m for CORA-17 test.

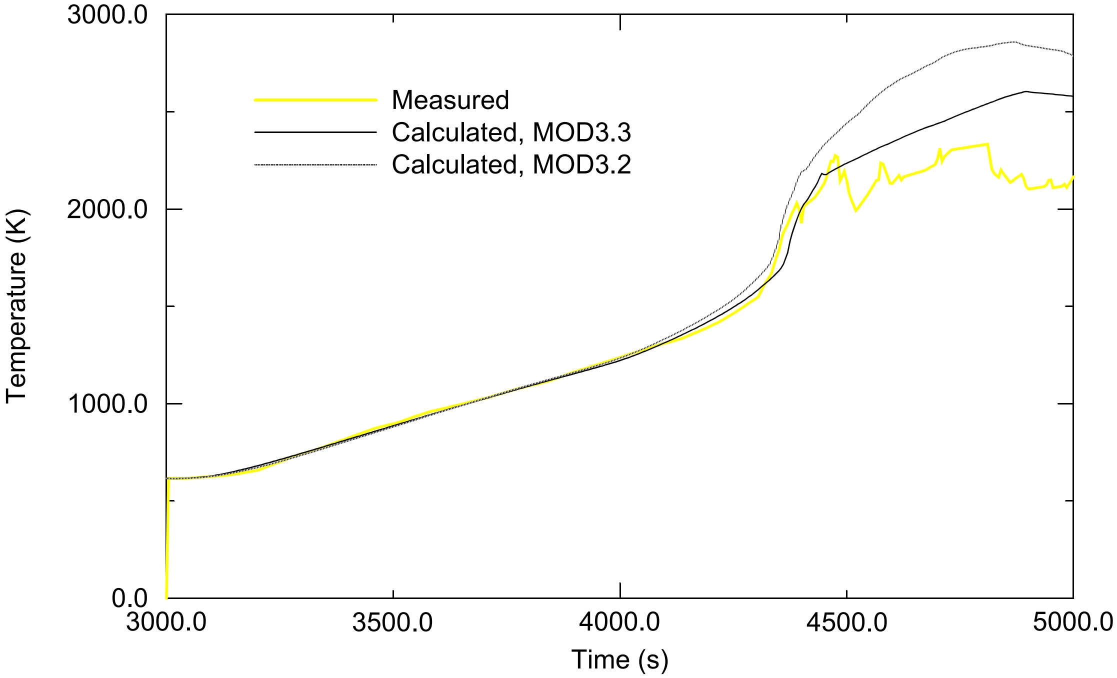

Figure A4-23. Calculated and measured temperatures of unheated fuel rod at elevation of 0.55 m for CORA-17 test.

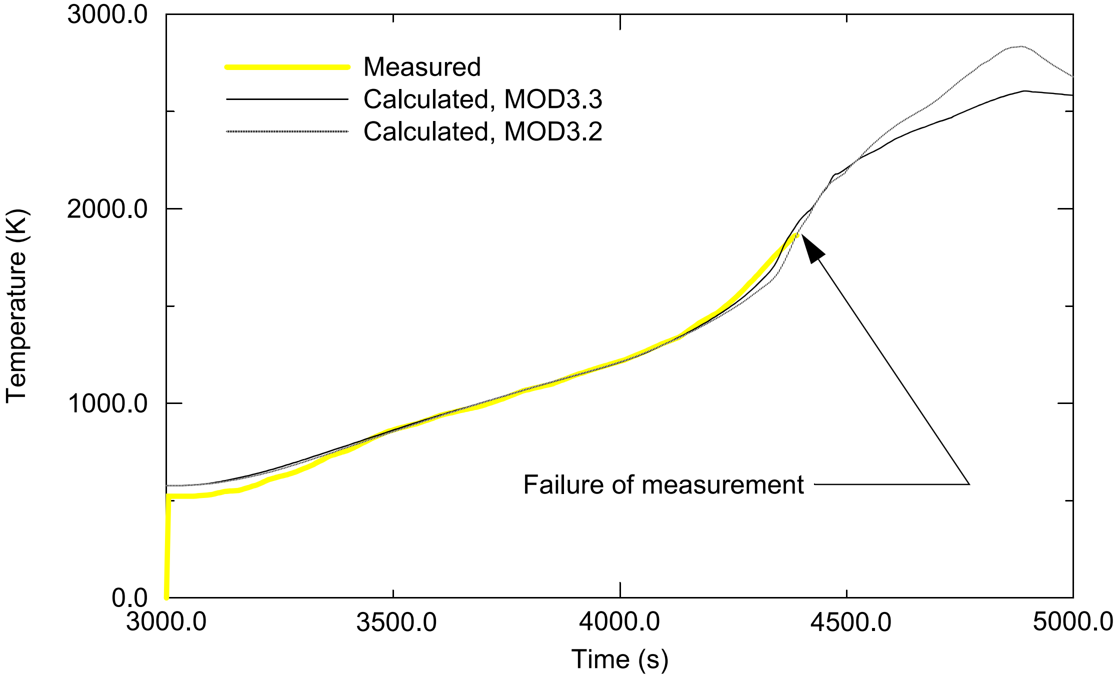

Figure A4-24. Calculated and measured temperatures of unheated rod at elevation of 0.75 m for CORA-17 test.

A5. PHEBUS B9+ TEST

The PHEBUS B9+ experiment, the fifth in a series of six severe fuel damage experiments using fresh PWR fuel rods, was performed by the Institut de Protection et de Surete Nucleaire at the PHEBUS test facility, Cadarache, France, in January of 1989.[A5-1] The purpose of this test was to study phenomena occurring during a PWR severe core damage accident. The test specifically focused on the following areas; (1) cladding oxidation, (2) the mechanical behavior of cladding which had an oxide layer of variable thicknesses and contained molten zircaloy, (3) the dissolution of UO_2 and ZrO_2 by molten zircaloy, and (4) core degradation and melt progression phenomena. This experiment was designated as International Standard Problem 28 by OECD/CSNI. The experiment had well defined thermal-hydraulic and boundary conditions and has been used to the assess the ICARE Severe Accident computer code for nearly all aspects of core degradation. The phenomena that can be assessed and verified by the PHEBUS experiments are (1) zircaloy oxidation and the resulting hydrogen production, (2) cladding mechanical damage, (3) material interactions occurring between zircaloy and fuel pellets, zircaloy and inconel spacer grids, fuel rod cladding and Ag-In-Cd absorber material, and (4) the relocation of molten material and blockages formed in the core region.

The test bundle for the PHEBUS B9+ experiment consisted of 2l fresh UO_2 fuel rods in a 12.6 mm square pitch matrix. The bundle configuration was a 5 x 5 array with the corners removed. The fuel rods were held in position by two 38 mm in height inconel grid spacers located at the 0.138 and 0.661 m elevations. Each fuel rod had a stack of fuel pellets that was 0.8 m in height. The fuel bundle was surrounded by a multilayer insulating shroud consisting of a 0.6 mm thick zircaloy liner, a 21.25 mm thick porous zirconia insulating layer, and a 1 mm thick layer of high density zirconia. The shrouded bundle was inserted in an 8 mm thick stainless steel tube. The stainless steel shrouded bundle was then inserted in the driver core of the test reactor. The driver core supplied nuclear power to heat the test bundle. Thermal-hydraulic conditions close to what would be expected in a commercial reactor core in a beyond design based accident were replicated during the test. Numerous temperature, flow, pressure, and hydrogen measurements were recorded during the test.

The PHEBUS B9+ test was conducted in three separate phases; (1) oxidizing, (2) heatup in pure helium, and (3) a slow cool down. During the oxidizing phase, superheated steam flowed through the bundle at a rate of 2.0 g/s. The steam flow continued until the zircaloy cladding at the mid-plane of the bundle was completely oxidized. The second phase of the experiment was initiated when bundle temperatures exceeded 1,800 K. The flow of steam was replaced with helium at a flow rate of 0.5 g/s. The purpose of this phase of the experiment was to produce fuel dissolution by pure zircaloy under steam-starved conditions. The nuclear power was increased in steps over a period of 5,500 s until the desired maximum core temperature of 2,750 K was reached. The third and final phase of the experiment was a slow cool down. The cool down was accomplished through step reductions in the nuclear power as helium continued to flow through the test bundle. The purpose of the slow cool down was to assure that the bundle geometry at the maximum test temperature was not changed during the cooling phase.

A5.1 Bundle Nodalization

The PHEBUS B9+ test section was modeled using a single thermal-hydraulic channel to represent the test facility. Two time-dependent volumes connected by time-dependent junctions to a single mixing volume were used to control the steam and helium flow through the bundle. The subcooled water source on the outside of the shroud was also modeled using RELAP5 volumes. The RELAP5 system nodalization is shown in Figure A5-1. The test bundle was represented by four SCDAP components; (1) a central fuel rod, (2) a middle ring of fuel rods consisting of 8 fuel rods, (3) an outer ring of fuel rods consisting of 12 fresh fuel rods, and (4) the shroud. Figure A5-2, a bundle cross-section, shows the SCDAP representation of the test bundle. The 0.8 m high active fuel zone containing the fuel rods and insulating shroud was divided into 10 axial nodes each 0.08 m high. Six radial nodes were used at each axial node to represent the fuel rods radially and 16 radial nodes were used at each axial node to represent the insulating shroud. All geometric data used to model the test facility were taken from the test specification report.

A5.2 Boundary and Initial Conditions

The inlet fluid temperature was defined to be 528 K, and the system pressure was defined to be 1.2 MPa. The steam flow rate during the oxidizing phase of the experiment was 2.0 g/s and the helium flow rate during the fuel dissolution stage of the experiment was 0.5 g/s. The helium flow replaced the steam flow at 8370 s. A mass flow rate of 10 kg/s was defined for the subcooled water used to cool the outside of the shroud. The thermal conductivity of the insulating shroud as supplied by the PHEBUS organizers was input as a user defined material property. The calculations were started at 640 s, one second before the initiation of nuclear power to the test bundle, and continued until fuel dissolution was predicted to occur.

A5.3 Comparison of Calculations and Measurements

The MOD3.3 calculated temperature behavior of the test fuel assembly was in good agreement with its measured temperature for the upper part of the test fuel assembly and overpredicted the temperature for the lower part of the test fuel assembly. The MOD3.3 calculated and measured temperature histories are shown in Figure A5-3 through Figure A5-6 for the elevations of 0.2 m. 0.4 m, and 0.6 m, and 0.7 m, respectively. The elevations are referenced with respect to the bottom of the fuel rods. The MOD3.2 calculated temperature histories are also shown. Before the stop of steam flow and the start of helium flow at 8370 s, the calculated and measured temperatures are in good agreement at all elevations. After the stop of steam flow, the calculated temperature overpredicts the measured temperature at the elevations of 0.2 m and 0.4 m. Since MOD3.3 calculated a complete cessation of oxidation after 8380 s due to the absence of steam in the test fuel assembly, this overprediction of the temperature increase is not due to the calculation of oxidation after 8380 s. The nuclear heat generation and the oxidation heat generation in the test fuel assembly as a function of time are shown in Figure A5-7. The overprediction in calculated temperature may be due to some combination of the following factors; (1) retaining too much insulation capability in the flow shroud after the input of helium into the test fuel assembly, (2) underprediction of heat loss by conduction from the blockage area to the part of the flow shroud in contact with the blockage, (3)

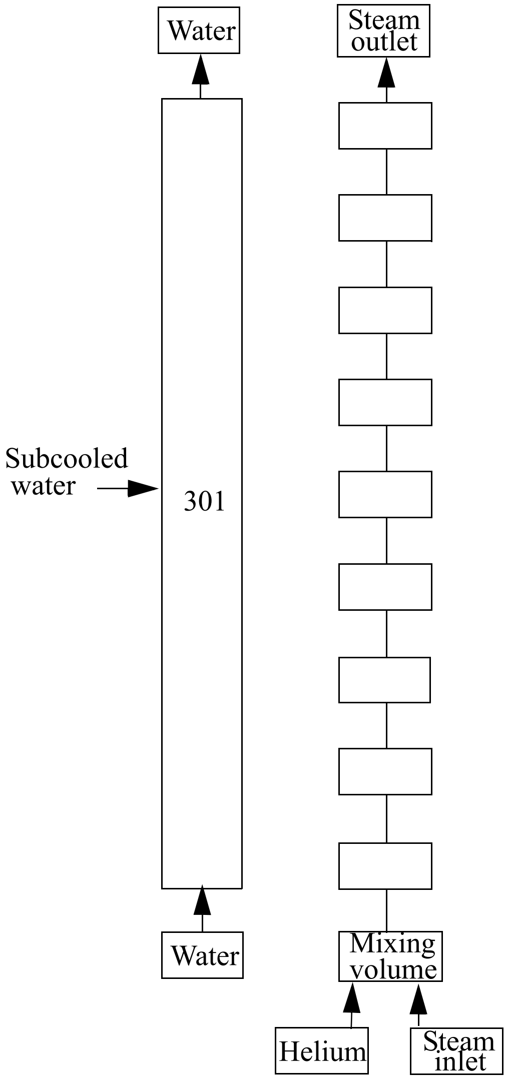

Figure A5-1. RELAP5 nodalization used for the PHEBUS B9+ experiment.

underprediction of the cooling of the test fuel assembly by the helium flowing through the test fuel assembly, and (4) incorrect power history after 8380 s. After 9370 s, the calculated temperature at the elevation of 0.2 m and 0.4 is calculated to increase significantly due to the increase in nuclear heat generation in the test fuel assembly.

The calculated axial distribution in oxidation of the cladding of the test fuel rods was in general agreement with the axial distribution obtained from the PIE performed on the test fuel assembly. The measured and the MOD3.3 and MOD3.2 calculated axial distributions in the fraction of the fuel rod cladding oxidized are tabulated in Table A5-1. The locations in the table without any entry are due to data

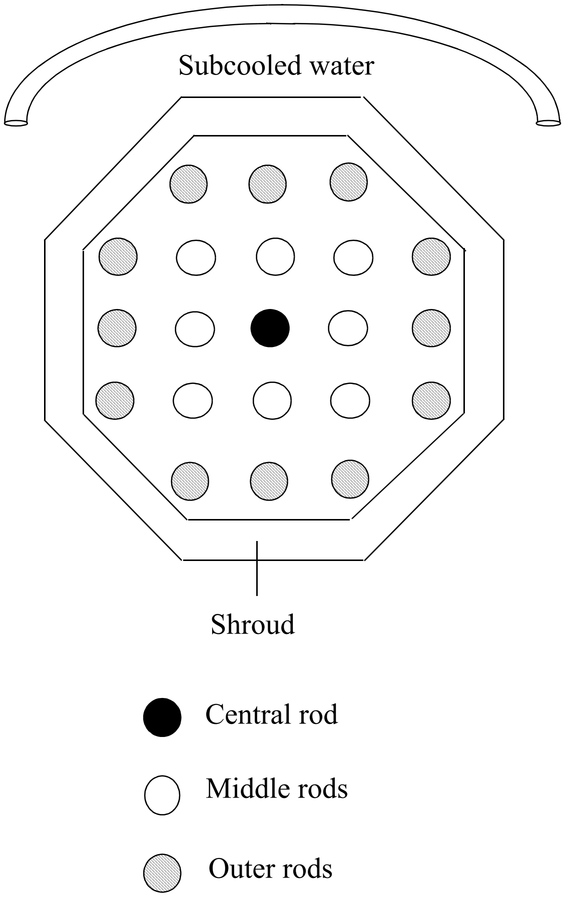

Figure A5-2. SCDAP representation of the fuel bundle.

not being available for that location. Double-sided oxidation of the fuel rod cladding was calculated to occur in the elevation interval of 0.56 m to 0.64 m. The PIE results showed almost 100% oxidation of the cladding of the test rods in the elevation interval of 0.48 m to 0.76 m. MOD3.3 calculated almost 100% oxidation of the cladding in this same interval of elevation. MOD3.3 overpredicted somewhat the extent of oxidation of the bottom part of the test fuel assembly and MOD3.2 underpredicted the extent of oxidation at the top of the test fuel assembly. The MOD3.3 overprediction of the extent of oxidation in the bottom part of the test fuel assembly may be due to an incomplete modeling of the boundary conditions at the bottom of the test fuel bundle and the cooling affect of these boundary conditions. Since cladding meltdown has an influence on the axial distribution in oxidation, the calculated locations of cladding slumping and blockages are also shown in Table A5-1. The blockage is defined to be the fraction of pre-blockage coolant space filled with slumped material. The PIE indicated a significant blockage due to meltdown in the interval of elevation from 0.2 m to 0.3 m and minor blockages in the elevation interval of 0.0 m to 0.2 m. The location and extent of blockage calculated by MOD3.3 is in good agreement with the test results. After the stop of steam flow into the test fuel assembly, MOD3.3 calculated a significant dissolution of the oxide layers on the fuel rod cladding in the elevation interval of 0.0 m to 0.40 m of the test assembly, and as a result, slumping of the metallic part of the cladding in this interval of elevation after it was heated to its melting temperature.

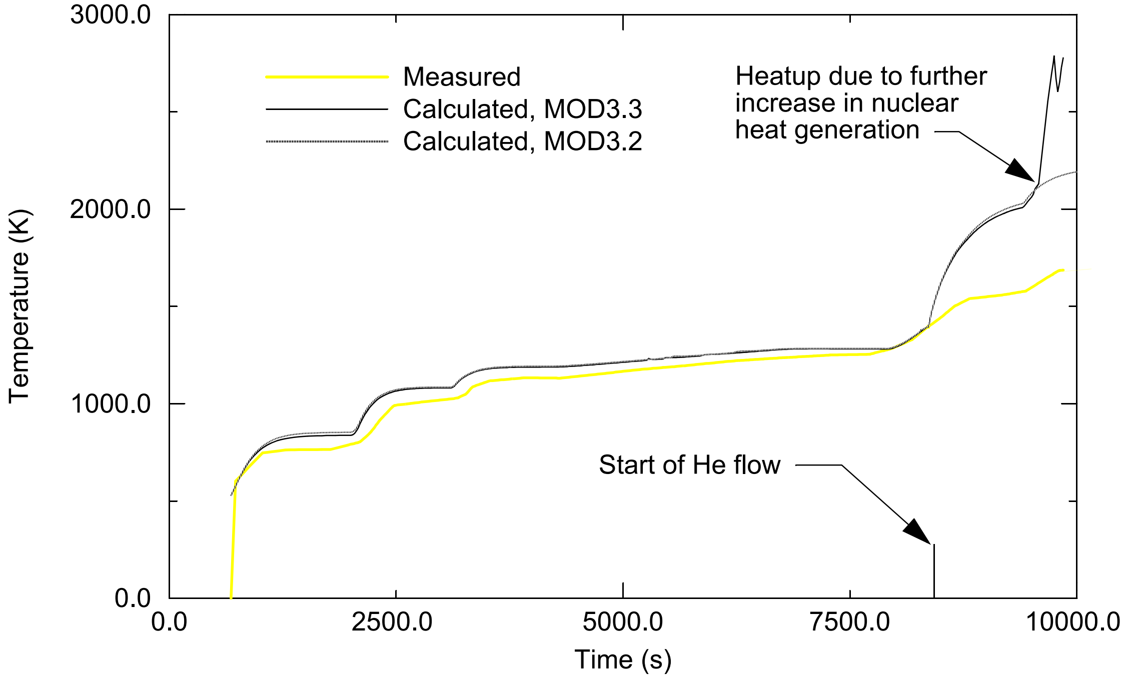

Figure A5-3. Calculated and measured cladding temperatures at 0.2 m elevation for PHEBUS B9+ test.

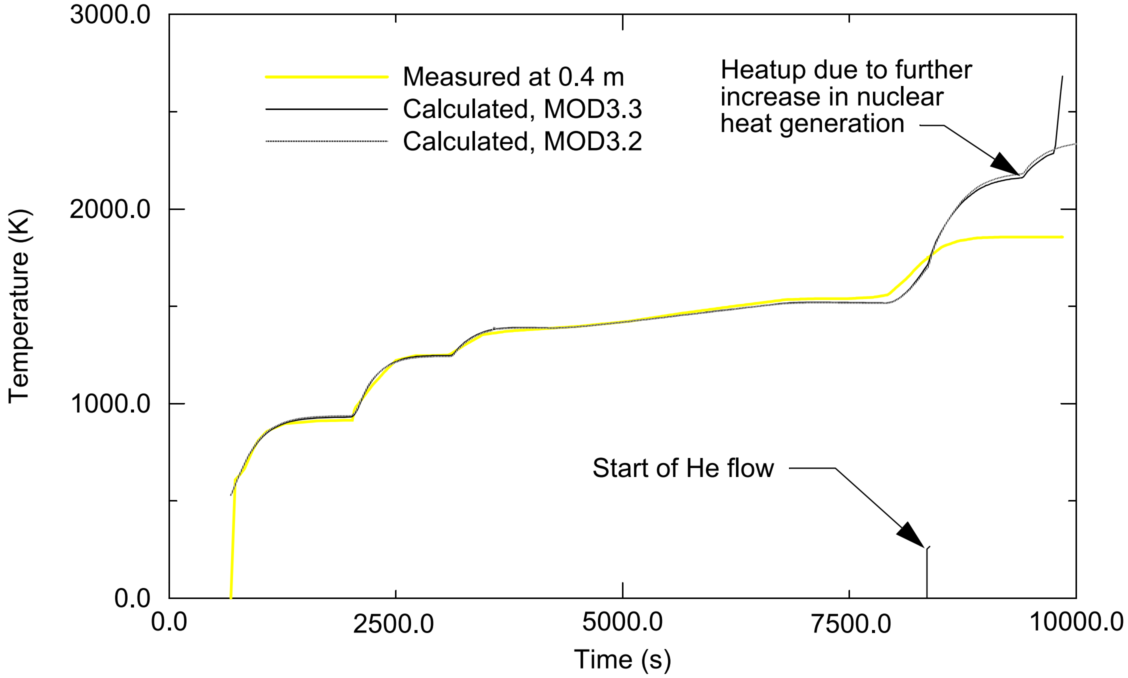

Figure A5-4. Calculated fuel temperatures at 0.4 m elevation for PHEBUS B9+ test.

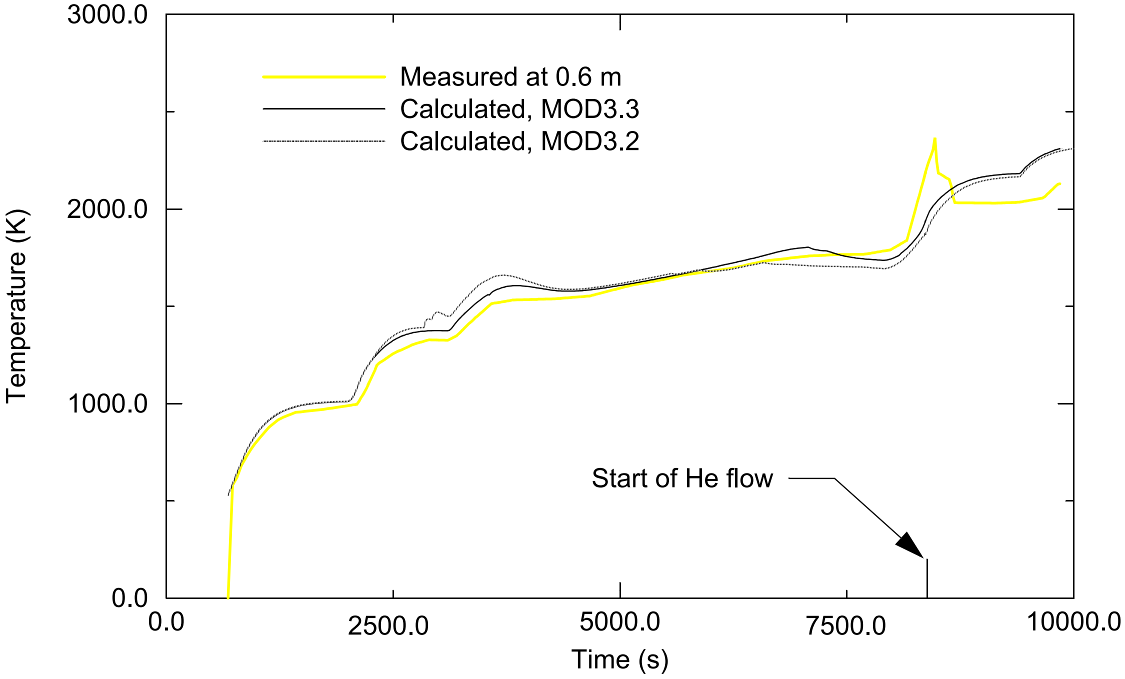

Figure A5-5. Calculated and measured fuel temperatures at 0.6 m elevation for PHEBUS B9+ test.

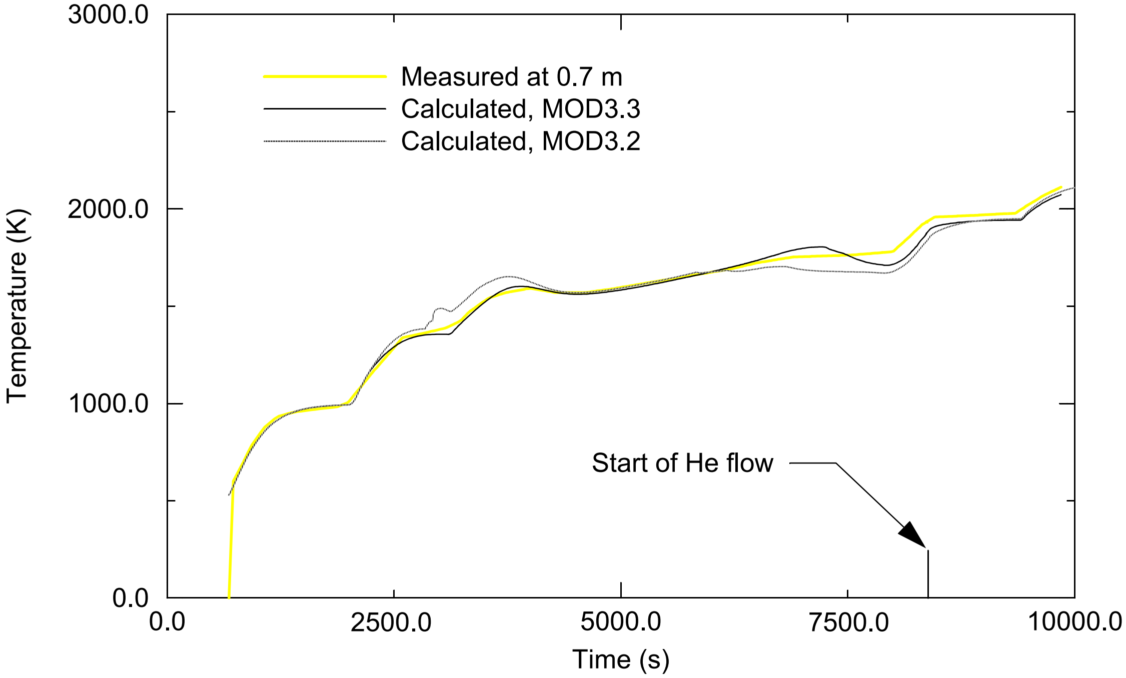

Figure A5-6. Calculated and measured cladding temperatures at 0.7 m elevation for PHEBUS B9+ test.

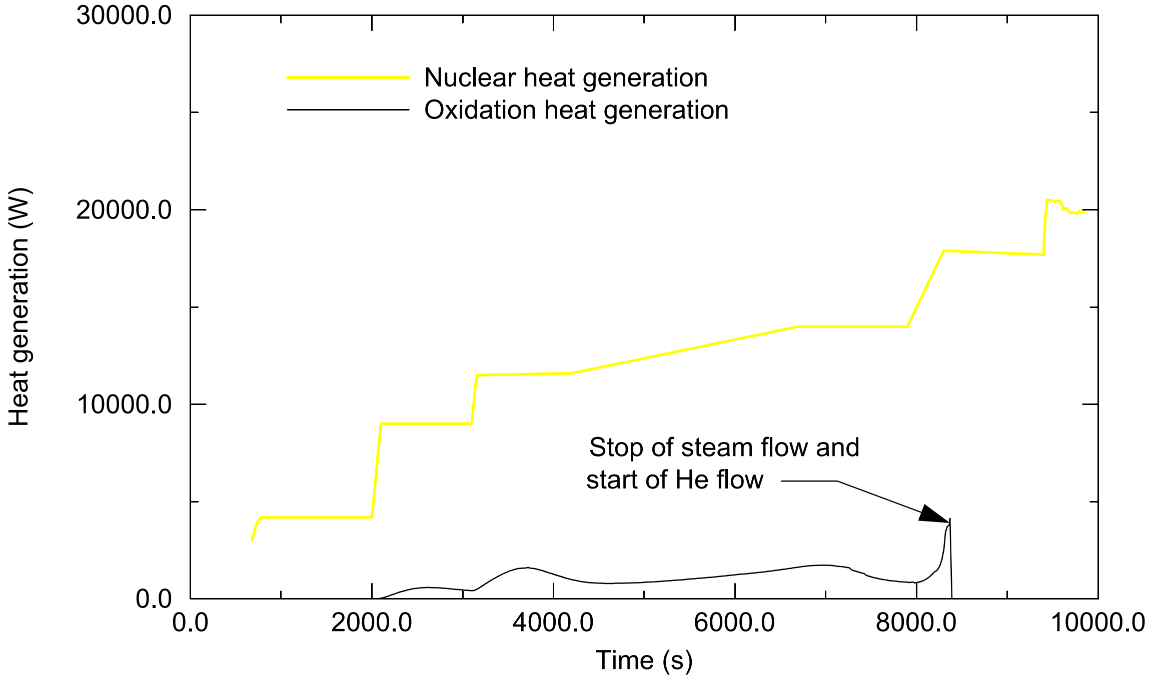

Figure A5-7. MOD3.3 calculated nuclear and oxidation heat generation histories in test fuel assembly for PHEBUS B9+ test.

Table A5-1. Comparison of calculated and measured axial distributions in oxidation and meltdown for PHEBUS B9+ test.

Elev.	Fraction cladding oxidized			Fraction blockage due to meltdown/slumping from location (yes or no)		
(m)	MOD3.3	MOD3.2	Measured	MOD3.3	MOD3.2	Measured
0.04	0.02	0.02	0.0	0.5/yes	-/yes	-
0.12	0.07	0.06	0.03	0.0/yes	-/yes	-
0.20	0.16	0.11	0.05	1.0/yes	1.0/yes	-
0.28	0.30	0.21	0.10	1.0/yes	1.0/yes	1.0/-
0.36	0.49	0.31	0.25	0.0/yes	0.0/yes	-
0.44	0.70	0.86	0.40	0.0/no	0.0/yes	-
0.52	1.00	1.00	0.70	0.0/no	0.0/yes	-
0.60	1.00	1.00	1.00	0.0/no	0.0/yes	-

Table A5-1. Comparison of calculated and measured axial distributions in oxidation and meltdown for PHEBUS B9+ test.

Elev.	Fraction cladding oxidized			Fraction blockage due to meltdown/slumping from location (yes or no)		
(m)	MOD3.3	MOD3.2	Measured	MOD3.3	MOD3.2	Measured
0.68	0.99	1.00	1.00	0.0/no	0.0/no	-
0.76	0.90	0.52	0.75	0.0/no	0.0/no	-

The MOD3.3 calculated hydrogen production was about 15% greater than the measured value. The cumulative hydrogen productions calculated by MOD3.3 and MOD3.2 are shown in Figure A5-8. The MOD3.3 and MOD3.2 cumulative hydrogen productions were 46 g and 39 g, respectively. The measured hydrogen production was 39 g. MOD3.3 calculated that no production of hydrogen occurred after the flow of steam into the test fuel assembly stopped. The overprediction of hydrogen production by MOD3.3 was due to an overprediction of the extent of oxidation of the bottom part of the test fuel assembly.

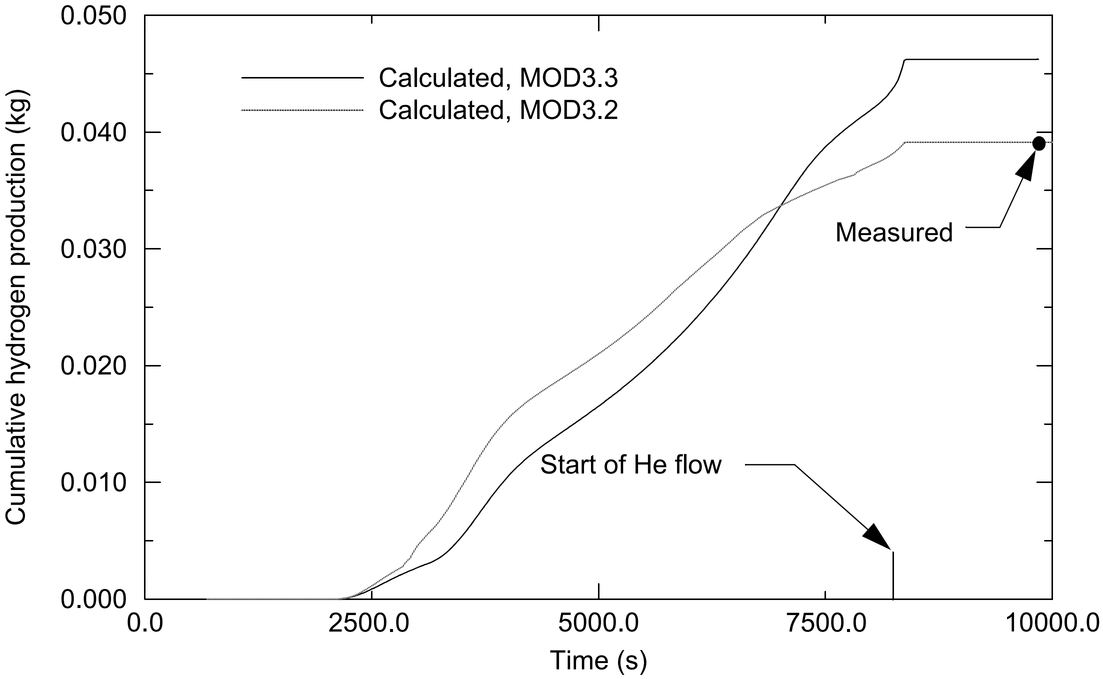

Figure A5-8. Calculated cumulative hydrogen production for PHEBUS B9+ test.

In summary, the B9+ test problem tested the capability of MOD3.3 to calculate the behavior of fuel assemblies for the condition of extreme steam starvation. For the upper half of the test fuel assembly, the extent of oxidation of the fuel rod cladding was in good agreement with the measured extent. For the bottom half of the test fuel assembly, MOD3.3 overpredicted by about a factor of two the extent of oxidation of the fuel rod cladding. MOD3.3 correctly calculated that all oxidation in the test fuel assembly stopped after the flow of steam was replaced by the flow of helium. The total hydrogen production calculated by MOD3.3 was in fairly good agreement with the measured value. MOD3.3 correctly calculated the interval of elevation at which a blockage of almost 100% occurred due to liquefaction of fuel. The code overpredicted the heatup of the lower part of the test assembly after the flow of steam was stopped. This overprediction may have been due to a degradation to the insulation capability of the shroud after the flow of helium began, but which was not taken into account in the calculations.

A5.4 Reference

A5-1. B. Adroguer et al., *Comparison Report for the OECD/CSNI International Standard Problem 28,* OECD NEA CSNI Report No. 28, December 1992.

A6. PHEBUS FPT0 TEST

A6.1 Introduction

The PHEBUS FPT0 test problem assessed the models for early phase damage progression and the modeling of the transition into late phase damage progression. The test problem is based on the PHEBUS FPT0 experiment,[A6-1] which was conducted in the PHEBUS reactor in France. This experiment was one of a few experiments that heated fuel to ceramic melting by nuclear heat generation under severe accident conditions. The heat up and damage phase of the experiment occurred through a period of 18,000 s, which is a long period of time compared with most other severe accident experiments.

A6.2 Test Description

The test bundle for the PHEBUS FPT0 experiment consisted of 20 typical PWR fuel rods and one Ag-In-Cd control rod. The cross-section of the test bundle is shown in Figure A6-1. The flow area of the test bundle was 0.002556 m^2. The rods were arranged as a 5 x 5 array with the corner rods removed. The control rod was located in the center of bundle of fuel rods. The test fuel rods had a 1.0 m high stack of fuel pellets. The fuel rods had a trace of burnup. The fuel rods had a fill gas of He at a pressure of 2.8 MPa at a temperature of 293 K. The test bundle had two spacer grids composed of Zr. One spacer grid was 0.29 m above the bottom of the fuel stack and the other was 0.81 m above the bottom of the fuel stack. The array of rods were surrounded by an insulated shroud. The insulated shroud was composed of two layers of low porosity ZrO_2. Unlike the shroud in the PBF SFD tests, the FPT0 shroud surface that faces the fuel rods did

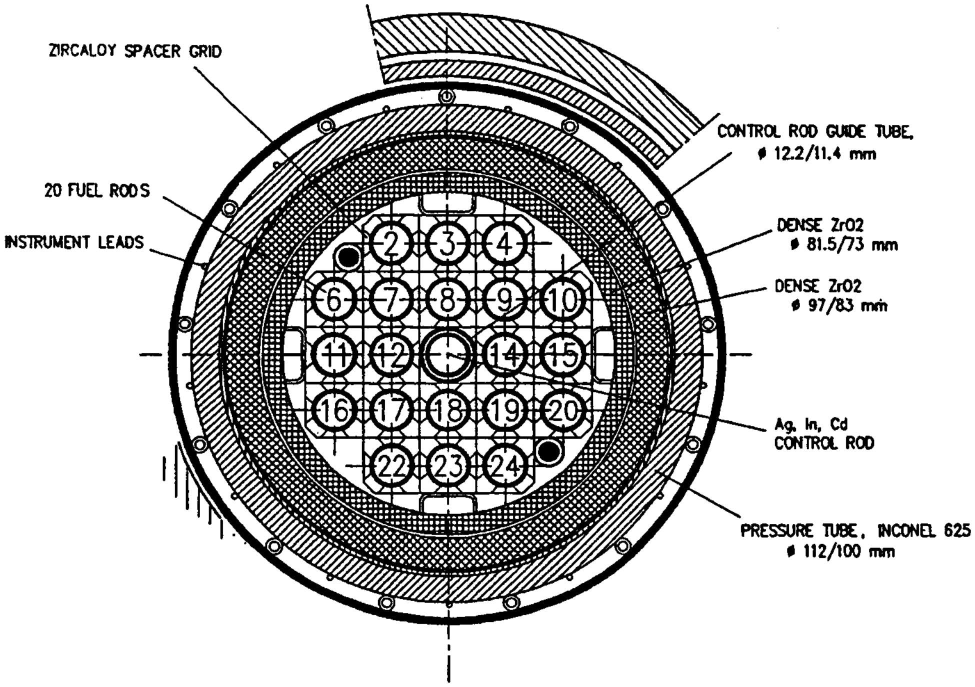
ZIRCALOY SPACER GRID
20 FUEL RODS
INSTRUMENT LEADS
CONTROL ROD GUIDE TUBE, ∅ 12.2/11.4 mm
DENSE ZrO2 ∅ 81.5/73 mm
DENSE ZrO2 ∅ 97/83 mm
Ag, In, Cd CONTROL ROD
PRESSURE TUBE, INCONEL 625 ∅ 112/100 mm
2
3
4
6
7
8
9
10
11
12
14
15
16
17
18
19
20
22
23
24

Figure A6-1. Cross-section of bundle of test rods for PHEBUS FPT0 experiment.

not have a Zr liner.The test fuel rods were cooled by steam during the heat up and damage phase of the experiment. The steam was at a pressure of 0.22 MPa. The temperature of the steam at the inlet varied from 452 to 484 K. The inlet flow rate varied from 0.5 x 10^{-3} to 3 x 10^{-3} kg/s during the heat up and damage phase of the experiment. A plot of the inlet flow rate history is shown in Figure A6-2.

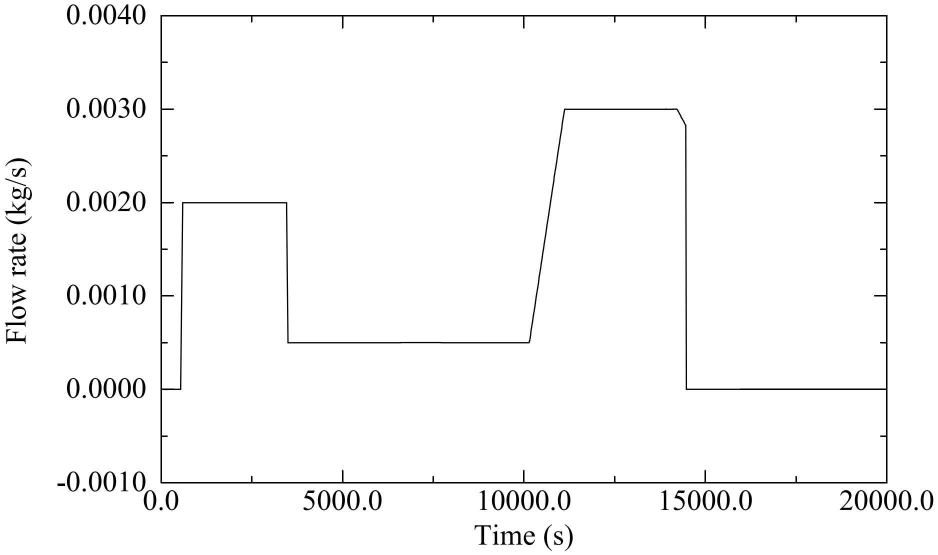

Figure A6-2. Inlet flow rate history of test bundle.

The insulated flow shroud was cooled on its outside surface by an annular coolant channel with a constant flow rate of 10 kg/s. The pressure of the coolant was 8 MPa and the inlet temperature of the coolant was 438 K. The flow area of the channel was 0.00166 m^2.

The bundle power was increased in steps during the heat up and damage phase of the experiment. The bundle power was produced by nuclear heat generation. The bundle power increased from 0 to 50.7 kW over a period of 18,000 s. The bundle power history is shown in Figure A6-3. The bundle power was rapidly decreased after reaching its maximum value of 50.7 kW.

A6.3 Nodalization of Test Fuel Assembly

The 21 test rods, insulated shroud and coolant channels were represented by the SCDAP/RELAP5 MOD3.2 model of the experiment. The input file for the model was constructed at ENEA in Italy by G. Bandini.[A6-2] A schematic of the nodalization of the test bundle, insulated shroud and flow channels is shown in Figure A6-4. The test rods were divided into three components; (1) component number 1 represented the eight inner fuel rods in the test bundle, (2) component number 2 represented the single control rod at the center of the bundle, and (3) component number 3 represented the twelve fuel rods in the outer part of the fuel bundle. The insulated shroud was represented by component number 4. The test bundle and insulated shroud were divided into eleven axial nodes with the middle nine axial nodes having a height of 0.1 m and the bottom and top axial nodes having a height of 0.05 m. The two fuel rod components had six radial nodes at each axial node; the fuel was represented by four radial nodes and the cladding by two radial nodes. The shroud was represented by nineteen radial nodes at each axial node. The

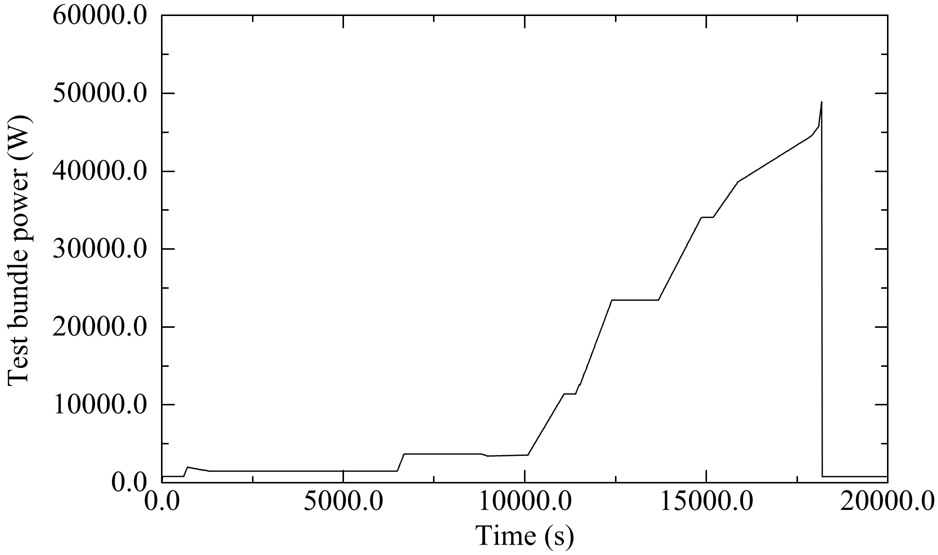

Figure A6-3. Power history of test bundle.

coolant in the test bundle and the annular flow channel next to the outside surface of the test bundle were represented by RELAP5 control volumes. Three parallel flow channels were modeled. The first flow channel represented the flow of coolant past the test rods and next to the inside surface of the insulated shroud. This flow channel was represented by the RELAP5 control volume 100 and its eleven subvolumes which corresponded in location with the eleven axial nodes of the test rods and insulated shroud. The second flow channel represented flow past a blockage in the bundle of test rods. This flow channel was represented by the RELAP5 control volume 102 and its eleven subvolumes. The third flow channel represented the annular flow channel next to the outside surface of the insulated shroud. This flow channel was represented by RELAP5 control volume 200. Crossflow was modeled between the two flow channels inside the insulated shroud. The conditions of coolant into the bundle was controlled by the RELAP5 time-dependent volume 80. The rate of flow into the bundle was controlled by RELAP5 time-dependent junction 85. The conditions of the coolant next to the outside surface of the insulated shroud was controlled by RELAP5 time-dependent volume 180 and the rate of flow of this coolant was controlled by RELAP5 time-dependent junction 185.

A6.4 Comparison of Calculations and Measurements

The results of the PHEBUS FPT0 test were applied to the assessment of MOD3.3 by comparing calculated results with measured results. First, the calculated temperature histories for three different elevations in the test fuel assembly are compared with the measured temperature histories at those elevations. Second, the calculated meltdown and axial distribution in oxidation of the test fuel assembly are described. Third, the calculated hydrogen production is compared with the measured hydrogen production.

The MOD3.3 calculated temperatures of the test fuel assembly were in good agreement with the measured temperatures for the first and latter parts of the test and overpredicted the rate of heatup during the intermediate part of the test. The calculated and measured temperatures are compared in Figure A6-5,

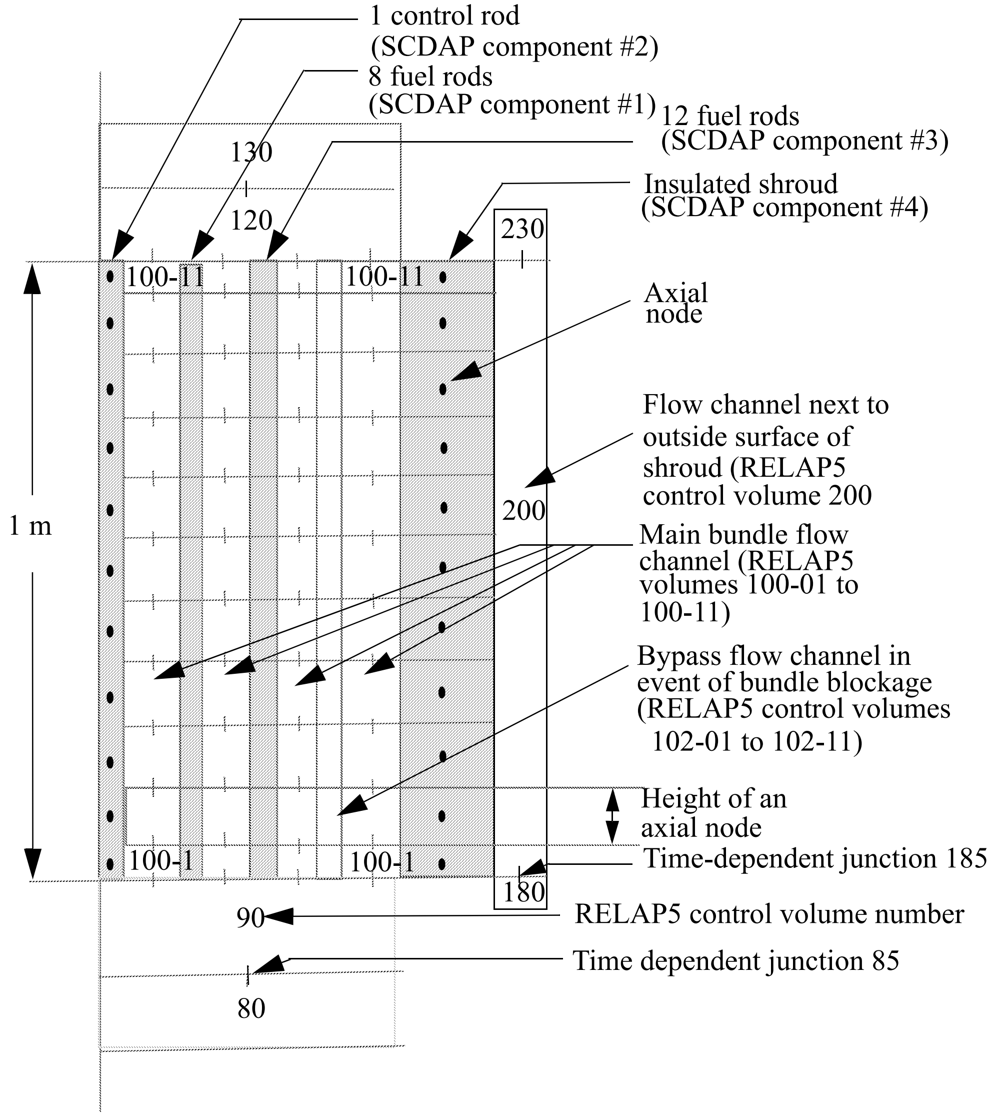
1 control rod
(SCDAP component #2)
8 fuel rods
(SCDAP component #1)
12 fuel rods
(SCDAP component #3)
Insulated shroud
(SCDAP component #4)
130
120
230
100-11
100-11
Axial node
Flow channel next to outside surface of shroud (RELAP5 control volume 200
200
1 m
Main bundle flow channel (RELAP5 volumes 100-01 to 100-11)
Bypass flow channel in event of bundle blockage (RELAP5 control volumes 102-01 to 102-11)
Height of an axial node
100-1
100-1
Time-dependent junction 185
180
90
RELAP5 control volume number
Time dependent junction 85
80

Figure A6-4. Schematic of nodalization of test rods, insulated shroud, and flow channels.

Figure A6-6, and Figure A6-7 for the elevations of 0.7 m, 0.4 m, and 0.3 m, respectively. The MOD3.2 calculated temperatures are also shown for the elevations of 0.7 m and 0.4 m. As shown in Figure A6-5, the calculated and measured temperatures are in good agreement for the period of 0.0 s to 11000 s, wherein the fuel rod cladding temperatures increased from 645 K to 1500 K and rapid oxidation of the fuel rod cladding had not yet begun, and for the period of 11750 s to the end time of the measurement (14350 s), wherein oxidation was reduced due to meltdown. The rate of heatup in the period of 11000 s to 11750 s, when a rapid heatup from 1500 K to 2200 K was calculated to occur, was overpredicted by MOD3.3. The maximum calculated rate of heatup was 19 K/s. The maximum measured rate of heatup during this period was about 9 K/s. At 11120 s, the cladding was calculated to melt and relocate in the circumferential direction. This relocation of the cladding decreased its surface area in contact with steam and resulted in a decrease in the rate of heatup. The same trend between calculated and measured temperatures was seen at the 0.4 m and 0.3 m elevations. Double-sided oxidation was calculated to occur in the elevation interval of 0.45 m to 0.65 m. Since double-sided oxidation was not calculated to occur at the elevations of 0.4 m and 0.3 m, the overprediction in the rate of heatup at these locations is due to factors other than double-sided oxidation. Three possibilities for the overprediction of temperature in the 11000 s to 11750 s period are; (1) overprediction of the insulation capability of the shroud around the test fuel assembly, (2) prediction of double-sided oxidation in the elevation interval of 0.45 m to 0.65 m, although the rate of heatup was also overpredicted in elevation interval of 0.25 m to 0.45 m, where double-sided oxidation was calculated to not occur, and (3) phase diagram for the FPT0 fuel rod cladding different from that applied by MOD3.3.

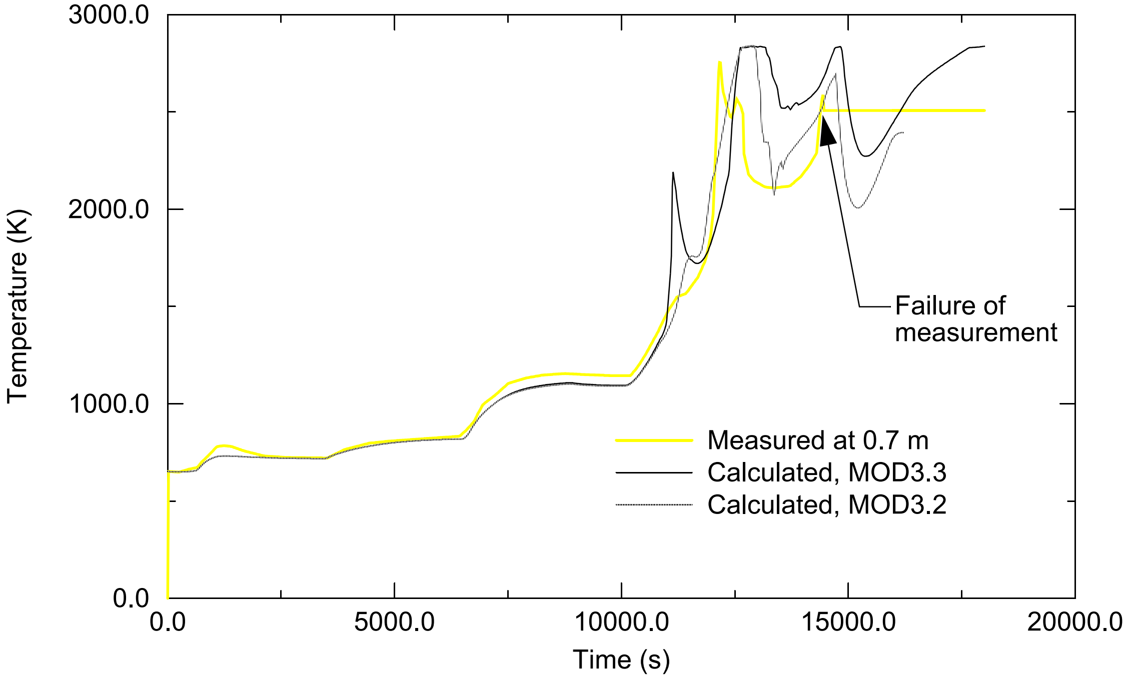

Figure A6-5. Calculated and measured cladding temperatures at 0.7 m elevation for PHEBUS FPT0.

Metallic meltdown of the cladding in the test fuel assembly was calculated to occur at the locations in the test fuel assembly with double-sided oxidation. These locations were in the elevation interval of 0.45 m to 0.65 m. The axial distribution in oxidation and meltdown in the test fuel assembly show some of the basis for the calculated temperature behavior of the test fuel assembly.The calculated axial distribution in oxidation and meltdown are shown in Table A6-1. Measurements of these aspects of behavior are for the most part unavailable. One available result is the measured elevation interval with a 100% blockage. The PIE indicated a 100% blockage in the elevation interval of 0.16 m to 0.23 m. The MOD3.3 calculated elevation interval with a 100% blockage was 0.0 m to 0.45 m. The overprediction of the elevation interval with 100% blockage may be due to MOD3.3 overpredicting the insulation capability of the flow shroud and thus overpredicting the amount of ceramic melting that occurred in the test fuel assembly.

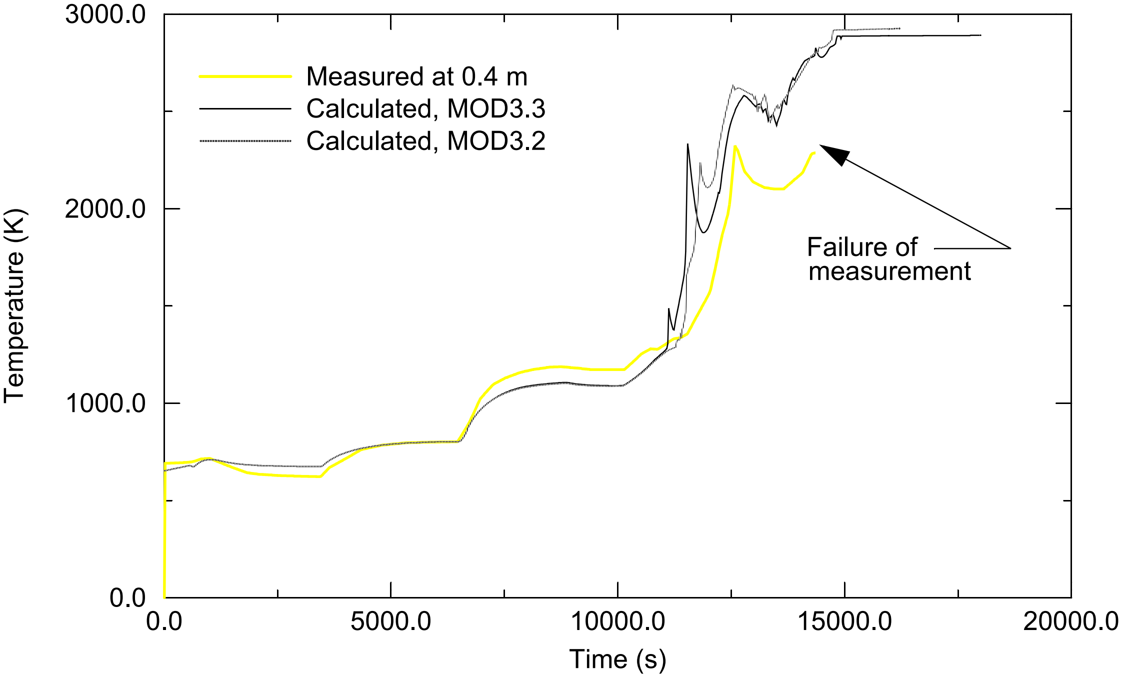

Figure A6-6. Calculated and measured cladding temperatures at 0.4 m elevation for PHEBUS FPT0 test.

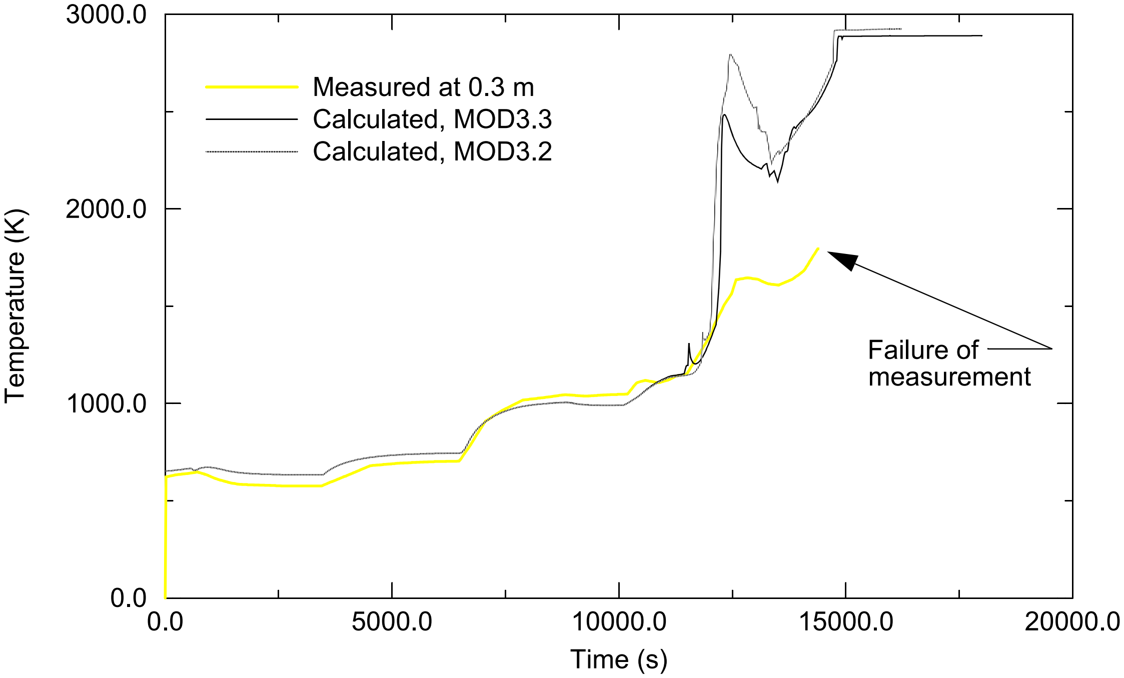

Figure A6-7. Calculated and measured cladding temperatures at 0.3 m elevation for PHEBUS FPT0 test.

Table A6-1. MOD3.3 calculated axial distribution in oxidation and meltdown for PHEBUS FPT0 test.

Elevation (m)	Fraction cladding oxidized	Fraction blockage due to meltdown	Slumping of metallic cladding from location (yes or no)	Melting and slumping of fuel at location (yes or no)
0.025	0.01	1.00	no	no
0.10	0.89	1.00	no	yes
0.20	0.86	1.00	no	yes
0.30	0.84	1.00	no	yes
0.40	0.86	1.00	no	yes
0.50	0.54	0.0	yes	no
0.60	0.56	0.0	yes	no
0.70	0.76	0.0	no	no
0.80	0.90	0.0	no	no
0.90	0.89	0.0	no	no
0.975	0.96	0.0	no	no

MOD3.3 underpredicted by about 15% the amount of hydrogen produced by oxidation of the metallic parts of the test fuel assembly. The calculated cumulative hydrogen production is shown in Figure A6-8. The total calculated and measured hydrogen production were 77 g and 90 g, respectively. The underprediction in hydrogen production was probably due to metallic meltdown being calculated to occur where in reality it did not occur. The overprediction of metallic meltdown, in turn, was probably due to double-sided oxidation being calculated to occur where in reality it did not occur. The overprediction of the elevation interval with double-sided oxidation, in turn, was probably due to an overprediction of cladding ballooning.

In summary, the PHEBUS FPT0 test problem showed that MOD3.3 has the capability to calculate the behavior of fuel assemblies through the beginning of late-phase damage progression, when blockages occur due to the melting of fuel. The comparisons of MOD3.3 calculated versus measured temperatures showed good agreement during the early and latter stages of fuel assembly heatup under severe accident conditions. For heatup in the intermediate stage, where cladding temperatures range from 1500 K to 2200 K, the rate of heatup calculated by MOD3.3 was about a factor of two greater than the measured value. Three possibilities for the overprediction of the rate of heatup during the intermediate stage are: (1) overprediction of the insulation capability of the shroud around the test fuel assembly, (2) overprediction of cladding ballooning, and (3) the phase diagram for fuel rod cladding being different from that applied by the oxidation model in MOD3.3. The total hydrogen production for FPT0 was underpredicted by about 25%. This underprediction in hydrogen production was probably due to an overprediction of the metallic ballooning. MOD3.3 overpredicted the amount of fuel melting which occurred during the test. This overprediction may have been due to an overprediction of the insulation capability of the flow shroud surrounding the test fuel assembly.

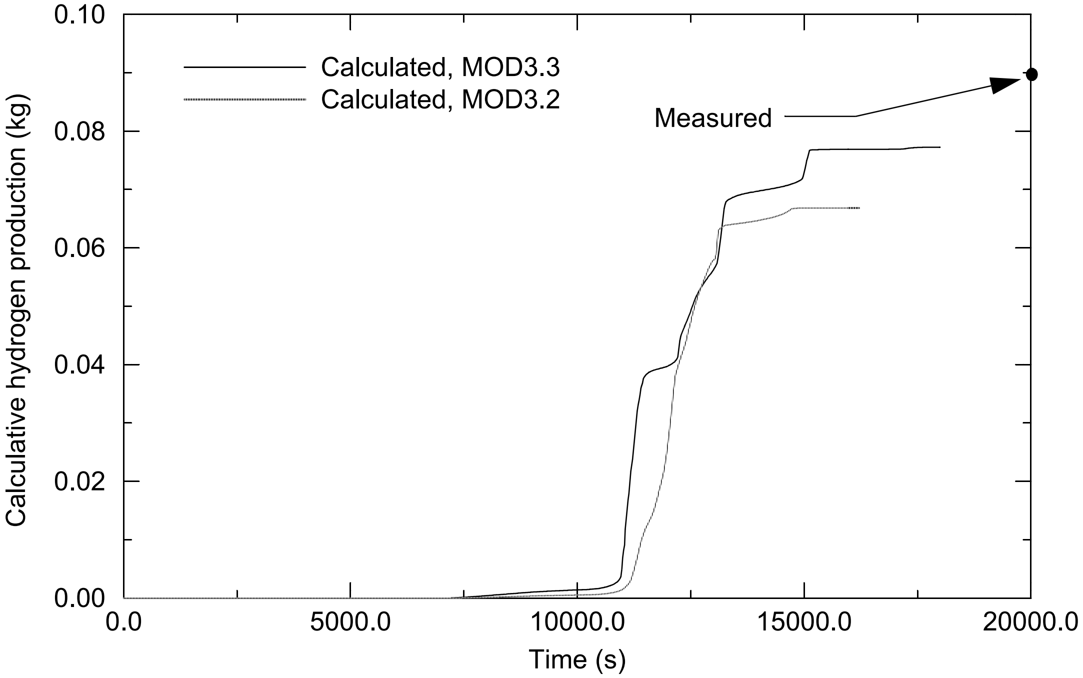

Figure A6-8. Calculated cumulative hydrogen production for PHEBUS FPT0 test.

A6.5 References

A6-1. N. Hanniet, et al., *PHEBUS PF FPT0 Test - Preliminary Report*, DRS/SEA/LERES IP/94/211, Institute de Protection et Surete Nucleaire, France, May 6, 1994.

A6-2. G. Bandini, "Sensitivity Calculations for FPT-0 Bundle with SCDAP/RELAP5/MOD3.1 Code," *Presentation to the 4th Meeting for the Bundle Degradation Interpretation Circle*, ISPRA, June 28, 1995, SAWG 95-031/1, Joint Research Centre of European Commission, Safety Technology Institute.

A7. ACRR DF-4 TEST

The DF-4 experiment was designed to examine phenomena associated with the heatup, oxidation, and meltdown of a BWR fuel assembly.[A7-1, A7-2] The experiment was conducted in the Annular Core Research Reactor (ACRR) at Sandia National Laboratories. The experimental bundle, designed to represent a small section of a General Electric D-lattice core, consisted of fourteen 0.5-m-long fuel rods, a Zircaloy channel box enclosing a representation of the tip region of a BWR control blade, and an insulated shroud consisting of porous ZrO_2, which contained a fully dense, ceramic, ZrO_2 tube.

Seven Zircaloy-4-clad fuel rods were situated on either side of the channel box structure. The cross section of the experiment bundle is shown in Figure A7-1. The spacing between the fuel rods in the bundle, the fuel rod cladding, and the channel box wall were prototypical of a BWR, but the fuel rod diameter was not. The fuel rods used were pressurized water reactor (PWR)-type rods, somewhat smaller in diameter than BWR rods, and were situated in a triangular 0.5-in. (12.7-mm) pitch to improve the effectiveness of heating the channel box.

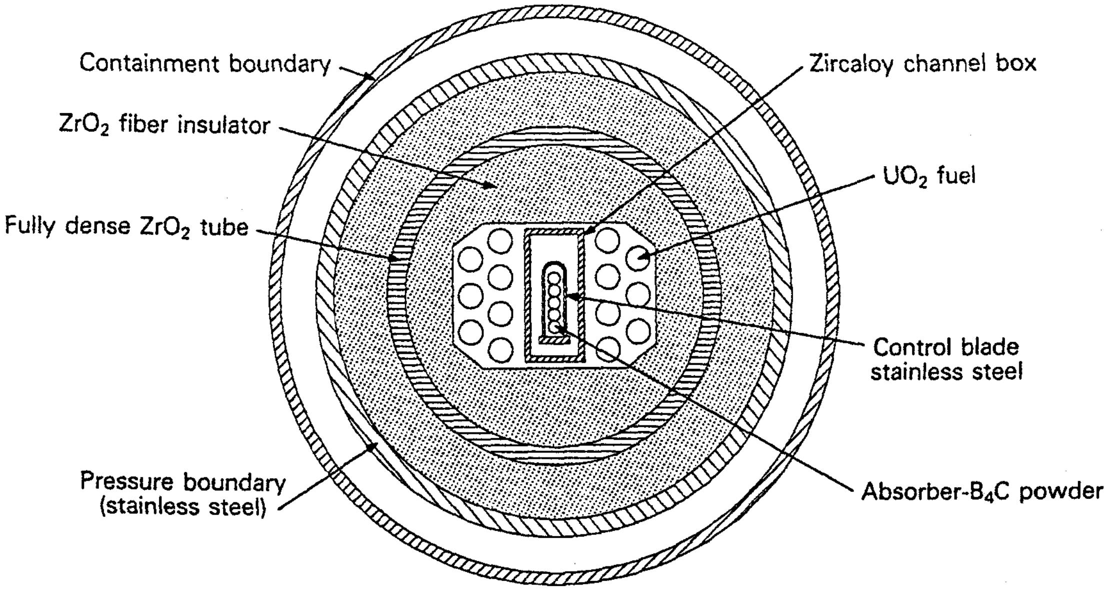
Containment boundary
ZrO_2 fiber insulator
Fully dense ZrO_2 tube
Pressure boundary (stainless steel)
Zircaloy channel box
UO_2 fuel
Control blade stainless steel
Absorber-B_4C powder

Figure A7-1. Cross section of the DF-4 experiment bundle.

The channel box consisted of a Zircaloy-4 rectangular box that represented the fuel canister walls on either side of the control element in an actual BWR. The offset-from-center control blade situated in the channel box consisted of five stainless steel tubes containing boron carbide (B_4C) powder surrounded by a stainless steel sheath. The blade was positioned in the channel box to represent a tip region of a reactor control blade.

A high-temperature oxidation transient was initiated by injecting superheated steam into the bundle. Fission product decay heat was simulated by fission heating of the 10% ^{235}U-enriched fuel rods using the ACRR driver core to drive the heatup. Steam was fed to the two separate flow regions in the DF-4 experiment bundle through the use of orifices. To duplicate the steam flow in a BWR core, 80% of the steam was directed into the flow channel containing the fuel rods, and the remaining 20% was directed into flow channel containing the B_4C control blade. The steam flow rate and distribution were consistent with those anticipated to occur during a station blackout in a large plant.

Test thermal behavior was monitored through the use of platinum/rhenium and tungsten/rhodium thermocouples mounted at various location in the bundle. The hydrogen production rate and the quantity produced, including hydrogen produced during the Zircaloy oxidation phase of the experiment, were derived from temperature measurements of a CuO-H_2 bed through which the test section effluent flowed.

A7.1 Nodalization of Test Fuel Assembly and Boundary Conditions

Figure A7-2 shows the SCDAP/RELAP5 nodalization diagram of the ACRR test train used in the analysis of the DF-4 experiment. The RELAP5 thermal-hydraulic modeling used for the analysis employed two parallel channels. Each channel contained five equal axial volumes in the 0.5-m test section. In Figure A7-2, the outermost channel, represented by volume 20, modeled the region bounded by the outer wall of the channel box and the stainless steel pressure boundary. This region contained the 14 fuel rods and the ZrO_2 insulation, both porous and ceramic. The innermost channel, represented by volume 30, modeled the Zircaloy channel box that contained a control blade. Pressure boundaries at the inlet and outlet of the test section were modeled by the use of two time-dependent volumes (10 and 60). The steam flow was modeled by the use of two time-dependent junctions (111 and 112).

The components in the test fuel assembly were represented using the following SCDAP component models: (1) fuel rod model for the Zircaloy-clad 10% ^{235}U-enriched UO_2 fuel rods, (2) BWR control blade model for the B_4C stainless steel-clad control blade, (3) general structural component model for both the porous and ceramic ZrO_2-insulated shroud surrounding the fuel rods and channel box and the Zircaloy channel box surrounding the B_4C control blade. Each component represented in the bundle consisted of five axial nodes in the 0.5-m active zone. Radial detail varied between the components, from two nodes for both the channel box and control blade to nine for the insulating shroud.

The power history input into SCDAP/RELAP5 duplicated the experimental power history and the experimentally measured axial power profile during the time frame considered important for a complete analysis of the DF-4 experiment: 5000 to 8000 s. The power history input into the code contained the following: (1) representation of the initial nuclear heating phase, the rapid increase in reactor power to 1 MW to initiate heating of the fuel rods, (2) equilibration phase, the decrease in reactor power to 0 -.4 MW as soon as fuel rod temperatures attained 1000 K to allow the temperatures of the channel box walls and stainless steel control blade to equilibrate with the fuel, (3) preoxidation phase, a stepwise boost in reactor power to full, (4) nuclear phase when full reactor power was maintained for 400 s to simulate a boiloff

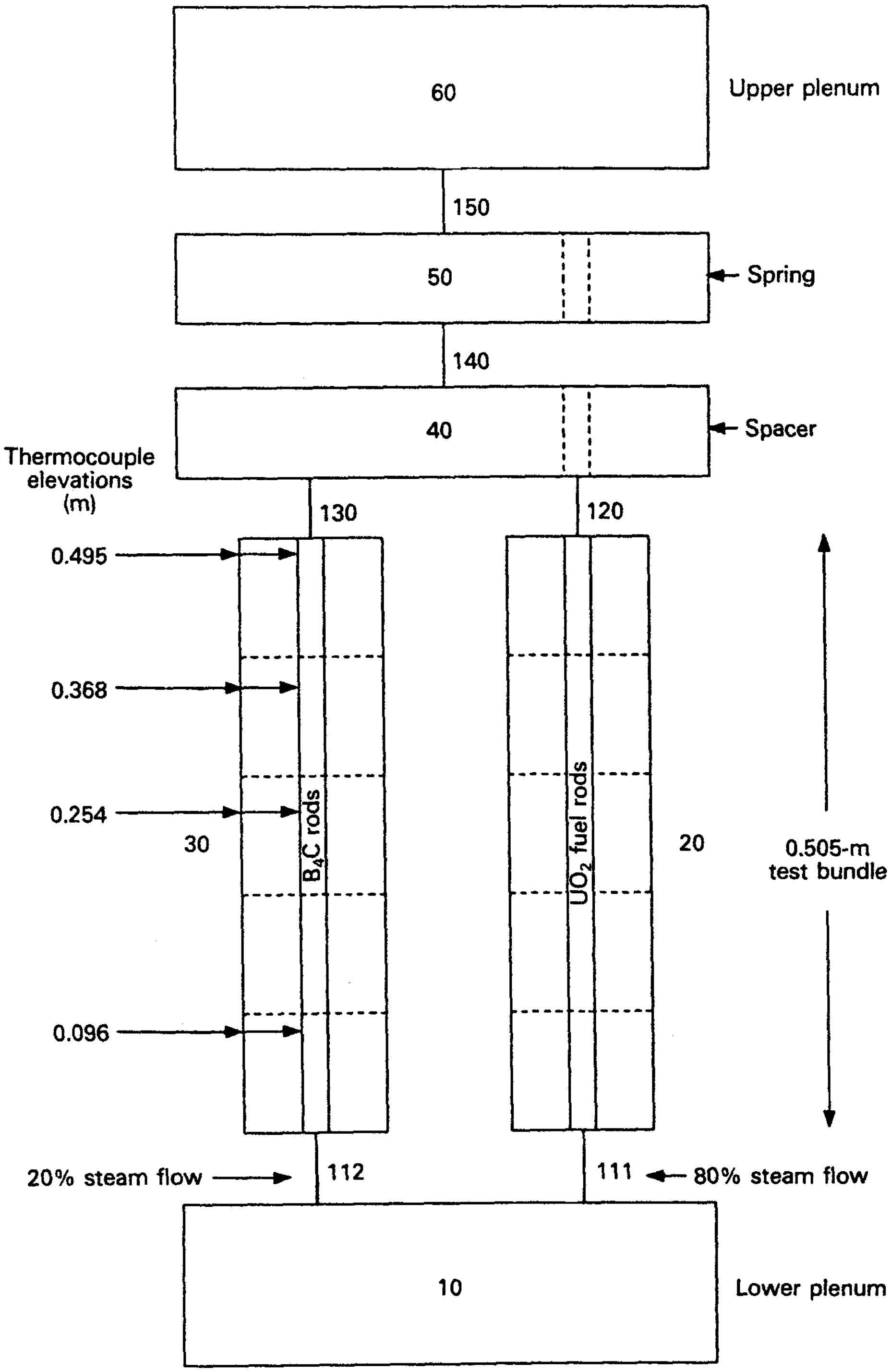
60
Upper plenum
150
50
Spring
140
40
Spacer
Thermocouple elevations (m)
130
120
0.495
0.368
0.254
0.096
30
B4C rods
UO2 fuel rods
20
0.505-m test bundle
20% steam flow
112
111
80% steam flow
10
Lower plenum

Figure A7-2. SCDAP/RELAP5 nodalization for the DF-4 experiment analysis.

resulting in core meltdown.

The steam flow history used as input for the analysis duplicated the steam flow used during the experiment to simulate the boiloff. The steam flow ratio in the flow channels was kept constant throughout the experiment. During the initial stages of bundle heatup, the steam flow was half of that delivered during the nuclear phase of the experiment.

A7.2 Comparison of Calculations and Measurements

The results of the DF-4 test were applied to the assessment of MOD3.3 by comparing calculated temperature histories and hydrogen production with the measured temperature histories and hydrogen production. The calculated and measured hydrogen production were also compared. The MOD3.3 calculated temperature behavior of the test fuel assembly was in good agreement with the measured temperature behavior. The MOD3.3 calculated and measured temperature histories of a fuel rod are shown in Figures A7-3 and A7-4 for the elevations of 0.254 m and 0.096 m, respectively.

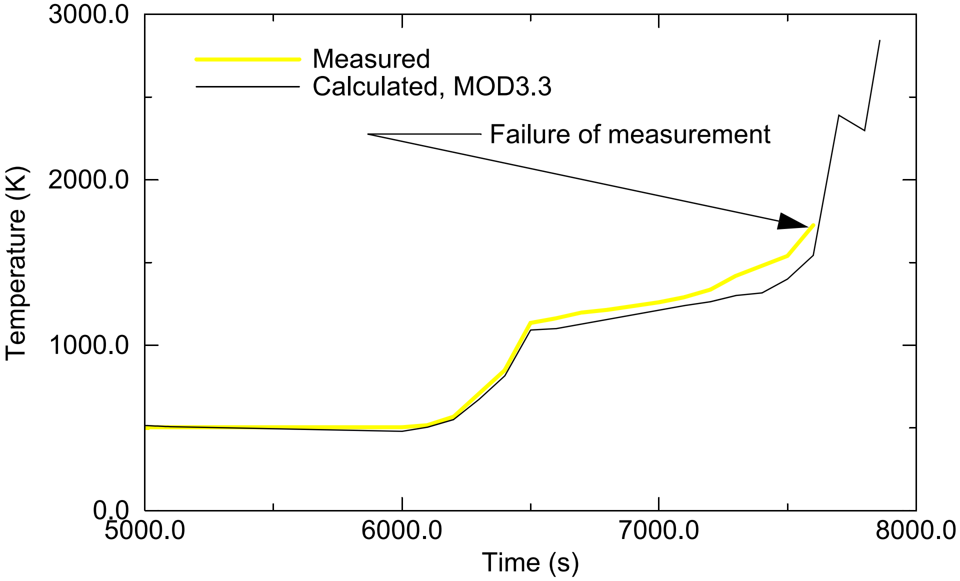

Figure A7-3. Calculated and measured temperatures of fuel rod at elevation of 0.254 m for DF-4 test.

The elevations are referenced with respect to the bottom of the fuel rods. The elevation of 0.254 m is about midway between the bottom and top elevations of the fuel pellet stack. At both the 0.254 m and 0.096 m elevations, the calculated and measured temperature are in good agreement.

The calculated hydrogen production was about 30% less than the measured hydrogen production. The calculated and measured hydrogen production were 28.5 g and 40 g, respectively. The underprediction of hydrogen production was due in part to the calculations not being performed out to the time of the cooldown of the test fuel assembly.

In summary, this test problem confirms that the integral diffusion model in MOD3.3 correctly calculates the heatup of fuel rods due to oxidation. The MOD3.3 calculated rates of heatup of the fuel rods

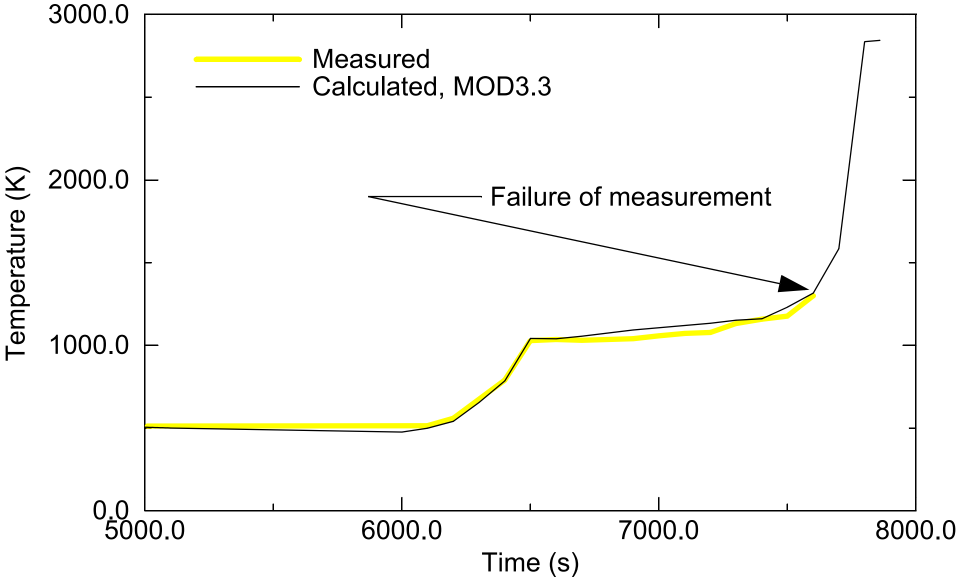

Figure A7-4. Calculated and measured temperatures of fuel rod at elevation of 0.096 m for DF-4 test.

in the test fuel assembly were generally in good agreement with the measured rates of heatup. The calculated hydrogen production was 30% less than the measured hydrogen production.

A7.3 References

A7-1. R.O. Gauntt, R. D. Gasser, and L. J. Ott, “The DF-4 Fuel Damage Experiment in the ACRR with a BWR Control Blade and Channel Box,” NUREG-/CR-4671, SAND86-1443, Sandia National Laboratories, November 1989.

A7-2. J. K. Hohorst and C. M. Allison, “DF-4 Analysis Using SCDAP/RELAP5,” Nuclear Technology, Vol. 98, May 1992.

A8. FLOW LOSS AND HEAT TRANSFER IN POROUS DEBRIS

The models for thermal hydraulic behavior in porous debris were assessed by comparisons of SCDAP/RELAP5 calculated behavior of debris with that evaluated by measurements and benchmarked models presented in the literature. In particular, the models for flow loss were assessed by comparing the pressure drop calculated by SCDAP/RELAP5 with that calculated by benchmarked pressure drop models. The models for heat transfer were assessed by comparing calculated and measured temperatures for the case of reflood from the bottom of an initially hot debris bed. The implementation of the porous debris thermal hydraulic models into the COUPLE model was assessed by evaluating the behavior calculated for a flooded porous debris bed located in the lower head of a reactor vessel.

A.8.1 Flow Loss

The assessment problems for pressure drop involved the steady state analyses of the coolant conditions in a porous debris bed with forced flow at the bottom boundary of the debris bed. A schematic of the system analyzed is shown in Figure A8-1. The assessment was performed for the following coolant conditions; (1) superheated steam, (2) subcooled liquid, and (3) two-phase water. The third case analyzes a debris bed representative of a debris bed resulting from a severe accident in a LWR.[A8-1] The debris and coolant conditions for the three cases are described inTable A8-1

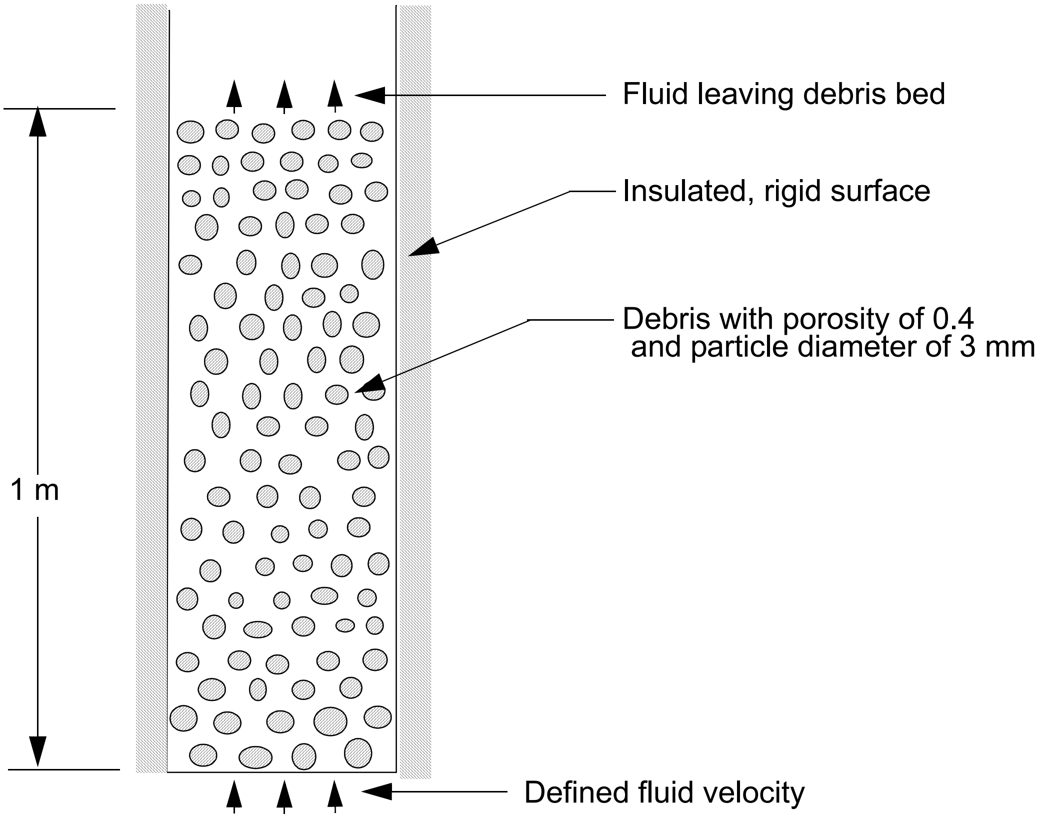

Figure A8-1. Schematic of debris bed analyzed for assessment of flow loss calculations.

Table A8-1 . Characteristics of debris bed and coolant conditions for pressure drop calculations.

Parameter	Case		
	steam	subcooled	two-phase
porosity of debris	0.4	0.4	0.4
size of particles in debris bed (mm)	3.0	3.0	3.0
height of debris bed (m)	1.0	1.0	1.0
heat generation in debris bed (MW/m^3)	0	0	7.5
coolant pressure (Mpa)	6.9	6.9	6.9
superficial velocity of fluid at bottom of debris bed (m/s)	0.132	1.39×10^{-2}	1.47×10^{-2}
temperature of fluid at bottom of debris bed (K)	1050	400	558.
quality of fluid at bottom of debris bed	1.0	0.0	0.0
density of heaviest phase of fluid (kg/m^3)	15.2	940.7	740
hydrostatic head (Pa)	149	9.22×10^3	3.4×10^3

For all three cases, two boundary conditions were defined. The first boundary condition was the velocity of the fluid at the bottom of the debris bed. The second boundary condition was the temperature and quality of the fluid at the bottom of the debris bed. The heat generation in the debris bed was defined to be zero for the two cases involving single-phase coolant and was defined to be 7.5 MW/m^3 for the two-phase fluid case. The nodalization diagram for the analyses is shown in Figure A8-2.

For each case, the debris bed was divided into ten nodes and the fluid in the debris was represented by a stack of ten RELAP5 control volumes. The relative permeabilities and passabilities of the liquid and vapor phases were calculated using the Catton and Chung model.[A8-4] The calculation of the flow losses in porous debris was assessed by comparing SCDAP/RELAP5 calculated pressure drops with independent calculations published in the literature[A8-1, A8-2] and shown to agree with experimental results.

The assessment of the modeling of flow losses showed that the SCDAP/RELAP5 is correctly calculating the flow losses in porous debris. The SCDAP/RELAP5 flow losses for the three cases identified in Table A8-1 and those presented in the literature for the corresponding cases are compared in Table A8-2. The SCDAP/RELAP5 calculated flow losses are in approximate agreement with the values presented in the literature.

A8.3 Heat Transfer

The modeling of heat transfer in porous debris was assessed using the results of a BNL debris experiment involving the quenching from the bottom of a hot porous debris bed.[A8-3] During this experiment, the transient temperature distribution in the debris bed was measured. Since the transient temperature distribution is a function of the flow losses in the debris bed, this experiment in an indirect manner also assessed the modeling of flow losses. A schematic of the experiment is shown in Figure A8-3.

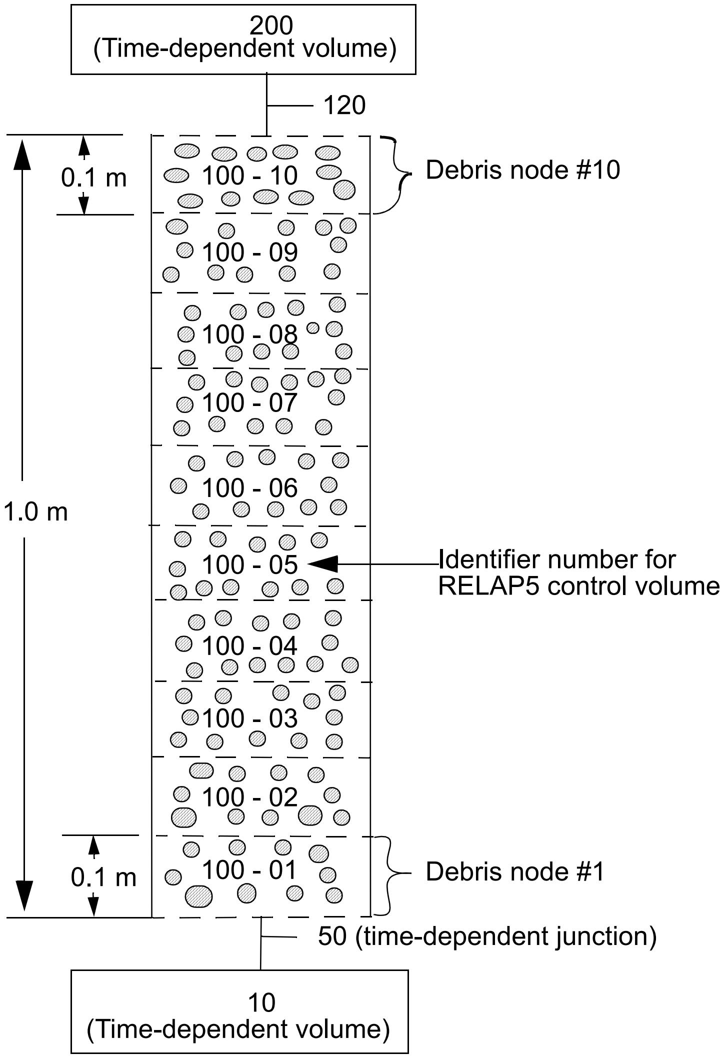
200
(Time-dependent volume)
120
0.1 m
100 - 10
Debris node #10
100 - 09
100 - 08
100 - 07
100 - 06
1.0 m
100 - 05
Identifier number for RELAP5 control volume
100 - 04
100 - 03
100 - 02
0.1 m
100 - 01
Debris node #1
50 (time-dependent junction)
10
(Time-dependent volume)

Figure A8-2. Nodalization of debris bed analyzed for assessment of flow loss calculations.

Table A8-2. Comparisons of SCDAP/RELAP5 calculated flow losses with those presented in literature for corresponding cases.

Case	Pressure drop due to flow losses (Pa)	
	SCDAP/RELAP5	Literature
superheated steam	1.03×10^3	1.14×10^3
subcooled liquid	1.00×10^3	1.28×10^3
two-phase water	10.6×10^3	12.6×10^3

Except for representing the fluid in the debris bed by a stack of twelve instead of ten RELAP5 control volumes, the nodalization for the experiment is as shown in Figure A8-2. Each RELAP5 control volume represented a segment of the debris bed that was 35 mm in height. A summary description of the experiment is shown in Table A8-3 .

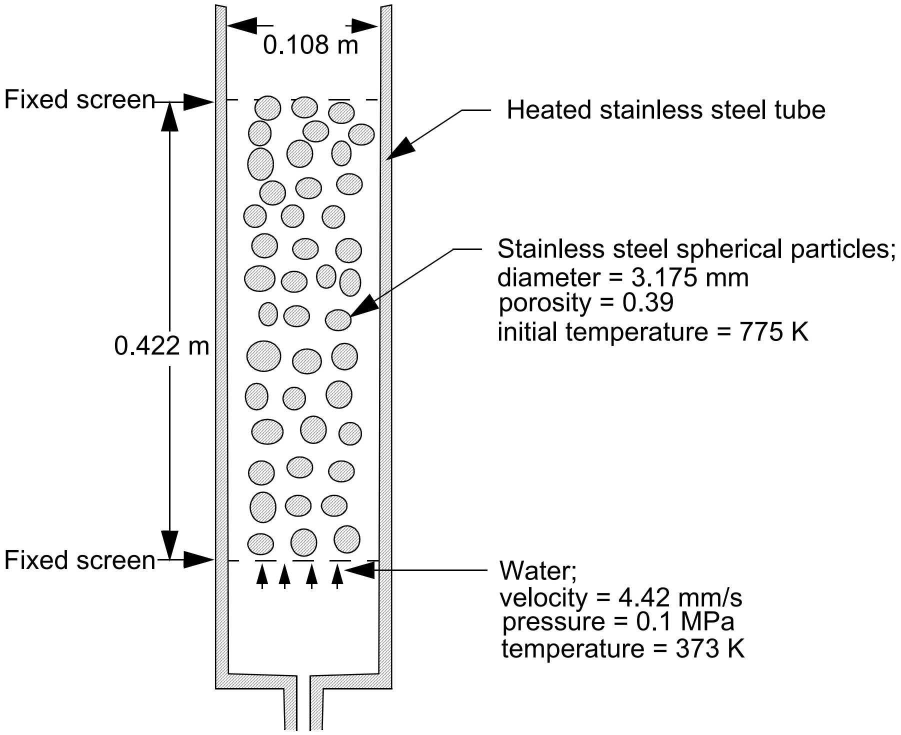
0.108 m
Fixed screen
Heated stainless steel tube
Stainless steel spherical particles;
diameter = 3.175 mm
porosity = 0.39
initial temperature = 775 K
0.422 m
Fixed screen
Water;
velocity = 4.42 mm/s
pressure = 0.1 MPa
temperature = 373 K

Figure A8-3. Schematic of BNL quenching experiment.

Table A8-3. Summary description of BNL quenching experiment.

Parameter	Value
Porosity of debris	0.39
Composition of particles in debris bed	stainless steel
Diameter of particles in debris bed (mm)	3.175
Height of debris bed (m)	0.422
Diameter of debris bed (m)	0.108
Initial temperature of debris bed (K)	775
Coolant	water
Temperature of coolant at bottom of debris bed (K)	373

Table A8-3. Summary description of BNL quenching experiment. (Continued)

Parameter	Value
Quality of coolant at bottom of debris bed	0.0
System pressure (MPa)	0.1
Superficial velocity of coolant at bottom of debris bed (mm/s)	4.42

The calculated transient temperatures at two different elevations along the centerline of the debris bed were in general agreement with the measured transient temperatures. The calculated and measured transient temperatures for the two elevations are compared in Figure A8-4. The elevation of 0.025 m is near the bottom of the debris bed, where reflood began, and the elevation of 0.24 m is slightly above the midplane of the debris bed. The overprediction of the temperature at the 0.24 m elevation in the period from 40 s to 50 s is considered to be due to MOD3.3 not modeling two-dimensional hydrodynamic behavior, wherein the liquid phase moved up along the wall, formed a pool at the top, and then some of the water flowed down the center region of the debris bed. Nevertheless, the calculated and measured trend in quenching are in good agreement.

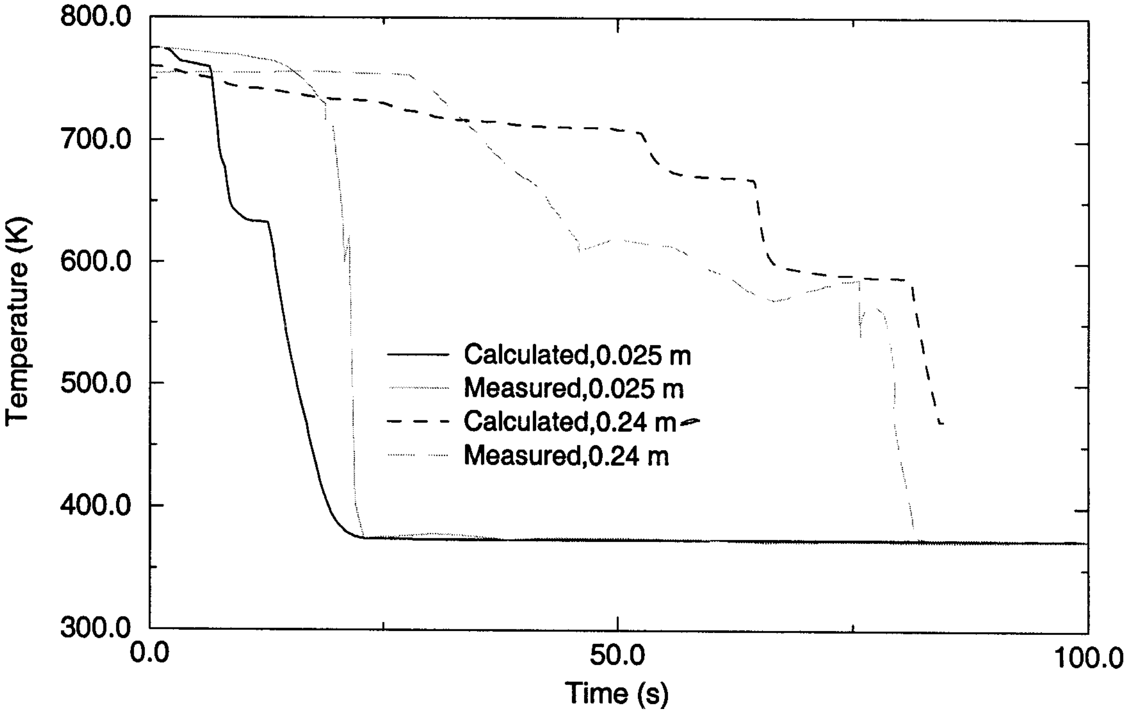

Figure A8-4. Comparison of calculated and measured transient temperature distribution in debris bed

A8.3 Thermal Hydraulic Behavior in Lower Head

The implementation of the porous debris thermal hydraulic models into the COUPLE model was assessed by the analysis of a porous debris bed in the lower head of a reactor vessel A schematic of the system analyzed is shown in Figure A8-5.

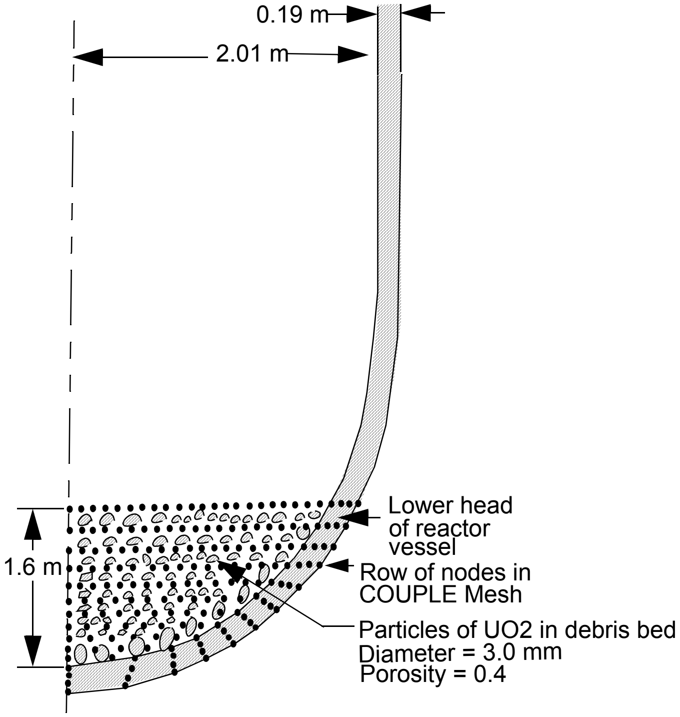
0.19 m
2.01 m
1.6 m
Lower head of reactor vessel
Row of nodes in COUPLE Mesh
Particles of UO2 in debris bed
Diameter = 3.0 mm
Porosity = 0.4

Figure A8-5. Nodalization of debris bed in lower head of reactor vessel.

This figure also shows the COUPLE model nodalization of the porous debris. The porous debris had a total internal heat generation rate of 16.3 MW. The porosity of the debris is 0.4. The debris particles were composed of UO_2. The particles were spherical in shape and had a diameter of 3 mm. The initial temperature of the particles was 600 K. The debris particles slumped into the lower head in the 10s interval of time beginning at 11378 s, which was the start time of the analysis. The RELAP5 nodalization for the analysis is shown in Figure A8-6. At the start of the analysis, the lower head was empty of water. Beginning at the start of the analysis, the lower head was flooded with water at the rate of 80.3 kg/s. The system pressure was 0.2 MPa.

An assessment was performed of the energy balance in the debris bed and the coolant that flooded the debris bed. A plot is shown in Figure A8-7 of the transient volume of liquid in the RELAP5 control volume containing the flooded debris bed. The volume fraction of liquid increased from 0.0 to 0.5 during the first 200 s of flooding. The transient temperature at the center of the debris bed is shown in Figure A8-8. At this location, the debris cooled in about 200 s from 600 K to a temperature near the saturation temperature of the coolant. The debris bed power and the heat transfer to the coolant are compared in Figure A8-9.After the initial internal energy was removed from the debris, the debris bed power and heat transfer to the coolant converge to the same value. This equality indicates that the COUPLE model for porous debris has been properly interfaced with the RELAP5 model.

A8.4 Conclusions

The SCDAP/RELAP5/MOD3.3 calculations of flow losses and heat transfer in porous debris are in general agreement with the calculations of benchmarked models and with experiment results. The SCDAP/

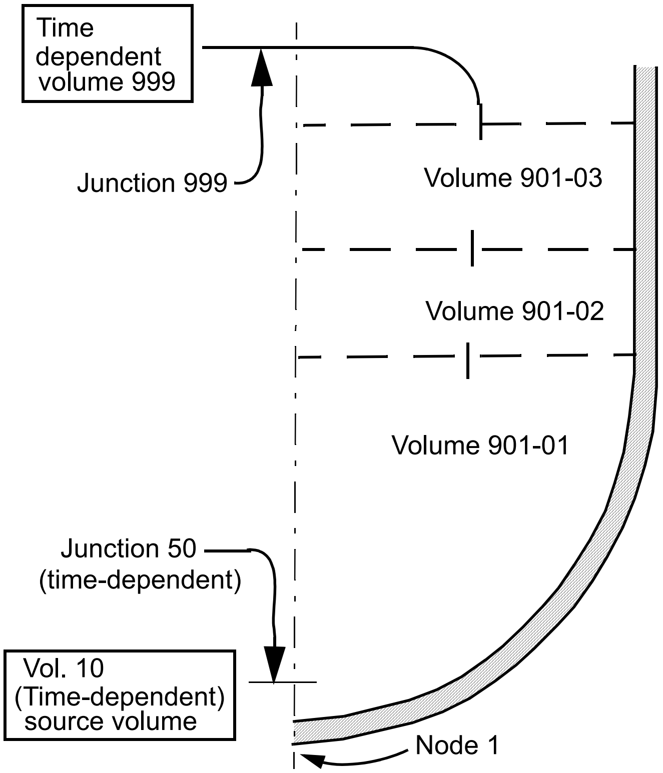
Time dependent volume 999
Junction 999
Volume 901-03
Volume 901-02
Volume 901-01
Junction 50 (time-dependent)
Vol. 10 (Time-dependent) source volume
Node 1

Figure A8-6. RELAP5 nodalization for analysis of porous debris in lower head

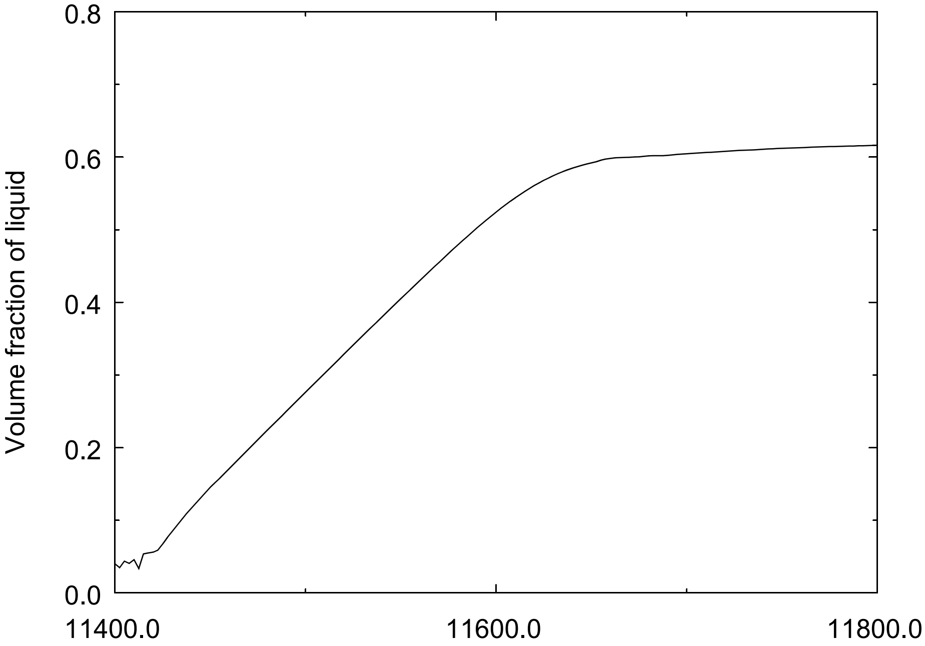

Figure A8-7. Volume fraction of liquid in RELAP5 control volume containing the flooded debris bed.

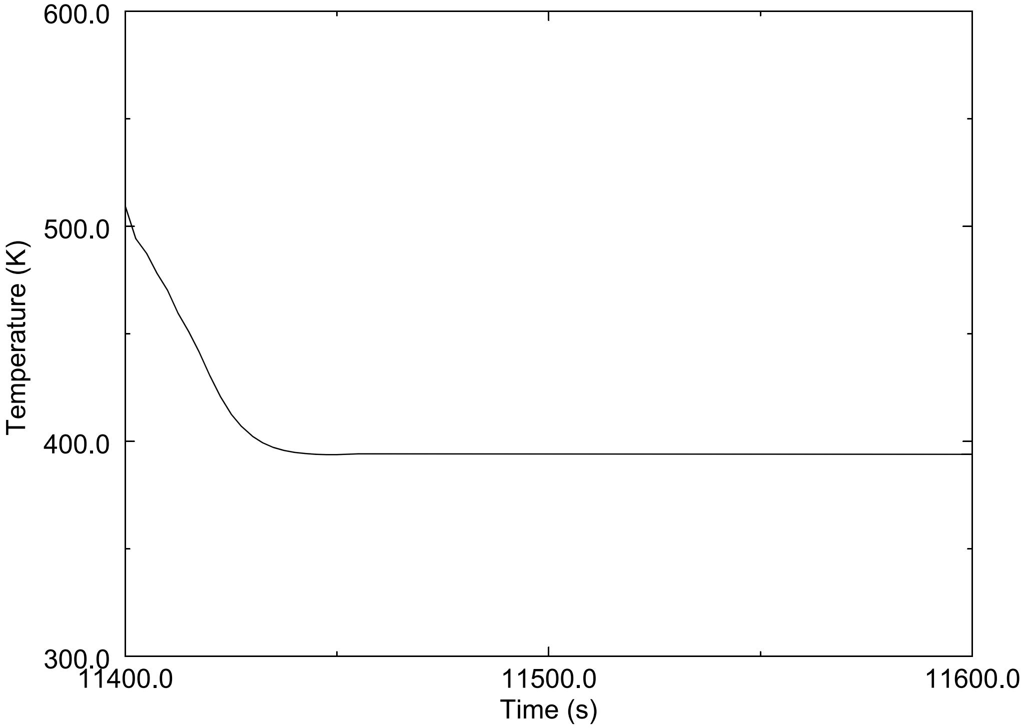

Figure A8-8. Transient temperature at center of debris bed.

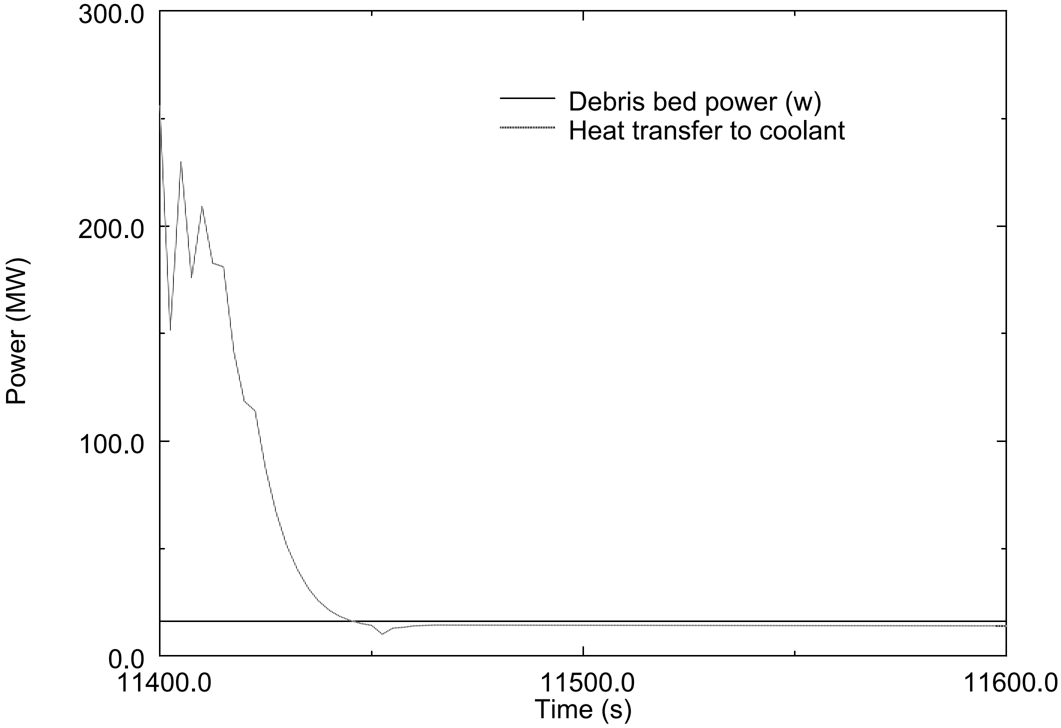

Figure A8-9. Comparison of debris bed power and heat transfer to coolant

RELAP5 calculated flow losses for three different conditions of coolant were similar to those presented in the literature for corresponding conditions. The SCDAP/RELAP5 calculated transient temperature distribution in a hot debris reflooded from the bottom was similar to the measured transient temperature distribution. The COUPLE model representation of heat transfer in porous debris flooded with water results in a correct energy balance in the overall system analyzed. As a result of the models that have been implemented, SCDAP/RELAP5/MOD3.3 calculates in a more thorough manner the heatup of porus debris in the core region and in the lower head.

A8.5 References

A8-1. V. X. Tung, V. K. Dhir and D. Squarer, "Forced Flow Cooling Studies of Volumetrically Heated Porous Layers," *Second International Topical Meeting on Nuclear Reactor Thermal-Hydraulics*; Santa Barbara, California, USA, January 11-14, 1983.

A8-2. V. X. Tung, "Hydrodynamic and Thermal Aspects of Two-Phase Flow Through Porous Media," Ph. D. Thesis, University of California, Los Angeles, 1988.

A8-3. N. K. Tutu et al, "Debris Bed Quenching Under Bottom Flood Conditions (In-Vessel Degraded Core Cooling Phenomenology)," NUREG/CR-3850, 1984.

A8-4. I. Catton and M. Chung, "Two-Phase Flow in Porous Media with Phase Change: Post-Dryout Heat Transfer and Steam Injection," *Nuclear Engineering and Design*, Vol. 151, pp. 185 - 202.

A9. HEAT TRANSFER IN STRATIFIED MOLTEN POOL

The model for heat transfer in a stratified molten pool was assessed by comparing its steady state calculations with those of another model.[A9-1] that was benchmarked against experiment results using simulant materials. The model was also assessed by examining for internal consistency its calculation of the transient analysis of a stratified molten pool and by examining the sensitivity of its calculations to various combinations of heat transfer correlations. The lack of experimental data for LWR materials and geometry excluded the assessment of the model by direct comparison of calculations with measurements.

A9.1 Comparison of Calculations With Benchmarks

A total of three test problems were solved to produce information for comparing the model calculations against benchmarks and for evaluating the calculations for internal consistency. All three test problems involved the analysis of a stratified molten pool in the lower head of a PWR reactor vessel submerged in a deep pool of water. A schematic of the system analyzed is shown in Figure A9-1.

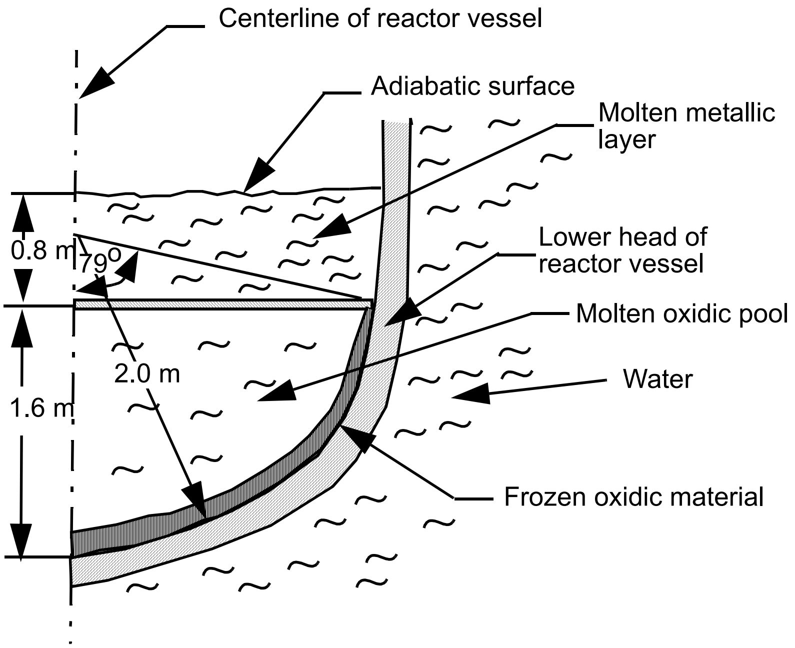

Figure A9-1. Molten pool system analyzed in literature and by SCDAP/RELAP5.

Each of the test problems analyzed this basic configuration. The characteristics of the system that were the same in each of the test problems are shown in Table A9-1. These characteristic included; (1) lower head of reactor vessel composed of carbon steel, inner surface with radius of 2.0 m, and thickness of 0.158 m, (2) oxidic pool composed of 86 wt% UO_2 and 14 wt% ZrO_2, (3) metallic pool composed of stainless steel, and (4) volumetric heat generation in oxidic pool of 1.4 MW/m^3. The liquidus temperature of the oxidic pool was 3000 K and the liquidus temperature of the metallic pool was 1630 K. The liquidus temperatures were fixed to these values to be consistent with the solutions for Test Problems 1 and 2 presented in Reference A9-1. No heat transfer occurred from the top surface of the metallic pool. The depths of the metallic and oxidic parts of the molten pool and the time for molten pool stratification varied with the test problems. The values of these characteristics for each of the test problems is shown in Table A9-2. The depth of the metallic pool was relatively large for Test Problems 1 and 3, and was relatively shallow for Test Problem 2. The molten pool was stratified into oxidic and metallic parts from the start for Test Problems 1 and 2, and became stratified at 2000 s for Test Problem 3. Thus, Test Problems 1 and 2 involve a steady state solution and Test Problem 3 involves a transient solution.

Table A9-1. Characteristics of system analyzed that were same for each test problem.

Characteristic	Units	Value
Radius of inner surface of lower head	m	2.00
Thickness of wall of lower head	m	0.158
Volumetric heat generation rate in oxidic pool	MW/m^3	1.40
Volumetric heat generation rate in metallic pool	MW/m^3	0.0
Composition of oxidic pool	wt%	86%UO_2, 14% ZrO_2
Composition of metallic pool	wt%	100% Stainless steel
Liquidus temperature of oxidic pool	K	3000
Liquidus temperature of metallic pool and lower head	K	1630

Table A9-2. Characteristics of molten pool that varied with test problems.

Characteristic	Units	Test Problem 1	Test Problem2	Test Problem 3
Depth of oxidic pool	m	1.60	1.18	1.60
Depth of metallic pool	m	0.80	0.22	0.80
Mass of UO_2 in oxidic pool	kg	$93.9x10^3$	$58.3x10^3$	$93.9x10^3$
Mass of stainless steel in metallic pool	kg	$70.0x10^3$	$19.4x10^3$	$70.0x10^3$
Time of stratification into oxidic and metallic parts	s	0.0	0.0	2000.

The SCDAP/RELAP5 steady state solutions for Test Problems 1 and 2 were compared to the solutions in Reference A9-1. The most important results in the solutions were the sideward heat fluxes into the lower head at the location of the metallic pool. For stratified molten pools, the heat flux into the lower head is expected to be maximum at this location, and thus the margin to CHF on the external surface of the lower head may be a minimum at this location. Other important results from a calculation of the system behavior include; (1) heat flux to lower head at various locations in the oxidic pool, (2) temperature of the metallic pool, (3) temperature of the oxidic pool, and (4) thickness of the crust of top of the oxidic pool.

The MOD3.3 steady state solutions for Test Problems 1 and 2 were similar to the solutions in Reference A9-1. The SCDAP/RELAP5 calculated steady state behavior for Test Problem 1 is compared in Table A9-3 with the behavior for this case presented in Reference A9-1. For the sideward heat flux, the SCDAP/RELAP5 and Reference A9-1 values were 0.66 MW/m^2 and 0.55 MW/m^2, respectively. For the heat flux in the oxidic pool at a polar angle of zero degrees (bottom center), the SCDAP/RELAP5 and Reference A9-1 values were 0.06 MW/m^2 and 0.13 MW/m^2, respectively. For the heat flux in the oxidic pool at the location of the interface of the oxidic and metallic pools (polar angle of 78 degrees), the SCDAP/RELAP5 and Reference A9-1 values were 0.83 MW/m^2 and 0.77 MW/m^2, respectively. The SCDAP/RELAP5 and Reference A9-1 calculations of the temperature of the metallic pool were 1691 K and 1680 K, respectively. The SCDAP/RELAP5 and Reference A9-1 calculations of the temperature of the oxidic pool were 3102 K and 3110 K, respectively. For the thickness of the crust at the interface of the oxidic and metallic pools, the SCDAP/RELAP5 and Reference A9-1 values were 3.7 mm and 5.5 mm, respectively.

The SCDAP/RELAP5 and Reference A9-1 calculations for Test Problem 2 both show a significantly greater sideward heat flux in the metallic pool compared with Test Problem 1, where the depth of the metallic pool was 0.80 m instead 0f 0.22 m. The two calculations are compared in Table A9-4. The SCDAP/RELAP5 and Reference A9-1 values for the sideward heat flux were 1.91 MW/m^2 and 1.22 MW/m^2, respectively. The SCDAP/RELAP5 and Reference A9-1 calculations of the steady state oxidic and metallic pool temperatures are similar; the values for the oxidic pool are 3080 K and 3086 K, respectively, and the values for the metallic pool are 1799 K and 1736 K, respectively.

The margin to CHF on the external surface of the lower head was calculated to not be significantly greater for the shallow metallic pool (Test Problem 2) than for a deep metallic pool (Test Problem 1). This result may in part be due to relatively more conduction of heat in the axial direction in the lower head after transfer from the metallic pool for the case of the shallow metallic pool than the deep metallic pool. For both cases, the minimum margin to CHF was calculated to be at the elevation of the interface of the oxidic and metallic pools.

The margin to CHF is a function of the critical heat flux model applied for the external surface of the lower head; SCDAP/RELAP5 used the Cheung model,[A9-2] which is dependent on the depth of the pool of water in which the lower head is submerged. Other factor influencing the calculation of CHF margin include the modeling of the ablation of melted reactor vessel material and the modeling of heat transfer across the interface of frozen oxidic material and the inner surface of the lower head.

Table A9-3. SCDAP/RELAP5 and Reference A9-1 solutions for Test Problem 1 (deep metallic pool).

Variable	Value	
	SCDAP/ RELAP5	Reference A9-1
Sideward heat flux of metallic pool (MW/m^2)	0.66	0.55
Heat flux in oxidic pool at bottom center (MW/m^2)	0.06	0.13
Heat flux in oxidic pool at interface with metallic pool (MW/m^2)	0.83	0.77
Bulk temperature of metallic pool (K)	1691	1680
Bulk temperature of oxidic pool (K)	3102	3110
Thickness of crust on top of oxidic pool (mm)	3.7	5.5
Minimum CHF margin on external surface of vessel (heat flux/critical heat flux)	1.30	--

Table A9-4. SCDAP/RELAP5 and Reference A9-2 solutions for Test Problem 2 (shallow metallic pool).

Variable	Value	
	SCDAP/ RELAP5	Reference A9-2
Sideward heat flux of metallic pool (MW/m^2)	1.91	1.22
Heat flux in oxidic pool at bottom center (MW/m^2)	0.04	0.14
Heat flux in oxidic pool at interface with metallic pool (MW/m^2)	0.55	0.50
Bulk temperature of metallic pool (K)	1799	1736
Bulk temperature of oxidic pool (K)	3080	3086
Thickness of crust on top of oxidic pool (mm)	4.6	6.2
CHF margin on external surface of vessel at elevation of metallic pool (heat flux/critical heat flux)	1.35	--

The stratification of a molten pool may result in a temporary decrease in the margin to CHF on the external surface of the reactor vessel. This aspect of molten pool behavior is indicated by the SCDAP/RELAP5 solution for Test Problem 3. In this test problem, the molten pool is well-mixed for the first 2000 s of the analysis. Then, the metallic material in the molten pool was defined to instantly separate from the oxidic material and form a pool on top of the oxidic pool. The metallic pool was initially at the temperature of the well-mixed pool, and then gradually cooled down to the temperature at which all the heat received from the oxidic pool was transferred to the reactor vessel. The transient temperatures of the metallic and oxidic parts of the molten pool are shown in Figure A9-2. At the instant of stratification of the pool (2000 s), the temperature of the metallic and oxidic materials was 2970 K. After stratification, the temperature of the oxidic material increased to 3110 K in about 500 s and the temperature of the metallic material decreased to 1690 K in about 500 s. After 2000 s, the molten pool was again in steady state condition. The change in margin to CHF caused by stratification of the molten pool materials is shown in Figure A9-3. In this figure, the ratio of the heat flux on the external surface of the reactor vessel to the critical heat flux is plotted. The heat flux ratio is plotted for the location at which this ratio had its maximum value, which was the external surface at the same elevation as the interface of the oxidic and metallic pools. At the instant of stratification, the heat flux ratio was calculated to be 0.26. After stratification, the heat flux ratio was calculated to increase in 320 s to a maximum value of 0.33, and then gradually decrease to a steady state value of 0.26.

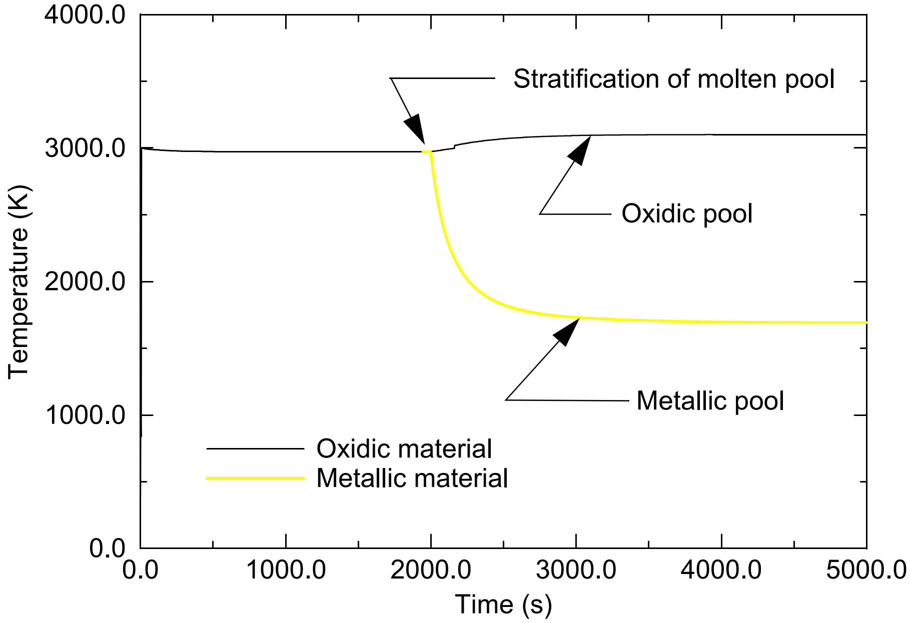

Figure A9-2. Temperature histories of oxidic and metallic parts of molten pool before and after stratification.

A study was also made of the sensitivity of calculated results to models for which two correlations are available. One of these models is the correlation for the shape of the heat flux on a hemisphere containing oxidic molten material with internal heat generation. The two available correlations are; (1) mini-ACOPO correlation[A9-1] and (2) UCLA correlation.[A9-3] Another model with two available correlations is the model for sideward heat flux from a metallic molten pool. The two available correlations are; (1) Churchill and Chu correlation,[A9-4] which contains the Prandtl number of the metallic pool, and (2) modified Globe and Dropkin.[A9-5] Calculations were performed using various combinations of these sets of correlations and for the molten pool configurations corresponding with Test Problem 1 in Table A9-2 namely the case of the deep metallic pool. The results of the sensitivity study are presented in Table A9-5.

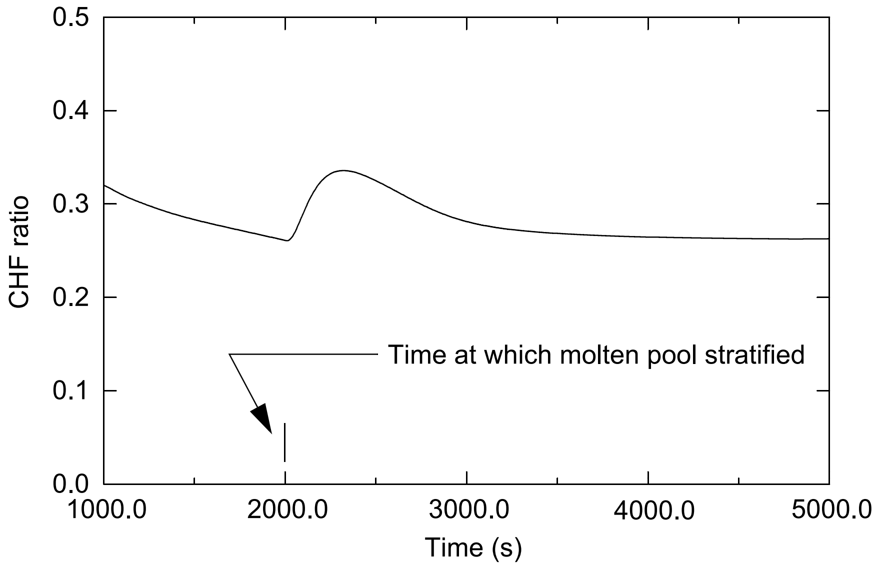

Figure A9-3. Ratio of heat flux to critical heat flux on external surface of lower head before and after stratification of molten pool.

The results show that the calculated behavior of the molten pool is not sensitive to the selection of correlations for flux shape and sideward heat transfer in the metallic pool.

Table A9-5. Sensitivity of calculated molten pool behavior to correlations for flux shape and sideward heat transfer in metallic pool

Flux shape correlation for oxidic pool	Sideward heat transfer correlation for metallic pool	Sideward heat flux of metallic pool (MW/m^2)	Maximum heat flux at oxidic pool and wall interface (MW/m^2)	Maximum ratio of heat flux to CHF on external surface
mini-ACOPO	Modified Globe and Dropkin	0.66	0.83	1.30
UCLA	Modified Globe and Dropkin	0.70	0.88	1.30
mini-ACOPO	Churchill-Chu	0.64	0.83	1.25

A9.2 Conclusions

The SCDAP/RELAP5 model for heat transfer in a stratified molten pool was assessed by; (1) comparison of its calculations with the calculations of a steady state model presented in the literature, (2) applying the model to the transient analysis of a stratified molten pool, and (3) examining the sensitivity of the model calculations to various combinations of heat transfer correlations. The SCDAP/RELAP5 and literature solutions of the steady state heat behavior of a stratified molten pool were generally in agreement for important aspects of heat transfer behavior such as the sideward heat flux from the metallic pool and the location of minimum margin to CHF on the external surface a hemispherical-shaped lower head containing the molten material. Both SCDAP/RELAP5 and the literature solutions calculated the minimum margin to CHF to occur at the elevation of the interface of the oxidic and metallic pools. Both SCDAP/RELAP5 and the literature solutions calculated that the sideward heat flux in a shallow metallic pool is about twice as large as that in a pool four times deeper. The SCDAP/RELAP5 calculations showed that the margin to CHF was not significantly affected by the depth of the metallic pool. The transient analysis of a molten pool showed that the occurrence of stratification after heatup of a previously well-mixed pool results in a significant temporary decrease in the margin to CHF. In the case analyzed, the margin to CHF decreased by 27% in the first 320 s after stratification, and then the margin to CHF gradually returned to a value nearly the same as that before stratification. The sensitivity study on heat transfer correlations showed that the calculated behavior of a stratified molten pool is not sensitive to the flux shape applied to the heat transfer from the oxidic pool or to the correlation for sideward heat transfer from the metallic pool.

A9.3 References

A9-1. T. G. Theofanous, C. Liu, S. Additon, S. Angelini, O. Kymalainen, and T. Salmassi, "In-Vessel Coolability and Retention of a Core Melt," Report DOE/ID-10460, Vol. 1, Chapter 5, July 1995.

A9-2. F. B. Cheung, K. H. Hadded, and Y. C. Liu, “A Scaling Law for the Local CHF on the External Bottom Side of a Fully submerged Reactor Vessel, NUREG/CR-0157, Vol. 2, February 1997, pp. 253-277.

A9-3. F. J. Afsia and V. K. Dhir, "An Experimental Study of Natural Convection in a Volumetrically Heated Spherical Pool Bounded on Top with a Rigid Wall, in In-Vessel Coolability and Retention of a Core Melt,” edited by Theofanous et al., Report DOE/ID-10460, Vol. 1, Appendix C, July 1995.

A9-4. Churchill, S. W. and H. S. Chu, *Int. J., Heat Mass Transfer,* 18, 1323 (1975).

A9-5. S. Globe and D. Dropkin, "Natural Convection Heat Transfer in Liquid Confined by Two Horizontal Plates and Heated from Below," J. Heat Transfer, 81, 1959, pp. 24-28.

A10. FLOW OF MELTED MATERIAL THROUGH POROUS DEBRIS

A10.1 Testing By Application To PWR Severe Accident Situation

The model for movement of melted core plate material through porous debris was tested by applying it to the analysis of a situation that may occur in a PWR during a severe accident. A schematic of the situation is shown in Figure A10-1. In this situation, melted core plate material is slumping onto the top of a porous debris bed in the lower head of the reactor vessel. This situation may occur after break up of jets of molten core material slumping into a pool of water in the lower head, and then boil off of all the water in the lower head by the broken up core material configured as a porous debris bed. The evaluation of the integrity of the lower head in this situation requires the analysis of the movement of the melted core plate material through the porous debris and the affect of this movement on the heatup of the lower head. If the ratio of the heat flux to the critical heat flux on the external surface of the lower head is not significantly increased by the movement of melted core plate material through the porous debris, then the structural integrity of the lower head is not adversely affected by a melting core plate.[A10-1]

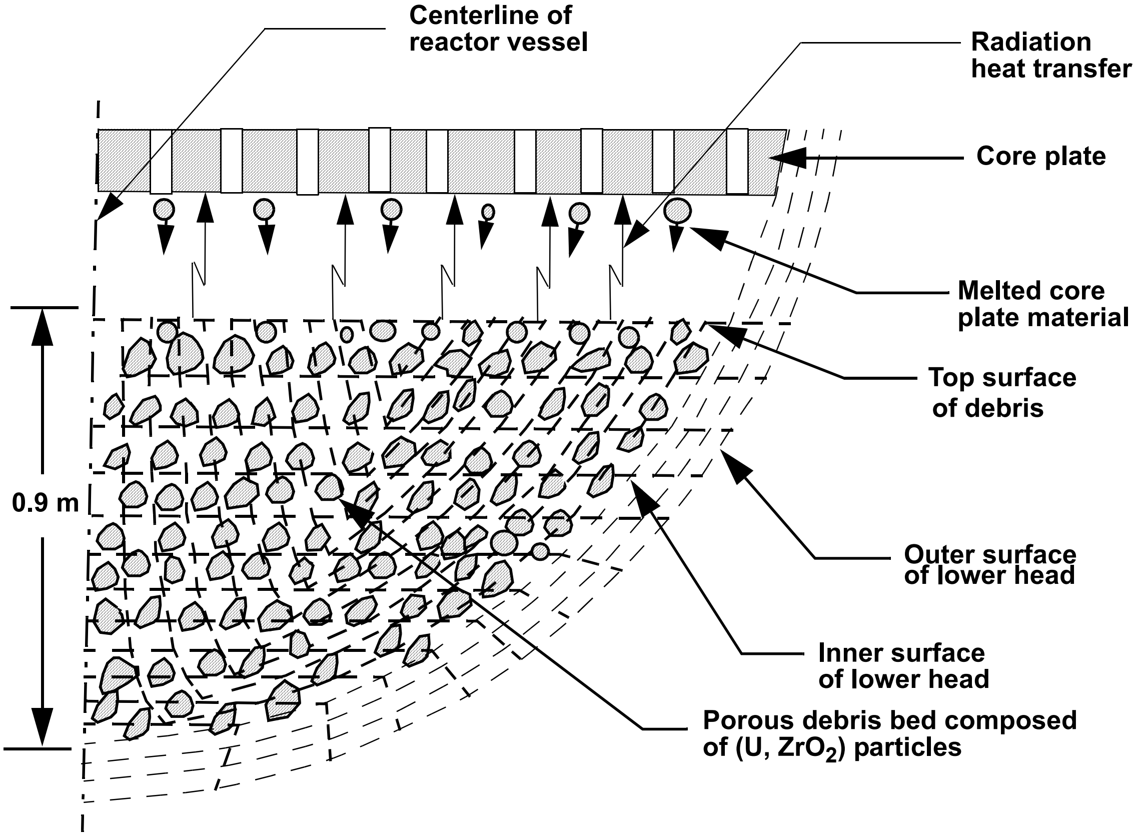
Centerline of reactor vessel
Radiation heat transfer
Core plate
Melted core plate material
Top surface of debris
Outer surface of lower head
0.9 m
Inner surface of lower head
Porous debris bed composed of (U, ZrO_2) particles

Figure A10-1. Schematic of system analyzed and nodalization of system.

In the assumed severe accident situation in a PWR, a 0.9 m deep porous debris bed is resting on the inner surface of the lower head of the reactor vessel. Decay heat in the debris has boiled all water out of the vessel. As a result, the vessel is filled with steam at a pressure of 0.2 MPa. Heat radiating from the top surface of the debris bed is melting the bottom of the stainless steel core plate located above the debris bed. The melted core plate material is slumping to the top of the debris bed and then permeating into the debris bed. The dashed lines in Figure A10-1 describe the finite elements and control volumes used in the numerical solution to represent the debris, lower head, and the core plate material permeating the debris. The intersections of the dashed lines are the nodes at which temperature was calculated. The bottom of the debris bed interfaces with the inner surface of the lower head. The outer surface of the lower head is in contact with a pool of water. The initial conditions and boundary conditions are summarized in Table A10-1. The initial temperature of the debris bed is 1727 K, which corresponds with the liquidus temperature of the core plate. The entire lower head is assumed to have an initial temperature of 400 K. The debris has an internal heat generation rate due to decay heat in the UO_2 of 1 MW/m^3. The debris bed has a porosity of 0.4 and is composed of UO_2 particles with a diameter of 3 mm. The analysis starts at a time of 0.0 s.

Table A10-1. Initial conditions and boundary conditions.

Characteristic	Value
Core plate material	stainless steel
Mass of core plate (kg)	25,000
Debris bed material	UO_2
Debris bed porosity	0.4
Maximum depth of debris bed (m)	0.9
Initial temperature of debris bed (K)	1727
Nuclear heat generation rate in debris bed (MW/m^3)	1
Diameter of particles in debris bed (mm)	3
Initial temperature of lower head of reactor vessel (K)	400
Thickness of lower head (m)	0.158
Composition of lower head	carbon steel
Heat transfer coefficient at interface of debris and lower head (W/m2 · K)	500

The melted core plate material was calculated to permeate to within 0.05 m of the bottom of the debris bed. Figure A10-2 is a plot of the axial distribution in debris bed saturation and temperature along its centerline for the time of 1500 s, when 30% of the core plate was calculated to have melted and slumped onto the debris bed. In general, the liquefied stainless steel was calculated to move downward through the debris at a rate of about 2 mm/s. Due to the cold temperature of the debris near the lower head, a crust of frozen core plate material formed about 0.05 m above the surface of the lower head. Above this crust, an ever increasing region of the debris bed was calculated to become saturated with core plate material. At 2000 s, when 50% of the core plate was calculated to have melted, a 0.4 m deep region along the centerline of the debris bed was calculated to be saturated.

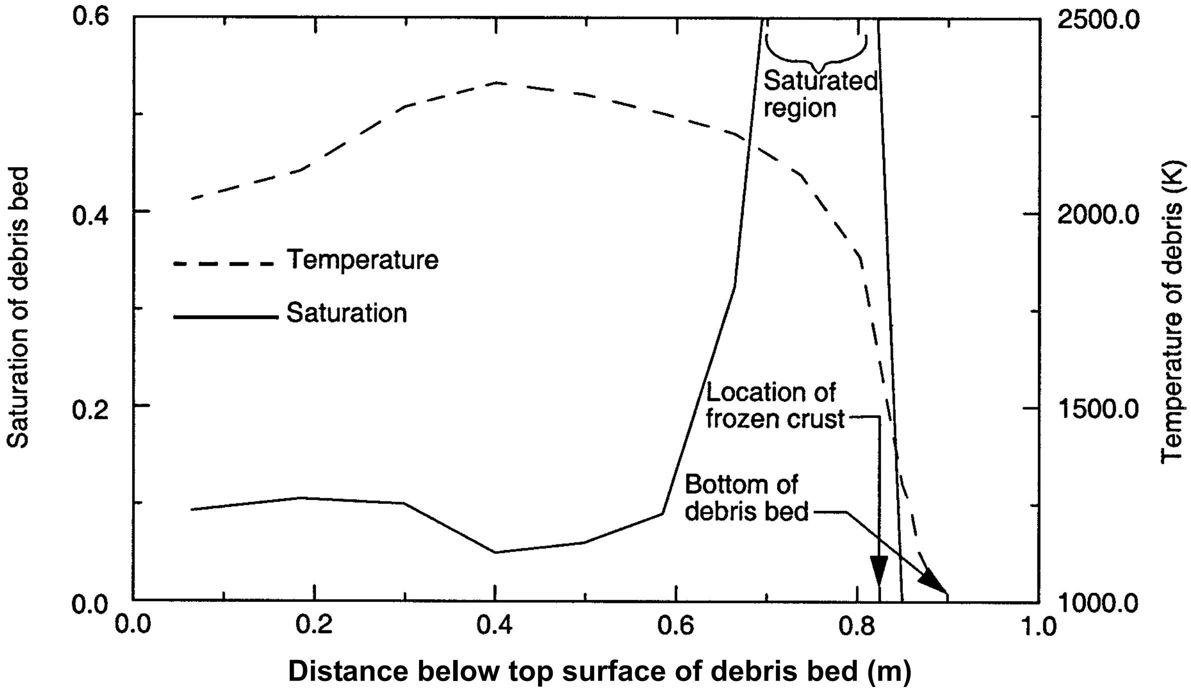

Figure A10-2. Distribution of debris bed saturation and temperature after melting of 30% of core plate (time of 1500 s).

The temperature of the debris bed was calculated to continually increase with time due to inadequate cooling. The calculated transient temperature distribution in the debris bed is plotted in Figure A10-3 for two locations along the centerline of the debris bed. The first location is at the top of the debris bed and the second location is 0.7 m below the top of the debris bed. At the location 0.7 m below the top surface, the temperature of the debris was calculated to increase at a rate of about 0.35 K/s. The temperature of the location at the top surface was calculated to increase at a slower rate due to contact with the relatively cool liquefied core plate material and due to convective and radiative cooling. At 2500 s, the temperatures of these two locations were calculated to be 2115 K and 2540 K, respectively.

The permeation of core plate material into the porous debris bed did not significantly increase the heat flux on the external surface of the lower head. Plots of the ratio of heat flux to critical heat flux (CHF) at the bottom center of the lower head for the cases of core plate material permeating through the debris bed and core plate material staying above the debris are compared in Figure A10-4. The CHF was calculated using the Cheung model.[A10-2]

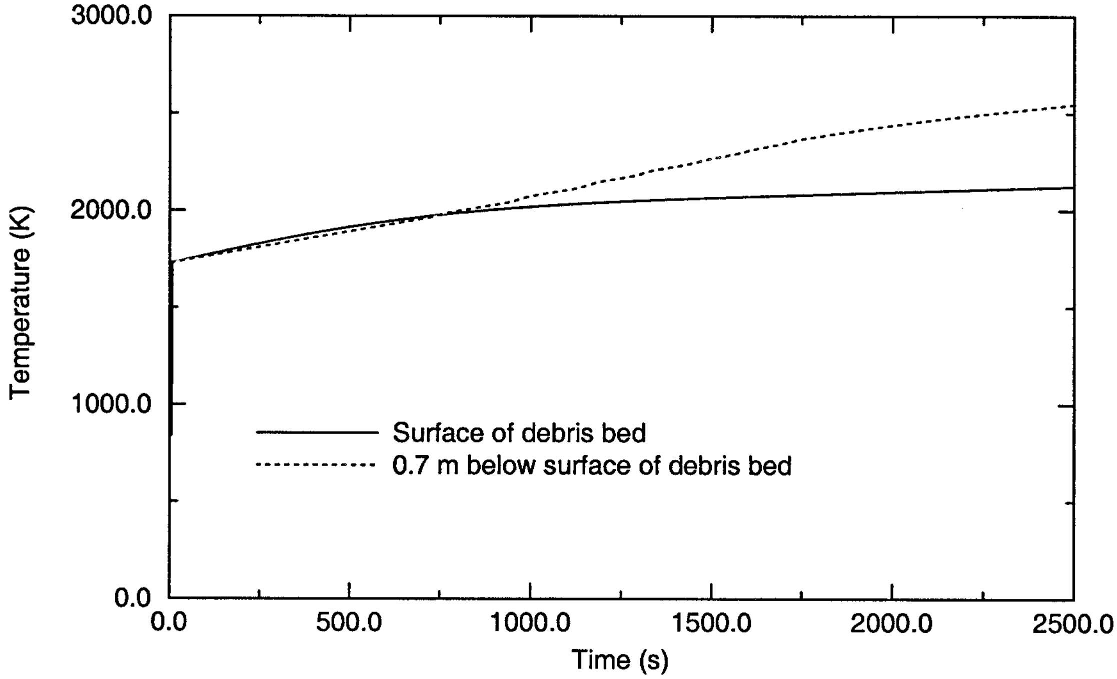

Figure A10-3. Temperature history of debris bed along its centerline.

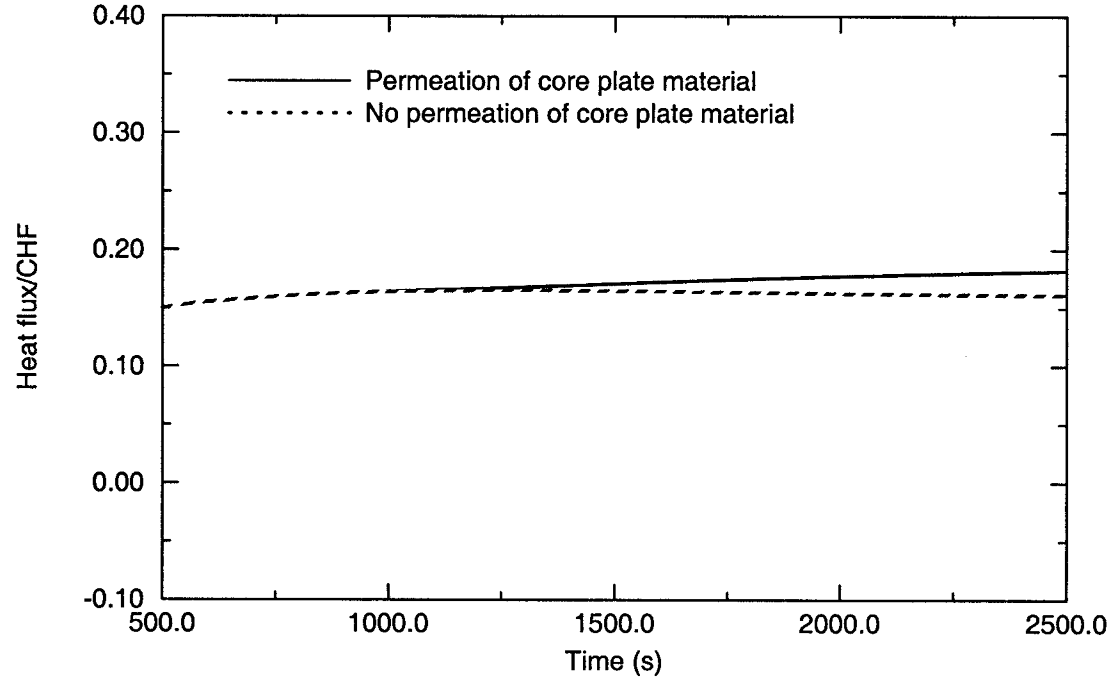

Figure A10-4. Ratio of heat flux to CHF on external surface at bottom center of lower head.

Generally, the value of CHF is smallest at the bottom center. As shown in this figure, the heat flux ratios for the two cases are nearly equal until 1000 s, after which the heat flux ratio becomes about 2%

greater for the case of core plate permeation. The somewhat higher heat flux for the case with permeation is due to the increase in effective thermal conductivity caused by the presence of core plate material in the debris. The calculated effective thermal conductivity for three levels of debris saturation are shown in Table A10-2. The effective thermal conductivity ranges from 2.5 $W/m \cdot K$ for a saturation value of zero to 9.4 $W/m \cdot K$ for fully saturated debris. This increase in thermal conductivity of the debris increases the rate of heat transfer from the interior of the debris to the lower head supporting the debris. Nevertheless, the heat flux is considerably less than the critical heat flux even for the case of permeation of core plate material into the debris bed.

Table A10-2. Effect of level of debris saturation on thermal conductivity of debris.

Level of debris saturation	Effective thermal conductivity $(W/m^2 \cdot K)$
0.0	2.5
0.20	4.7
1.0	9.4

A10.2 Testing By Evaluation of Internal Consistency and Reasonability

While experimental results do not exist as a benchmark for a direct assessment of the model for movement of melted core plate through porous debris, nevertheless an indirect assessment of the model can be performed by evaluating for internal consistency and reasonableness the calculations of the model. First, an evaluation of the capability of the model to conserve mass can be made by comparing the mass of stainless steel in the porous debris at any time with the cumulative mass of melted core plate material that slumped onto the top of the debris bed. Second, the implementation of the momentum equation for melted material can be checked for reasonableness by comparing the calculated rate of permeation of melted core plate material with an independent calculation of the rate of permeation. Third, an evaluation of the capability of the model to conserve energy can be made by checking the affect of the permeating core plate material on the temperature distribution in the porous debris.

Figure A10-2 has information for evaluating the capability of the melt movement model to conserve mass. This figure describes the distribution of melted core plate material in the porous debris bed at 1500 s. At the centerline of the lower head, a layer of debris with a thickness of 0.21 m is saturated with porous debris. By projecting a similar thickness of saturated layer under the entire core plate, the mass of core plate material is the saturated zone of the core plate is estimated to be 7300 kg. The mass of core plate material in the unsaturated zone of the debris bed is estimated to be 500 kg. Thus, the total mass of core plate material in the debris bed is estimated to be 7800 kg. The cumulative mass of melted core plate material that slumped onto the top of the debris bed at 1500 s was calculated to be 7600 s. The approximate agreement of the estimated mass in the debris bed with the cumulative mass slumping onto the top of the debris bed indicates the melt movement model is conserving mass.

The implementation of the momentum equation into the melt movement model was checked for reasonableness by comparing its calculation of the rate of permeation of melted material with an independent analysis of the rate of permeation. A plot as a function of elevation of the velocity of melted material as calculated by the melt movement model is shown in Figure A10-5. The velocity is plotted for the time of 1500 s. The calculations were part of the same calculations as shown in Figures A10-2 through A10-4. The plotted velocity is equal to the calculated superficial velocity divided by the product of the debris bed porosity times the debris bed saturation. The independent analysis was performed for a debris bed with the same porosity as that analyzed by the melt movement model but with a smaller particle diameter and somewhat different debris bed saturation.[A10-3] For the calculations shown in Figure A10-5, the debris bed porosity was 0.4, the diameter of the debris particles was 6 mm, and the average debris bed saturation was 0.07. For the independent analysis, the porosity of the debris bed was 0.4, the diameter of the debris particles was 2 mm, and the debris bed saturation was 0.1. As shown in Figure A10-5, the average velocity in the upper 0.6 m of the debris bed was about 7.5 mm/s. For a similar debris bed except for a smaller particle size, the independent analysis calculated a velocity of 2.4 mm/s for the rate of permeation of the melted material. This difference in calculated velocities is consistent with the difference expected for the difference in particle sizes in the debris beds analyzed by these two calculations. Thus, the comparison of the velocity calculated by the melt movement model in SCDAP/RELAP5/MOD3.3 with the independent analysis indicates the momentum equation for the melt movement model was correctly implemented into the code.

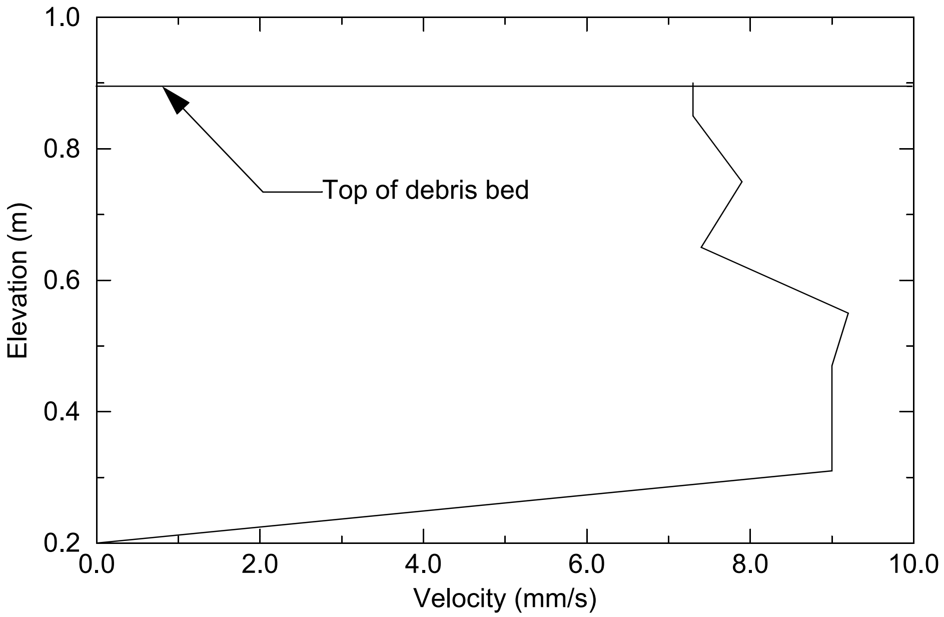

Figure A10-5. Axial distribution in velocity of melted material at 1500 s as calculated by melt movement model.

The reasonableness of temperature histories in Figure A10-3 indicates that the energy equation for the melt movement model was correctly implemented. The melting and slumping core plate material has a temperature of 1700 K and thus is cooler than the debris. The core plate material permeating into the debris is heated by the debris and thus has more influence on cooling the debris at the top surface than at the elevation of 0.7 m below the top surface. At the 0.7 m elevation, the temperature increase corresponds with almost an adiabatic heatup and the influence of the core plate material on the temperature of the debris is slight. These trends in the temperature histories at the two elevations indicate a correct implementation of the energy equation for the melt movement model into SCDAP/RELAP/MOD3.3 model.

A10.3 References

A10-1. T. G. Theofanous, C. Liu, S. Addition and A. Angelini, O. Kymalaien, and T. Salmani, "In-Vessel Coolability and Retention of Core Melt," DOE/ID-10460, Vol. 1.

A10-2. F. B. Cheung, K. H. Hadded, and Y. C. Liu, "A Scaling Law for the Local CHF on the External Bottom Side of a Fully Submerged Reactor Vessel," NUREG/CP-0157, Vol. 2, February 1997, pp. 253-277.

A10-3. L. J. Siefken, "SCDAP/RELAP5 Modeling of Movement of Melted Material Through Porous Debris in the Lower Head," INEEL/EXT-98-01178 Rev. 2, October 1999.

A11. MOLTEN FUEL-COOLANT INTERACTION

The Fuel-Coolant Interaction (FCI) model was assessed using the results of two FCI experiments. The first FCI experiment used for the assessment was one of the MAGICO-2000 series of experiments performed at the University of California, Santa Barbara, California.[A11-1] This experiment involved slumping of a cloud of small hot particles into a column of water and measuring the transient void fraction in the water and the transient position of the particles. The second FCI experiment used for assessment was one of the FARO experiments performed by Magallon and Hohmann at the Safety Technology Institute, Ispra, Italy.[A11-2] This experiment involved slumping a jet of hot material into a column of water and measuring the transient pressure in the water and the fraction of break up of the jet of slumping material.

The applicability of the FCI Model to severe accident analysis was tested by calculating the affect of FCI on reactor coolant system behavior for several different ambiences.

A11.1 Assessment with a MAGICO-2000 experiment

An experiment identified as Run Z1500/0.2 in the MAGICO-2000 series of experiments was used to assess the capabilities of the FCI model to calculate the motion and heat transfer of a cloud of hot particles made of ZrO_2.[A11-1] A schematic of the experiment is shown in Figure A11-1.

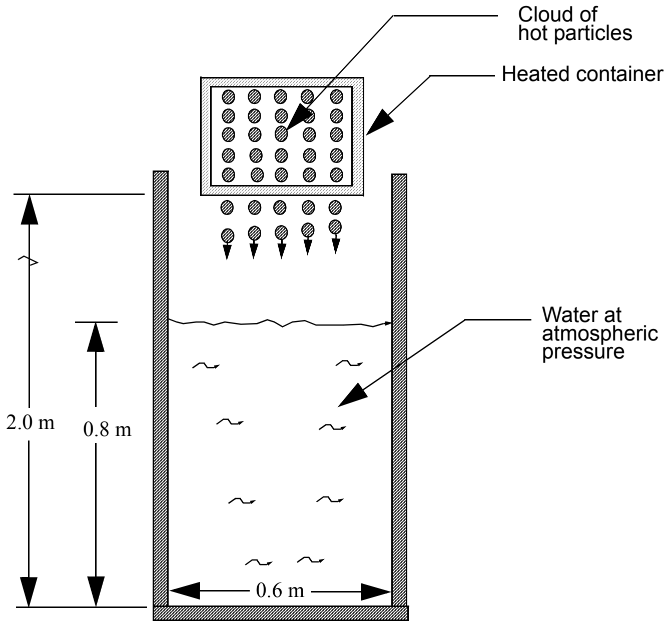

A11-1. Schematic of MAGICO - 2000 Test Arrangement.

The characteristics of Run Z1500/0.2 are shown in Table A11-1. An important feature of this experiment is its accurate characterization of the cloud of hot particles plunging into a column of water. This feature is the result of the absence of break-up of the material interacting with water, which in turn is a result of using a cloud of hot particles instead of a jet of molten material. The measurements obtained during the experiment included: (1) void fraction for a small period of time at one location in the test facility, (2) location of the cloud of particles as a function of time, and (3) transient swell of water level.

Table A11-1. Characteristics of Run Z1500/0.2 of MAGICO-2000 Experiment.

Characteristic	Value
Initial height of column of water (m)	0.8
Diameter of test vessel (m)	0.6
Distance of free fall of particles (distance from initial position to initial water surface) (m)	1.2
Initial pressure in test vessel (MPa)	0.1
Water subcooling (K)	0.0
Velocity of particles at surface of water (m/s)	4.8
Initial temperature of particles (K)	1648
Mass of particles (kg)	6.2
Pour equivalent diameter (m)	0.225
Pour duration (s)	0.33
Chemical composition of particles	ZrO_2

SCDAP/RELAP5/MOD3.3 with the FCI model was used to calculate the particle-coolant interaction observed in Run Z1500/0.2 of the MAGICO-2000 series of experiments and the calculated results were found to be in fairly good agreement with the measured results. The calculated and measured location of the front of the cloud of plunging particles are compared in Figure A11-2. The good agreement of calculations with the measurements indicates that the FCI model is correctly calculating the motion of the particles in response to gravity and drag from contact with water. The calculated and measured liquid volume fraction in the test vessel at an elevation of 0.65 m above the bottom of the test vessel are compared in Figure A11-3. The only available measurement of liquid volume fraction occurred at 0.45 s (0.35 s after initial contact of the particles with water). At this time, the calculated liquid volume fraction is significantly greater than the measured value. The calculated and measured water level swell as a function of time are compared in Figure A11-4. As shown in Figure A11-4, the approximate agreement of the calculations with the measurements indicates that the calculations for the macroscopic hydrodynamic behavior of the coolant account for the basic phenomena. .   .

The comparisons shown in Figures A11-3 and A11-4 indicate that the drag force on vapor may be overpredicted for the situation of vapor production during fuel-coolant interaction. In Figure A11-3, the calculated volume fraction of liquid at the 0.65 m elevation at the time of 0.45 s is greater than the measured value. This discrepancy may be due to vapor produced below this elevation being calculated to flow too slowly upward due to an overprediction of the drag force on the vapor. In Figure A11-4, the calculated swell of water is greater than the measured swell after 0.4 s. This discrepancy may be due to an underprediction of the rate at which vapor leaves the top of the water column, and in turn due to an overprediction of the drag force on the vapor.

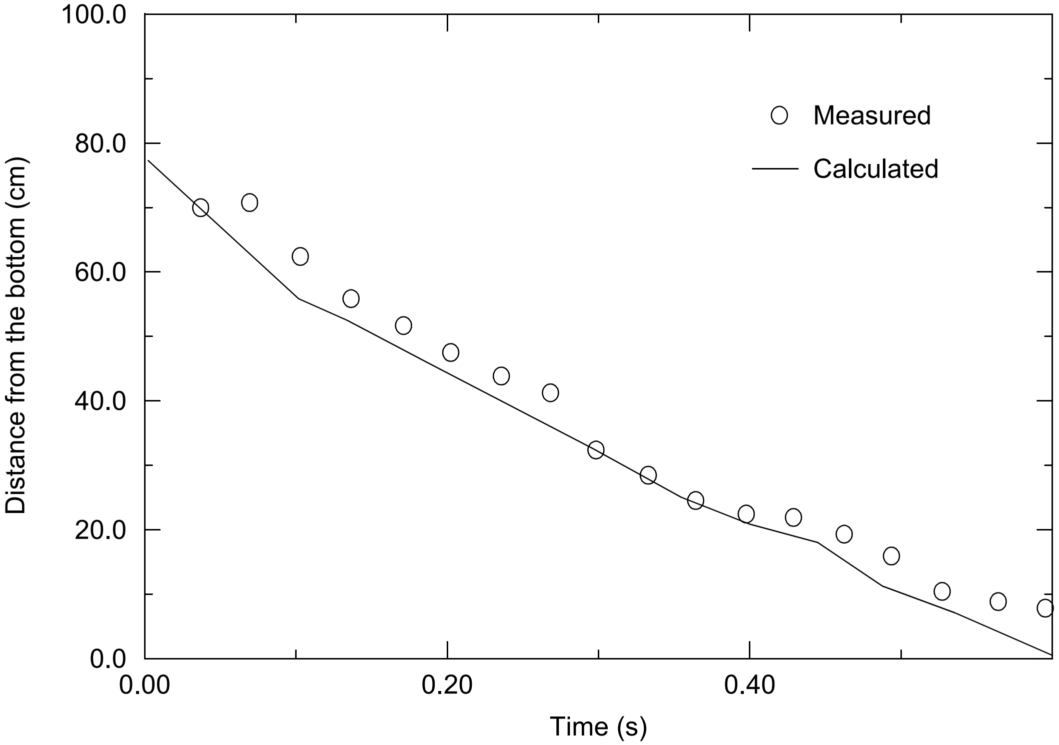

A11-2. Comparison of calculated and measured advancement of the front of cloud of particles for MAGICO-2000 experiment.

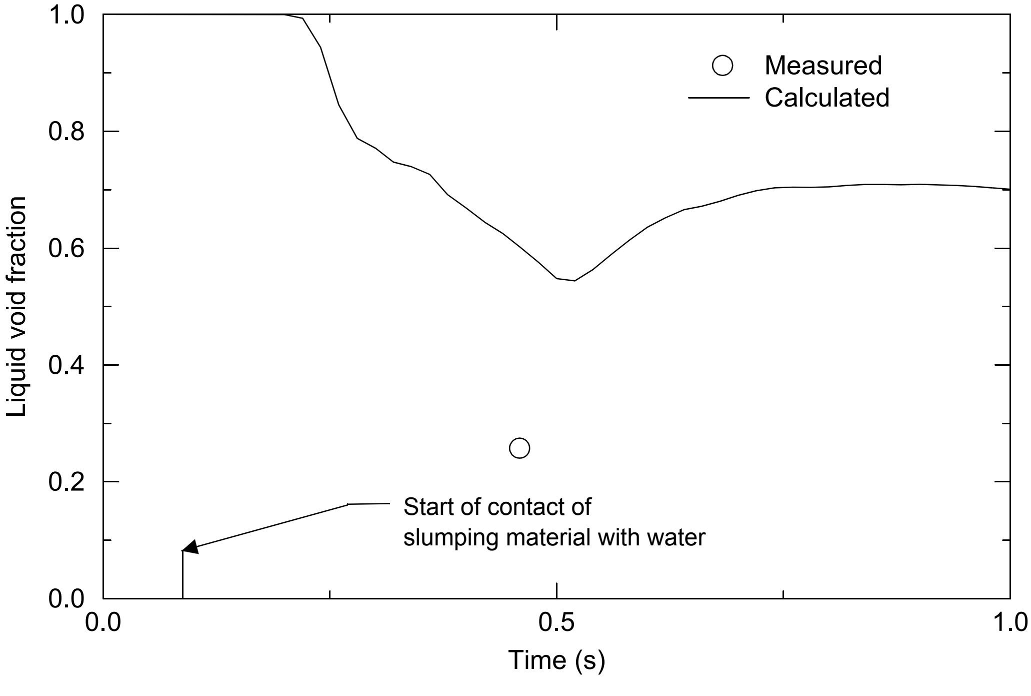

A11-3. Calculated and measured volume fraction of liquid at elevation of 0.65 m for MAGICO-2000 experiment.

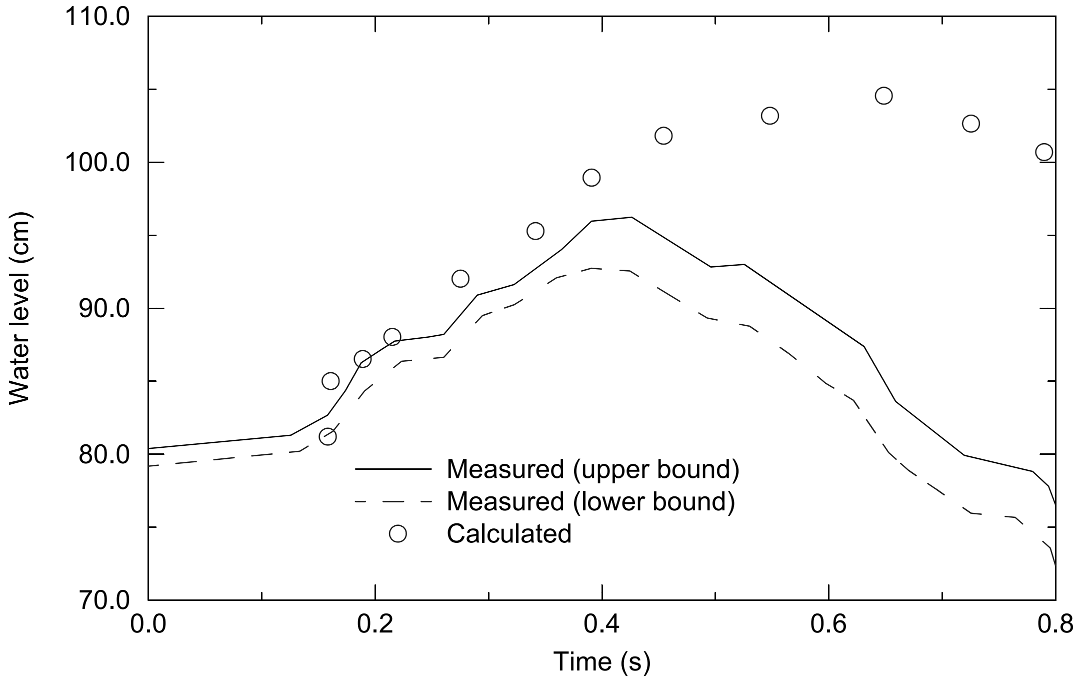

A11-4. Calculated and measured water level swell for MAGICO-2000 experiment.

A11.2 Assessment with a FARO Experiment

An experiment identified as Test L-08 in the FARO series of experiments was used to assess the capabilities of the FCI model to calculate the break-up of a jet of molten material that plunges into a column of water and to calculate the heat transfer between the material and the water with which it interacts.[A11-2] The characteristics of Test L-08 are shown in Table A11-2. A schematic of the experiment is shown in Figure A11-5. An important feature of this experiment is the measurement of the fraction of the jet of molten material that broke up and the size of the particles resulting from break-up. The measurements obtained during the experiment that are useful for comparison with calculations include; (1) transient pressure in the test vessel, (2) fraction of break-up of the jet of molten material, (3) size of particles resulting from break-up, and (4) transient temperature of the plate onto which the slumping material settled.

Table A11-2. Characteristics of Test L-08 of FARO Experiments

Characteristic	Value
Initial height of column of water (m)	1.0
Diameter of test vessel (m)	0.71
Diameter of jet nozzle (m)	0.1
Distance of free fall of jet (distance from jet nozzle to initial water surface) (m)	1.53
Initial pressure in test vessel(MPa)	5.8

Table A11-2. Characteristics of Test L-08 of FARO Experiments (Continued)

Characteristic	Value
Volume of gas (H_2O, Ar) above initial surface of water (m^3)	0.875
Initial temperature of column of water (K)	536
Water subcooling (K)	10
Velocity of jet at surface of water (m/s)	~10
Initial temperature of material in jet (K)	3023
Mass of material that slumped (kg)	44
Composition of material that slumped (wt %)	80% UO_2, 20% ZrO_2
Pour duration (s)	0.37

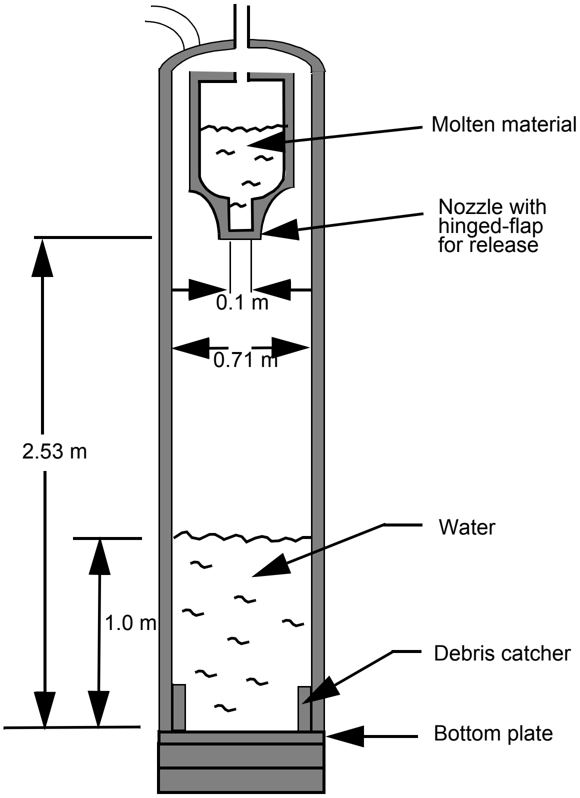

A11-5. Schematic of FARO Test Arrangement.

SCDAP/RELAP5/MOD3.3 with the FCI model was used to calculate the fuel-coolant interaction occurring in Test L-08 of the FARO series of experiments and the calculated results were found to be in fairly good agreement with the measured results. The calculated and measured pressure in the test vessel are compared in Figure A11-6. The calculated and measured pressure histories were similar in shape but the calculated rate of increase in pressure was about 50% more rapid than the measured rate of increase in pressure. The maximum calculated increase in pressure was 112% of the measured maximum increase in pressure. No other transient measurements were available for comparing with calculations. A summary of the experimental data and the corresponding calculated values is shown in Table AA11-3. A break-up of 70% of the jet of slumping material was calculated, which is slightly greater than the 68% break-up that was measured. The mean size of the broken-up material based on weight was calculated to be 0.56 mm, which is significantly less than the measured mean size of 3.8 mm. The plate at the bottom of the test vessel was heated by material that settled on the plate. The calculated and measured maximum increases in temperature of this plate were 352 K and 275 K, respectively. The level swell of water is a measure of the rate of steam production and of the spatial distribution of steam production. The calculated and measured level swells of water were 0.25 m and 0.15 m, respectively.

Table A11-3. Summary of comparison of measured and calculated values for Test L-08 of FARO.

Variable	Measured	Calculated
Fraction of break-up of slumping material	0.68	0.70
Mean size of broken up material based on weight (mm)	3.8	0.56
Maximum pressure increase due to FCI (MPa)	1.70	1.90
Maximum temperature increase of bottom plate (K)	275	352
Level swell of water (m)	0.15	0.25

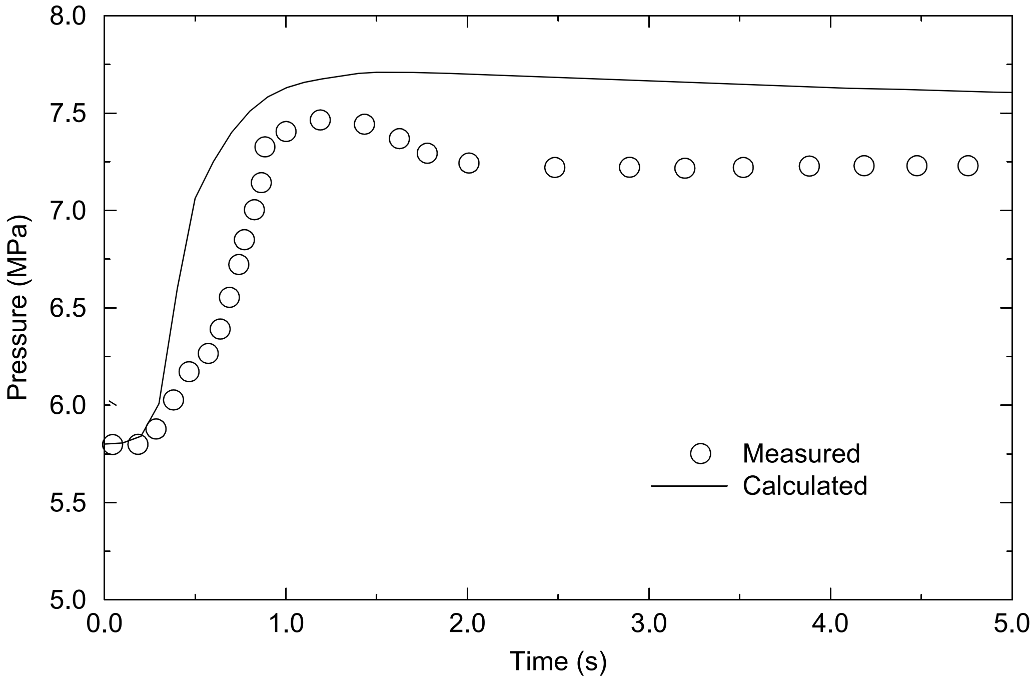

A11-6. Calculated and measured pressure histories for FARO Test L-08.

The greatest discrepancy between calculated and measured values for Test L-08 of the FARO experiments was in the mean size of particles resulting from break-up of the slumping material. The calculated size was significantly smaller than the measured size. This discrepancy was a factor in the calculated rate of increase in pressure being about 50% more rapid than the measured rate of increase in pressure. The discrepancy between calculated and measured particle size may be due to one or more reasons. One reason may be the use of an incorrect value for the interfacial surface tension of a mixture of UO_2 and ZrO_2 that is in contact with liquid water and steam. The calculated mean particles size is proportional to the value of this material property. A value of 0.45 N/m was used in the calculations, which is the most appropriate value available from MATPRO. This value is applicable for a mixture of Zr-U-O that is in contact with Zr cladding. This value has a large expected standard error; its upper bound value is estimated to be 1.45 N/m. The use of the upper bound value in the calculations would result in a significant increase in the calculated mean size of the broken-up material.

A11.3 Application of FCI Model to Severe Accident Analysis

This section evaluates the applicability of the FCI model to severe accident analysis. Five cases of a test problem are calculated that involve calculations of FCI under conditions that are possible in the event of a severe accident in a PWR. For each case, a core meltdown in a PWR is assumed to have occurred that results in molten material slumping into a pool of water in the lower head of the reactor vessel. A schematic of the test problem is shown in Figure A11-7.

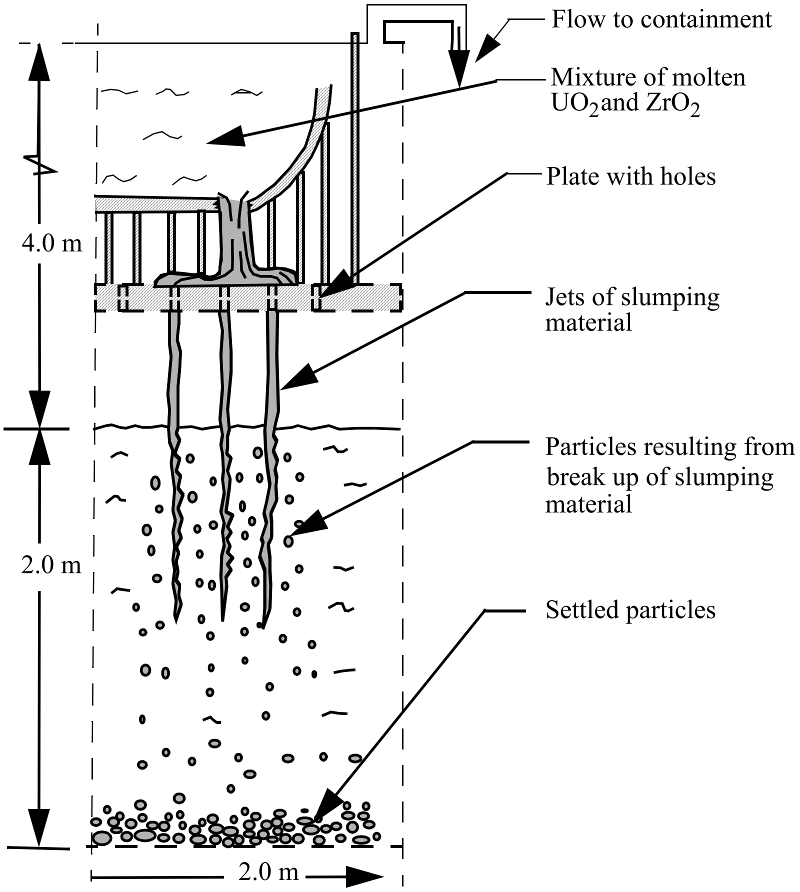
Flow to containment
Mixture of molten UO_2 and ZrO_2
Plate with holes
Jets of slumping material
Particles resulting from break up of slumping material
Settled particles
4.0 m
2.0 m
2.0 m

A11-7. Schematic of application of FCI model to severe accident analysis.

Table A11-4 identifies the slumping parameters for each of the five cases that were analyzed.

Table A11-4. Characteristics of typical severe accident conditions with possibility for FCI.

Characteristic	Case 1	Case 2	Case 3	Case 4	Case 5
Initial height of column of water (m)	2.0	2.0	2.0	2.0	2.0
Diameter of vessel (m)	2.0	2.0	2.0	2.0	2.0
Diameter of jets (mm)	137.	27.5	27.5	27.5	27.5
Number of jets	1	25	1	2	4
Velocity of jet (m/s)	5.0	5.0	6.25	6.25	6.25
Initial pressure in vessel (MPa)	0.17	0.17	0.17	0.17	0.17
Volume of steam above initial surface of water (m^3)	50	50	50	50	50
Initial temperature of pool of water (K)	388.3	388.3	388.3	388.3	388.3
Water subcooling (K)	0.0	0.0	0.0	0.0	0.0
Initial temperature of material in jet (K)	3023.	3023.	3023.	3023.	3023.
Total mass flow rate of slumping material (kg/s)	600	600	30	60	120
Wt% UO_2 in slumping material	66.7	66.7	66.7	66.7	66.7
Wt% ZrO_2 in slumping material	33.3	33.3	33.3	33.3	33.3
Duration of slumping (s)	10	10	10	10	10

In each of the cases, the system pressure at the start of slumping was 0.17 MPa and the water had no subcooling. Also, the initial height of the column of water, the diameter of the reactor vessel, and the initial volume of steam above the water level were the same for all of the cases. The initial volume of steam above the water level was assumed to be 50 m^3, which is a volume that is of the same order of magnitude as the volume of a typical PWR reactor vessel. The number of jets varied from 1 to 25 for the five cases and the diameter of the jets was 27.5 mm for four of the cases and 137.3 mm for one case. The dividing of a single large jet into several small jets is possible when a single jet slumps onto the core plate and then the material in the jet spreads out over the plate and flows through holes in the core plate. The diameter and number of jets were adjusted so as to maintain a jet velocity at the time of initial contact with water that was in the range of 5.0 m/s to 6.25 m/s. The total mass flow rate of the jets varied from 30 kg/s to 600 kg/s. The mass flow rate of 600 kg/s is representative of the mass flow rate of the slumping core material in the TMI-2 accident.[A11-3] In all cases, the slumping material was at a temperature of 3023 K and was composed of 66.7 wt% UO_2 and 33.3 wt% ZrO_2. Each case may have about an equal probability of occurring. For each case, the material was assumed to slump at a constant rate for 10 s. For each case, calculations were performed of the behavior of the slumping material and of the behavior of the water and steam in the reactor vessel. Calculation results are presented that provide a basis for evaluating the internal consistency and realism of the model and that show the sensitivity of FCI to parameters such as the rate of slumping and the number and size of the jets of slumping material.

SCDAP/RELAP5/MOD3.3 with the FCI model was used to calculate the behavior of the slumping material for the five cases, and the results showed that the extent of break-up of the slumping material is a strong function of the rate of slumping of material. The results of the calculations for the five cases are summarized in Table A11-5.

Table A11-5. Summary of results for FCI under conditions typical for severe accident in PWR.

Variable describing FCI	Case 1	Case 2	Case 3	Case 4	Case 5
Fraction of break-up of slumping material	0.15	0.28	1.0	0.95	0.74
Pressure increase after 10 s of slumping (MPa)	0.10	0.17	0.01	0.08	0.11
Swell of water level (m)	0.65	2.00	0.15	0.35	0.85

Time in this table refers to time since start of slumping. The fraction of break-up varied from 1.0 for the case of a single small diameter jet with a mass flow rate of 30 kg/s to 0.15 for the case of a single large diameter jet with a mass flow rate of 600 kg/s. The increase in pressure caused by FCI was a function of the number of jets of slumping material. For the cases with small jets (diameter of 27.5 mm). the maximum increase in pressure for the case of four jets was approximately nine times greater than the maximum increase in pressure for the corresponding case of a single jet.

Plots of the calculated pressure in the vessel provide additional insights into the performance of the FCI model. The calculated transient pressures in the vessel for the first two cases (600 kg/s rate of slumping) are compared in Figure A11-8. This figure shows that slumping material which divides into several jets will produce a significantly more rapid rate of steam production and thus a more rapid rate of increase in pressure than slumping material that remains a single jet. The dividing of a single large jet into several small jets is possible when a single large jet slumps onto the core plate and then the material in the jet spreads out over the plate and flows through holes in the core plate. For both the single jet and 25 jet cases in Figure A11-8, the pressure history indicates that the calculated FCI was most vigorous during the first 4 s of slumping. The calculated transient pressures for the last three cases are compared in Figure A11-9. For these three cases, the mass flow rate per jet was 30 kg/s and the number of jets varied from a single jet for Case 3 to four jets for Case 5. The pressure increase for the four jet case was about double the pressure for the single jet case.

The calculated behavior of the water is indicated by plots of the calculated volume fraction of liquid water as a function of elevation. The transient volume fractions of liquid for a range of elevations above and below the initial elevation of the top of the column of water are plotted in Figure A11-10 for Case 1 (single large jet). This figure shows that a swell of 0.5 m occurred in the column of water. Figure A11-11 shows the calculated transient volume fractions of liquid for Case 2 (25 small jets) for elevations 1.0 m

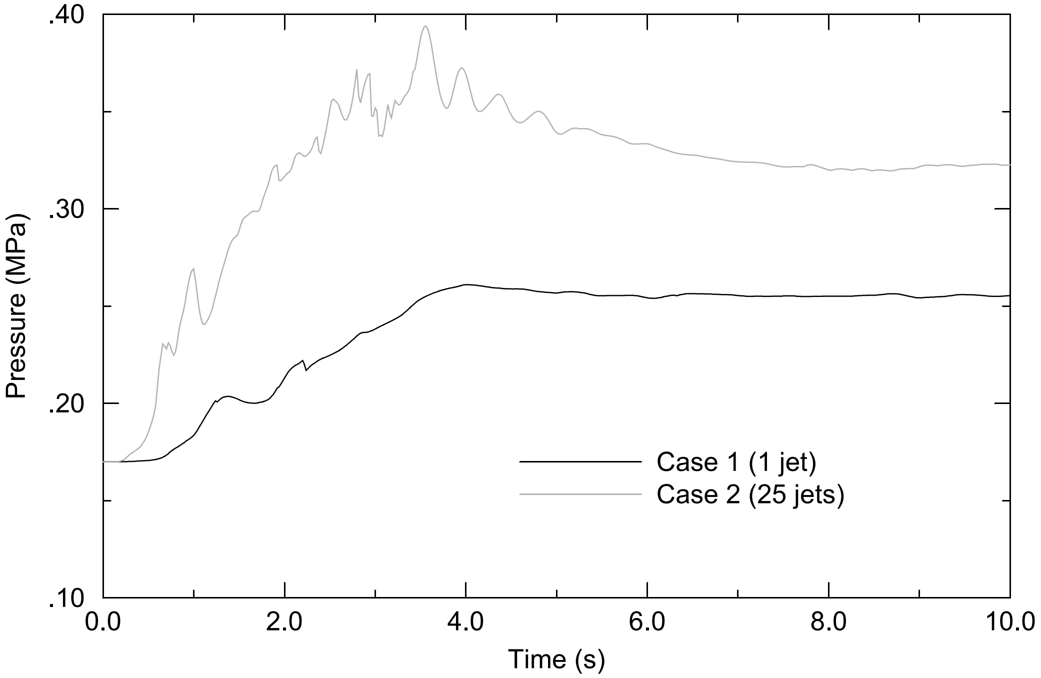

A11-8. Calculated transients pressures in vessel for Case 1 (1 large jet) and Case 2 (25 small jets).

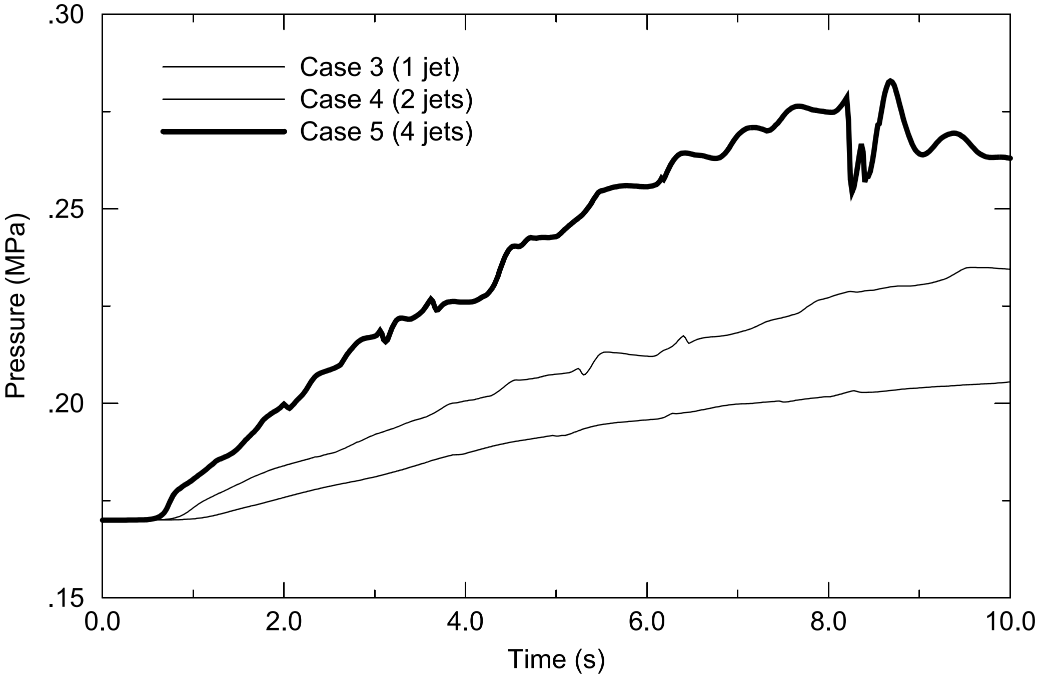

A11-9. Calculated transient pressure in vessel for Case 3 (1 small jet), Case 4 (2 small jets) and Case 5 (4 small jets).

above and below the initial elevation of the top of the column of water. This figure shows that a significant amount of water was pushed upwards a distance of 1.0 m for about 8 s.

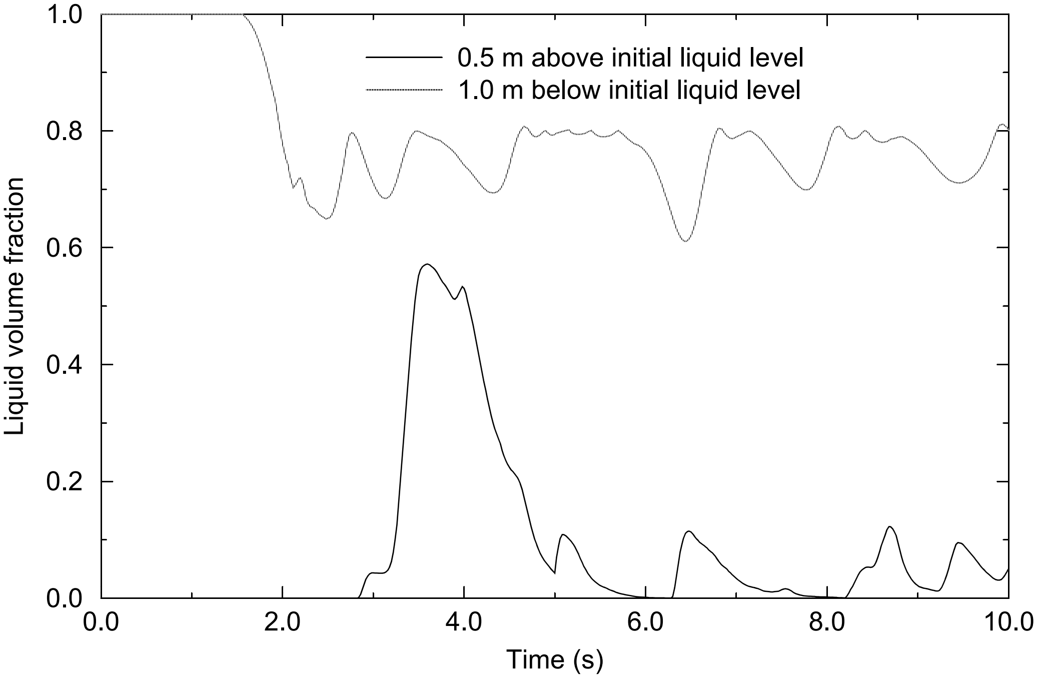

A11-10. Transient volume fractions of liquid water at various elevations for Case 1 (single large jet).

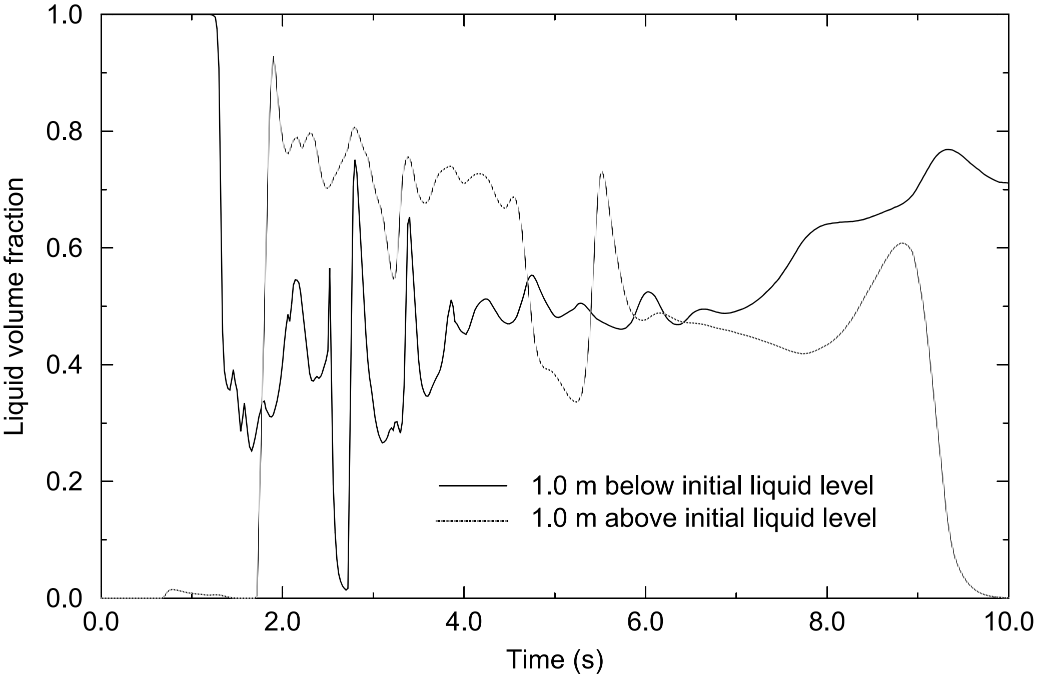

A11-11. Transient volume fractions of liquid at various elevations for Case 2 (25 small jets).

A11.4 Summary of Assessment Results

The FCI model implemented into the SCDAP/RELAP5/MOD3.3 code was subjected to an assessment that was limited in scope but which indicates that the model and its implementations are complete enough for preliminary calculations for severe accident analysis. The model and its implementation were assessed using the results of MAGICO-2000 and FARO experiments. The assessment showed that the model is calculating several important features of FCI fairly well, including the motion of particles resulting from FCI, the fraction of break-up of slumping material, the rate of steam production from FCI, and the maximum pressure increase in a region in which FCI is occurring. The FCI model calculates that a jet that divides into several jets due to contact with a porous structure such as a core plate will break up significantly more than when a division into several jets does not occur. This result is consistent with the results of experiments on FCI performed at ANL.[A11-4]

The assessment also showed that the FCI model and its implementation and material property data base are open to improvement. The assessment showed that the FCI model underpredicts the size of particles resulting from FCI and underpredicts the volume fraction of steam in regions where FCI is occurring. The resolution of these discrepancies between calculated and measured results may require the following actions. First, a more accurate correlation for the interfacial surface tension of a mixture of molten UO_2 and ZrO_2 in contact with water needs to be obtained. Second, the RELAP5 calculation of flow regime mapping and steam velocity in a region with FCI may need to be improved. The first two steps to this improvement are suggested to be; (1) impose a flow regime that is consistent with the configuration of steam in a region where FCI is occurring, and (2) eliminate in the implementation of the FCI model the assumption that the momentum change of the slumping material is small compared to the momentum of the water and steam.

A significant number of experiments other than those used in this report are available for assessing the FCI modeling in SCDAP/RELAP5/MOD3.3 and for providing insights on how to best improve the modeling. These experiments include other FARO experiments[A11-5,A11-6,A11-7A11-8,A11-12] and the fragmentation and quenching experiments performed at ANL.[A11-3, A11-9] Table A11-6 lists some of the experimental conditions from the FARO test series and Table A11-7 gives results obtained from the tests. The tests performed at ANL differed somewhat from those performed in the FARO test series. The ANL experiments had a lower system pressure, water subcooling, metal contents in the melt, and melt jet leading edge information. The data from the ANL experiments CCM-5 and CCM-6 are given in Table A11-8. Several other sources of data for assessing the FCI model are also available. There are test results available from KROTOS series of experiments[A11-8] (number 33 and 37, without steam explosion) performed by the Joint Research Center, Ispra, Italy, FITS series of experiments performed by Sandia National Laboratory,[A11-10] and other MAGICO experiments performed by Theofanous and coworkers.[A11-11]

Table A11-6. Experiment parameters for FARO series of experiments

	L-06 (Scoping test)	L-08 (Quenching test)	L-11	L-14
Melt:				
Composition (wt%) -				
$UO_2 + ZrO_2 + Zr$	80 + 20 + 0	80 + 20 + 0	76. +19.2+ 4.1	80 + 20 + 0
Mass (kg)	18	44	151	125
Temperature (K)	2923	3023	2823	3073 $\pm$ 50
Delivery nozzle diam. (m)	0.1	0.1		0.1
Metallostatic head in			0.1	
release vessel (m)	0.34	0.47	0.59	0.57
Free fall in gas (m)	1.66	1.53	1.09	1.04
Water:				
Mass (kg)	120	255	608	623
Depth (m)	0.87	1.00	2.00	2.05
Initial mean temp. (K)	539	536	535	537
Gas phase:				
Composition (wt(%) -				
steam + argon	83 + 17	70 + 30	77 + 23	77 + 23
Volume (m^3)	0.464	0.875	1.280	1.260
Initial pressure (MPa)	5.0	5.8	4.9	5.0
Initial mean temp. (K)	543	536	536	536
Water container:				
Diameter (m)	0.470	0.710	0.710	0.710
Volume (m^3)	0.640	1.3	1.3	1.3

Table A11-7. Summary of FARO experimental results.

	L-06 (Scoping test)	L-08 (Quenching test)	L-11	L-14
Melt:				
Delivery time (s)	0.28	0.37	~ 1	~ 1
Broken-up particles (kg)	12	30	151	105
Collected at the bottom plate (kg)	6	14	0	20
Particles mean diam. (mm)	4.5	3.8	3.5	4.8
Pressure increase (MPa):				
Before melt-water contact	0.4	0.3	0.3	0.1
Shortly after contact	1.1 (at 1.2 s)	1.8 (at 1.2 s)	5.1 (at 2.15 s)	2.8 (at 2.4 s)
Long-term maximum	1.6 at 12 s)	1.8 (at 20 s)	2.8 (at 22 s)	3.4 (at 30 s)
Maximum rate (MPa/s)	1.6	3.3	4.8	2.4

Table A11-7. Summary of FARO experimental results. (Continued)

	L-06 (Scoping test)	L-08 (Quenching test)	L-11	L-14
Temperature increase (K):				
Gas phase (top of vessel)	40	43	67	77
Water	15	23	27	28
Level swell:				
Maximum indicated by level meters (m)	0.130	0.410	1.000	1.100
Bottom plate:				
Maximum temperature increase (K)	Not available	275	20	330

Table A11-8. Summary of CCM-5 and CCM-6 experimental parameters

	CCM-5	CCM-6
Melt:		
Composition (wt%)		
- $UO_2 + ZrO_2$ + stainless steel (Fe + Cr + Ni)	60 + 16 + 24 (67 + 21 + 12)	60 + 16 + 24 (67 + 21 + 12)
Mass (kg)	10.87	11.34
Initial melt superheat (K)	157	157
Delivery nozzle diam. (m)	0.0508	0.0508
Free fall in gas (m)	0.34	0.34
Water:		
Depth (m)	1.07	1.07
Initial water subcooling (K)	49.0	2.50
Gas phase:		
Composition (mole%) - steam + argon	17 + 83	96 + 4
Volume (m3)	0.46	1.14
Initial pressure (MPa)	0.117	0.114
Initial mean temperature (K)	363	404
Water container:		
Pressure at onset of melt release (MPa)	0.117	0.202

A11.5 References

A11-1 S. Angelini, T. G. Theofanous and W. W. Yuen, "The Mixing of Particle Chloride Plunging into Water," *Proceedings of the 7-th International Meeting on Nuclear Reactor Thermal-Hydraulics, (NURETH-7), Saratoga Springs, NY, September 1995, NUREG/CP-0142*, pp. 2359-2389.

A11-2 D. Magallon and H. Hohmann, "Experimental Investigation of 150-kg scale Corium Melt Jet Quenching in Water," *Proceedings of the 7th International Meeting on Nuclear Reactor Thermal Hydraulics (NURETH-7)*, *Saratoga Springs, NY, September 1995, NUREG/CP-0142*, pp. 1688-1711.

A11-3 J. M. Broughton, P. Kuan, D. A. Petti, and E. L Tolman, "A Scenario of Three Mile Island Unit 2 Accident," *Nuclear Technology, 87, August 1989*, pp. 34-53.

A11-4 C. C. Chu, J. J. Sienicki, and B. W. Spencer, "Validation of the THERMAL-1 Melt-Water Interaction Code," *Proceedings of the 7th International Meeting on Nuclear Reactor Thermal Hydraulics (NURETH-7), Saratoga Springs, NY, September 10-15, 1995, NUREG/CP-0142,* pp. 2359-2389.

A11-5 D. Magallon and H. Hohmann, "High Pressure Corium Melt Quenching Tests in FARO," *Nuclear Engineering and Design, 155, 1995*, pp. 253-270.

A11-6 H. Hohmann, D. Magallon, H. Schins, and A. Yerkess, "FCI Experiments in the Aluminum Oxide/ Water System," *Nuclear Engineering and Design*, *155, 1995*, pp. 391-403.

A11-7 D. Magallon and H. Hohmann, "Experimental Investigation of 150-kg-Scale Corium Melt Jet Quenching in Water," *Proceedings of the 7th International Meeting on Nuclear Reactor Thermal-Hydraulics (NURETH-7), Saratoga Springs, NY, September 1995*, NUREG/CP-0142, pp. 1588-1711.

A11-8 I. Huhtiniemi, H. Hohmann, and D. Magallon, "FCI Experiments in the Corium/Water System," *Proceedings of the 7th International Meeting on Nuclear Reactor Thermal-Hydraulics (NURETH-7), Saratoga Springs, NY, September 1995, NUREG/CP-0142*, pp. 1712-1727.

A11-9 B. W. Spencer, S. K. Wang, C. A. Blomquist, L. M. McUmber, and J. P. Schneider, "Fragmentation and Quench Behavior of Corium Melt Streams in Water," Argonne National Laboratory Report ANL-93-32, NUREG/CR-6133, February 1994.

A11-10 B. W. Marshall, Jr., "Recent Fuel-Coolant Interaction Experiments Conducted in the FITS Vessel," *ANS Thermal Hydraulic Division Proceedings, 25th ASME/AIChE National Heat Transfer Conference*, *Houston, Tx, July 24-27, 1988*, pp. 265-275.

A11-11 S. Angelini, E. Takara, W. Yuen, and T. G. Theofanous, "Multi-Phase Transients in the Premixing of Steam Explosions," *Proceedings of the FIfth International Meeting on Nuclear Reactor Thermal-Hydraulics (NURETH-5)*, *Salt Lake City, UT, September 21-24, 1992*, pp. 471-478.

A11-12 A. Annunziato, C. Addabbo, A. Yeikess, R. Silverii, W. Brenka, and G. Leva, "OECD/CSNI International Standard Problem 39 on FARO Test L-14 on Fuel Coolant Interaction and Quenching - Analysis of the Results," EUR17736EN, 1998.

A12. TMI-2 ACCIDENT

A12.1 Introduction

The TMI-2 Accident Test Problem provides under full scale conditions an assessment of virtually every in-core damage progression model in the SCDAP/RELAP5/MOD3.3 code. Since the accident was not an experiment, the measured behavior of the reactor during the accident was limited. Nevertheless, the limited amount of information obtained during the accident and the post-accident examinations of the reactor provide a significant amount of information for assessing at least in an indirect manner most of the in-core damage progression models in the code. The TMI-2 accident involved spacer grid meltdown, cladding ballooning, control rod meltdown, fuel rod oxidation, hydrogen production, cladding meltdown, fuel melting, molten pool formation, quenching of hot and embrittled fuel rods, and molten pool slumping. The measurements obtained during the accident and inferences made from observations after the accident only provide quantitative assessment of a few of the damage progression models, such as models that calculate total hydrogen production, location of previously molten frozen material, and total amount of molten material. Nevertheless, since one damage progression event in the overall chain of damage progression events is dependent upon all the other previous damage progression events in the chain, the correct calculation of a few of the damage progression events cannot be made without a correct calculation of the other damage progression events. So an indirect assessment can be made of virtually every in-core damage progression model in the code.

A12.2 Description of TMI-2 Accident Problem

All major components of the TMI-2 primary system were represented in the TMI-2 Accident Test Problem. The RELAP5 module was used to simulate the thermal-hydraulics of the reactor vessel, primary coolant loops, steam generators, and pressurizer. Steam generator secondary side coolant levels, pressures, and feedwater temperatures, and primary side makeup and letdown flow rates were supplied as boundary conditions. The SCDAP module was used to simulate the reactor core, which was divided into five radial regions by grouping similarly powered fuel assemblies together.

The TMI-2 accident is generally divided into four distinct phases for analysis purposes.[A12-1] Phase 1 (0 - 100 min) is a small-break loss-of-coolant accident (LOCA) through the stuck-open pilot-operated relief valve (PORV). One or more reactor coolant system (RCS) pumps operated continuously during Phase 1 of the accident, thereby providing adequate core cooling. Phase 2 (100 - 174 min) is a continuation of a small break LOCA without the RCS pumps. Core uncovery, heatup, and initial melting occurred during Phase 2. Phase 3 (174 - 200 min) begins with a restart of reactor coolant pump 2B. Approximately 30 m^3 of coolant was injected into the reactor vessel in less than one minute, cooling the peripheral fuel assemblies and forming an upper core debris bed with significant zircaloy oxidation. Heatup of the degraded core region, with the formation and growth of a pool of molten material, continued during Phase 3. Phase 4 (200 - 300 min) begins with the initiation of high pressure injection (HPI). The central region of the partially molten core material was not coolable by HPI even through the water level reached the level of the hot legs by 207 min. Between 224 and 226 min, the crust encasing and supporting the molten core region is believed to have failed, allowing molten material to relocate to the lower plenum. Summaries of the measured and observed reactor core damage are given in References A12-2 and A12-3.

The RELAP5 portion of the TMI-2 model was derived from an Oconee plant model described in Reference A12-4. Both TMI-2 and Oconee are PWR's having a two-by-four coolant loop configuration, i.e., two primary coolant loops, each containing one hot leg and two cold legs. Both plants were built by Babcock & Wilcox in the 1970's and have nearly identical design and operating characteristics. Consequently, the Oconee RELAP5 model was easily adapted to represent TMI-2. Figure A12-1 through Figure A12-4 are nodalization diagrams of the reactor vessel, primary piping, steam generators, and pressurizer respectively.

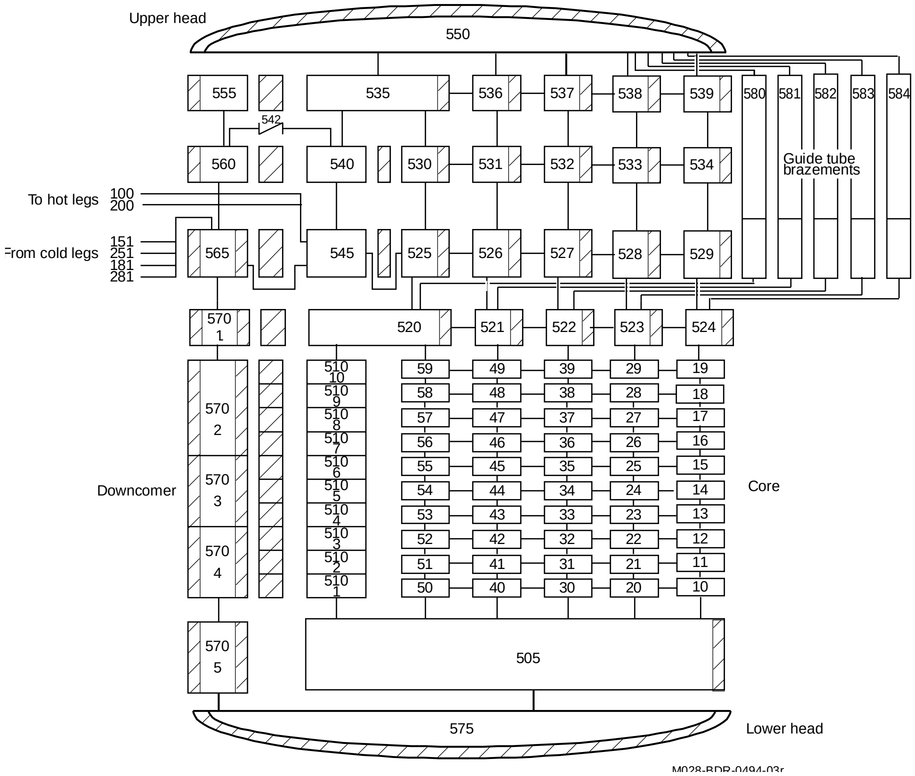
Upper head
550
555
542
535
536
537
538
539
580
581
582
583
584
560
540
530
531
532
533
534
Guide tube brazements
To hot legs
100
200
From cold legs
151
251
181
281
565
545
525
526
527
528
529
570 1
520
521
522
523
524
510 10
510 9
510 8
510 7
510 6
510 5
510 4
510 3
510 2
510 1
59 58 57 56 55 54 53 52 51 50
49 48 47 46 45 44 43 42 41 40
39 38 37 36 35 34 33 32 31 30
29 28 27 26 25 24 23 22 21 20
19 18 17 16 15 14 13 12 11 10
570 2
570 3
570 4
570 5
Downcomer
Core
505
575
Lower head
M028-RDR-0494-03r

Figure A12-1. RELAP5 nodalization of the reactor vessel and core.

The RELAP5 vessel model (Figure A12-1) represent all major components of the reactor vessel, including the inlet annulus, downcomer, lower plenum, core, core bypass, upper plenum, upper head, reactor vessel vent valves, and the control rod guide tube brazements. The core is divided into five parallel channels, each consisting of ten subvolumes (branch components 10 through 59). Lateral flow between adjacent core channels is simulated using the RELAP5 crossflow model. Annulus component 570 represents the downcomer and pipe component 510 the core bypass. Branch components 505 and 575 represent the lower plenum. The upper plenum is also divided into five parallel regions that are connected laterally by crossflow junctions. This arrangement allows for the development of in-vessel natural circulation under appropriate conditions. Valve component 542 represents the reactor vessel vent valves and pipe components 580 through 584 the guide tube brazements. Fifty-one heat structures were used to model the thermal behavior of reactor vessel metal structures.

Figure A12-2 is a nodalization diagram of the primary coolant loop A, which consists of one hot leg (components 100 through 114), one steam generator (discussed subsequently), two pump suction legs (pipe components 135 and 165), and two cold legs (components 140 through 151 and 170 through 181).

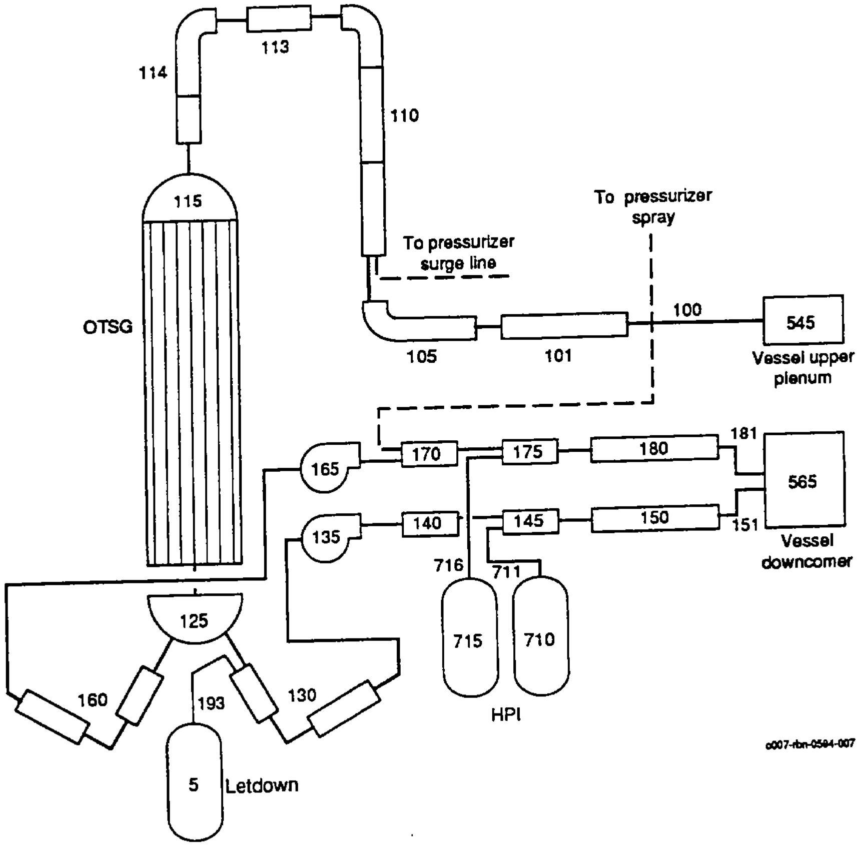
114
113
110
115
OTSG
To pressurizer
surge line
To pressurizer
spray
100
545
Vessel upper
plenum
105
101
165
170
175
180
181
565
135
140
145
150
151
Vessel
downcomer
716
711
715
710
HPI
125
160
193
130
5
Letdown
c007-rbn-0594-007

Figure A12-2. RELAP5 nodalization of primary coolant loop A.

Primary loop B is identical to loop A, except it does not contain a letdown flow path (time-dependent junction 193) or connections to the pressurizer spray and surge lines. The component numbers for loop B are also increased by 100 (e.g., the primary pumps are numbered 235 and 265 rather than 135 and 165). The high pressure injection (HPI) system is represented by time-dependent volumes 710 and 715, which are connected to the cold legs by time-dependent junctions 711 and 716. HPI flow is assumed to be split equally between the A and B loops while makeup flow is injected only into the B loop. Eighteen heat structures (per loop) were used to model the thermal behavior of the primary piping.

The nodalization of steam generator A is shown in Figure A12-3. Steam generator B is identical except that all component numbers are increased by 100. The boiler region is divided into two parallel flow channels: an inner channel (volumes 310 through 323), connected to 90% of the steam generator tubes, and an outer channel (volumes 360 through 373), connected to 10% of the steam generator tubes. Crossflow junctions connect the two boiler regions. Auxiliary feedwater is normally injected into the top of the 10% region. Pipe component 120 represents the primary side of the steam generator tube bundle, while branch components 115 and 125 represent the inlet and outlet plena. The steam generator downcomer is modeled by component 305, and components 345 and 350 represent the steam line. To preheat the feedwater, a portion of the steam flow is bled into the downcomer through an aspirator near mid-boiler (modeled with a junction between component 365 and 305). Valve component 821 represents the main steam valve. Forty-three heat structures were used to model the thermal behavior of steam generator metal structures (including the tube bundle).

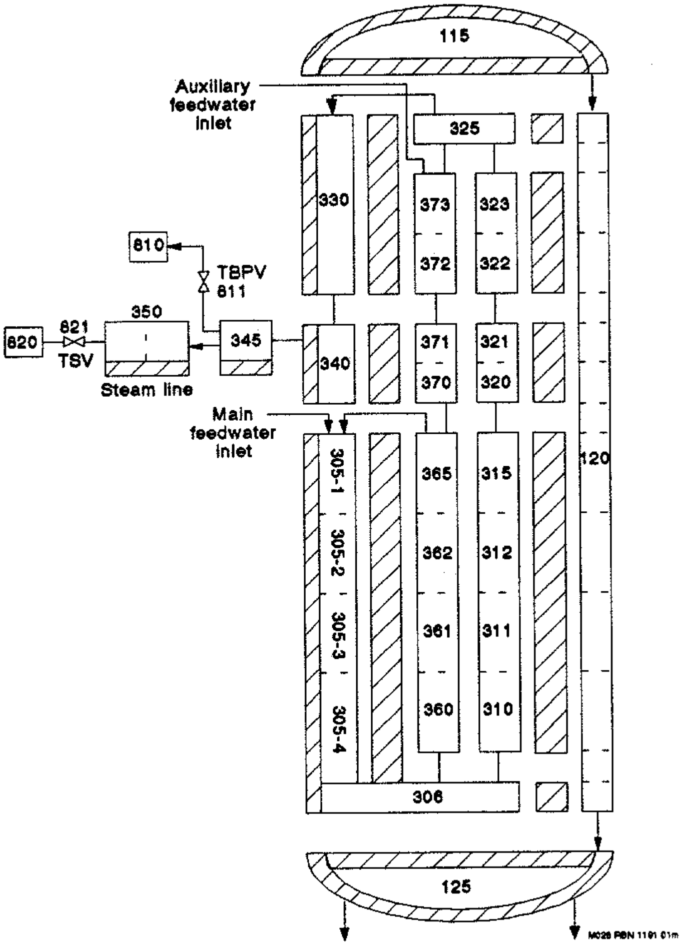
115
Auxiliary feedwater inlet
325
330
373
372
323
322
810
TBPV 811
350
821
820
TSV
345
340
Steam line
371
370
321
320
Main feedwater inlet
305-1
305-2
305-3
305-4
365
362
361
360
315
312
311
310
120
306
125

Figure A12-3. RELAP5 nodalization of steam generator A.

It should be noted that for all the calculations reported here, auxiliary feedwater was injected into the steam generator downcomer rather than into the tube bundle as indicated in Figure A12-3. A previous TMI-2 analyses using SCDAP/RELAP5[a] indicated that feedwater injection directly onto the steam generator tubes resulted in too much primary-side condensation, which in turn caused the primary system pressure to be underpredicted. It should also be noted that the nodalization of the steam generators differs somewhat from that recommended in the SCDAP/RELAP5 user's guide.[A12-5] Although the boiler is divided into two parallel regions, the tube bundle (pipe 120) is not. Dividing the tube bundle into a 10% region and a 90% region may alleviate some of the condensation problems encountered previously.

Figure A12-4 is a nodalization diagram of the pressurizer. The pressurizer upper head is modeled with branch component 615 and the pressurizer cylindrical body and lower head with pipe component 610. Valve 801 represents the pilot operated relief valve (PORV). Pipes 600 and 620 represent the pressurizer surge and spray lines, respectively, and valve 616 models the spray valve. Single volume component 949

---

[a] C. A. Dobbe, private communication, EG&G Idaho, Inc., March 15, 1994.

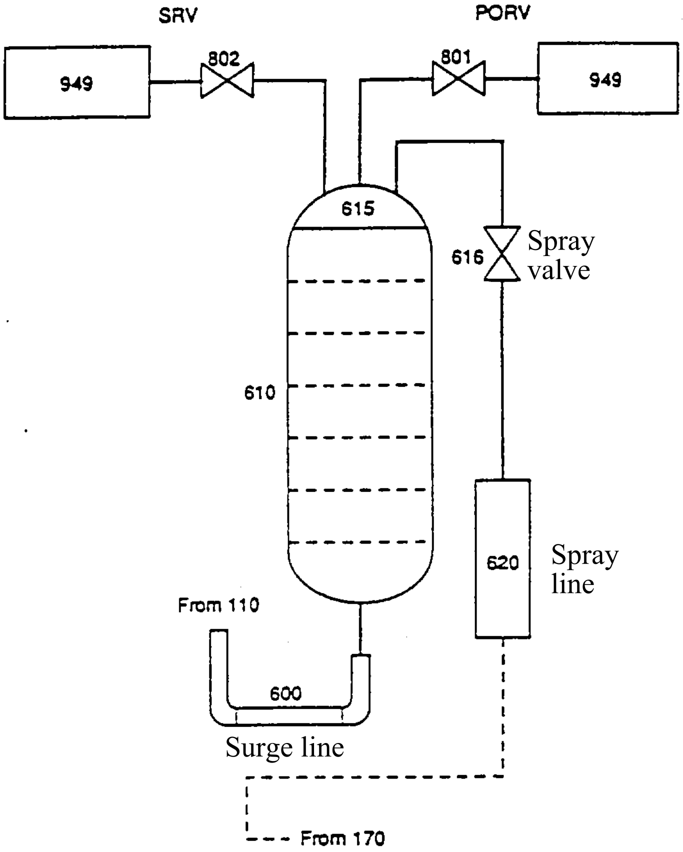

Figure A12-4. RELAP5 nodalization of the pressurizer.

represents the containment building, which is initially filled with air at 101 kPa. Twelve heat structures are used to model the thermal behavior of the pressurizer shell, upper and lower heads, and the surge line; one heat structure is used to simulate operation of the pressurizer heaters; and five heat structures are used to model the thermal behavior of the containment building.

It should be noted that critical flow through the PORV is modeled using the homogeneous (single velocity) two-phase flow option in RELAP5. Previous TMI-2 calculations using SCDAP/RELAP5[a] have shown that this option better predicts the PORV flow history reported in the TMI-2 initial and boundary conditions (ICBC) data base[A12-6] than other options. [The PORV flow rates reported in Reference A12-7 were calculated using the Henry-Fauske critical flow model for subcooled conditions and the homogeneous equilibrium critical flow model (HEM) for two-phase conditions.] It should also be noted that for all calculations reported here, a servo valve was installed between the pressurizer and the surge line at 117 min to prevent the pressurizer from draining. In preliminary calculations, the pressurizer drained completely after the PORV block valve was closed at 139 min, which effectively terminated core heatup. More accurate representations of the surge line and pressurizer might eliminate some of the problems encountered in this and previous TMI-2 analyses. For example, the junction connecting the surge line to hot leg A should be oriented horizontally rather than vertically (to reflect its true alignment) and the countercurrent flow limitation (CCFL) model should be activated at the junction connecting the surge line to the pressurizer, rather than at the hot leg junction. Also, the CCFL input parameters (currently set to default values) should be reviewed for applicability.

---

[a] C. A. Dobbe, private communication, EG&G Idaho, Inc., March 15, 1994.

The TMI-2 core was divided into five regions for this analysis by grouping similarly powered fuel assemblies together. Figure A12-5 is a cross-section of the core illustrating each region and its average radial power peaking factor. Table A12-1 lists the average axial power peaking factors for each region. Both the axial and radial peaking factors were derived from detailed peaking factor data presented in Appendix A of Reference A12-6.

Table A12-1. TMI-2 axial power peaking factors.

	Power factor				
Distance from bottom of fuel (m)	**Region 1**	**Region 2**	**Region 3**	**Region 4**	**Region 5**
01.183	0.665	0.674	0.729	0.690	0.670
0.549	0.933	0.919	0.962	0.951	0.944
0.914	1.134	1.099	1.112	1.132	1.145
1.280	1.216	1.164	1.112	1.168	1.213
1.646	1.248	1.202	1.138	1.192	1.238
2.012	1.262	1.221	1.153	1.206	1.248
2.377	1.225	1.232	1.251	1.241	1.222
2.743	1.078	1.124	1.174	1.131	1.083
3.109	0.792	0.853	0.880	0.834	0.794
3.475	0.448	0.512	0.488	0.455	0.442

One SCDAP fuel rod component is used to represent all the fuel rods in each core region. One SCDAP control rod component is used to represent all the full and part-length control rods, all the guide tubes (including those containing burnable poison rods), and all the instrument tubes in each core region (except region five which contains no control rods). The control rod radii in regions one through four have been adjusted so that the total mass of zircaloy, Ag-In-Cd absorber, and stainless steel is conserved (the burnable poison mass is neglected). In core region five, a dummy fuel rod component is used to represent all the guide and instrument tubes. By specifying a small fuel diameter and zero power, this component essentially behaves as a hollow zircaloy tube. The SCDAP grid spacer model is used to represent the eight inconel spacer grids that are uniformly distributed along the length of each fuel assembly.

Much of the SCDAP input data was obtained from Reference A12-8 and is summarized in Table A12-2. Table A12-3 lists the total number of fuel assemblies, fuel rods, control rods, burnable poison rods, and orifice rods in each core region.

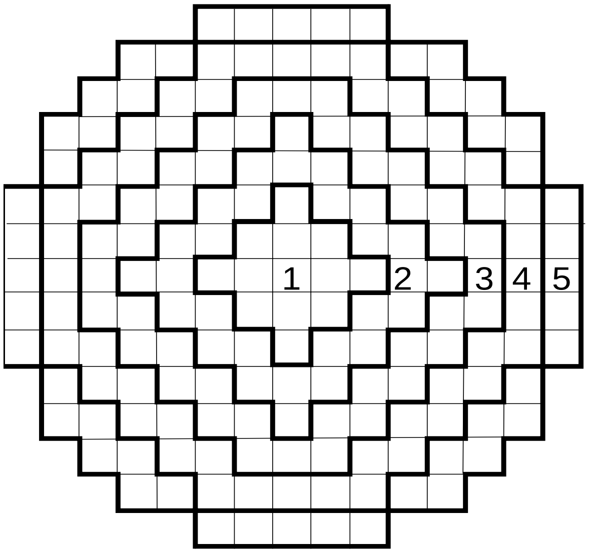

Region	Radial Peaking Factor
1	1.245
2	1.136
3	1.074
4	1.061
5	0.733

M028-BDR-0494-001

Figure A12-5. Cross-sections of core showing fuel assembly grouping and radial peaking factors.

Table A12-2. Total fuel assemblies, fuel rods, and control rods in each core region.

Core regions	Fuel assemblies	Fuel rods	Full-length control rods	Part-length control rods	Burnable poison rods	Instrument tubes	Orifice rods
1	13	2704	144	0	64	13	0
2	28	5824	256	0	192	28	0
3	40	8320	192	128	320	40	0
4	48	9984	384	0	384	48	0
5	48	9984	0		128	48	640
Total	177	36816	976	128	1088	177	640

Table A12-3. SCDAP input parameters.

Parameter	Value
Fuel rods	
Active height (m)	3.568
Rod pitch (m)	1.443×10^{-2}
Cladding inner radius (m)	4.788×10^{-3}
Cladding outer radius (m)	5.461×10^{-3}
Fuel pellet radius (m)	4.699×10^{-3}
Fuel density (% T.D.)	92.5
Mass of He fill gas (estimated) (kg)	1.265×10^{-4}
Upper and lower plenum void volume (m^3)	1.490 x 10-5
Control rods	
Guide tube inner radius (m)	6.325×10^{-3}
Guide tube outer radius (m)	6.731×10^{-3}
Cladding inner radius (m)	5.055×10^{-3}
Cladding outer radius (m)	5.588×10^{-3}
Absorber radius (m)	5.004×10^{-3}
Instrument tubes	
Tube inner radius (m)	5.601×10^{-3}
Tube outer radius (m)	6.261×10^{-3}
Grid spacers	
Grid spacer mass (kg)	0.86
Grid spacer height (m)	3.30×10^{-2}
Grid spacer thickness (m)	5.08×10^{-4}

Table A12-4 compares the initial conditions in the SCDAP/RELAP5 model to those recommended in the ICBC data base.[a] with the exception of steam generator pressures and temperatures, the calculated (or specified) initial conditions are in good agreement with the data base. For steady-state calculations, a control system is used in the SCDAP/RELAP5 model to automatically adjust steam generator pressures (by varying the flow areas of the main steam valves) until user-specified cold leg temperatures are obtained. For simplicity, the target coolant temperature for all four cold legs was specified to be 565 K. Table A12-5 compares the calculated initial conditions on the secondary side of each steam generator to the initial conditions recommended in Reference A12-9. It is seen that the calculated steam generator pressures are in much better agreement with the Reference A12-9 data than with the ICBC data base.[a] Calculated steam generator coolant levels, however, differ considerably from those reported in Reference A12-9. For future calculations, it is recommended that the steam generator models should be adjusted to better represent the Reference A12-9 data. One way to accomplish this may be to increase the pressure drop across the tube support plates as was done for a TMI-2 analysis performed with the CATHARE code.[A12-10]

---

[a] All initial conditions correspond to the time of turbine trip: 04:00:37 hours on March 28, 1979.

Table A12-4. TMI-2 initial conditions at turbine trip.

Parameter	ICBC data base	SCDAP/ RELAP5
Reactor power (MW)	2700	2700
Primary system pressure (MPa)	15.2	15.2
Pressurizer level (m)	5.77	5.76
Pressurizer heater power (MW)	1.39	1.39
Cold leg temperature 1A (K)	561	565
Cold leg temperature 2A (K)	548	565
Hot leg temperature loop A (K)	592	593
Hot leg temperature loop B (K)	592	593
Makeup flow (kg/s)	5.44	0.0
Letdown flow (kg/s)	4.18	0.0
PORV flow (kg/s)	2.59	0.0
Feedwater temperature (K)	513	
Steam generator A pressure (MPa)	7.31	6.34
Steam generator B pressure (MPa)	7.24	6.28
Steam generator A steam temperature (K)	586	576
Steam generator B steam temperature (K)	585	582

---

[a] The pressures reported in Reference A12-9 are average steam line pressures measured 10 to 0.1 min before turbine trip.

Table A12-5. Steam generator initial conditions.

Parameter	Reference A12-9	SCDAP/ RELAP5
Steam generator A feedwater flow (kg/s)	722	723
Steam generator B feedwater flow (kg/s)	718	717
Steam generator A pressure (MPa)a	6.38	6.34
Steam generator B pressure (MPa)a	6.24	6.28
Steam generator A steam temperature (K)	586	576
Steam generator B steam temperature (K)	586	582
Steam generator A riser level (cm)	526	197
Steam generator B riser level (cm)	538	183
Steam generator A downcomer level (cm)	660	559
Steam generator B downcomer level (cm)	669	543
Steam generator A power (MW)	1346	1332
Steam generator B power (MW)	1339	1378

A0.2.1 Boundary Conditions

All boundary conditions, except HPI/makeup flow rates, were obtained from the ICBC data base (Reference A12-6). The HPI/makeup flow rate history reported in Reference A12-11 was adjusted until the time of core uncovery (as inferred from hot leg temperature measurements), the time of initial fuel rod cladding failure (as inferred from containment radiation measurements), and the primary system pressure history were predicted reasonable well.[a] Figure A12-6 compares the HPI/makeup flow rate history used for the best-estimate SCDAP/RELAP5 calculation discussed subsequently to that recommended in Reference A12-6. In a previous SCDAP/RELAP5 analysis of the TMI-2 accident,[A12-12] using a previous version of the code, better results were obtained by reducing the makeup flow rate from 4 to 2 kg/s between 100 and 174 min. In an analysis performed with the MELPROG/TRAC code,[A12-13] it was concluded that the makeup flow rate recommended in Reference A12-6 was too high between 12 and 100 min. For that analysis, the flow was reduced from 6.5 to 1 kg/s between 12 and 100 min (which was the nominal value given in the original issue of the ICBC data base). Core power as a function of time for the first 400 s following reactor scram was estimated using the reactor (point) kinetics and decay heat models in the RELAP5 code. The decay power from 617 minutes onward was obtained from Reference A12-14. Figure A12-7 shows the reactor power versus time curve in the SCDAP/RELAP5 model.

---

[a] The uncertainty in HPI/makeup flow is large, particularly between 100 and 174 min.[A12-11] Consequently, as noted in Reference A12-12, it isn't possible to determine which assumptions are better.

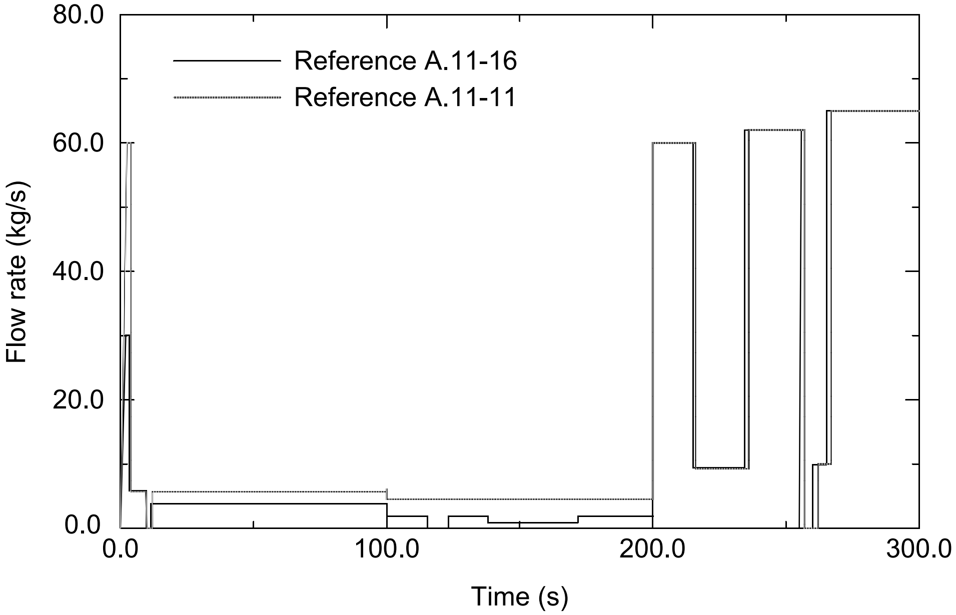

Figure A12-6. Makeup flow history for TMI-2 calculation.

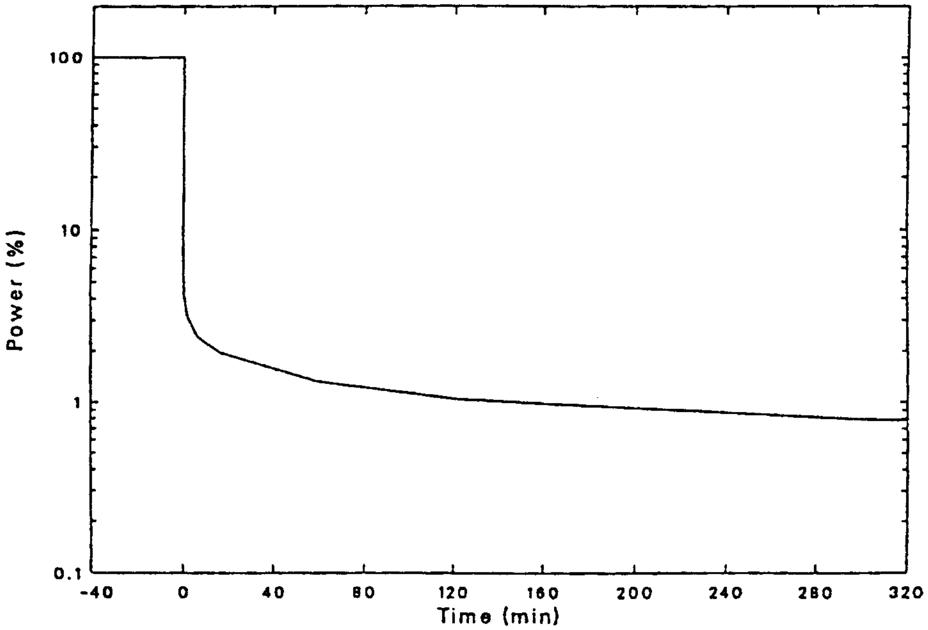

Figure A12-7. Reactor power versus time curve used for TMI-2 calculation.

A12.3 Assessing Using TMI-2 Accident

The timing of the opening and closing of the PORV block valve is an important boundary condition for the TMI-2 accident. Figure A12-8 is a plot that shows the times at which the block valve was opened and closed and the calculated rate of mass flow through the valve for the periods of time that it was open. The plot also shows the calculated rate of flow through the PORV valve. The calculated rate of flow through the open PORV valve ranged from 5 to 35 kg/s.

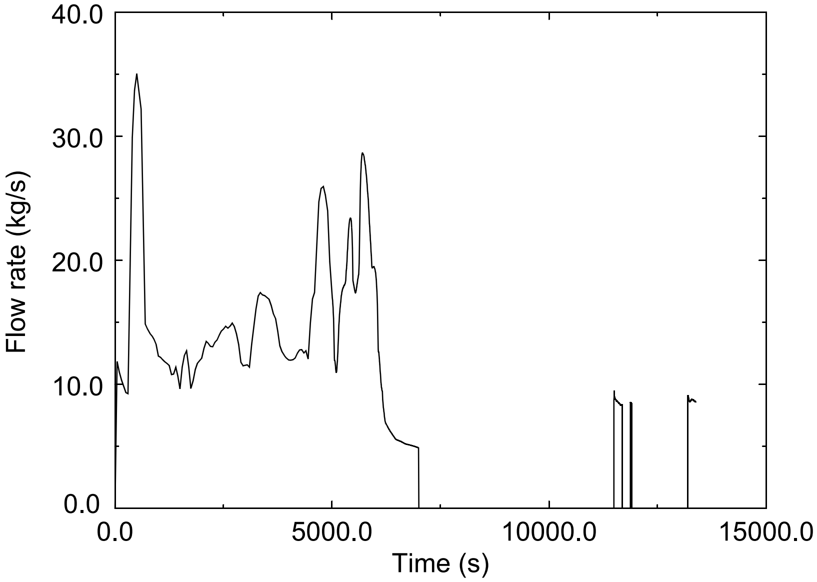

Figure A12-8. Timing of closure of PORV block valve and history of calculated rate of flow through PORV valve.

The SCDAP/RELAP5 MOD3.3 solution to the TMI-2 Accident test Problem is presented next. The calculated timing of the damage progression is described and calculated results are presented for which measurements are available for comparison and assessment. These calculated results are; (1) location of core material, (2) maximum amount of molten material, (3) reactor system pressure, and (4) hydrogen production. Default values were used for all the modeling parameters subject to being defined by the code user.

The damage to the TMI-2 reactor core began with the ballooning and rupture of the cladding of the fuel rods and advanced to the slumping of a significant amount of molten core material to the lower head of the reactor vessel. The MOD3.3 calculated and measured progression of damage are compared in Table A12-6. The results of the MOD3.2 calculation of the TMI-2 accident are included in the table. After core uncovery was calculated to occur at 6270 s, core damage was calculated to occur quite rapidly. Cladding failure due to ballooning was calculated by MOD3.3 to begin at 8445 s. MOD3.2 calculated cladding failure to be due to chemical attack by the Inconel spacer grids and to not occur until 9417 s. After cladding failure, double-sided oxidation of the cladding was calculated by MOD3.3 to occur in the vicinity of the cladding failure. The melting of fuel and the formation of a molten pool were calculated by MOD3.3 to begin at 9500 s. MOD3.2 calculated molten pool formation to begin at 10,330 s. The start-up of the

2B-pump at 10,446 s was calculated by both MOD3.3 and MOD3.2 to cause a rapid increase in the pressure of the primary coolant system and to accelerate the rate of hydrogen production. These calculations are in agreement with the measurements. MOD3.3 calculated 9,530 kg of molten material in the core region at the start of the 2-B pump and 27,600 kg of molten material in the core just before the slumping of core material to the lower head at 12,890 s. MOD3.2 calculated 1734 kg of molten material in the core region at the start-up of the 2B-pump and 37,400 kg of molten material in the core just before the slumping of core material to the lower head at 13,379 s. The post-accident examination of the TMI-2 reactor indicated that 40,800 kg of the reactor core was molten at some time. Inferences from the measured system pressure and other measurements indicate that 15,800 kg of molten material slumped to the lower head at 13,500 s. Both the MOD3.3 and MOD3.2 calculated masses of molten material and the time of slumping are in approximate agreement with the measured values. The MOD3.3 calculated location of molten core material was in fair agreement with the post-accident observation of the TMI-2 reactor. The elevations of the bottom surface of the in-core molten pool at the centerline of the core were calculated and observed to be 1.10 m and 0.11 m, respectively. The highest location in the core to become molten was calculated to be 2.9 m and to be located along the centerline of the core. The molten pool was calculated to extend in the radial direction from the centerline of the reactor vessel to the periphery of the reactor core. The bottom surface of the molten pool at the periphery of the core was calculated by MOD3.3 to be at the elevation of 2.2 m. These calculated results are in agreement with the post-accident observation of the TMI-2 core.

Table A12-6. Calculated timing and sequence of core damage progression.

Damage progression parameter	Measured or inferred	MOD3.2	MOD3.3
Beginning of long term core uncovery (s).	-	6,390	6,270
Beginning of cladding failure due to ballooning (s).	-	9,417	8,445
Beginning of spacer grid slumping (s).	-	9,418	9,112
Beginning of molten pool (s).	-	10,330	9,530
Cumulative hydrogen production at start-up of 2B-pump at 10,446 s (kg).	300	275	365
Primary coolant system pressure at start-up of 2B-pump (MPa).	8.20	5.03	6.96
Mass of molten material at start-up of 2B-pump (kg).	-	1734	15,000
Increase in primary coolant system pressure after start-up of 2B-pump (MPa).	6.30	5.21	7.00
Final cumulative hydrogen production (kg).	460	453	417
Mass of core material that was molten during some period of accident (kg).	40,800	37,400	27,600

Table A12-6. Calculated timing and sequence of core damage progression. (Continued)

Damage progression parameter	Measured or inferred	MOD3.2	MOD3.3
Elevation of bottom of molten region relative to bottom of core (m).	0.71	1.46	1.10
Smallest distance from side of molten pool to periphery of core (m).	0.0	0.0	0.0
Time at which bulk of material in molten material slumped to lower head (s).	13,500	13,379	12,890
Mass of molten material that slumped to lower head (kg).	15,800	37,400	27,600
Percent of molten material that slumped to lower head (%).	39	100	100

MOD3.3 calculated a greater rise of the water level in the reactor core after activation of the 2B-pump than did MOD3.2. Both MOD3.3. and MOD3.2 calculated damage progression to be a strong function of the calculated collapsed liquid level in the reactor vessel. Figure A12-9 are plots of the MOD3.3 and MOD3.2 calculated collapsed liquid levels as a function of time. A temporary core uncovery was calculated by MOD3.3 to begin at 4800 s and the long term uncovery was calculated to begin at 6330 s. After 6330 s, the core continued to uncover until the 2-B pump activation at 10,446 s. The collapsed liquid level was calculated by MOD3.3 to be 0.3 m above the bottom of the reactor core just before activation of the 2-B pump. MOD3.2 calculated the collapsed liquid level just before start-up of the 2B-pump to be 0.2 m above the bottom of the reactor core. After activation of the 2-B pump, MOD3.3 calculated the water level to rise 3.0 m and MOD3.2 calculated the water level to rise 0.8 m. This difference in calculated rise in water level is due to MOD3.3 calculating a significantly greater fraction of the reactor core to be molten at the start-up of the 2B-pump than MOD3.2. Both MOD3.3 and MOD3.2 calculated activation of the HPIS at 12,012 s to cover the entire reactor core with water within 600 s.

The level of water in the pressurizer has an influence on the level of water in the reactor vessel. Figure A12-10 is a plot of the measured water level in the pressurizer and the levels calculated by MOD3.3 and MOD3.2. In the period of 10,000 s to 13,000 s, both MOD3.3 and MOD3.2 calculated a lower level of water in the pressurizer than the measured level.

MOD3.3 calculated severe core damage to begin about 800 s earlier than MOD3.2. The onset of melting of the reactor fuel and the beginning of molten pool formation is a mark of the beginning of severe core damage. The timing of damage progression is indicated by plots of the history of the maximum temperature in the reactor core and of the effective radius of the molten pool, as shown in Figures A12-11 and A12-12, respectively. The effective radius is the radius of a hemisphere with a volume equal to the calculated volume of molten material. The MOD3.3 and MOD3.2 calculated timings for the beginning of fuel melting were 9530 s and 10,330 s, respectively. MOD3.3 calculated a significantly more rapid heatup of the reactor core after the beginning of oxidation than did MOD3.2. In the temperature range of 1800 K to 2200 K, when rapid oxidation occurs, MOD3.3 calculated a heatup rate of nearly 50 K/s. The MOD3.2

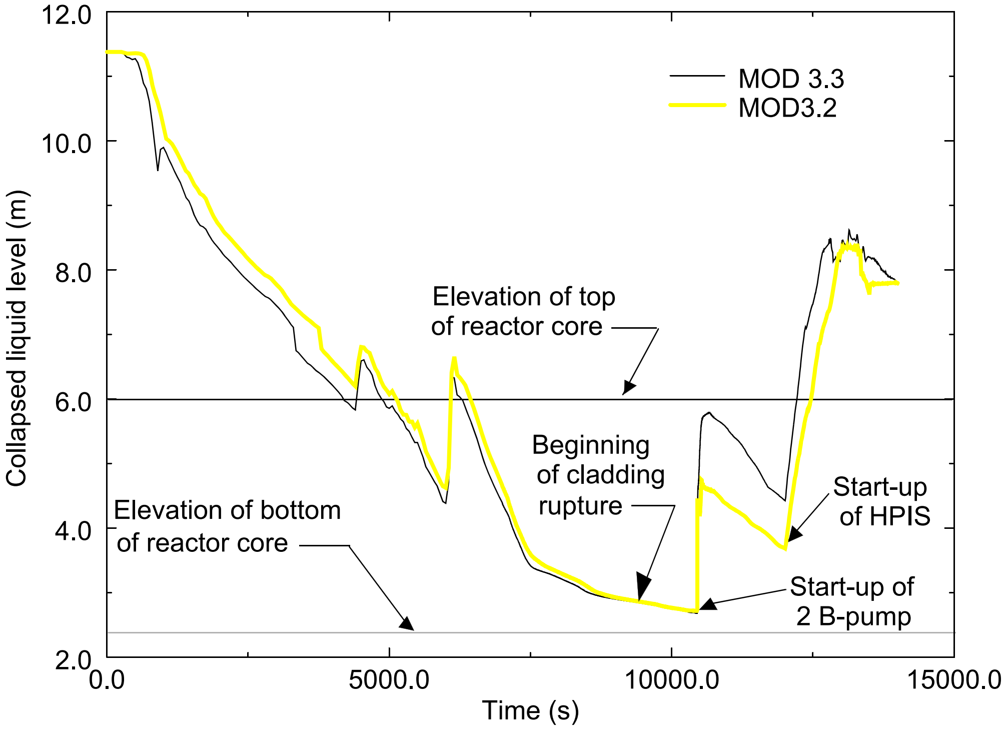

Figure A12-9. History of calculated collapsed liquid level in reactor vessel.

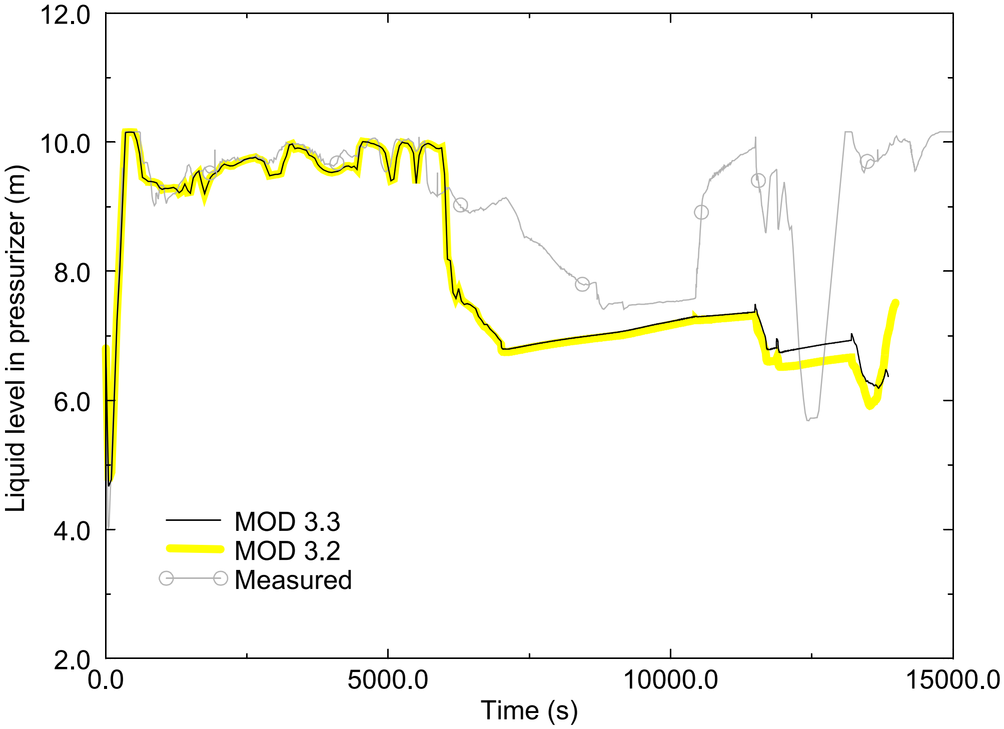

Figure A12-10. Comparison of calculated and measured liquid level in pressurizer.

calculated rate of heatup in this range of temperature was significantly less than that calculated by MOD3.3. Both MOD3.3 and MOD3.2 calculated that activation of the 2B-pump at 10,446 s did not result in any reduction in the maximum core temperature. A reduction in temperature was calculated to not occur because a significant part of the core was in the form of a large molten pool and because of an increase in oxidation of fuel rod cladding due to cracking of oxide layers and more flow of steam. The activation of HPIS at 12,012 s was calculated to not cause any cooling of the molten part of the reactor core. MOD3.3 calculated no further melting of fuel after 10,480 s (34 s after activation of 2B-pump), while MOD3.2 calculated fuel melting to occur until 13,000 s. MOD3.3 calculated the maximum effective radius of the molten pool to be 1.20 m. This value is in general agreement with the corresponding measured value of 1.40 m.

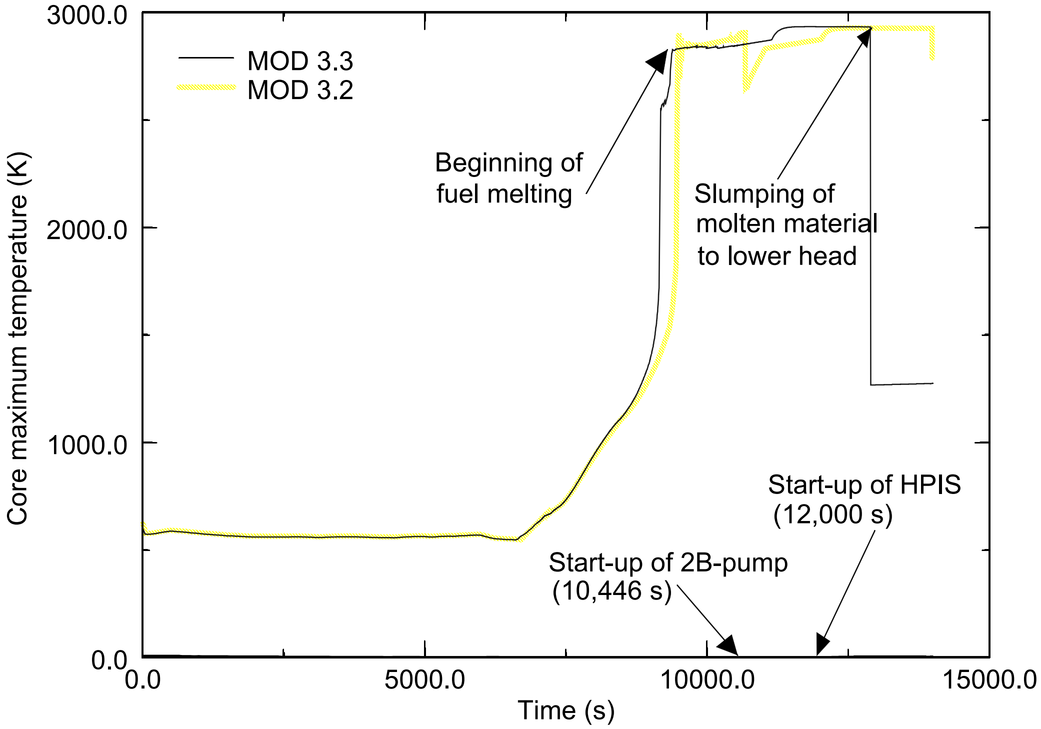

Figure A12-11. History of calculated maximum temperature in reactor core.

The MOD3.3 calculated and measured histories of the primary coolant system pressure were in partial agreement. The measured and calculated pressure histories are compared in Figure A12-13. The MOD3.2 calculated pressure history is also shown. The calculated and measured pressures were in good agreement from the start of the accident until 7,500 s. In the period of 7,500 s to start-up of the 2B-pump at 10,446 s, the calculated pressure was significantly less than the measured pressure. The coolant system pressure was calculated to increase about 7 MPa after start-up of the2-B pump. This calculated increase in pressure was in general agreement with the measured pressure increase of 6.3 MPa. The increase in pressure was calculated to be due to steam generated by pumping of water into the hot reactor core and by heatup of the reactor core by an acceleration in the oxidation of fuel rod cladding. In the period of 10,500 s to activation of HPIS at 12,012 s, the pressure was calculated and measured to gradually decrease a few MPa. After activation of the HPIS, the pressure was calculated and measured to increase a few MPa.

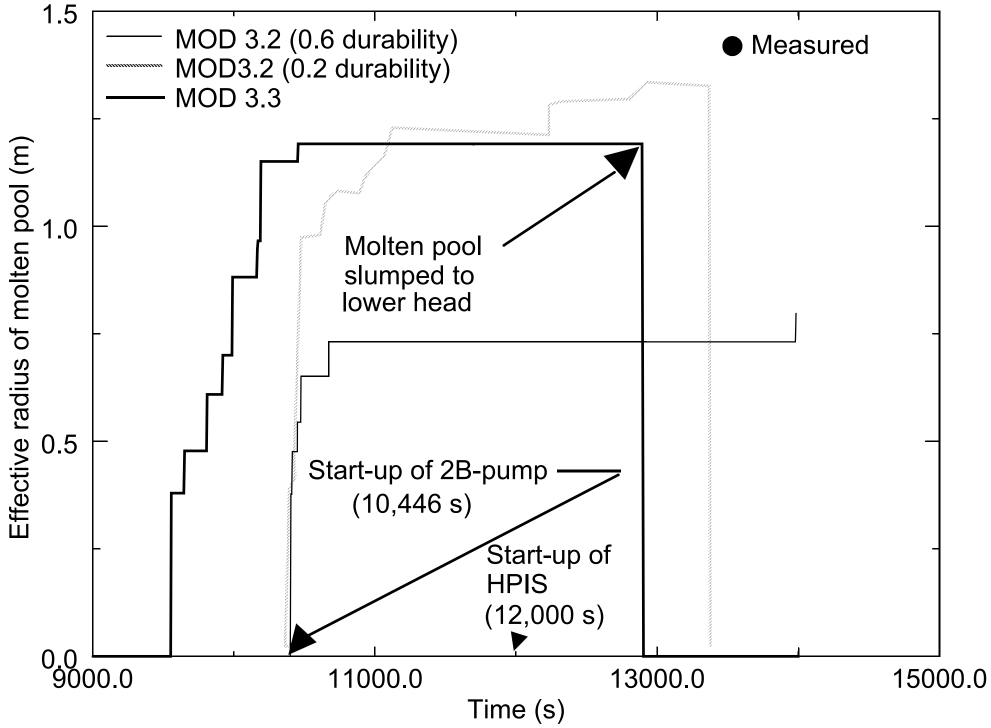

Figure A12-12. History of calculated effective radius of molten pool.

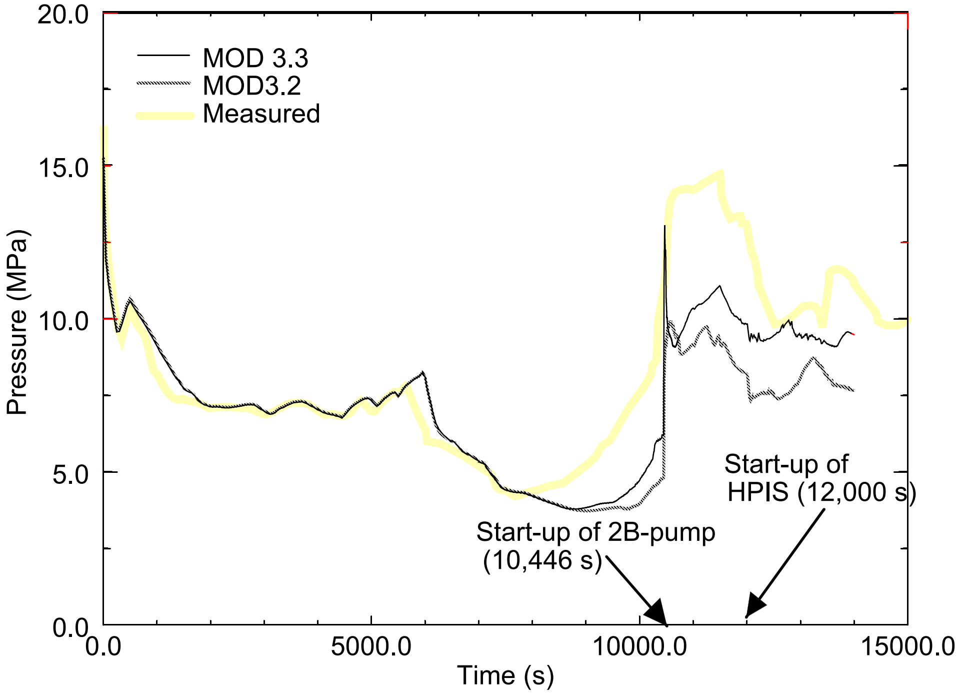

Figure A12-13. Calculated and measured pressures of primary coolant system.

The MOD3.3 calculated pressure history of the primary coolant system was improved using the boundary conditions for the TMI-2 accident applied by Annunziato et al.[A12-17] The TMI-2 accident has a large degree of uncertainty in boundary conditions that influence the pressure of the primary coolant system. The accident has uncertainties in boundary conditions such as make-up flow rate, performance of the 2B-pump, flow rate through the PORV, and time of its closure. Since there are uncertainties in these boundary conditions, the TMI-2 accident was also calculated by MOD3.3 using the boundary conditions used by Annunziato at al. The pressure history calculated by a slightly earlier version of MOD3.3 with these boundary conditions is compared with the measured pressure history in Figure A12-14. The calculated pressure history in the period of 7500 s to 10,000 s was in general agreement with the measured pressure history. Other aspects of reactor behavior, such as the total hydrogen production and total mass of molten material, were also in general agreement with measurements and the post-accident observation.

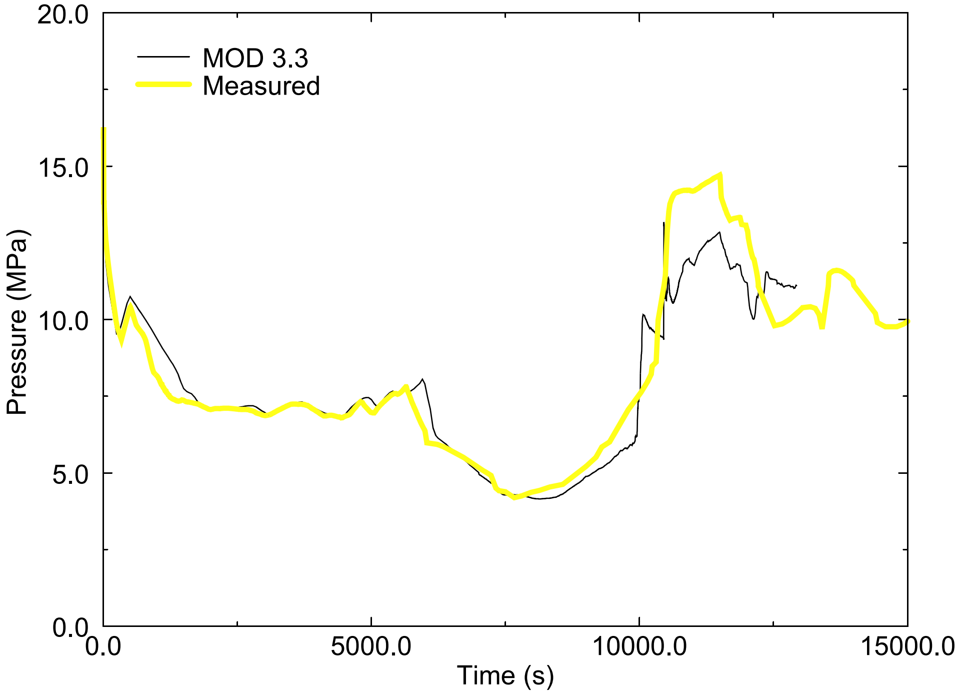

Figure A12-14. Comparison of calculated and measured pressure histories of primary coolant system for case of boundary conditions from Annunziato.

The calculated hydrogen production was in general agreement with the hydrogen production estimated from post-accident observations and inferences. The MOD3.3 calculated cumulative hydrogen production is compared with the measured hydrogen production in Figure A12-15. The MOD3.2 calculated hydrogen production is also shown in the figure. MOD3.3 calculated the rapid production of hydrogen to begin sooner than MOD3.2. Nevertheless, both the MOD3.3 and MOD3.2 calculations of hydrogen production are in approximate agreement with the measured hydrogen production. At the start-up of the 2B-pump, the MOD3.3 and MOD3.2 calculations of cumulative hydrogen production were 275 kg and 365 kg, respectively. The measured hydrogen production at the start-up of the 2B-pump was 300 kg. The MOD3.3 calculated and measured total hydrogen productions were 417 kg and 460 kg, respectively. Both MOD3.3 or MOD3.2 calculated that no significant amount of hydrogen production occurred 50 s after the start-up of the 2B-pump (10,500 s). Hydrogen production was calculated to not occur after 10,500 s because the portions of the core with intact fuel rods and some metallic cladding were too cool to rapidly oxidize. This behavior is shown in Figure A12-16, where the MOD3.3 calculated temperature histories are shown of the fuel rods in the outer most fuel assemblies of the reactor core at the elevations of 3.11 m and 3.47 m, respectively. As shown in this figure, hydrogen production at the 3.11 m and 3.47 m elevations was calculated to stop due to the cooling caused by the start-up of the 2B-pump. The oxide layer at this location was calculated to be too thin to crack during the reflood caused by start-up of the 2B-pump.

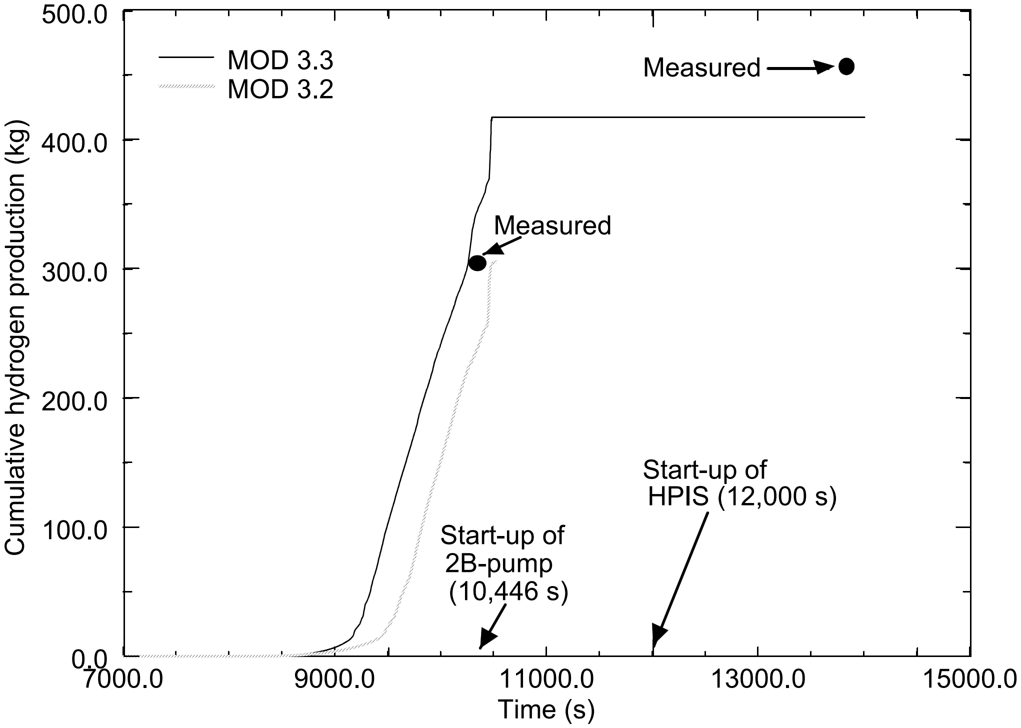

Figure A12-15. Calculated hydrogen production during TMI-2 accident.

The MOD3.3 calculation of the disintegration of fuel rods into porous debris was in agreement with the post-accident observation of the locations in the reactor core with porous debris. Porous debris regions were calculated to form in the outer most fuel assemblies in the elevation interval of 0.5 m to 1.2 m and across the entire diameter of the reactor core in the elevation interval of 2.6 m to 3.6 m. The calculation of porous debris in the elevation interval of 2.6 m to 3.6 m was consistent with the post-accident observation of the state of the reactor core.

The porous debris thermal hydraulic models in MOD3.3 performed properly after activation of the HPIS, which resulted in two-phase coolant conditions in porous debris in the upper part of the reactor core. The calculated temperature history at a location with porous debris is shown in Figure A12-17. The plot applies for the location 2.7 m in elevation and in the fourth ring of fuel assemblies. This location disintegrated from intact fuel rods to porous debris soon after start-up of the 2B-pump, and thus was porous debris at the time of start-up of HPIS. As a result, the flow losses and heat transfer at this location during the reflood period beginning with the start-up of HPIS were calculated with the porous debris thermal hydraulic models implemented into MOD3.3. The debris had a porosity of 0.46 and a particle

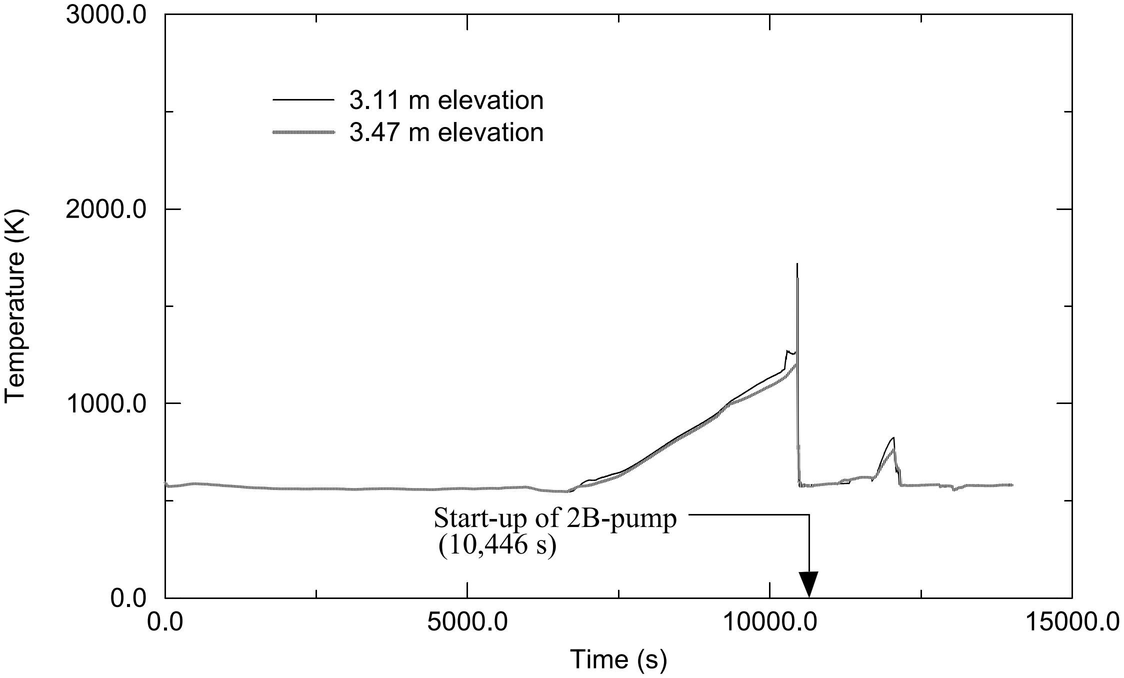

Figure A12-16. MOD3.3 calculated temperature histories of fuel rods in upper part of outer most fuel assemblies in reactor core.

diameter of 3.5 mm. Since the molten pool was located below this location and blocked the upward flow of water from the HPIS, the debris was flooded from the top down. The calculated temperature history of this location following reflood of the reactor core beginning at 12,012 s was consistent with that seen in experiments on the quenching of porous debris, as described in Section A8.

The implementation into MOD3.3 of the integral diffusion model for fuel rod oxidation caused it to calculate a more rapid progression of damage to the reactor core than calculated by MOD3.2. The onset of severe damage was calculated to begin at 9530 s by MOD3.3 and at 10,330 s by MOD3.2. This difference is due to the integral diffusion model for oxidation in MOD3.3 calculating a more rapid heatup due to oxidation at locations with a rich supply of steam than that calculated by the parabolic kinetics model for oxidation in MOD3.2. These differences in calculated behavior also occurred in the analyses of severe fuel damage experiments described in Sections A2 through A4.

The MOD3.3 calculation of the TMI-2 accident was improved by the implementation into MOD3.3 of the stress-based model for calculating the time of failure of an oxide layer retaining the melted metallic part of the fuel rod cladding. While MOD3.2 applied one model for failure of the oxide layer for analysis of severe fuel damage experiments and another model for the analysis of the TMI-2 accident, MOD3.3 applied the same oxide failure model for analysis of severe fuel damage experiments and the TMI-2 accident. The calculations of the oxide failure model have a strong influence on the calculations of hydrogen production and the extent melting of fuel assemblies. With the stress-based model for calculating oxide failure, MOD3.3 calculated hydrogen production and extent of melting in general agreement with measurements for both severe fuel damage experiments and the TMI-2 accident. On the other hand, when using the same oxide failure model for the TMI-2 analysis as used for analysis of severe fuel damage

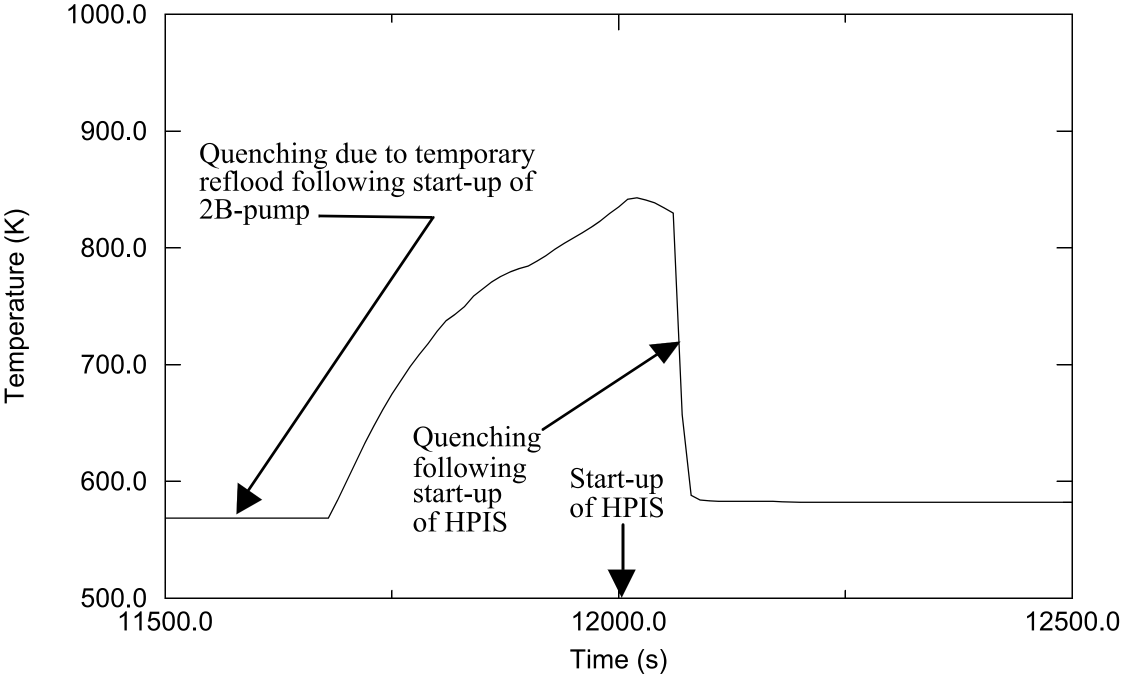

Figure A12-17. MOD 3.3 calculated temperature history of location with porous debris (2.7 m elevation of fourth ring of fuel assemblies).

experiments, MOD3.2 underpredicted by a factor of two the extent of melting of the reactor core, and did not predict any slumping of molten core material to the lower head.

Another difference in calculated reactor core behavior between MOD3.3. and MOD3.2 was in the calculated ballooning and rupture of fuel rods; MOD3.3 calculated ballooning and rupture of fuel rod cladding to occur significantly earlier than MOD3.2. This difference in calculated behavior is due to corrections made in MOD3.3 to the model for ballooning of the fuel rod cladding.

A12.4 Conclusions

The MOD3.3 calculation of the TMI-2 accident showed that its new models result in calculated behavior of the reactor core and primary coolant system in general agreement with measurements and post-accident observations. The calculated and measured hydrogen productions were 417 kg and 460 kg, respectively. The calculated and measured masses of molten material in the core region were 27,600 kg and 40,800 kg, respectively. The MOD3.3 calculation of the locations of porous debris regions in reactor core was for the most part in agreement with the observed locations of porous debris. The calculated temperature behavior of the porous debris was consistent with temperature behavior observed in debris quenching experiments. The calculated and measured rapid increase in primary coolant system pressure following the start-up of the 2B-pump were in good agreement. Except for an intermediate period of the accident, the calculated primary coolant system pressure was in good agreement with the measured pressure for all periods of the accident. An adjustment of boundary conditions within their range of uncertainty resulted in good agreement of calculated and measured pressure also during this intermediate period. The calculated location of molten material in the core region and the timing of the slumping of this molten material to the lower head were in general agreement with inferences from measurements and the post-accident observation of the reactor core.

The MOD3.3 calculations of the TMI-2 accident differed from the MOD3.2 calculations in some aspects of behavior. MOD3.3 calculated damage progression in the reactor core to occur significantly more rapid than MOD3.2. This difference is due to oxidation of fuel rod cladding in MOD3.3 being calculated by the integral diffusion model instead of by the parabolic kinetics model in MOD3.2. MOD3.3 calculated the ballooning and rupture of fuel rod cladding to occur significantly earlier than MOD3.2. This difference is due to corrections to the ballooning model implemented into MOD3.3. The stress-based model in MOD3.3 for the failure of an oxide layer retaining melted cladding resulted in good agreement of calculations with measurements for both the analysis of the TMI-2 accident and the analyses of severe fuel damage experiments. On the other hand, MOD 3.2 underpredicted the extent of core melting by a factor of two when using for the TMI-2 analysis the same oxide failure model as used for the analyses of severe fuel damage experiments. In the modeling of phenomena causing damage to fuel assemblies during severe accident conditions, MOD3.3 does not require a distinguishing of models for the analyses of severe fuel damage experiments from the models for the analyses of nuclear power plants; one set of models applies for both types of analyses, and all of the models used for nuclear power plant analyses have been assessed using severe fuel damage experiments.

A12.5 References

A12-1. D. F. Guessing, “The Three Mile Island Analysis Exercise,” *Nuclear Technology, 87,* August 1989, pp. 298-301.

A12-2. J. M. Broughton, P. Kuan, D. A. Petti, and E. L. Tolman, “A Scenario of the Three Mile Island Unit 2 Accident,” *Nuclear Technology, 87,* August 1989, pp. 34-53.

A12-3. J. R. Wolf et al., *TMI-2 Vessel Investigation Project Integration Report,* NUREG/CR-6197, TMI V(93)EG10, EGG-2734, March 1994.

A12-4. D. A. Brownson, L. N. Haney, and N. D. Chien, *Intentional Depressurization Accident Management Strategy for Pressurized Water Reactors,* NUREG/CR-5837, EGG-2688, April 1993.

A12-5. E. W. Coryell et al., *SCDAP/RELAP5/MOD3.2 Code Manual Volume III: User's Guide and Input Manual,* NUREG/CR-6150, INEL-95/6422, Revision 1, November 1996.

A12-6. R. W. Brower L. J. Fackrell, D. W. Golden, M. L. Harris, and C. L. Olaveson, *ICBC Version 3.1, TMI-2 Initial and Boundary Conditions Data Base,* GEND-INF-078, January 1988.

A12-7. Y. Nomura, *PORV Discharge Flow During the TMI-2 Accident,* EGG-TMI-7825, July 1987.

A12-8. D. Coleman, “As-Built Design and Material Characteristics of the TMI-2 Core,” *Part III in TMI-2 Accident Core Heatup Analysis, A Supplement, NSAC-25,* June 1981.

A12-9. J. L. Anderson, *TMI-2 Once Through Steam Generator Secondary Level Analysis,* EGG--TMI-7359, January 1987.

A12-10. P. Dumaz, "Three Mile Island Unit 2 Analysis Exercise: CATHARE Computations of Phases 1 and 2 of the Accident," *Nuclear Technology, 87,* December 1989, pp. 946-955.

A12-11. J. L. Anderson, *Recommended HPI Rates for the TMI-2 Analysis Exercise (0 - 300 Minutes),* EGG-TMI-7833, September 1987.

A12-12. D. W. Golden and N. Ohnishi, *SCDAP/RELAP5 Demonstration Calculation of the TMI--2 Accident,* EGG-TMI-8473, March 1989.

A12-13. F. E. Motley and R. P. Jenks, "Modeling of the Three Mile Island Unit 2 Accident with MELPROG/TRAC and Calculation Results for Phases 1 and 2," *Nuclear Technology, 87,* August 1989, pp. 302-309.

A12-14. T. R. England and W. B. Wilson, *TMI-2 Decay Power: LASL Fission-Product and Actinide Decay Power Calculations for the President's Commission on the Accident at Three Mile Island,* LA-8041-MS, Revised, March 1980.

A12-15. E. L. Tolman et al., *TMI-2 Accident Scenario Update,* EGG-TMI-7489, December 1986.

A12-16. J. K. Hohorst et al., TMI-2 Analysis using SCDAP/RELAP5/MOD3.1, INEL-94/0157, November 1994.

A12-17. A. Annunziato, A. Franceschini, and C. Addabbo, "TMI-2 Simulation by RELAP5/SCDAP and COMETA Codes," 8th International Conference on Nuclear Engineering, April 2-6, Baltimore, MD USA.

A13. BROWNS FERRY BWR LOCA SEVERE ACCIDENT

The large break loss-of-coolant accident (LOCA) model for the Browns Ferry Nuclear Plant was developed from a short term station blackout input deck developed by Oak Ridge National Laboratory (ORNL). To model a LOCA, the short-term station blackout input deck was modified to include a break in one of the two recirculation loops in the power plant. The ECCS was assumed to not be activated.

The conversion of the ORNL short-term station blackout input deck to a LOCA deck for use in the current assessment was done to take advantage of model improvements and error corrections implemented by ORNL.

A13.1 Nodalization

The nodalization diagram used for the Browns Ferry reactor vessel and associated piping is shown in Figure A13-1. The Browns Ferry reactor coolant system is modeled from the feedwater inlet to the turbine inlet and includes the reactor pressure vessel, two recirculation loops, the feedwater piping, the control rod drive cooling water, and the steam piping. The Browns Ferry containment is not explicitly modeled. Safety relief valves are used to discharge coolant and release gases into a single large volume representing the containment. This volume is maintained at a constant pressure of 0.31 MPa (45 psia) during the postulated severe accident.

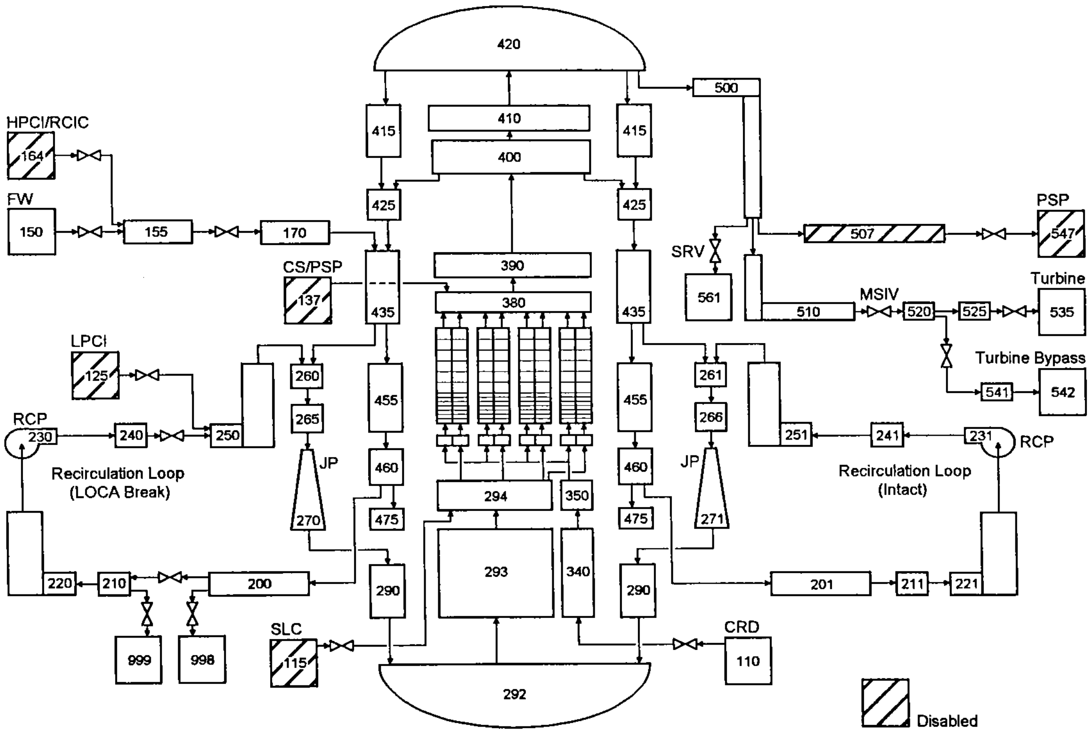
420
500
HPCI/RCIC
164
410
415
415
400
FW
150
155
170
425
425
PSP
507
547
SRV
CS/PSP
390
137
380
435
435
561
Turbine
MSIV
510
520
525
535
LPCI
125
260
261
Turbine Bypass
455
455
541
542
RCP
230
240
250
265
266
251
241
231
RCP
JP
460
294
350
460
JP
Recirculation Loop
(LOCA Break)
Recirculation Loop
(Intact)
270
475
475
271
293
340
220
210
200
290
290
201
211
221
SLC
CRD
999
998
115
110
292
Disabled

Figure A13-1. Nodalization diagram of Browns Ferry.

Figure A13-1 shows a detailed nodalization of the lower half of the reactor pressure vessel. The hydrodynamic volumes are represented by open boxes and the solid structures represented by shaded boxes in the diagram. The active core is divided into four radial rings and thirteen axial nodes. The center-most ring of the core represents approximately 55 percent of the fuel assemblies in the core, while each of the other three rings represent approximately 15 percent of the fuel assemblies in the core. The power density in the peripheral ring is greatly reduced from that in the central ring. The lower 1.07 m (3.5 feet of the active core is divided into seven axial nodes, while the upper 2.74 m (9.0 ft.) of the active core is divided into six axial nodes. The lower head of the Brown Ferry Nuclear Power Plant reactor vessel is modeled with a COUPLE mesh.

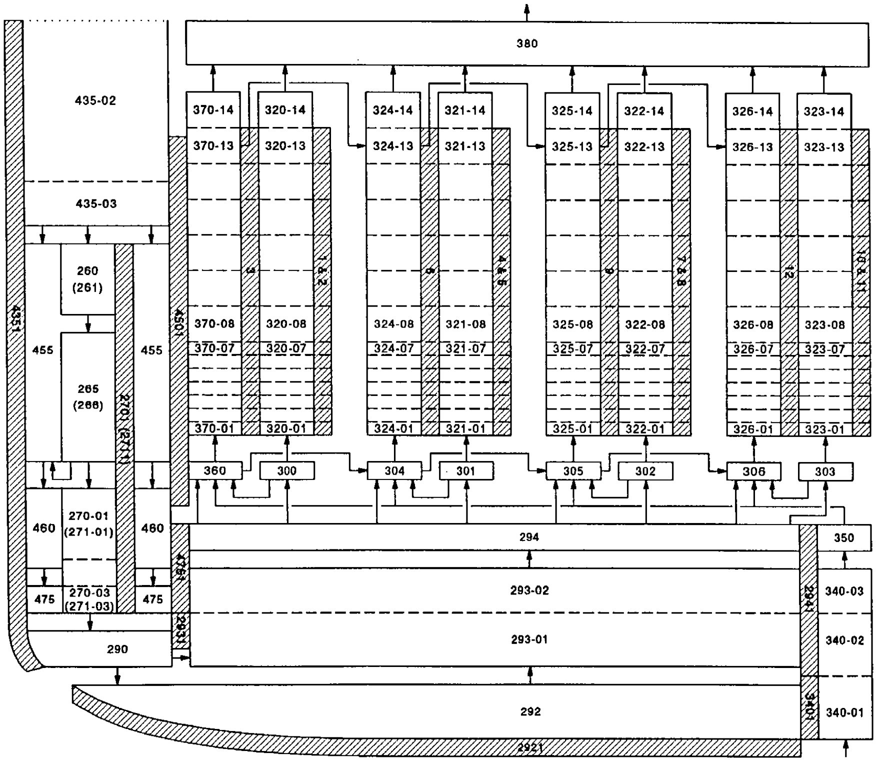
380
435-02
435-03
260
(261)
265
(266)
270-01
(271-01)
270-03
(271-03)
455
455
460
460
475
475
4351
4501
2701 (2711)
4761
2931
290
370-14
370-13
370-08
370-07
370-01
320-14
320-13
320-08
320-07
320-01
324-14
324-13
324-08
324-07
324-01
321-14
321-13
321-08
321-07
321-01
325-14
325-13
325-08
325-07
325-01
322-14
322-13
322-08
322-07
322-01
326-14
326-13
326-08
326-07
326-01
323-14
323-13
323-08
323-07
323-01
3
1 & 2
6
4 & 5
9
7 & 8
12
10 & 11
360
300
304
301
305
302
306
303
294
350
293-02
293-01
2941
340-03
340-02
292
3401
340-01
2921

Figure A13-1. Nodalization diagram of lower reactor vessel.

In each of the four radial rings, there is one pipe volume that represents the coolant flow inside the fuel assemblies, and one pipe volume that represents the coolant flow outside the fuel assemblies in the interstitial region surrounding the control blade. The interstitial volumes outside the fuel assemblies are connected by crossflow junctions to the volumes surrounding the fuel so that coolant is able to flow horizontally between the center and the periphery of the core. Only the crossflow junctions at the top of the core are represented in the diagram, even though all internal volumes are connected by crossflow junctions.

The primary coolant flow through the core, approximately 90 percent, is from the lower plenum through the fuel support pieces and lower tie plates into the fuel assemblies. The remaining 10 percent of the core coolant flow is through the interstitial region. Coolant enters the interstitial region by flowing through holes machined in the lower tie plates, leaking past the core plate, or flowing through the control rod guide tubes from the control rod drive cooling water pumps.

The jet pumps in the Browns Ferry reactor are represented by three volumes in each of the recirculation loops. In a BWR, the upper mixing sections of the jet pumps are connected to the lower diffuser sections by mechanical slip fits for easy removal during maintenance. The leakage through the slip joints is represented by junctions that connect the jet pumps to the annulus region.

The SCDAP components representing the core structures are shown in Figure A13-1. Eight SCDAP components were used to represent the core. Component 1 represents 432 fuel assemblies at the center of the core; Component 2 represents the 108 control blades in the central core region; Component 3 represents the 104 fuel assemblies in ring 2; Component 4 represents the 26 control blades in ring 2; Component 5 represents the 128 fuel assemblies in ring 3; Component 6 represents the associated 32 control blades in ring 3; Component 7 represent the 100 fuel assemblies in the peripheral ring; and Component 8 represents the 19 control blades in the periphery of the reactor core.

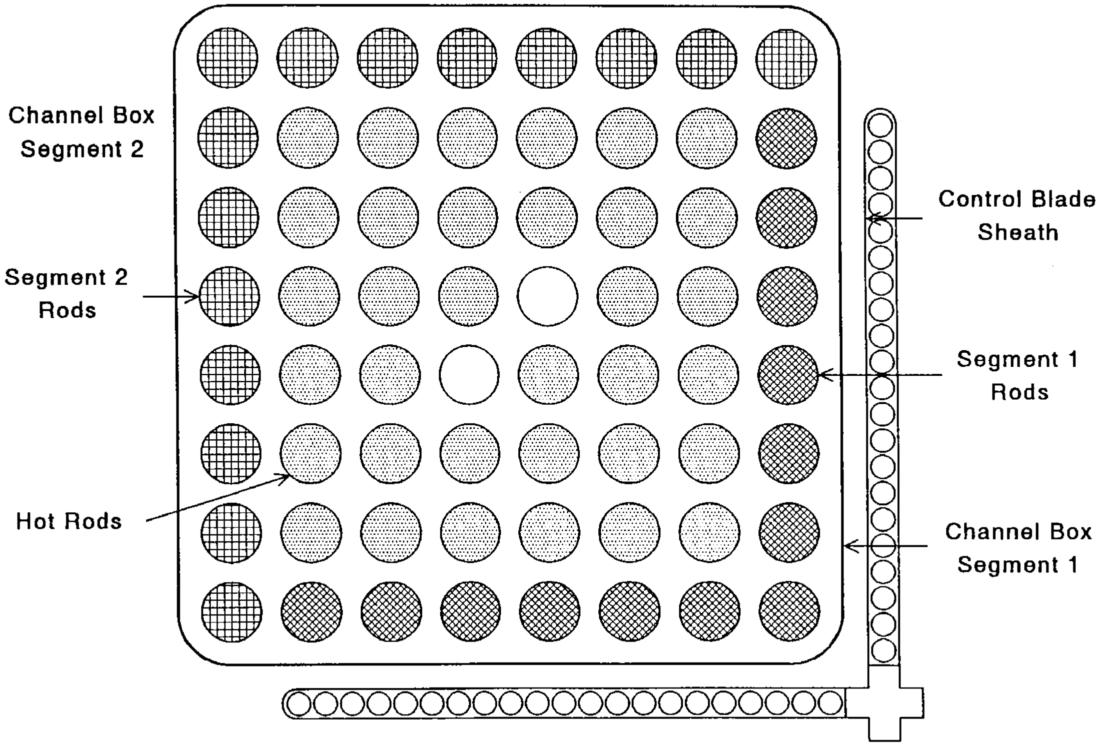

Figure A13-1. Component guide for detailed Browns Ferry SCDAP model.

The radial and axial power profiles used for the Browns Ferry accident simulation are shown in Figure A13-1 and Figure A13-1. As shown in these figures, the peripheral fuel assemblies produce only one third as much power as the center fuel assemblies. As shown in Figure A13-1, the peak power in the center fuel region is near the bottom of the core.

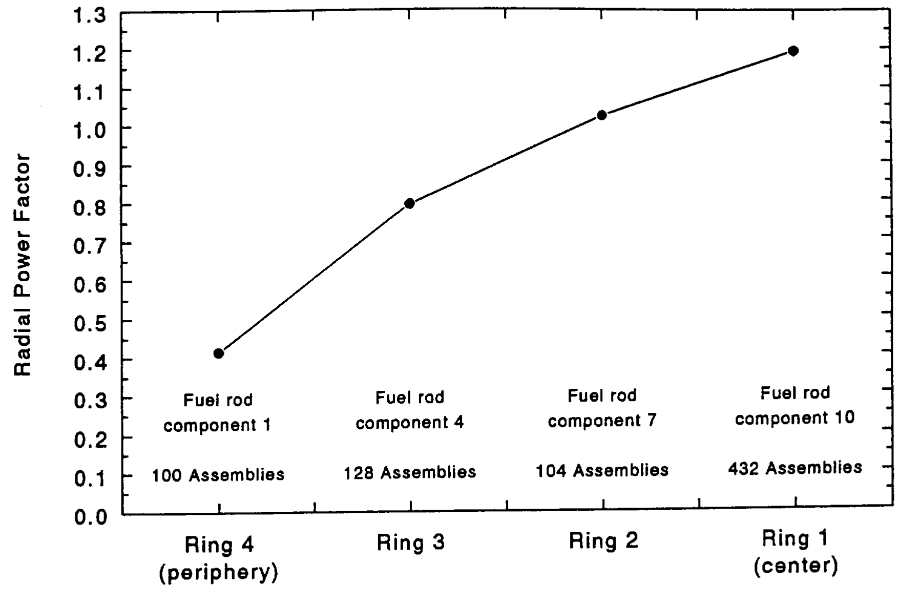

Figure A13-1. Browns Ferry radial power profile for 4 radial rings.

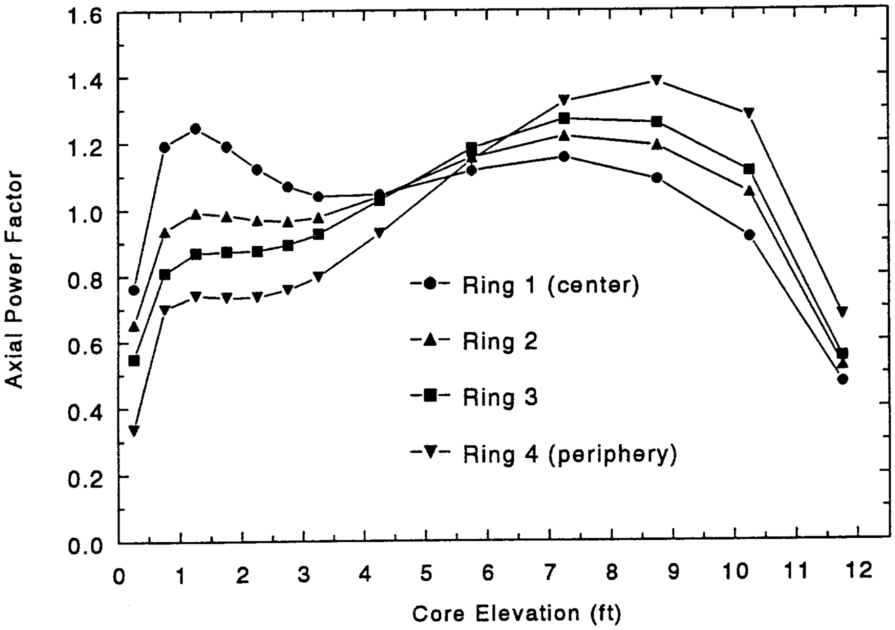

Figure A13-1. Browns Ferry power profiles for 13 axial nodes.

A13.2 Description of the Modeled BWR Severe Accident

The simulated LBLOCA was initiated with a break in one of the recirculating loops 300 seconds after the start of the transient. The reactor was scrammed 0.5 seconds after initiation of the break. Immediately after initiation of the accident the following events occurred. The water level in the annulus surrounding the reactor core dropped from approximately 15 to 4 m within a short period of time, fuel temperatures in the core dropped rapidly, and the pressure in the upper plenum of the reactor dropped from 7 MPa at the start of the accident to 0.40 MPa by the end of the accident. Immediately after the reactor scram, the main steam isolation valve (MSIV) opened and a recirculation pump tripped on. The voiding of the cooling water and the lowering of pressure in the reactor vessel triggered core uncovery. In the modeled accident the core uncovered over a period of ~25 seconds. Once a region in the core uncovered temperatures began rising, initially quite fast and later at a gradual rate. The upper elevations of the core heated faster and to higher temperatures than the lower elevations.

The containment for the Browns Ferry Nuclear Power plant was modeled as filled with saturated air at a constant pressure of 0.1 MPa. Before the start of the accident, the initial system pressure was 7.03 MPa. The initial system temperature was 558 K and the power was 3,000 MW. The initial inlet flow to the hot region in the reactor core was 2,900 kg/s.

A13.3 Results

This accident scenario, though not probable for a BWR, demonstrates that SCDAP/RELAP5/MOD3.3 is able to predict heating, cladding oxidation and melt relocation of the fuel rods, heating, oxidation and the subsequent relocation of the control blade and channel box into the lower head of the reactor, and eutectic interactions that occur between various core materials.

SCDAP/RELAP5/MOD3.3 predicts the first damage progression event, the formation and rupture of localized balloons in the fuel rod cladding, to occur 791 seconds into the simulated accident. The temperature of the fuel rod cladding at time of rupture is 1120 K. The first ballooning incident is predicted to occur in the center-most channel near the top (2.20 m) of the fuel rods in the reactor core. The ballooning and rupturing of fuel rods near the 2.20-m elevation of the modeled core is predicted to proceed radially outward through approximately 85% of the reactor core over a period of about 174 seconds as fuel rod cladding temperatures approach 1,200 K in each channel. Ballooning and rupture of fuel rods at the periphery of the core occur approximately 640 seconds later. The power produced in this peripheral region is approximately one third less than the power produced in the central region of the core, resulting in slower heating rates and the predicted delayed ballooning and rupture of the fuel rods.

As the reactor core continues to heat during the course of the simulated accident, the control blades begin melting as the zircaloy channel boxes oxidize. Eutectic interactions occur between the zircaloy of the channel box and the control blade stainless steel and boron carbide resulting in the melting and relocation of the control blades and finally the channel box. Figure A13-1 shows the predicted midplane radial temperature distribution across the reactor core of the stainless steel clad boron carbide control blades, and Figure A13-1 the predicted midplane radial temperature distribution across the reactor core of the channel boxes in the reactor core. As the temperature of the control blade in each channel reached 1,500 K, the blade melted and relocated into the lower head of the reactor. The relocation time for each blade channel is represented in Figure A13-1 as the transition from rapidly rising temperatures to a constant temperature of 1,500 K blade failure temperature. The control blade in the center-most channel begins relocating into the lower head of the reactor approximately 1,139 seconds into the simulated accident, when the blade temperature in the channel reaches 1,500 K. The blade in Channel 2 relocated 300 seconds later. Approximately 500 seconds after the blade in Channel 2 melted and relocated to the lower head, the blade in Channel 3 began to melt and relocate into the lower head of the reactor vessel. As shown in the figure the blade in the low power peripheral channel heated at a considerably slower rate and never completely relocated during the simulated LBLOCA. Once the blade attains 1,500 K at a specified elevation, the control material at that elevation relocates quickly into the lower head of the reactor. During the calculation the predicted relocation into the lower head is shown by increasing height of the debris bed.

As shown in Figure A13-1, the temperature histories of the channel boxes in each radial ring of the reactor show a behavior similar to the control blades. The disappearance of the channel box at midplane in the reactor core is shown by the transition to a constant temperature of 2,250 K, representative of the melting temperature of the zircaloy channel box material. Temperatures in the peripheral channel tend to be cooler due to the lower developed power, therefore, very little melting and relocation of the control blade and channel box material occurs.

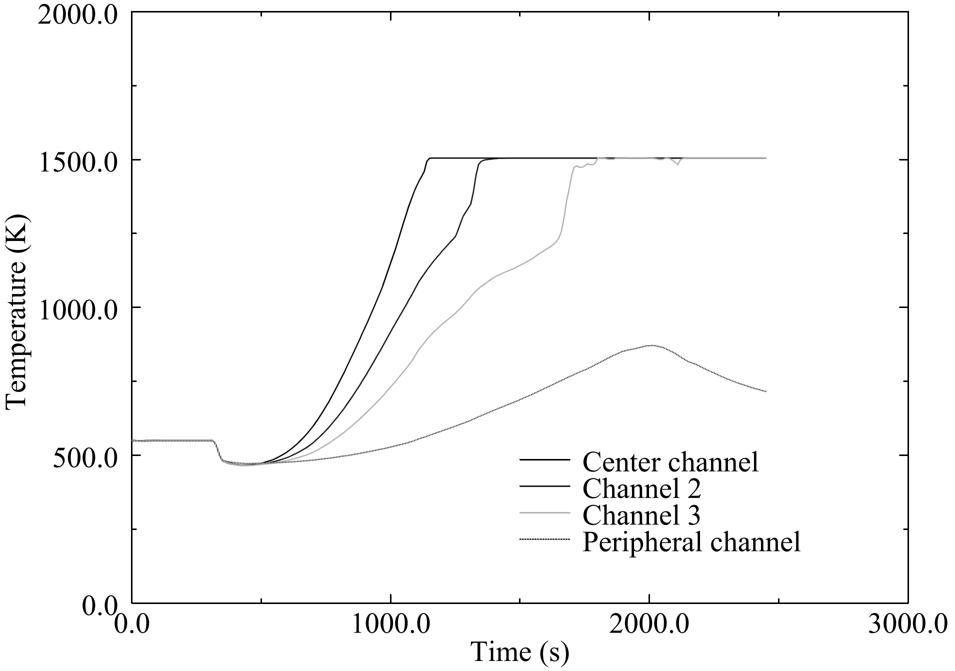

Figure A13-1. Predicted radial temperature distribution across reactor core of control blades.

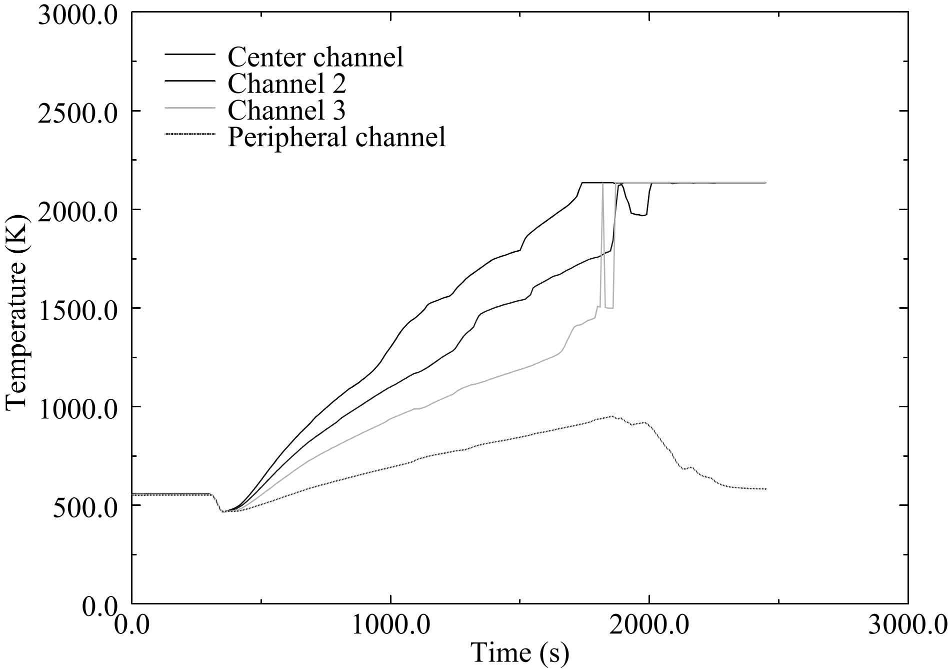

Figure A13-1. Predicted radial temperature distribution across reactor core of channel boxes.

Figure A13-1 to Figure A13-1 show predicted radial temperature distributions across the reactor core of fuel rods at three elevations, 0.5334, 0.9906, and 2.2210 m. As shown in the figures, the predicted radial temperature distribution follows the heating pattern established for the control blade and channel box. The temperatures in the inner two channels exceed 2,830 K, the temperature where the transition from intact geometry to molten material occurs, at the three elevations shown in the figures. The figures also show that rapid temperature changes in the two outermost channels are in response to the arrival of hot relocating material from higher elevations in the channel. The arrival of relocating material is indicated at a location by the sharp changes in the temperature of the fuel rod cladding.

The calculated system pressure is shown in Figure A13-1. Immediately after reactor scram (approximately 300 seconds into the transient), the system quickly depressurized to approximately 0.4 MPa. The depressurization coincided with the uncovery phase of the accident. Once the core uncovered, depressurization terminated and all elevations of the core entered a period of rapid heating. The period of zircaloy oxidation for all elevations indicated that the core had completely dried out. Fuel rod heating was mostly due to nuclear heat generation, as shown by the considerably slower heating rates in the peripheral regions of the core at all elevations.

The initial formation of molten material occurs near the upper middle of the reactor core and progresses upward and downward with time. The initial hot spot for each modeled component occurred near the axial center of the fuel assembly. The first area to begin the transition from intact geometry to molten material was in the highest power central channel.

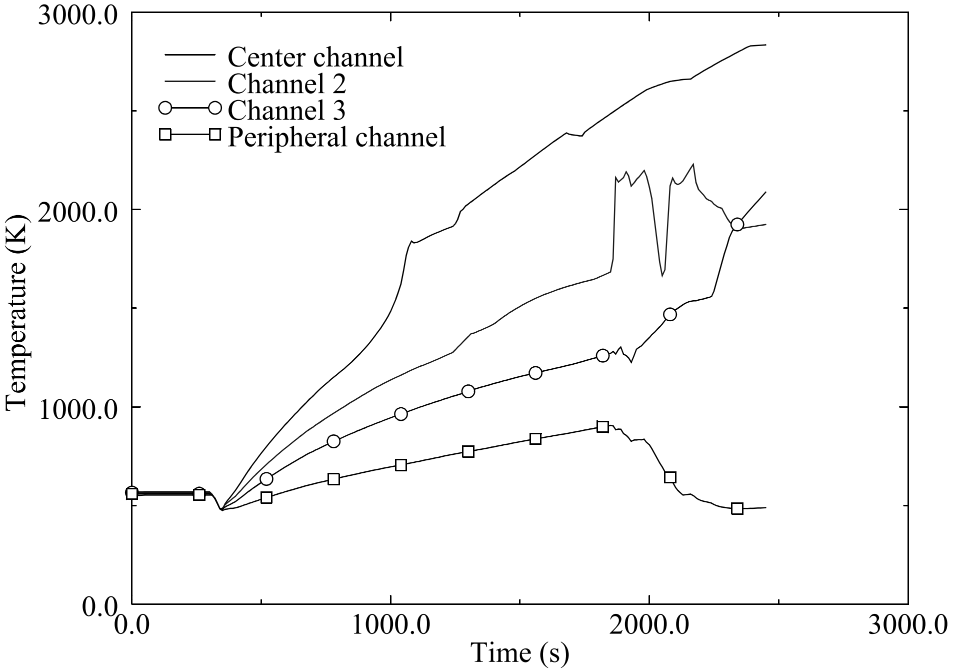

Figure A13-1. Predicted radial temperature distribution across reactor core of fuel rods at the 0.5334 m elevation.

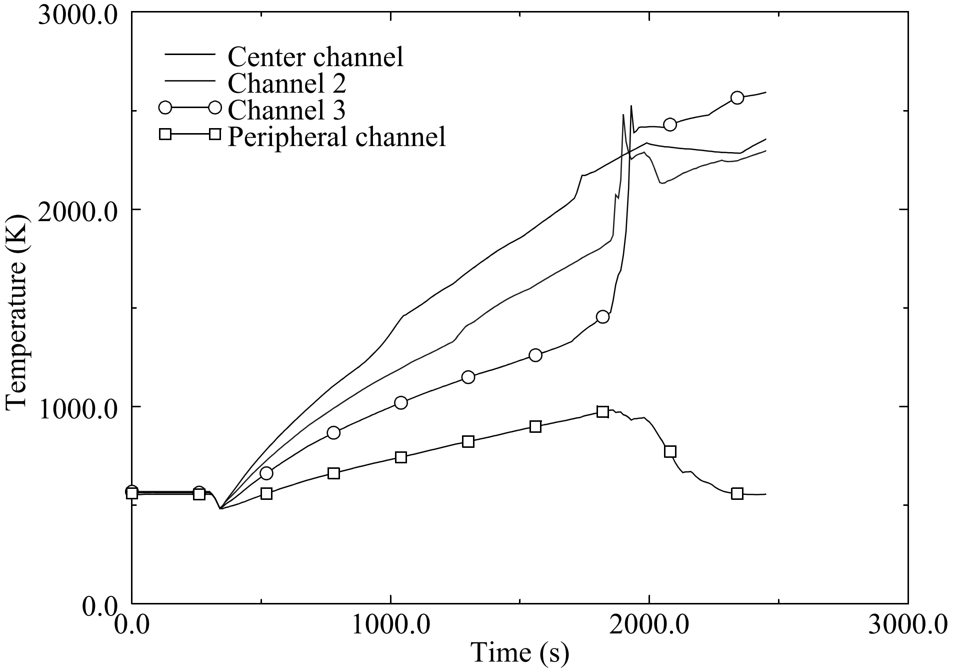

Figure A13-1. Predicted radial temperature distribution across reactor core of fuel rods at the 0.9906 m elevation.

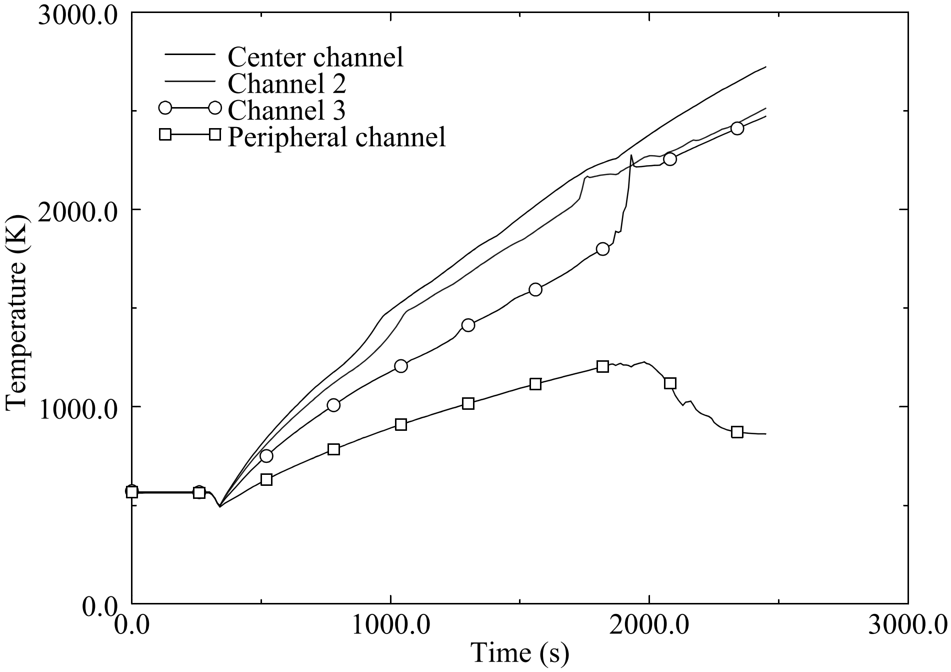

Figure A13-1. Predicted radial temperature distribution across reactor core of fuel rods at the 2.2210 m elevation.

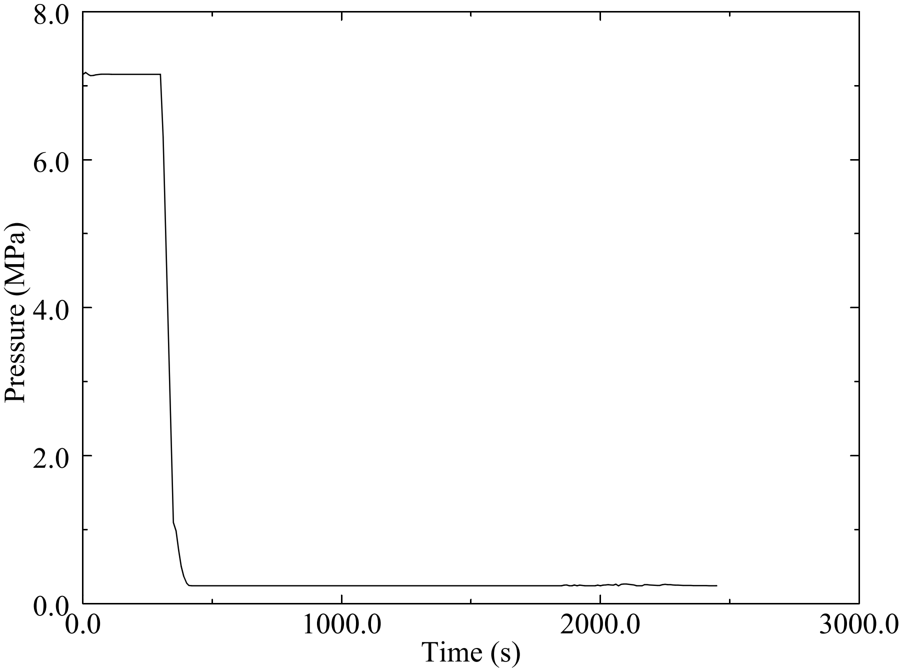

Figure A13-1. Predicted Browns Ferry system pressure.

Figure A13-1 shows the predicted hydrogen production during the simulation of the LBLOCA. As shown in this figure, approximately 350 kg of hydrogen were produced during this simulated severe accident.

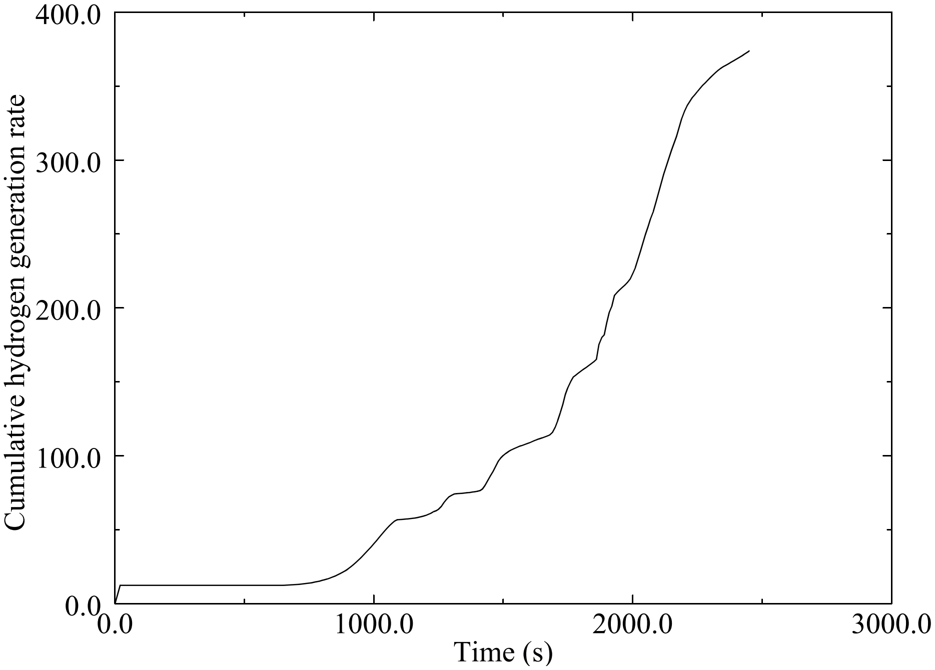

Figure A13-1. Predicted integral hydrogen production.

In summary, the Brown's Ferry BWR LOCA Severe Accident test problem demonstrated the capability to calculate the behavior of a BWR during a severe accident. Damage progression in the BWR was analyzed from its beginning out to the time of slumping of most of the reactor core to the lower head of the reactor vessel. All of the major damage progression that can occur in a BWR reactor core during a severe accident was calculated to occur during the analyzed accident sequence. The calculated damage progression included oxidation and meltdown of fuel rods, control blades, and channel boxes. The late phase damage progression was calculated to occur more rapidly than is the case for a TMLB' type of a severe accident in a PWR. The more rapid progression of damage was due to the rapid depressurization of the reactor core resulting from the imposed large break in the primary coolant system piping. The calculated damage progression also differed from that in a PWR in that damage to the bottom of the reactor core was calculated to occur almost as rapidly as damage to the top of the core.

A14. SURRY PWR SEVERE ACCIDENT

A14.1 Introduction

The analysis of a severe accident in the Surry nuclear power plant was performed to exercise and evaluate damage progression models in SCDAP/RELAP5/MOD3.3 under conditions typical of those expected in a typical plant severe accident analysis. The information in this section is arranged as follows: The design of the Surry nuclear power plant and the SCDAP/RELAP5/MOD3.3 nodalization of the plant are described in Section A14.2. The severe accident sequence that was selected for analysis is described in Section A14.3 and the calculation results are presented in Section A14.4.

A14.2 Model Description and Nodalization

The Surry nuclear power plant is a typical Westinghouse three-loop pressurized water reactor (PWR) with a rated thermal power of 2,441 MW_t. The core consists of 157 15 x 15 fuel assemblies with an active fuel height of 3.66 m. Each of the three primary coolant loops contains a U-tube steam generator, a reactor coolant pump (RCP), and associated piping. A single pressurizer is attached to the hot leg piping of one of the three primary coolant loops. The pressurizer surge line and the hot/cold leg piping are constructed of stainless steel. The steam generator tubes are made of Inconel. The power operated relief valves (PORV) is located at the top of the pressurizer and can be used to relieve excess pressure in Reactor Coolant System (RCS). Pressurizer Safety Relief Valves (SRV) are also available to handle pressure excursions in excess of the pressurizer PORV capacity. An accumulator, containing 29,100 kg of borated water at 322 K, is attached to each cold leg. The accumulators, which are initially pressurized to 4.24 MPa with a nitrogen cover gas, are the only operational part of the emergency core cooling system (ECCS) during a station blackout. A large, dry, subatmospheric pressure containment building surrounds the reactor system.

The RELAP5 nodalization of the reactor core and vessel is shown in Figure A14-1. In this figure the reactor core is represented using 5 radial segments (flow channels) and ten axial nodes. One assessment case was performed using 5 flow channels and 20 axial nodes in the reactor core as part of a sensitivity study. Each flow channel is connected to its neighboring flow channels by crossflow junctions, thus flow in the lateral direction through the core is modeled. Separate RELAP5 control volumes are used to represent the core bypass and the downcomer. The core bypass is represented by a RELAP5 control volume (pipe) containing five sub-volumes and the downcomer is represented by a RELAP5 control volume (pipe) with seven sub-volumes. Two RELAP5 control volumes are used to represent the lower plenum and seventeen RELAP5 control volumes to represent the upper plenum region of the reactor vessel.

The RELAP5 nodalization of the coolant loop with the pressurizer connected to the hot leg is shown in Figure A14-2. The non-pressurizer loops were modeled with nodalizations similar to that shown in Figure A14-2. The hot leg is represented by five RELAP5 control volumes, the cold leg by four RELAP5 control volumes, the surge line by three RELAP5 control volumes, and the pressurizer by eight RELAP5 control volumes. The primary side of the steam generator is represented by eight RELAP5 control volumes

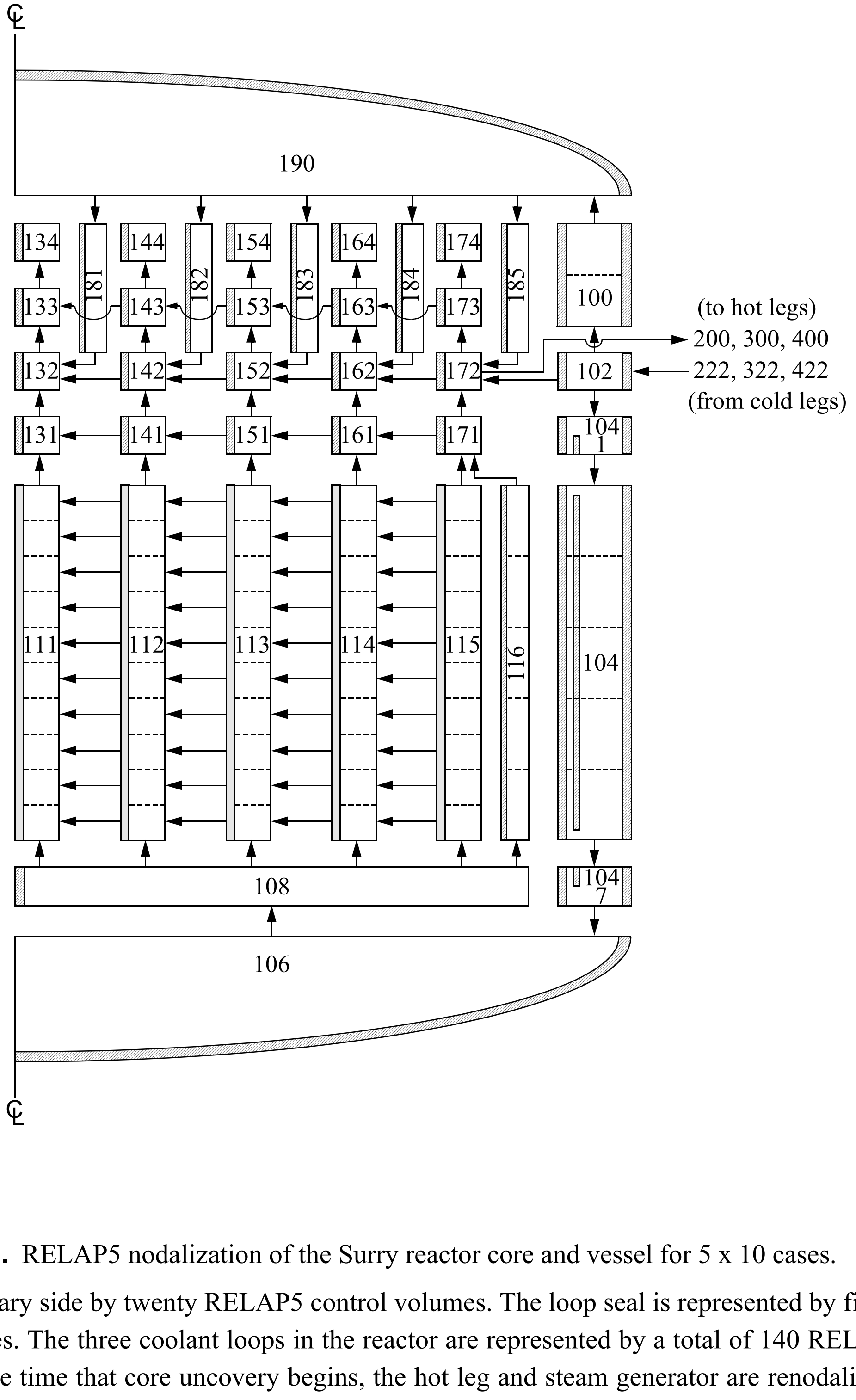
℄
190
134
144
154
164
174
181
182
183
184
185
100
133
143
153
163
173
(to hot legs)
200, 300, 400
132
142
152
162
172
102
222, 322, 422
(from cold legs)
131
141
151
161
171
104
1
111
112
113
114
115
116
104
108
104
7
106
℄

Figure A14-1. RELAP5 nodalization of the Surry reactor core and vessel for 5 x 10 cases.

and the secondary side by twenty RELAP5 control volumes. The loop seal is represented by five RELAP5 control volumes. The three coolant loops in the reactor are represented by a total of 140 RELAP5 control volumes. At the time that core uncovery begins, the hot leg and steam generator are renodalized to allow single-phase countercurrent flow in the hot leg.

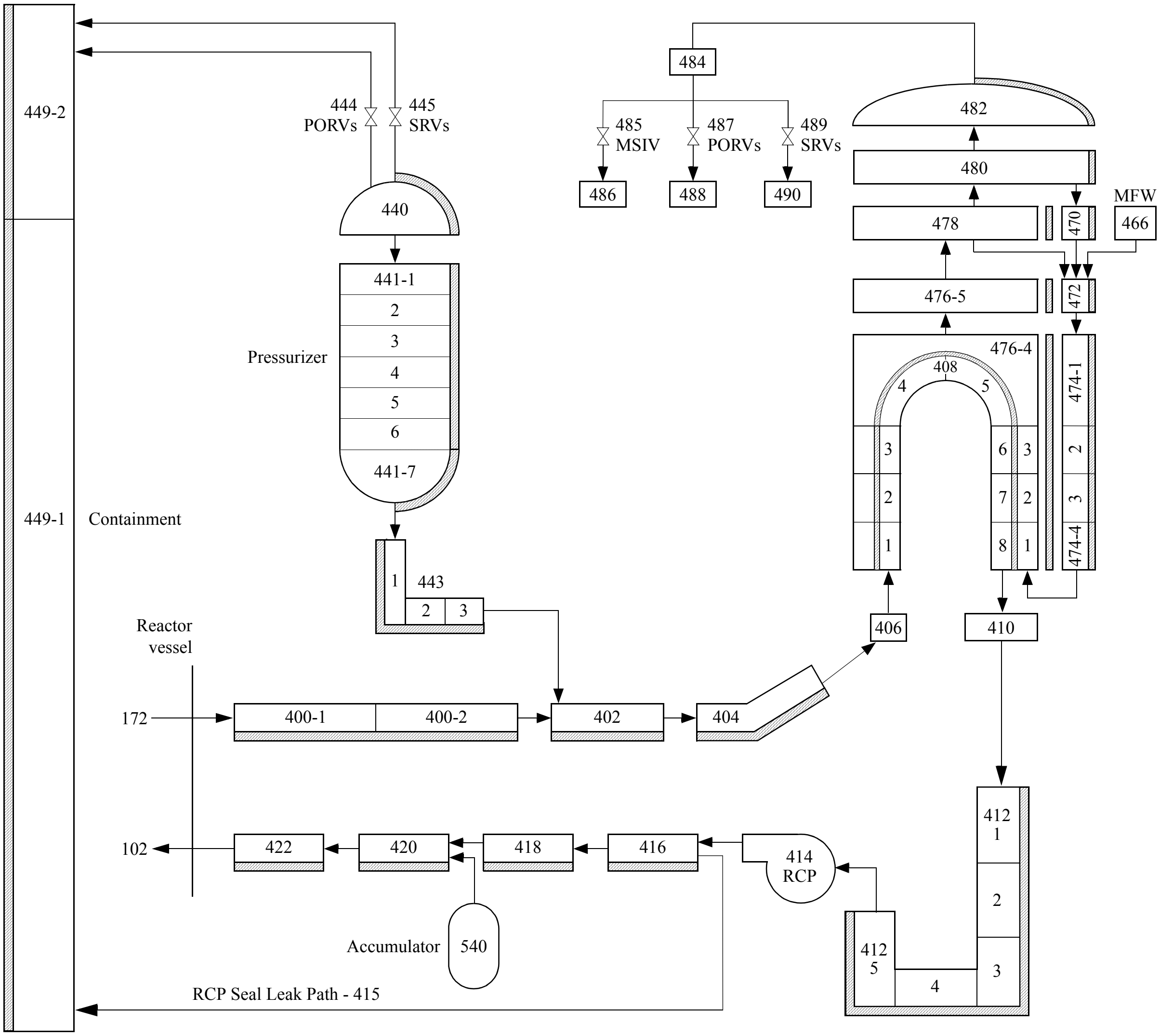
449-2
449-1
Containment
444
PORVs
445
SRVs
440
441-1
2
3
4
5
6
441-7
Pressurizer
443
1
2
3
Reactor
vessel
172
400-1
400-2
402
404
406
410
102
422
420
418
416
414
RCP
Accumulator
540
RCP Seal Leak Path - 415
412
1
2
3
4
412
5
484
485
MSIV
487
PORVs
489
SRVs
486
488
490
482
480
478
470
MFW
466
476-5
472
476-4
408
474-1
2
3
474-4
1
2
3
4
5
6
7
8

Figure A14-2. RELAP5 nodalization of the Surry primary system loop

A radial cross-section of the nodalization of the reactor core is shown in Figure A14-3. The first radial segment represents the 5 fuel assemblies at the center of the core. The second radial segment begins at the outer boundary of the first radial segment and extends to the inner boundary of the third segment. This segment represents 20 fuel assemblies. The third and fourth radial segments represent fuel assemblies progressing radially outward from the second radial segment and the fifth radial segment represents the fuel assemblies at the periphery of the core. The third segment represents 36 fuel assemblies, the fourth represents 60 fuel assemblies, and the fifth represents 36 fuel assemblies. Each of the radial segments corresponds to a flow channel represented by one of the RELAP5 pipe volumes for the reactor core. The numbering for the pipe volumes is as follows: radial segment 1 is 111, segment 2 is 112, segment 3 is 113, segment 4 is 114, and segment 5 is 115.

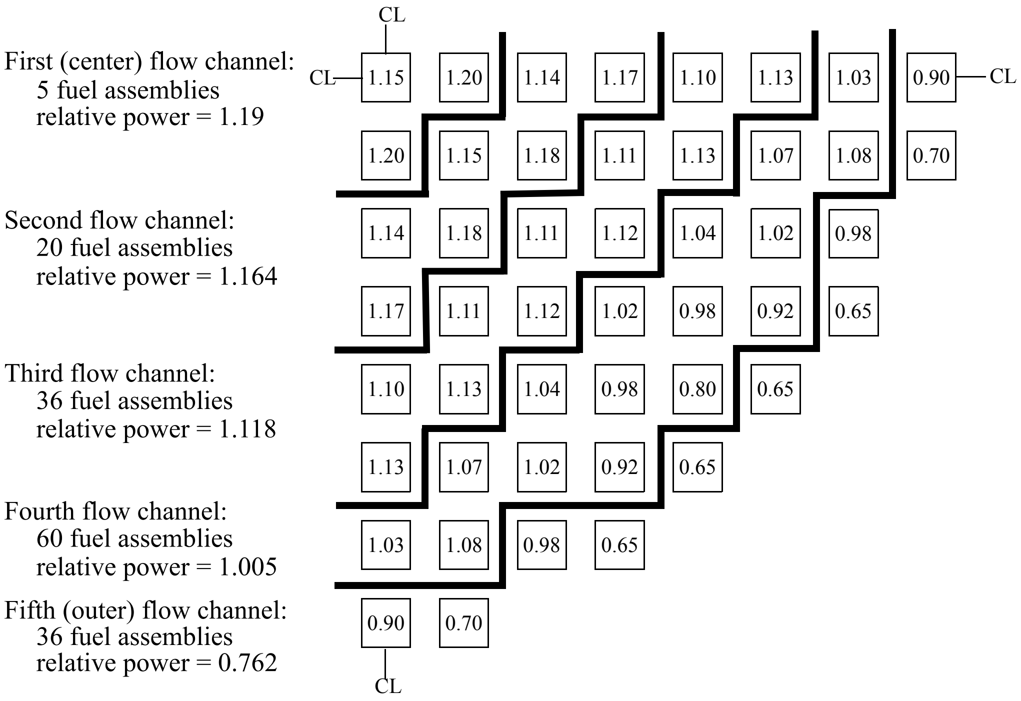
CL
CL
1.15 1.20 1.14 1.17 1.10 1.13 1.03 0.90
CL
1.20 1.15 1.18 1.11 1.13 1.07 1.08 0.70
1.14 1.18 1.11 1.12 1.04 1.02 0.98
1.17 1.11 1.12 1.02 0.98 0.92 0.65
1.10 1.13 1.04 0.98 0.80 0.65
1.13 1.07 1.02 0.92 0.65
1.03 1.08 0.98 0.65
0.90 0.70
CL
First (center) flow channel:
5 fuel assemblies
relative power = 1.19
Second flow channel:
20 fuel assemblies
relative power = 1.164
Third flow channel:
36 fuel assemblies
relative power = 1.118
Fourth flow channel:
60 fuel assemblies
relative power = 1.005
Fifth (outer) flow channel:
36 fuel assemblies
relative power = 0.762

Figure A14-3. Radial cross-section of Surry reactor vessel showing nodalization of the core.

The fuel rods in each fuel assembly were represented by a SCDAP fuel rod component and the control rods were represented by a SCDAP PWR control rod component. Each individual fuel assembly was represented as having 204 fuel rods and 21 control rods. Each fuel rod and control rod was divided into ten axial nodes. The water rods in the outermost radial segment were represented by a SCDAP control rod component model containing an extremely small quantity of control material and the empty zircaloy guide tubes in the center ring were represented by a fuel rod component model with an extremely small fuel pellet. The fuel rods have a fuel pellet stack that is 3.6576 m in length. The fuel pellets in each fuel rod have a radius of 4.634 mm. The outer radius of the fuel rod cladding was 5.359 mm with a cladding thickness of 0.617 mm. The reactor core was represented by a total of ten SCDAP components; two fuel rod component models in the center radial segment and a fuel rod and control rod component in each of the four other radial segments. The core of the reactor contained six Inconel spacer grids located at the following elevations, 0.0 m, 0.73 m, 1.46 m, 1.83 m, 2.19 m, and 2.93 m, respectively. These spacer grids were represented using the SCDAP spacer grid model.

The severe accident analyzed was a station blackout without operator actions. This type of accident is designated at a TMLB’ sequence. The accident is initiated by loss of off site power. Onsite ac power is also unavailable because the diesel generators fail to start or fail to supply power. Decay heat removal through the steam generators cannot be maintained in the long term because there is no ac power for the electrical pumps, and the steam driven auxiliary feedwater pumps also fail to supply water. As the RCS depressurizes during the accident, the RCP loop seals may clear.

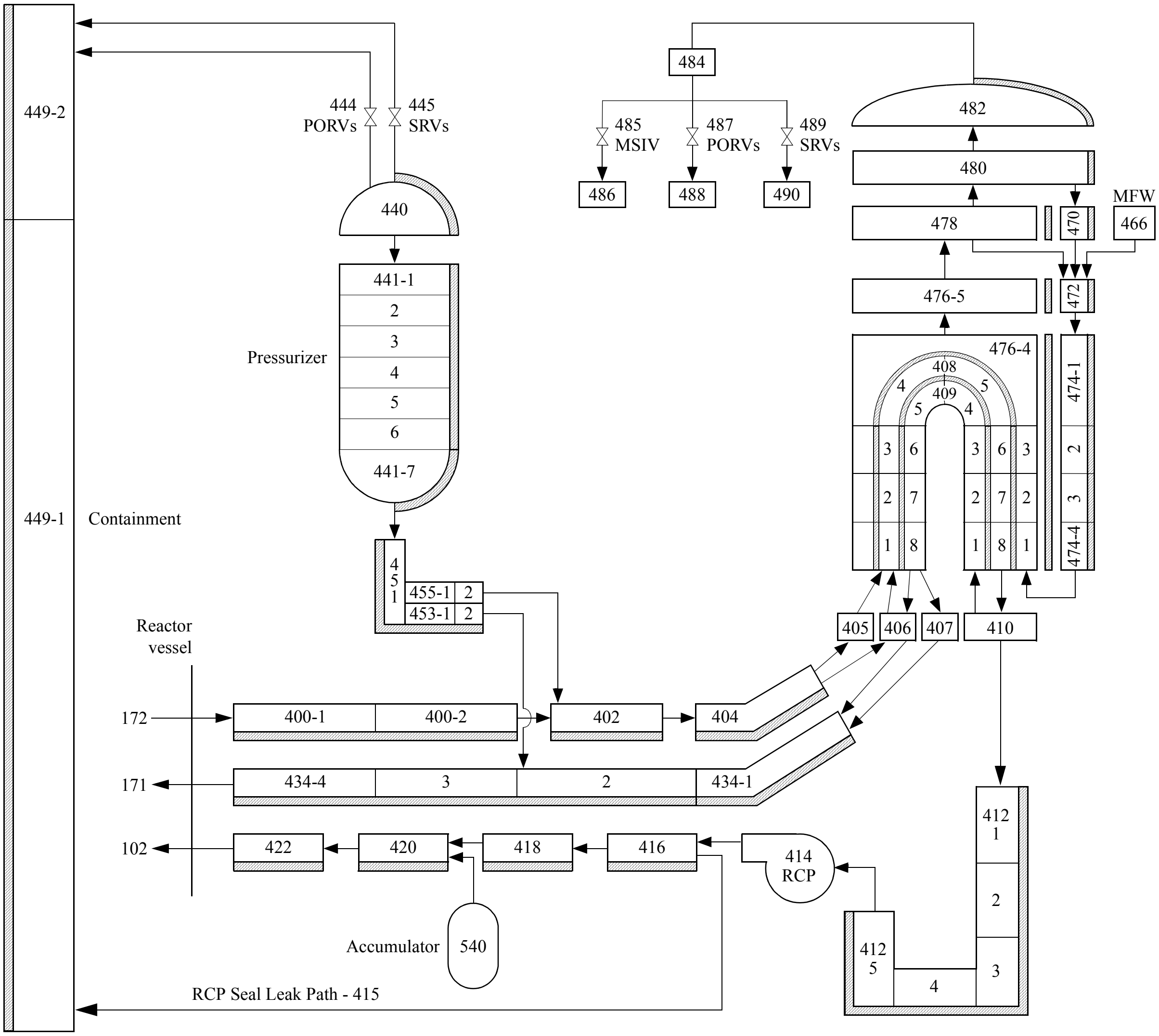
449-2
449-1
Containment
444 PORVs
445 SRVs
440
441-1
2
3
4
5
6
441-7
Pressurizer
451
455-1
453-1
2
Reactor vessel
172
171
102
400-1
400-2
402
404
434-4
3
2
434-1
422
420
418
416
414 RCP
412 1
2
3
4
412 5
Accumulator
540
RCP Seal Leak Path - 415
484
485 MSIV
487 PORVs
489 SRVs
486
488
490
482
480
478
470
MFW
466
476-5
472
476-4
408
409
474-1
474-4
405
406
407
410

Figure A14-4. Nodalization for modeling natural circulation in hot leg and steam generator.

When natural circulation began in the reactor vessel and the hot leg began draining, a renodalization of the hot leg and steam generators was performed. Figure A14-4 and Figure A14-5 show the ex-vessel nodalization used for Surry analyses after the hot leg drained. The new nodalization provided the additional flow paths needed to simulate hot leg countercurrent natural circulation, which develops only after the hot legs are voided. A horizontal section of the modeled surge line in the Surry PWR connects to the centerline of the hot leg piping. This orientation required the modeling of a split surge line to represent potential countercurrent flow in a manner similar to that used for the rest of the loop piping. The associated valves (component number 463 and 465 in Figure A14-5) open whenever the pressurizer PORV opens so that fluid from both halves of the hot leg will be drawn into both halves of the surge line during valve cycles.

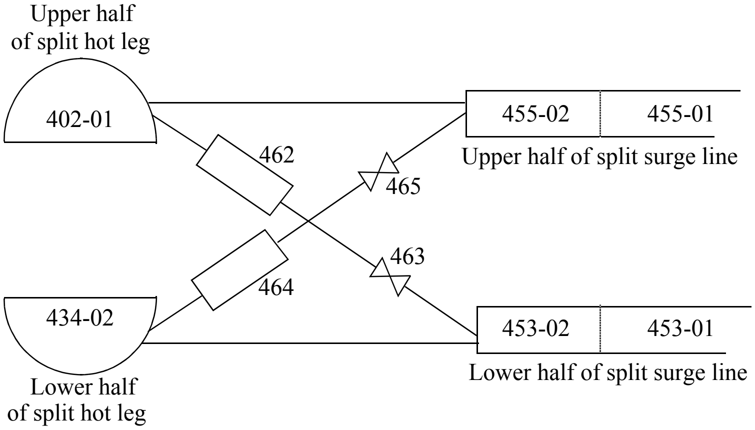

Figure A14-5. Arrangement of junction and valves for modeling natural circulation.

The nodalization changes shown in Figure A14-4 were needed to accommodate both full-loop and hot leg countercurrent natural circulation. These changes were accomplished by using servo valves to connect (a) the split hot leg to the split steam generator inlet plenum, (b) the split steam generator inlet plenum to the split steam generator tube bundle, and (c) the split steam generator tube bundle to the steam generator outlet plenum. The valves were configured with two sets of loss coefficients, one set consistent with those used to model normal plant operation and one set appropriate to model hot leg countercurrent natural circulation. The other loss coefficients in the loop network were unaltered relative to those used for normal plant operation. These loss coefficients were equivalent to those used prior to the draining of the hot leg. If the horizontal portion of the RCP loop seal in a given loop is full of liquid, control logic directs the code to use the countercurrent flow loss coefficients for all servo valves in the loop. Alternately, if voids begin to form in the horizontal portion of the RCP loop seal, control logic directs the code to use the loss coefficient values for normal plant operation for the servo valves in the loop. As a result of the use of this modeling logic, both full-loop and countercurrent natural circulation flow should be calculated correctly in each loop as the code responds to changing loop conditions during the accident.

The Surry PWR model used a simple two volume representation for the reactor containment (Volumes 449-1 and 449-2 in Figure A14-2 and Figure A14-4). This nodalization was not expected to adequately calculate condensation of the primary effluent. Without a reasonable prediction of primary effluent condensation, a reasonable prediction of containment pressure cannot be expected. To resolve this problem, the pressure in the reactor containment was not allowed to rise higher than 0.2 MPa. Input was included in the model to calculated creep rupture of the stainless steel surge line (Volume 455-2 in Figure A14-4), the three stainless steel hot legs (Volume 400-1 in Figure A14-4 and Volumes 200-1 and 300-1 in areas of the non-pressurizer loops which are not shown in the nodalization diagrams), the hottest of the Inconel steam generator tubes (Volume 408-1 in Figure A14-4), and Volumes 208-1 and 308-1 in areas of the non-pressurizer loops which are not shown in the nodalization diagrams).

A14.3 Boundary Conditions for TMLB' Severe Accident

A Surry TMLB' with a failed steam generator (SG) relief valve and intentional RCS depressurization was analyzed. The accident sequence was similar to that performed for the resolution of the issue of SG tube integrity.[A14-1] Reference A.14-1 provides details on the severe accident sequence analyzed, denoted Case 20. The sequence is basically a postulated station blackout transient in Surry with concurrent failure of the diesel generators and steam driven auxiliary feedwater pumps. Additionally, the pressurizer loop SG secondary side atmospheric dump valve (ADV) is assumed to fail open on the first challenge. Also, the operator is assumed to latch open the pressurizer PORV when the core exit steam temperature reaches 922 K. The sequence produces RCS depressurization by way of the latched open PORV, resulting in accumulator injection, core melting and relocation to the lower head with subsequent lower head failure. RCS piping was monitored for creep rupture failure but a break in the ruptured pipe was not imposed.

The MOD3.3 and MOD3.2 calculations of the timing of creep rupture of the surge line were similar. The calculated primary coolant system thermal hydraulic behavior and the overall damage progression for the two code versions were also similar. Comparisons of the calculated timing of events in the primary coolant system and in damage progression are shown in Table A14-1. The calculated timing of creep rupture of the surge line for MOD3.3 and MOD3.2 were 24,205 s and 22,515 s, respectively.

Table A14-1. Comparison of SCDAP/RELAP5/MOD3.3 and SCDAP/RELAP5/MOD3.2 calculations of timing of events in primary coolant system and in damage progression for Surry TMLB' with failed SG ADV and intentional RCS depressurization.

Event	**Time (s) for**	
	MOD3.3	**MOD3.2**
TMLB' initiation	0	0
Collapsed liquid level falls below top of fuel rods	8,916	8,915
Collapsed liquid level falls below bottom of fuel rods	10,600	10,618
Onset of fuel rod oxidation	11,590	11,045
Pressurizer surge line fails by creep rupture	24,205	22,515
Accumulators/core flood tank empty	25,000	25,865

The MOD3.3 coolant condition histories for the reactor core and primary coolant system are shown in Figures A14-6, A14-7, and A14-8 respectively. The primary system pressure response, reactor vessel collapsed liquid level, and the liquid inventory for the pressurizer loop accumulator (nonpressurizer loops accumulators are shown. The calculated thermal hydraulic response is similar to that calculated by MOD3.2.

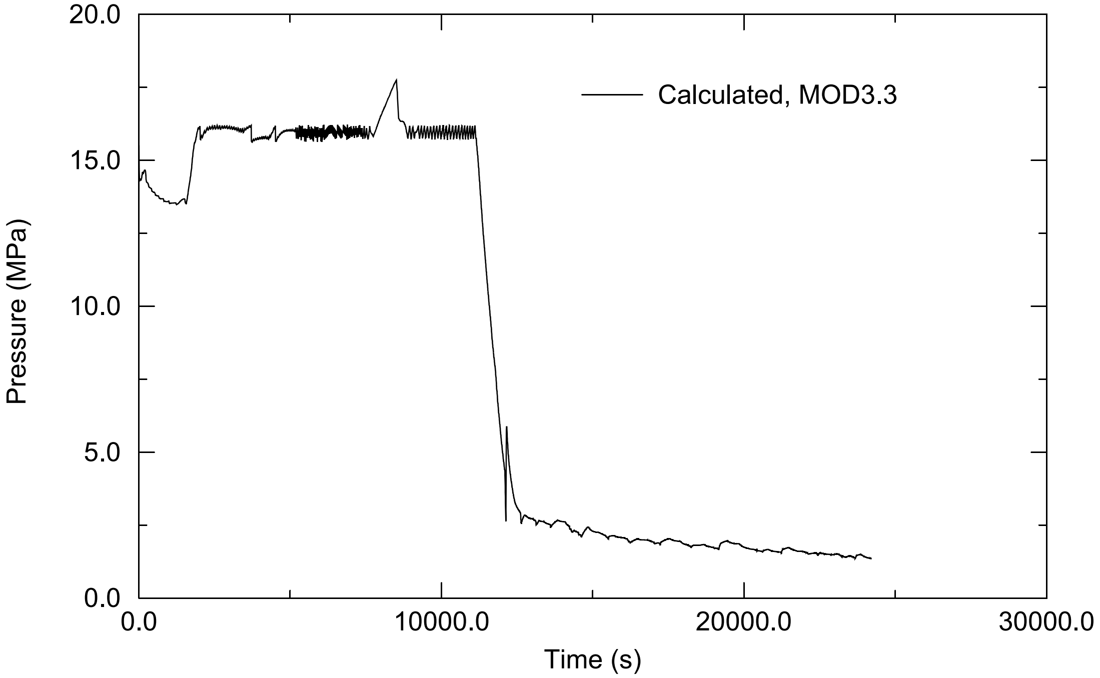

Figure A14-6. MOD3.3 calculation of pressurizer steam dome pressure for the Surry TMLB' with failed SG ADV and intentional depressurization.

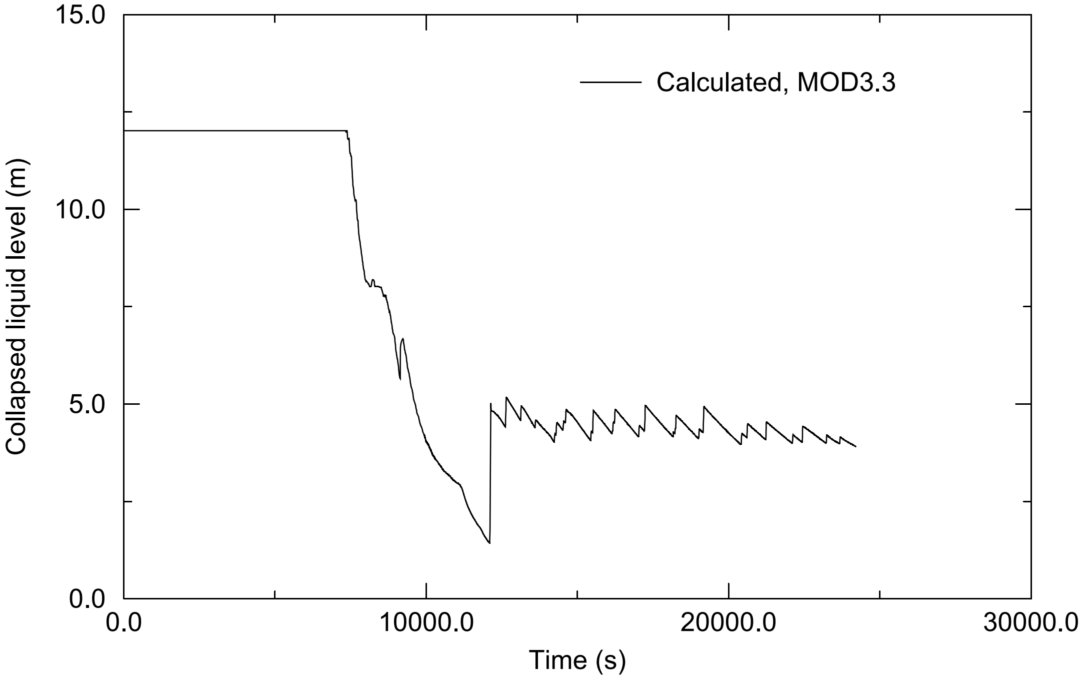

Figure A14-7. MOD3.3 calculation of reactor vessel collapsed liquid level for the Surry TMLB' with failed SG ADV and intentional depressurization.

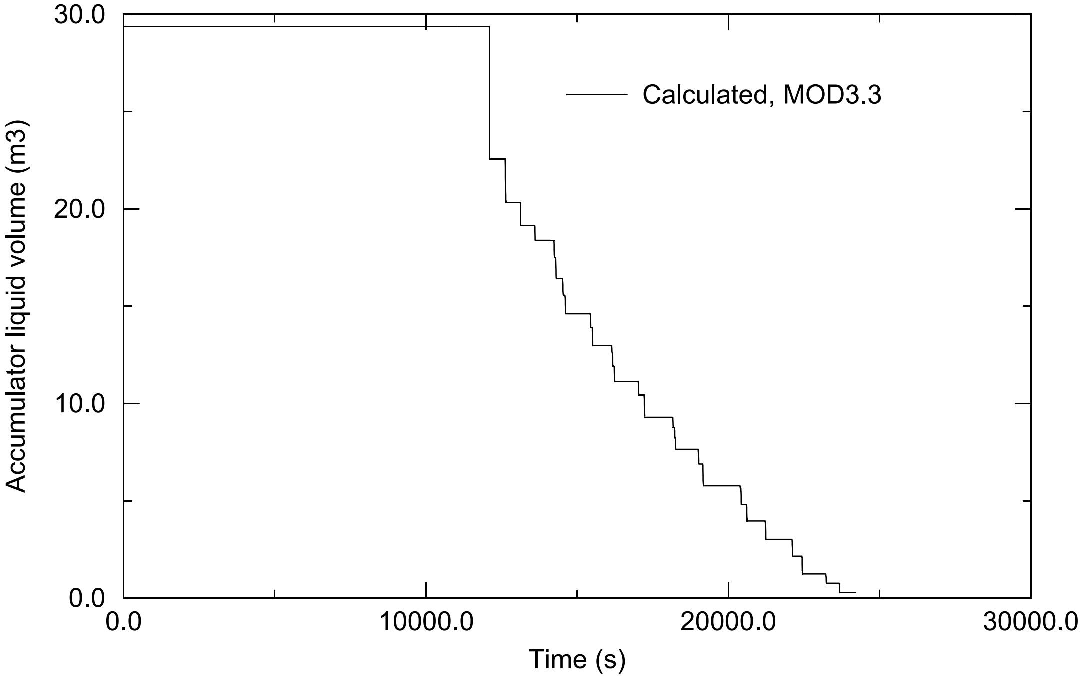

Figure A14-8. MOD3.3 calculation of pressurizer loop accumulator liquid inventory for the Surry TMLB' with failed SG ADV and intentional depressurization.

MOD3.3 calculated that accumulator injection delayed the onset of rapid oxidation of the reactor core. A plot of core maximum temperature is shown in Figure A14-9. A plot of the cumulative hydrogen production is shown in Figure A14-10. The cumulative hydrogen production was calculated to be 152 kg at the time of surge line failure. A plot of the temperature history of the surge line is shown in Figure A14-11.

A14.4 References

A14-1. D. L. Knudson and C. A. Dobbe, SCDAP/RELAP5 Evaluation of the Potential for Steam Generator Tube Rupture when the Reactor Coolant System is Depressurized, DLK-4-97, INEEL, May 23, 1997.

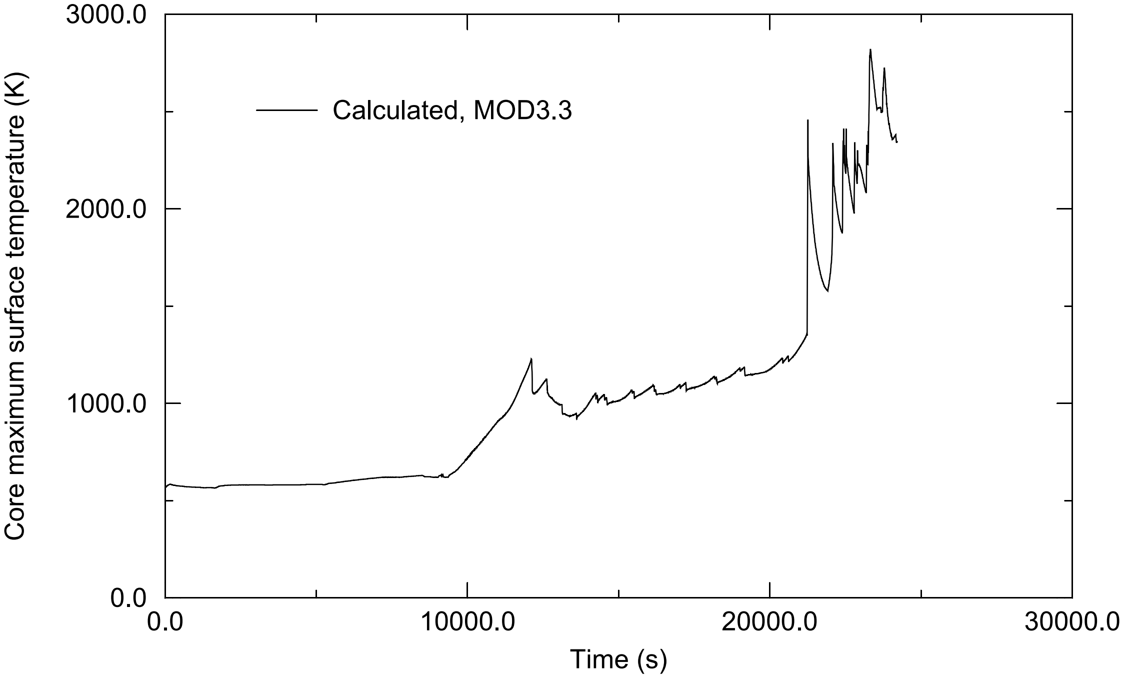

Figure A14-9. MOD3.3 calculation of core maximum peak cladding temperature for the Surry TMLB' with failed SG ADV and intentional depressurization.

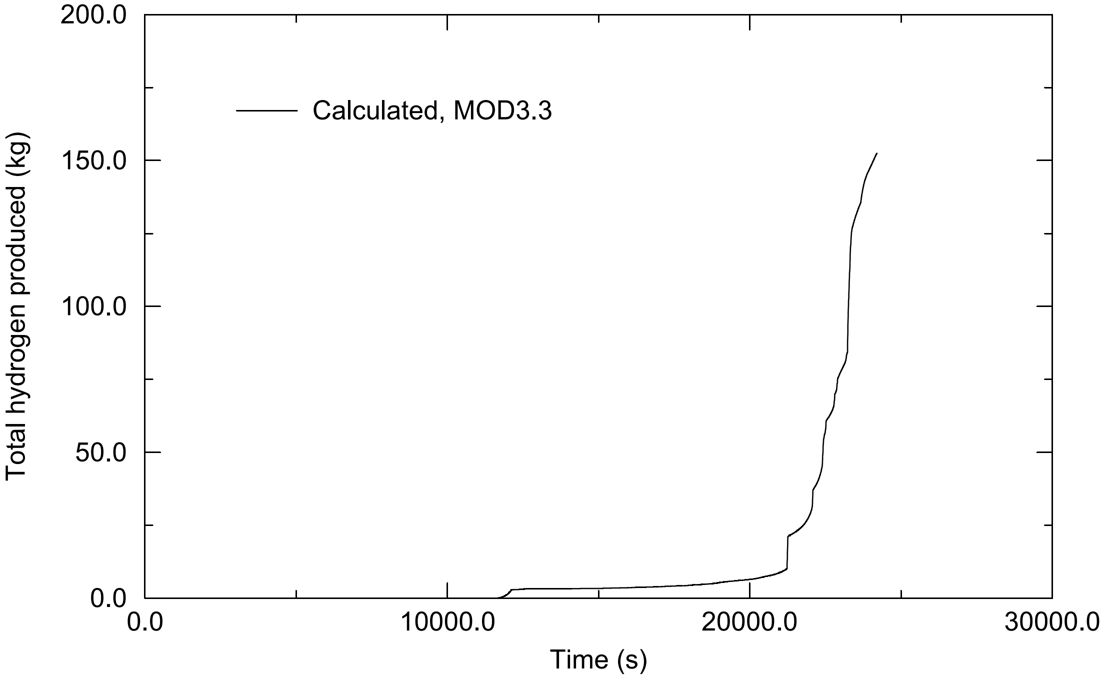

Figure A14-10. MOD3.3 calculation of total hydrogen production for the Surry TMLB' with failed SG ADV and intentional depressurization.

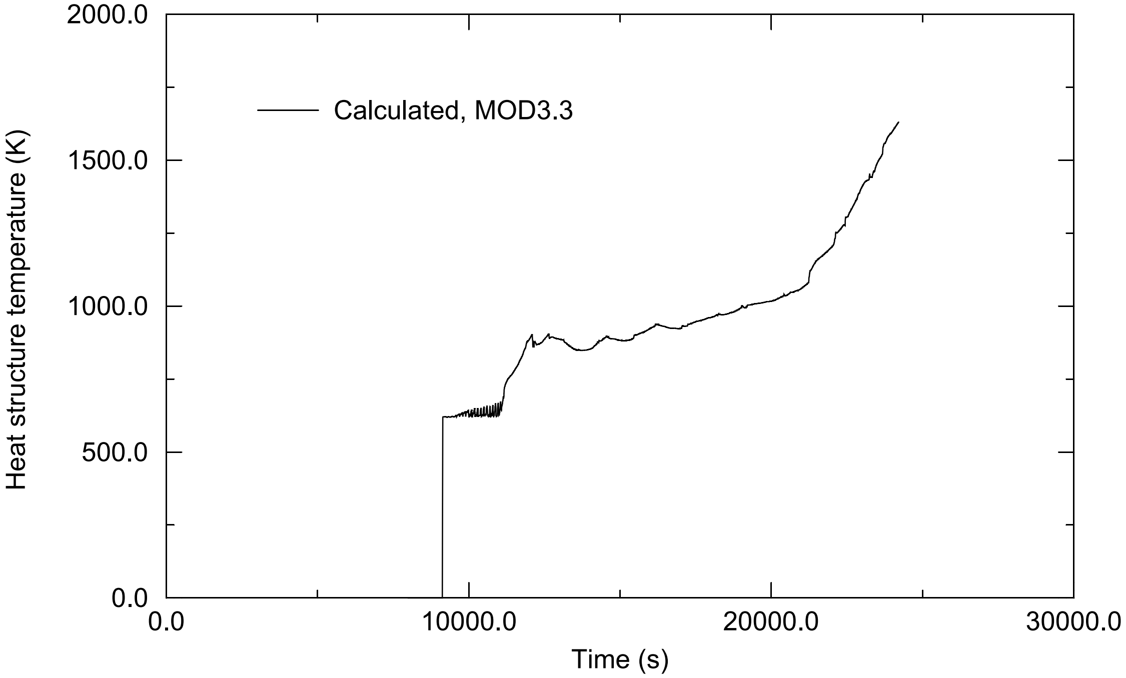

Figure A14-11. MOD3.3 calculation of surge line nozzle volume average temperature for the Surry TMLB’ with failed SG ADV and intentional depressurization.